UNIVERSITY OF CALIFORNIA SAN DIEGO

Dispersion, rheology and microfluidic flow actuation of active particle suspensions

A dissertation submitted in partial satisfaction of the
requirements for the degree
Doctor of Philosophy

in

Engineering Sciences (Mechanical Engineering)

by

Roberto Alonso-Matilla

Committee in charge:

Professor David Saintillan, Chair
Professor Juan C. del Alamo
Professor Juan C. Lasheras
Professor Jeremie Palacci
Professor William R. Young

2018

The dissertation of Roberto Alonso-Matilla is approved, and it is acceptable in quality and form for publication on microfilm or electronically:

Chair

University of California San Diego

2018

EPIGRAPH

... It is not the knowledge but the act of learning, not the possession but the acquiring, not the being-there but the getting there that afford the greatest satisfaction. When I have clarified and exhausted a subject, I leave it in order to go again into darkness. Thus is that insatiable person so strange: when completing a structure, it is not in order to dwell in it peacefully, but to start another.

Carl Friedrich Gauss

TABLE OF CONTENTS

LIST OF FIGURES

LIST OF TABLES

ACKNOWLEDGEMENTS

First and foremost, I want to thank my research advisor David Saintillan—an excellent professor and a fantastic scientist. It has been an honor and privilege working under his guidance and attending his classes. I have learnt a massive amount of knowledge from him, and I will always take him as an example in science. I appreciate him for his endeavors to support the strides in my research. He provided continuous feedback on my work, searched vigorously for funding, and provided a conducive environment for positive group dynamics, such as research meetings, journal clubs, scientific conferences and summer schools. Thanks to his effort, my Ph.D. experience has been very productive and stimulating. I want to highlight his superb writing skills, his systematic and efficient method of teaching, his human qualities and his encouragement for student's self-determination.

I would like to thank my thesis committee members Juan C. del Alamo, Juan C. Lasheras, Jeremie Palacci and William R. Young for all of their guidance and suggestions. I want to emphasize the constructive criticism and scientific curiosity of Prof. del Alamo and Prof. Lasheras, who have continuously motivated me to keep exploring new horizons and carry out meaningful investigations.

I am greatly indebted to the scientific legacy of Geoffrey I. Taylor, George K. Batchelor and Howard Brenner, who made numerous contributions, many of them very helpful for the current thesis. I am grateful to Yaniv Almog, Jörn Dunkel, Itzchak Frankel and Carlos Rinaldi for valuable research discussions. I would like to express my heartfelt thanks to my pre-doctoral advisor Juan Fernandez de la Mora, for teaching me how vital and important discipline and sacrifice are in science, and to my previous advisor Olivia Graeve for supporting me during my first stages of my Ph.D. program. I also want to express gratitude and feel thankful towards all the professors in the M.A.E. department who I have interacted with, either in official courses or in the numerous seminars and symposia held at U.C. San Diego.

All the members of Saintillan's group have contributed immensely to my personal and professional time at U.C. San Diego. The group has been a source of successful collaborations, such as those with Barath Ezhilan, Maxime Theillard and Brato Chakrabarti. I am particularly grateful to Barath Ezhilan, who helped me in the beginning of my Ph.D. program, and shared with me his passion for mathematics and computer codes. Other past and present group members that I have had the pleasure to work with and learnt from are graduate students Harishankar Manikantan, Debasish Das and Achal Mahajan, master's stu-

dents Yixuan Jia and Piyush Prakash, and undergraduate students Danny K. Chan, Aric Bandera, Elizabeth Diaz, Samuel Park, Maxime Bollard, Antoine Beringer and Gwendolyn Wang.

My time at U.C. San Diego has been made more enjoyable, to a great extent, due to many friends and groups, who have helped me cope with the uphill-battle feeling that accompanies a graduate degree. Particularly, I thank Vivek George for his mental support and stimulating conversations, Simone Sternini for fun times and laughs, and Andre Amador, Francesca Boso, Seongcheol Choi, Keyur Karandikar, Alvaro Ruiz and Justin Tran for making the beginning of my Ph.D. program less lonely and more gratifying. Also, the daily interaction with the numerous students that are part of the M.A.E. biomechanics group created a very positive working environment. Thanks to Ernesto Criado, Deepti Murali, Lorenzo Rossini, Ricardo Serrano, Mrunal Seshadri, Justin Tran, Ritvik Vasan, Shun Zhang and many others. I also want to express my gratitude to my basketball and bachata friends, whose common interests helped improve my overall mental clarity and deal with stress.

Words are powerless to express my gratitude to my friends from Spain for their support and love, in particular, Adrian Andaluz, Andrea Arranz, Jorge Carnicero, Arturo Alvaro Carballido, Irene de la Calle, Marta Carpio, Luis Miguel del Castillo, Elena Fraile, Sandra Garrosa, Luis Roberto Gonzalez, David Lara, Eduardo Martinez and Ismael Vicente. Time and distance are not barriers to our friendship. I wish to give special thanks to David Lara for coming to San Diego. Also, a special mention to my English tutor and friend Federico Garza-Carvajal for his invaluable lessons. Rest in peace, Federico.

I would like to thank my family, especially my parents Teresa and Carlos, for all their love, encouragement, and support. They have been role models as hard workers, sacrificed and cared for me throughout my pursuits in academia, and gave me a stable foundation for my life. Also, I thank my brother David for being the person who challenged me to excel at everything we did together. My hunger for excellence is, in part, due to him.

Lastly, my supportive, kind-hearted, encouraging and patient love has played a very important role during the second stage of my Ph.D. program. Anh Pham has been, among others, my motivator, psychologist and life-style advisor. She has changed my life in many ways and provided me with the necessary stability to do good work. I am forever grateful, blessed, and a better person thanks to her love and presence.

Chapter 2, in part, is a submitted manuscript; authored by R. Alonso-Matilla, B.

Chakrabarti and D. Saintillan, "Asymptotic transport and dispersion of active particles in periodic porous media". The dissertation author is the primary author of this work.

Chapter 3, in part, is a manuscript in preparation; authored by R. Alonso-Matilla and D. Saintillan, "Effect of chemical fields on the transport and spreading of active particles in periodic porous media". The dissertation author is the primary author of this work.

Chapter 4, in part, is a manuscript published in *J. Fluid Mech.*; authored by B. Ezhilan, R. Alonso-Matilla and D. Saintillan, "On the distribution and swim pressure of run-and-tumble particles in confinement". The dissertation author is the co-first author of this work.

Chapter 5, in part, is a manuscript in preparation; authored by R. Alonso-Matilla and D. Saintillan, "Stability of active fluid films". The dissertation author is the primary author of this work.

Chapter 6, in part, is a manuscript published in *Biomicrofluidics*; authored by R. Alonso-Matilla, B. Ezhilan and D. Saintillan, "Microfluidic rheology of active particle suspensions: Kinetic theory". The dissertation author is the primary author of this work.

Chapter 7, in part, is a manuscript published in *Europhysics Letters*; authored by R. Alonso-Matilla and D. Saintillan, "Microfluidic flow actuation using magnetoactive suspensions". The dissertation author is the primary author of this work.

Chapter 8, in part, is a manuscript published in *Soft Matter*; authored by M. Theillard, R. Alonso-Matilla and D. Saintillan, "Geometric control of active collective motion". The dissertation author is a co-author of this work.

VITA

2018	Ph. D. in Engineering Sciences (Mechanical Engineering). Mechanical and Aerospace Engineering department University of California, San Diego
2014	M.Sc. in Engineering Sciences (Mechanical Engineering). Mechanical and Aerospace Engineering department University of California, San Diego
2013	Research collaboration. Characterization of the aerodynamic stability of swirling flows in combustors. Fluid Dynamics Department University of Valladolid (Spain)
2011-2012	Research assistant. Discovery of a wide-range-specific-impulse propellant material with potential applications in electrically powered spacecrafts. Mechanical Engineering & Materials Science department Yale University
2010-2011	Research Engineer. Development of experimental devices aimed at detecting explosives and screening viruses. SEADM S.L.
2010	Master Thesis. Theoretical design of a condensation nucleus counter. University of Valladolid (Spain) - Yale University
2010	B.S. in Industrial Engineering. University of Valladolid (Spain)

Honors and Awards

M.A.E. Distinguished Fellowship Award, UC San Diego. Annual prize money award for excellence in Engineering, intended to reward the graduate student for their publications in premier Journals.

Peer reviewer

Journal of Fluid Mechanics (2017, 2018)

PUBLICATIONS

R. Alonso-Matilla, D. Saintillan, "Effect of chemical fields on the transport and spreading of active particles in periodic porous media", *to be submitted*.

R. Alonso-Matilla, D. Saintillan, "Stability of active fluid films", *to be submitted*.

R. Alonso-Matilla, B. Chakrabarti, D. Saintillan, "Asymptotic transport and dispersion of active particles in periodic porous media", *submitted*.

R. Alonso-Matilla, D. Saintillan, "Microfluidic flow actuation using magnetoactive suspensions", *Europhysics Letters*, **121** 24002 (2018).

M. Theillard, R. Alonso-Matilla, D. Saintillan, "Geometric control of active collective motion", *Soft Matter*, **13** 363-375 (2017).

R. Alonso-Matilla, B. Ezhilan, D. Saintillan, "Microfluidic rheology of active particle suspensions: Kinetic theory", *Biomicrofluidics*, **10** 043505 (2016).

B. Ezhilan, R. Alonso-Matilla, D. Saintillan, "On the distribution and swim pressure of run-and-tumble particles in confinement", *J. Fluid Mech.*, **781** R4 (2015).

R. Alonso-Matilla, J. Fernandez-Garcia, H. Congdon, J. Fernandez de la Mora, "Search for liquids electrospraying the smallest possible nanodrops in vacuo", *J. Appl. Phys.*, **116** 224504 (2014).

ABSTRACT OF THE DISSERTATION

Dispersion, rheology and microfluidic flow actuation of active particle suspensions

by

Roberto Alonso-Matilla
Doctor of Philosophy in Engineering Sciences (Mechanical Engineering)
University of California San Diego, 2018
Professor David Saintillan, Chair

The primary objective of this thesis is to develop and provide a theoretical framework based on hydrodynamic theory and statistical mechanics that furthers our physical understanding of active suspensions at a macroscopic level. These non-equilibrium systems are comprised of interacting units that extract and consume free energy from their environment, usually via chemical reactions, to produce directed motion. Examples include synthetic swimmers, biomimetic materials and living systems and their motile constituents. An intrinsic property of these active particles, biological and artificial, is the display of an enhanced diffusion in the absence of external fields, here termed "active diffusion", which leads to an additional pressure contribution as a consequence of their self-propulsion. During their motion, active particles additionally generate stresses that get transmitted to the surrounding medium, creating long-range hydrodynamic interactions that, along with steric and chemical effects, often lead to striking macroscopic features and highly correlated large-scale motions.

We first present a continuum model based on generalized Taylor dispersion theory, complemented by Langevin simulations, to predict the long-time asymptotic transport of active Brownian particles in periodic crowded media, when subjected to an applied flow

and chemical fields. We start from a micro-continuum level approach and show that the overall behavior of a dilute cloud of cells can be described by an obstacle-free advection-diffusion equation, whose effective long-time mean particle velocity and dispersivity dyadic are determined through a set of boundary value problems. The intrinsic complexity of particle transport arises from the activity of the swimmers, and the complex geometry of the flow paths, which originates from the mixing and re-splitting of streams at pore junctions. We unravel the roles of particle motility, applied fluid flow, chemotactic fields and porous lattice geometry on asymptotic particle transport properties, and provide a physical explanation for the trends observed. Particularly, we show that obstacles behave predominantly as entropic barriers at low flow rates and as regions of shear production at high flow rates, and find that shear-induced polarization as well as activity-driven cross-stream migration affect the axial particle dispersion. Our mathematical framework gives new insights and provides a simple approach to control the spreading of active particles in structured crowded environments.

We additionally study the mechanical force per unit area exerted by these active particles on confining boundaries. We also quantify and characterize the effect of these biological microorganisms on the suspension viscosity as well as on the onset of self-generated spontaneous flows in confinement. Our work captures the main qualitative patterns observed in experiments, and a close quantitative agreement is achieved between the developed theory and existing experiments. In particular, we capture and explain the superfluidity regime of rear-actuated suspensions, recently observed in experiments, a state of matter in which the suspension behaves as a frictionless fluid. This superfluidity regime has remarkable consequences on the onset of internally generated flows and the subsequent formation of coherent structures, most of them observed in past experiments and caused by bacterial activity and confinement, such as: the formation of bacterial vortices, bacterial traveling waves, chaotic dynamics, stabilization of inverted bacterial fluid films, unidirectional fluid pumping in channels, and control of the magnitude and direction of the self-generated flows upon simple application of uniform magnetic fields. Our theoretical and computational models enable us to reproduce and elucidate these phenomena within a single integrated framework.

The understanding, control and manipulation of the transport of active particles have important consequences in human health as well as in microbial ecology. Applications include the spreading of contaminants in soils and groundwater aquifers, design of medical devices, bacterial filtering, and biodegradation-bioremediation processes. The theoretical framework

developed in this thesis provides the scientific community with powerful tools that enable a better understanding of complex microbial systems, thus paving the way for the conceptual development of new revolutionary devices and processes involving active particles. A lot of progress needs to be done, a great diversity of challenges need to be faced, and many applications are yet to be discovered.

Chapter 1

Introduction

1.1 The Fokker-Planck equation

One of the central problems in microbial ecology is concerned with the time evolution of the macroscopic configuration of bacterial suspensions. These systems are usually subjected to external or internal fields that are non-deterministic in origin, often in part due to thermal fluctuations or noise. The Fokker-Planck equation, a partial differential equation originally applied to the Brownian motion of tracers, is a powerful tool that deals with these fluctuations, stem from many short-time disturbances that originate from the molecules of the fluid hitting the particle in an unpredictable way, and it can be used to successfully describe the dynamics of these complex fluids. Because of this noise, it is impossible to know the instantaneous exact position and orientation of all the particles. Instead, a probability density function of finding the particles at a given location with a certain orientation is introduced to describe their evolution. This Fokker-Plank approach is a very useful alternative to Langevin dynamics simulations because we can just solve a partial differential equation instead of solving a huge Langevin system of equations for all the particles. The continuum model is very powerful when the average properties of the system are time-dependent, when the system is non-linear and far from equilibrium, and when there exists interactions between particles (i.e. hydrodynamic). We can easily obtain statistical averages of the distribution function by simple quadratures and, in simple cases, we can obtain analytical expressions for some variables of interest or study their analytical asymptotic behavior.

1.1.1 Derivation from the Langevin equation

We first mathematically derive the Fokker-Planck equation from the Langevin equation, and focus on single-particle dynamics. Let's assume that particle motion results from self-propulsion with constant speed v_0 in the direction defined by the unit vector $\mathbf{p}$, from advection and rotation by the fluid velocity field $\mathbf{u}(\mathbf{R})$ originated from an external field or by the disturbance flow created by the active particles, from a point force and a point torque due to an external field (i.e. gravitational), and from translational and rotational diffusion. Its dynamics can thus be modeled by two Langevin equations

$$\dot{\mathbf{R}} = v_0\mathbf{p} + \mathbf{u}(\mathbf{R}) + \mathbf{M}\cdot\mathbf{F} + \boldsymbol{\eta}_t(t)\,, \tag{1.1}$$

$$\dot{\mathbf{p}} = \boldsymbol{\Omega}(\mathbf{R})\times\mathbf{p} + \gamma(\mathbf{I}-\mathbf{pp})\cdot\mathbf{E}(\mathbf{R})\cdot\mathbf{p} + G(\mathbf{I}-\mathbf{pp})\cdot\mathbf{e_g} + \boldsymbol{\eta}_r(t)\,. \tag{1.2}$$

The swimmer might be under the influence of an external gravitational field, whose leading order effect on a non-buoyant particle is a point force $\mathbf{F} = g(m_p - m_f)\mathbf{e_g}$ acting on it. Here, g is the acceleration of gravity, $\mathbf{e_g}$ is a unit vector pointing in the direction of the gravity field, and m_p and m_f denote the particle's mass and that of the displaced fluid, respectively. $\mathbf{M}$ is the orientation-dependent translational mobility tensor that can be expressed, for an axisymmetric particle, as a function of the mobility coefficients parallel and perpendicular to its symmetry axis

$$\mathbf{M} = M_{\parallel}\mathbf{pp} + M_{\perp}\left(\mathbf{I}-\mathbf{pp}\right). \tag{1.3}$$

The direction in which the particle swims at any instant is determined by the balance of viscous, external and Brownian torques. The third term in Eq. (1.2) originates from an external point torque acting on the particle, which could arise due to the interaction of a magnetic field and the magnetic moment of a ferromagnetic particle [4], or the interaction of a gravitational field and a particle whose center of mass does not coincide with its geometric center [5]. The orientation parameter G corresponds to an inverse time scale representing the inverse characteristic time for the reorientation of the particle due to a balance of external and viscous torques, and it can be expressed as $G = mg/\zeta_{\perp}$, where $\zeta_{\perp}$ is the rotational hydrodynamic resistance about the axis perpendicular to $\mathbf{p}$, and m is the particle dipole moment (gyrotactic or magnetic). The vectors $\boldsymbol{\eta}_t$ and $\boldsymbol{\eta}_r$ have a stochastic origin, due to random forces actin on the particle by the fluid molecules. The reason why we include an stochastic force is because if we wanted to solve the problem exactly, we would have to

solve the coupled equations of motion for all the molecules in the fluid and for the small particle. Due to the large number of molecules in the fluid, this problem is not manageable. Therefore, we consider the common practice of taking an ensemble of such system, where we specify the averages of this force for the ensemble. We assume that the average of $\boldsymbol{\eta}_t$ and $\boldsymbol{\eta}_r$ over the ensemble is zero: $\langle \boldsymbol{\eta}_t(t) \rangle = \mathbf{0}$ and $\langle \boldsymbol{\eta}_r(t) \rangle = \mathbf{0}$. The average value of the product of two Langevin forces at different times is zero for time differences $t' - t$ which are larger than the duration time τ_{coll} of a collision. Usually, the duration time of a collision is much smaller than the relaxation time of the velocity of the small particle. Therefore, following Brownian motion theory, we assume that $\boldsymbol{\eta}_t$ and $\boldsymbol{\eta}_r$ are Gaussian random variates with variance $\langle \boldsymbol{\eta}_t(t) \boldsymbol{\eta}_t(t') \rangle = 2 d_t \mathbf{I} \delta(t - t')$ and $\langle \boldsymbol{\eta}_r(t) \boldsymbol{\eta}_r(t') \rangle = 2 d_r \mathbf{I} \delta(t - t')$, results readily obtained from equipartition of energy [6]. A noise force of this type is commonly called white noise. d_t and d_r denote the constant translational and rotational diffusivities of the particle, respectively. The fluid vorticity $\nabla_R \times \mathbf{u} = 2\,\boldsymbol{\Omega}(\mathbf{R})$ and rate-of-strain $\mathbf{E}(\mathbf{R}) = \frac{1}{2}[\nabla_R \mathbf{u} + \nabla_R \mathbf{u}^\dagger]$ cause rotation and alignment of the particle in Eq. (1.2) according to Jeffery's equation [7], where the Bretherton constant γ characterizes shape anisotropy ($\gamma = 0$ for a sphere, $\gamma \approx 1$ for a slender particle). The symbol $\dagger$ indicates transpose. For later use, we additionally define the rate-of-vorticity tensor $\mathbf{W}(\mathbf{R}) = \frac{1}{2}[\nabla_R \mathbf{u} - \nabla_R \mathbf{u}^\dagger]$.

It is convenient to obtain a partial differential equation that describes the same system as Eqs. (1.1) and (1.2). We follow a similar analysis used for the derivation of a Fokker-Planck equation to model Brownian tracers [8, 9]. A similar study focused on a Fokker-Planck derivation with only Brownian rotations [10]. We define a conditional probability density $\psi(\mathbf{R}, \mathbf{p}, t)$ of finding the particle at a position $\mathbf{R}$, with orientation $\mathbf{p}$ at time t. It satisfies the following relation

$$\psi(\mathbf{R}, \mathbf{p}, t + \Delta t) = \int_{-\infty}^{\infty} d(\Delta \mathbf{R}) \int_{\Omega} d(\Delta \mathbf{p}) \psi(\mathbf{R} - \Delta \mathbf{R}, \mathbf{p} - \Delta \mathbf{p}, t) \times \Phi(\mathbf{R} - \Delta \mathbf{R}, \mathbf{p} - \Delta \mathbf{p} | \Delta \mathbf{R}, \Delta \mathbf{p}, \Delta t) \quad (1.4)$$

which is known as the Chapman-Kolmogorov equation [11]. It assumes a Markovian stochastic process, where there is only a memory of the configuration of the swimmer for the latest time. Here, $\Phi(\mathbf{R}, \mathbf{p} | \Delta \mathbf{R}, \Delta \mathbf{p}, \Delta t)$ is a transition probability and it indicates the conditional probability of finding the swimmer at position $\mathbf{R}$ with orientation $\mathbf{p}$ followed by subsequent translational and orientational displacements $\Delta \mathbf{R}$ and $\Delta \mathbf{p}$ during a time Δt. Eq. (1.4) says that the probability density for a particle being at position $\mathbf{R}$, with orientation $\mathbf{p}$ at time

$t + \Delta t$ is given by the product of the probability density for the particle being at $\mathbf{R} - \Delta\mathbf{R}$, with orientation $\mathbf{p} - \Delta\mathbf{p}$ at time t multiplied by the probability of experiencing a spatial displacement $\Delta\mathbf{R}$ and an orientational displacement $\Delta\mathbf{p}$ during time Δt, and integrated over all possible displacements. It should be pointed out that the total probability of experiencing a displacement of any magnitude is normalized to 1:

$$\int_{-\infty}^{\infty} d(\Delta\mathbf{R}) \int_{\Omega} d(\Delta\mathbf{p}) \Phi(\mathbf{R}, \mathbf{p}|\Delta\mathbf{R}, \Delta\mathbf{p}, \Delta t) = 1 \tag{1.5}$$

We expand $\psi(\mathbf{R} - \Delta\mathbf{R}, \mathbf{p} - \Delta\mathbf{p}, t)$ in Taylor series about $\mathbf{R}$ and $\mathbf{p}$. We get

$$\begin{aligned}
&\psi(\mathbf{R} - \Delta\mathbf{R}, \mathbf{p} - \Delta\mathbf{p}, t) = \psi(\mathbf{R}, \mathbf{p}, t) - \Delta\mathbf{R} \cdot \nabla_R \psi(\mathbf{R}, \mathbf{p}, t) - \Delta\mathbf{p} \cdot \nabla_p \psi(\mathbf{R}, \mathbf{p}, t) \\
&+ \frac{1}{2} \Delta\mathbf{R}\Delta\mathbf{R} : \nabla_R \nabla_R \psi(\mathbf{R}, \mathbf{p}, t) + \frac{1}{2} \Delta\mathbf{p}\Delta\mathbf{p} : \nabla_p \nabla_p \psi(\mathbf{R}, \mathbf{p}, t) \\
&+ \Delta\mathbf{R}\Delta\mathbf{p} : \nabla_R \nabla_p \psi(\mathbf{R}, \mathbf{p}, t) + \mathcal{O}((\Delta\mathbf{R})^3, (\Delta\mathbf{R})^2 \Delta\mathbf{p}, \Delta\mathbf{R}(\Delta\mathbf{p})^2, (\Delta\mathbf{p})^3)
\end{aligned} \tag{1.6}$$

Similarly, we Taylor-expand $\Phi(\mathbf{R} - \Delta\mathbf{R}, \mathbf{p} - \Delta\mathbf{p}|\Delta\mathbf{R}, \Delta\mathbf{p}, \Delta t)$ about $\mathbf{R}$ and $\mathbf{p}$. We get:

$$\begin{aligned}
&\Phi(\mathbf{R} - \Delta\mathbf{R}, \mathbf{p} - \Delta\mathbf{p}|\Delta\mathbf{R}, \Delta\mathbf{p}, \Delta t) = \Phi(\mathbf{R}, \mathbf{p}|\Delta\mathbf{R}, \Delta\mathbf{p}, \Delta t) \\
&- \Delta\mathbf{R} \cdot \nabla_R \Phi(\mathbf{R}, \mathbf{p}|\Delta\mathbf{R}, \Delta\mathbf{p}, \Delta t) - \Delta\mathbf{p} \cdot \nabla_p \Phi(\mathbf{R}, \mathbf{p}|\Delta\mathbf{R}, \Delta\mathbf{p}, \Delta t) \\
&+ \frac{1}{2} \Delta\mathbf{R}\Delta\mathbf{R} : \nabla_R \nabla_R \Phi(\mathbf{R}, \mathbf{p}|\Delta\mathbf{R}, \Delta\mathbf{p}, \Delta t) + \frac{1}{2} \Delta\mathbf{p}\Delta\mathbf{p} : \nabla_p \nabla_p \Phi(\mathbf{R}, \mathbf{p}|\Delta\mathbf{R}, \Delta\mathbf{p}, \Delta t) \\
&+ \Delta\mathbf{R}\Delta\mathbf{p} : \nabla_R \nabla_p \Phi(\mathbf{R}, \mathbf{p}|\Delta\mathbf{R}, \Delta\mathbf{p}, \Delta t) + \mathcal{O}((\Delta\mathbf{R})^3, (\Delta\mathbf{R})^2 \Delta\mathbf{p}, \Delta\mathbf{R}(\Delta\mathbf{p})^2, (\Delta\mathbf{p})^3)
\end{aligned} \tag{1.7}$$

Using the approximations in Eqs. (1.6,1.7), the integrand in Eq. (1.4) reduces to:

$$\begin{aligned}
&\psi(\mathbf{R} - \Delta\mathbf{R}, \mathbf{p} - \Delta\mathbf{p}, t)\Phi(\mathbf{R} - \Delta\mathbf{R}, \mathbf{p} - \Delta\mathbf{p}|\Delta\mathbf{R}, \Delta\mathbf{p}, \Delta t) = \\
&\psi(\mathbf{R}, \mathbf{p}, t)\Phi(\mathbf{R}, \mathbf{p}|\Delta\mathbf{R}, \Delta\mathbf{p}, \Delta t) - \Delta\mathbf{R} \cdot [\Phi\nabla_R\psi + \psi\nabla_R\Phi] \\
&- \Delta\mathbf{p} \cdot [\Phi\nabla_p\psi + \psi\nabla_p\Phi] + \frac{1}{2}\Delta\mathbf{R}\Delta\mathbf{R} : [\Phi\nabla_R\nabla_R\psi + \psi\nabla_R\nabla_R\Phi + 2\nabla_R\Phi\nabla_R\psi] \\
&+ \frac{1}{2}\Delta\mathbf{p}\Delta\mathbf{p} : [\Phi\nabla_p\nabla_p\psi + \psi\nabla_p\nabla_p\Phi + 2\nabla_p\Phi\nabla_p\psi] + \Delta\mathbf{R}\Delta\mathbf{p} : [\Phi\nabla_R\nabla_p\psi + \psi\nabla_R\nabla_p\Phi] \\
&+ \mathcal{O}((\Delta\mathbf{R})^3, (\Delta\mathbf{R})^2\Delta\mathbf{p}, \Delta\mathbf{R}(\Delta\mathbf{p})^2, (\Delta\mathbf{p})^3)
\end{aligned} \tag{1.8}$$

We additionally define the expected value $\overline{\mathbf{F}}$ of any field $\mathbf{F}$ as

$$\overline{\mathbf{F}}(\mathbf{R},\mathbf{p}|\Delta t)=\int_{-\infty}^{\infty}\int_{\Omega}\mathbf{F}\Phi(\mathbf{R},\mathbf{p}|\Delta\mathbf{R},\Delta\mathbf{p},\Delta t)d(\Delta\mathbf{p})d(\Delta\mathbf{R}) \tag{1.9}$$

The mean particle spatial displacement is determined by multiplying the displacement variable by its probability of occurring during the duration Δt at the current swimmer position and orientation, and integrated over all possible spatial and orientational displacements:

$$\overline{\Delta\mathbf{R}}(\mathbf{R},\mathbf{p}|\Delta t)=\int_{-\infty}^{\infty}\int_{\Omega}\Delta\mathbf{R}\Phi(\mathbf{R},\mathbf{p}|\Delta\mathbf{R},\Delta\mathbf{p},\Delta t)d(\Delta\mathbf{p})d(\Delta\mathbf{R}) \tag{1.10}$$

The mean square spatial displacement is obtained in the same way as

$$\overline{\Delta\mathbf{R}\Delta\mathbf{R}}(\mathbf{R},\mathbf{p}|\Delta t)=\int_{-\infty}^{\infty}\int_{\Omega}\Delta\mathbf{R}\Delta\mathbf{R}\Phi(\mathbf{R},\mathbf{p}|\Delta\mathbf{R},\Delta\mathbf{p},\Delta t)d(\Delta\mathbf{p})d(\Delta\mathbf{R}) \tag{1.11}$$

The divergence of the mean displacement can be expressed as

$$\nabla_R\cdot\overline{\Delta\mathbf{R}}(\mathbf{R},\mathbf{p}|\Delta t)=\int_{-\infty}^{\infty}\int_{\Omega}\Delta\mathbf{R}\cdot\nabla_R\Phi(\mathbf{R},\mathbf{p}|\Delta\mathbf{R},\Delta\mathbf{p},\Delta t)d(\Delta\mathbf{p})d(\Delta\mathbf{R}) \tag{1.12}$$

and also the operator $\nabla_R\nabla_R:$ applied to the mean square displacement is

$$\begin{aligned}&\nabla_R\nabla_R:\overline{\Delta\mathbf{R}\Delta\mathbf{R}}(\mathbf{R},\mathbf{p}|\Delta t)\\&=\int_{-\infty}^{\infty}\int_{\Omega}\Delta\mathbf{R}\Delta\mathbf{R}:\nabla_R\nabla_R\Phi(\mathbf{R},\mathbf{p}|\Delta\mathbf{R},\Delta\mathbf{p},\Delta t)d(\Delta\mathbf{p})d(\Delta\mathbf{R})\end{aligned} \tag{1.13}$$

Similar definitions can be applied to their orientational counterparts. We expand in Taylor series the left-hand-side of Eq. (1.4), substitute Eq. (1.8) into Eq. (1.4), and simplify the expressions with Eq. 1.9, to get:

$$\begin{aligned}\frac{\partial\psi}{\partial t}\Delta t=&-\nabla_R\cdot\left(\overline{\Delta\mathbf{R}}\psi\right)-\nabla_p\cdot\left(\overline{\Delta\mathbf{p}}\psi\right)+\frac{1}{2}\nabla_R\nabla_R:\left(\overline{\Delta\mathbf{R}\Delta\mathbf{R}}\psi\right)\\&+\frac{1}{2}\nabla_p\nabla_p:\left(\overline{\Delta\mathbf{p}\Delta\mathbf{p}}\psi\right)+\nabla_R\nabla_p:\left(\overline{\Delta\mathbf{R}\Delta\mathbf{p}}\psi\right)\\&+\mathcal{O}((\Delta\mathbf{R})^3,(\Delta\mathbf{R})^2\Delta\mathbf{p},\Delta\mathbf{R}(\Delta\mathbf{p})^2,(\Delta\mathbf{p})^3,(\Delta t)^2)\end{aligned} \tag{1.14}$$

The expected values present in Eq. (1.14) can be obtained from the Langevin equation:

$$\overline{\Delta \mathbf{R}} = \left[v_0 \mathbf{p} + \mathbf{u} + \mathbf{M} \cdot \mathbf{F}\right] \Delta t + \mathcal{O}((\Delta t)^2) \tag{1.15}$$

$$\overline{\Delta \mathbf{p}} = \left[\boldsymbol{\Omega} \times \mathbf{p} + \gamma \left(\mathbf{I} - \mathbf{pp}\right) \cdot \mathbf{E} \cdot \mathbf{p} + G \left(\mathbf{I} - \mathbf{pp}\right) \cdot \mathbf{e_g}\right] \Delta t + \mathcal{O}((\Delta t)^2) \tag{1.16}$$

$$\overline{\Delta \mathbf{R} \Delta \mathbf{R}} = 2 d_t \mathbf{I} \Delta t + \mathcal{O}((\Delta t)^2) \tag{1.17}$$

$$\overline{\Delta \mathbf{p} \Delta \mathbf{p}} = 2 d_r \mathbf{I} \Delta t + \mathcal{O}((\Delta t)^2) \tag{1.18}$$

$$\overline{\Delta \mathbf{R} \Delta \mathbf{p}} = \mathcal{O}((\Delta t)^2) \tag{1.19}$$

We insert the expected values obtained in Eqs. (1.15-1.19) into Eq. (1.14) to finally obtain the desired Fokker-Planck equation:

$$\frac{\partial \psi}{\partial t} + \nabla_R \cdot \mathbf{J} + \nabla_p \cdot \mathbf{j} = \mathcal{O}((\Delta t)^2) \tag{1.20}$$

where the spatial and orientational probability fluxes are

$$\mathbf{J} = \left[v_0 \mathbf{p} + \mathbf{u}(\mathbf{R}) + \mathbf{M} \cdot \mathbf{F}\right] \psi - d_t \nabla_R \psi, \tag{1.21}$$

$$\mathbf{j} = \left[\boldsymbol{\Omega}(\mathbf{r}) \times \mathbf{p} + \gamma (\mathbf{I} - \mathbf{pp}) \cdot \mathbf{E}(\mathbf{R}) \cdot \mathbf{p} + G (\mathbf{I} - \mathbf{pp}) \cdot \mathbf{e_g}\right] \psi - d_r \nabla_p \psi. \tag{1.22}$$

Therefore, a swimmer initially released at a position $\mathbf{R}_0$ with orientation $\mathbf{p}_0$ can be modeled, in a continuum manner, as

$$\frac{\partial \psi}{\partial t} + \nabla_R \cdot \mathbf{J} + \nabla_p \cdot \mathbf{j} = \delta(\mathbf{R} - \mathbf{R}_0) \delta(\mathbf{p} - \mathbf{p}_0) \delta(t), \tag{1.23}$$

where we have incorporated the initial condition as a source term on the right-hand side of Eq. (1.23), and we have deleted the order of validity $\mathcal{O}((\Delta t)^2)$.

We can use the same approach to model multi-particle systems. In the same manner, we define a probability distribution function $P(\mathbf{R}, \mathbf{p}, t)$ of finding a particle at a position $\mathbf{R}$ with orientation $\mathbf{p}$ at time t. P satisfies the following equation

$$\frac{\partial P}{\partial t} + \nabla_R \cdot \mathbf{J} + \nabla_p \cdot \mathbf{j} = 0, \tag{1.24}$$

subject to a given or random initial condition. The translational and rotational fluxes have

the same form as in Eqs. (1.21,1.22):

$$\mathbf{J} = [v_0\mathbf{p} + \mathbf{u}(\mathbf{R}) + \mathbf{M}\cdot\mathbf{F}]P - d_t\nabla_R P, \tag{1.25}$$

$$\mathbf{j} = [\boldsymbol{\Omega}(\mathbf{r})\times\mathbf{p} + \gamma(\mathbf{I}-\mathbf{pp})\cdot\mathbf{E}(\mathbf{R})\cdot\mathbf{p} + G(\mathbf{I}-\mathbf{pp})\cdot\mathbf{e_g}]\,P - d_r\nabla_p P. \tag{1.26}$$

In Eqs. (1.25) and (1.26) the fluid field can be an external imposed flow, the disturbance flow due to the presence of the particles or a combination of both. For more details, we refer the reader to § 1.3.1.

1.1.2 Orientational moments and closure approximations

To make analytical progress and simplify the numerical simulations, sometimes it is useful to approximate the high dimensional variable P in terms of its orientational moments. We define the k-th orientational moment of P as

$$\langle\underbrace{\mathbf{p}\cdots\mathbf{p}}_{k\text{ times}}\rangle = \int_\Omega (\underbrace{\mathbf{p}\cdots\mathbf{p}}_{k\text{ times}})P d\mathbf{p} \tag{1.27}$$

These moments are defined as integrals over the unit circle of orientations in two-dimensions and over the unit sphere of orientations in three-dimensions. We can approximate P as a function of the first three orientational moments [12, 13]

$$P(\mathbf{R},\mathbf{p},t) = \frac{1}{2(N_d-1)\pi}\left[c(\mathbf{R},t) + N_d\mathbf{p}\cdot\mathbf{m}(\mathbf{R},t) + \frac{N_d(N_d+2)}{2}\mathbf{pp}:\mathbf{D}(\mathbf{R},t)\right], \tag{1.28}$$

where N_d is the spatial dimensionality. The zeroth moment $c(\mathbf{R},t) = \langle 1\rangle$ corresponds to the local particle concentration, whereas the first and second moments $\mathbf{m} = \langle\mathbf{p}\rangle$ and $\mathbf{D} = \langle\mathbf{pp} - \mathbf{I}/N_d\rangle$ describe the local polarization and nematic alignment in the suspension, respectively. Note that we have made the second moment traceless to simplify the future mathematical calculations. The moment expansion in Eq. (1.28) can be interpreted as an expansion in surface harmonics ($N_d = 2$) or spherical harmonics ($N_d = 3$). In an isotropic suspension, $\mathbf{m} = \mathbf{D} = \mathbf{0}$. To gain more physical intuition about the meaning of $\mathbf{m}$ and $\mathbf{D}$, refer to Fig. (1.1). The first three orientational moments of the Fokker-Planck equation (1.24) read

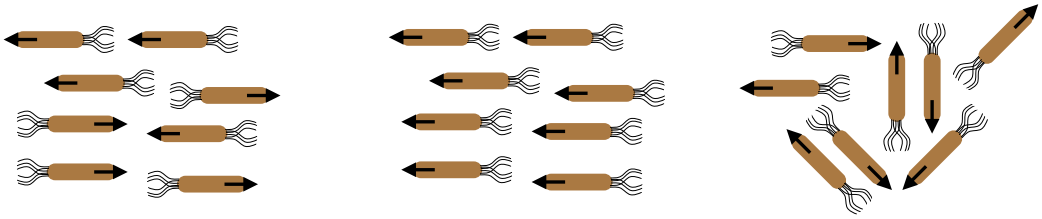

Figure 1.1: Polarization vector $\mathbf{m}$ and nematic order tensor $\mathbf{D}$ for three different particle configurations. The black arrow indicates the direction of each particle director $\mathbf{p}$. The vector $\mathbf{m}$ denotes the average polarization of the particles whereas $\mathbf{D}$ quantifies the alignment of the particles regardless of the direction they are pointing at (particles pointing in the directions $\mathbf{p}$ and $-\mathbf{p}$ contribute equally to the value of $\mathbf{D}$). *Left*: particles are nematically aligned horizontally and their net polarization vanishes; *middle*: particles are nematically aligned in the same way as the figure on the left but now they are polarized towards the left; *right*: isotropic suspension where both moments vanish.

$$\frac{\partial c}{\partial t} = -\nabla_R \cdot [(\mathbf{u} + \mathbf{M}\cdot\mathbf{F})c] - v_0 \nabla_R \cdot \mathbf{m} + d_t \nabla_R^2 c, \tag{1.29}$$

$$\begin{aligned}\frac{\partial \mathbf{m}}{\partial t} =& -\nabla_R \cdot [(\mathbf{u} + \mathbf{M}\cdot\mathbf{F})\mathbf{m}] - v_0 \left(\nabla_R \cdot \mathbf{D} + \frac{1}{N_d}\nabla_R c\right) + d_t \nabla_R^2 \mathbf{m} + \\ & (\mathbf{m}\mathbf{I} - \langle \mathbf{ppp}\rangle) : (\gamma \mathbf{E} - \mathbf{W}) + G\left(\frac{N_d - 1}{N_d} c\mathbf{I} - \mathbf{D}\right)\cdot \mathbf{e_g} - (N_d - 1) d_r \mathbf{m},\end{aligned} \tag{1.30}$$

$$\begin{aligned}\frac{\partial \mathbf{D}}{\partial t} =& -\nabla_R \cdot [(\mathbf{u} + \mathbf{M}\cdot\mathbf{F})\mathbf{D}] - v_0 \left(\nabla_R \cdot \langle \mathbf{ppp}\rangle - \frac{1}{N_d}\mathbf{I}(\nabla_R \cdot \mathbf{m})\right) + d_t \nabla_R^2 \mathbf{D} + \\ & (\mathbf{D}\cdot\mathbf{W} - \mathbf{W}\cdot\mathbf{D}) + G\left[\mathbf{m}\mathbf{e_g} + \mathbf{e_g}\mathbf{m} - 2\langle \mathbf{ppp}\rangle \cdot \mathbf{e_g}\right] - 2\gamma \langle \mathbf{pppp}\rangle : \mathbf{E} \\ & - 2N_d d_r \mathbf{m}\end{aligned} \tag{1.31}$$

The resulting equations involve higher moments of the probability distribution function. The simplest closure approximation corresponds to $\mathbf{D} = \mathbf{0}$ and neglecting higher order moments, which sometimes turns out to be a very good approximation. Because the active particle stress involves the nematic order tensor $\mathbf{D}$, as shown in §. 1.3.2, this closure cannot be used when active stresses on the fluid medium are included in the problem. Other closures involve the approximations for the third and fourth moments $\langle \mathbf{ppp}\rangle$ and $\langle \mathbf{pppp}\rangle$ as a function of lower moments. By neglecting the coefficients in front of all harmonics of degree 3 and

higher, the third and fourth moments can be approximated as [12, 13]

$$\langle p_i p_j p_k \rangle \approx \frac{1}{N_d+2}\left(m_i\delta_{jk}+m_j\delta_{ik}+m_k\delta_{ij}\right), \tag{1.32}$$

$$\langle p_i p_j p_k p_m \rangle \approx \frac{c}{N_d(N_d+2)}\left(\delta_{ij}\delta_{km}+\delta_{ik}\delta_{jm}+\delta_{im}\delta_{jk}\right)+ \frac{1}{N_d+4}\left(\delta_{ij}D_{km}+\delta_{ik}D_{jm}+\delta_{im}D_{jk}+\delta_{jk}D_{im}+\delta_{jm}D_{ik}+\delta_{km}D_{ij}\right) \tag{1.33}$$

If the probability density is not a smooth function in orientational space due to the presence of orientational boundary layers or discontinuities, it is required to include the infinite series in the spherical harmonic expansion to accurately determine the probability distribution, as in [14]; a truncation approximation using a closure would fail to give good quantitative agreement.

1.2 Chemotactic fields

Chemical fields play a very important role on the behavior and transport of living matter. Examples include the motion of human spermatozoa [15], the migration of white blood cells [16] or the locomotion of bacteria [17, 18]. In Chapter 3, we study the main characteristics that describe the asymptotic long-time transport of run-and-tumble bacteria in ordered crowded media, when the suspension is subjected to chemical fields.

Swimming bacteria such as Escherichia Coli or Salmonella Typhimurium rotate their flagella, mostly counterclockwise, in order to propel themselves through the environment. The flagellar motor switches the direction of rotation either spontaneously or in response to signals received from their receptors. The result is an alternation between fairly straight-line runs with brief intermissions of clockwise rotation and pauses (tumbles). In the absence of any stimuli, the number of tumbles per interval of time follows a Poisson distribution, and the time duration between consecutive tumbles follows an exponential distribution [17]. When they experience an increasing chemoattractant gradient or a decreasing chemorepellent gradient, the probability of tumbling decreases and bacteria swim longer along those favorable conditions. As a consequence, they experience a biased random walk towards the attractant chemical species. In the next sections, we investigate how this Poisson process can be modeled through single-particle simulations (§ 1.2.1) and as a continuum (§ 1.2.2).

1.2.1 Poisson statistics: Particle simulations

We let N be the number of tumbles in a fixed interval of time of duration t. N follows a Poisson distribution, and we denote its mean by λ. According to Poisson statistics, the probability that k tumbles occur in a finite time t is:

$$P(N(t) = k) = e^{-\lambda t}\frac{(\lambda t)^k}{k!} \qquad k = 0, 1, 2... \tag{1.34}$$

We let T be the time until the next tumbling event. The probability of T arriving in less than a time t is

$$\Phi_{CDF}(t) = P(T \leq t) = 1 - e^{-\lambda t}, \tag{1.35}$$

which corresponds to the cumulative distribution function (CDF) for the exponential distribution. We define the complimentary cumulative distribution function as

$$\hat{\Phi}_{CDF}(t) = 1 - \Phi_{CDF}(t) = e^{-\lambda t}, \tag{1.36}$$

The fact that N follows a Poisson process implies that the time distribution between consecutive tumbles follows an exponential distribution.

$$\Phi_{PDF}(t) = \frac{d\Phi_{CDF}(t)}{dt} = \lambda e^{-\lambda t} \tag{1.37}$$

An important property of the exponential distribution is that it lacks memory. The probability of a tumble arriving after a certain amount of time is independent of the history of tumbling events. We can easily prove this property by deriving the conditional probability $P(T > s + t|T > t)$:

$$P(T > s + t|T > t) = \frac{P(T > s + t \ \cap \ T > t)}{P(T > t)} = e^{-\lambda s} \tag{1.38}$$

The conditional probability is independent on t, which means that every instantaneous time is the beginning of a new time period, which has the same distribution regardless of how much time has already elapsed. We consider the probability of responding to a chemical stimulus to be dependent only on the instantaneous position and orientation of the cell. These Markovian locomotion is an approximation to a more realistic behavior experienced by bacteria such as E. Coli, which undergo a more complex time integration mechanism [19–21]; an

approximation whose validity holds for weak chemotactic fields. We can take advantage of this property to carry out Brownian particle simulations. In the Poisson process, the variable time is continuous. We can describe the Poisson process as a discrete-time analogue using a Bernoulli process, and divide the bacterial motion into time intervals of duration Δt, where Δt is small. We advance bacterial position and orientation during a time Δt. Each time step $\Delta t \to 0$ corresponds to an independent Bernoulli trial, such that in each interval, independently of every other interval, there is a tumble with probability $\lambda \Delta t$. We can rigorously prove this equivalence. We define the Bernoulli process as $\{B(t) : t = 0, \Delta t, 2\Delta t, ...\}$, where $B(t)$ is the number of tumbles up to time t. In this process, events occur randomly in time, with a rate that increases as λ increases. For a given time t of the form $t = n\Delta t$ (n integer), we know the exact distribution of $B(t)$. Up to time t, there are n independent trials, each with probability $\lambda \Delta t$ of tumble occurring. We can prove that the probability of $B(t) = k$ follows a Poisson process as $n \to \infty$ and $\Delta t \to 0$. According to the binomial distribution:

$$P(B(t) = k) = \frac{n!}{(n-k)!k!} (\lambda \Delta t)^k (1 - \lambda \Delta t)^{n-k} \tag{1.39}$$

Making use of the asymptotic limits

$$\lim_{n\to\infty} \left(1 - \frac{\lambda t}{n}\right)^n = e^{-\lambda t}, \qquad \lim_{n\to\infty} \left(1 - \frac{\lambda t}{n}\right)^{-k} = 1, \qquad \lim_{n\to\infty} \frac{n!}{(n-k)!k!} = 1 \tag{1.40}$$

and being aware of the equivalence $t = n\Delta t$, the binomial probability in Eq. 1.39 approximates that of Poisson and becomes exact when $\Delta t \to 0$

$$\lim_{t\to 0} P(B(t) = k) = \frac{(\lambda t)^k}{k!} e^{-\lambda t} \tag{1.41}$$

Using Eq. (1.35), the probability of not tumbling in a time Δt is $P(N(\Delta t) = 0) = e^{-\lambda \Delta t}$. The probability of at least tumbling once during the same time interval Δt is $P(N(\Delta t) > 0) = 1 - e^{-\lambda \Delta t}$. Therefore, we can determine if a tumbling event will take place in a time step Δt by generating a random number $N_{rand} \in [0, 1]$. Then,

$$\begin{cases} \text{If } N_{rand} < 1 - e^{-\lambda \Delta t} & \to \text{ Tumble occurs during the time } \Delta t. \\ \text{If } N_{rand} > 1 - e^{-\lambda \Delta t} & \to \text{ No tumble occurs during the time } \Delta t. \end{cases} \tag{1.42}$$

where $e^{-\lambda \Delta t} \approx 1 - \lambda \Delta t$ for small Δt. We are just assuming that the cell either does not tumble or tumbles once. Notice that if Δt is not small enough, the probability of more than one tumbling event occurring during a time step is not negligible. If pre- and post-tumbling directions were correlated, the new bacterial direction would get affected by this approximation.

1.2.2 Run-and-tumble processes: Fokker-Planck derivation

In this section, we aim to derive a continuum framework that mimics the Poisson statistics of the run-and-tumble processes described in § 1.2.1. We based our derivation on the work by Othmer et al. [22], where they derive an analogous equation for the 'kangaroo process', where the particle undergoes spatial jumps instead of experiencing jumps in orientational space. For simplicity, we assume spatial homogeneity. The presence of spatial gradients make the derivation more complicated. We define the probability density function $\psi(\mathbf{p}, t|\mathbf{p_0}, 0)$ as the probability of finding the cell with orientation $\mathbf{p}$ at time t given that initially it had orientation $\mathbf{p_0}$, and also define $Q_k(\mathbf{p}, t|\mathbf{p_0}, 0)$ as the conditional probability that a k tumbling event manifests at time t and ends with orientation $\mathbf{p}$. Q_k satisfies the following first-order difference equation

$$Q_{k+1}(\mathbf{p}, t|\mathbf{p_0}, 0) = \int_0^t \int_\Omega \Phi_{PDF}(t-\tau) K(\mathbf{p}, \mathbf{p}') Q_k(\mathbf{p}', \tau|\mathbf{p_0}, 0) d\mathbf{p}' d\tau \tag{1.43}$$

The correlation between the direction of motion before and after tumble events is captured through the tumbling kernel or angular correlation function, $K(\mathbf{p}, \mathbf{p}')$, which was found to be independent of the chemical field [23]. The meaning of Eq. (1.43) is that the conditional probability that a $k+1$ tumbling event occurs at time t with post-tumbling orientation $\mathbf{p}$ is equal to the conditional probability that a k tumbling event occurs at time τ with post-tumbling orientation $\mathbf{p}'$ multiplied by the probability of tumbling from orientation $\mathbf{p}'$ to orientation $\mathbf{p}$ and multiplied by the probability that the time between tumbling events is $t - \tau$, all of it integrated over all possible pre-orientations $\mathbf{p}'$ and possible times between tumbling events. We can sum all Q_k over k to obtain the probability density function of having an orientation $\mathbf{p}$ at time t^- regardless of the number of tumbling events that already

took place. We get:

$$Q(\mathbf{p},t)=\sum_{k=0}^{\infty}Q_k(\mathbf{p},t)=\delta(\mathbf{p}-\mathbf{p_0})\delta(t)+\int_0^t\int_\Omega \Phi_{PDF}(t-\tau)K(\mathbf{p},\mathbf{p}')Q(\mathbf{p}',\tau)d\mathbf{p}'d\tau \quad (1.44)$$

where we have used the initial condition $Q(\mathbf{p},0)=\delta(\mathbf{p}-\mathbf{p_0})$. The probability density function $\psi(\mathbf{p},t|\mathbf{p_0},0)$ that the swimmer has orientation $\mathbf{p}$ at time t can be obtained as the product of the probability density of reaching that orientation at some time $\tau<t$ multiplied by the probability that no tumbling event will occur in the remaining time $t-\tau$:

$$\psi(\mathbf{p},t|\mathbf{p_0},0)=\int_0^t\hat{\Phi}(t-\tau)Q(\mathbf{p},\tau)d\tau \quad (1.45)$$

We insert Eq. (1.44) into Eq. (1.45). Upon simplification, we get:

$$\begin{aligned}\psi(\mathbf{p},t|\mathbf{p_0},0)=&\delta(\mathbf{p}-\mathbf{p_0})\hat{\Phi}(t)\\&+\int_0^t\int_\Omega\int_s^t\left(\hat{\Phi}_{CDF}(t-\tau)\Phi_{PDF}(t-s)\right)d\tau K(\mathbf{p},\mathbf{p}')Q(\mathbf{p}',s)d\mathbf{p}'ds \quad (1.46)\end{aligned}$$

From Eqs. (1.36) and (1.37), we can easily see that

$$\hat{\Phi}_{CDF}(t-\tau)\Phi_{PDF}(t-s)=\hat{\Phi}_{CDF}(t-s)\Phi_{PDF}(t-\tau) \quad (1.47)$$

We introduce this property into Eq. (1.46) and use Eq. (1.45) to get:

$$\psi(\mathbf{p},t|\mathbf{p_0},0)=e^{-\lambda t}\delta(\mathbf{p}-\mathbf{p_0})+\int_0^t\int_\Omega\lambda e^{-\lambda(t-\tau)}K(\mathbf{p},\mathbf{p}')\psi(\mathbf{p}',\tau|\mathbf{p_0},0)d\mathbf{p}'d\tau \quad (1.48)$$

We take the temporal derivative of Eq. (1.48) and apply Leibniz's theorem:

$$\begin{aligned}\frac{\partial\psi}{\partial t}=&-\lambda e^{-\lambda t}\delta(\mathbf{p}-\mathbf{p_0})+\int_0^t\int_\Omega-\lambda^2e^{-\lambda(t-\tau)}K(\mathbf{p},\mathbf{p}')\psi(\mathbf{p}',\tau|\mathbf{p_0},0)d\mathbf{p}'d\tau\\&+\int_\Omega\lambda K(\mathbf{p},\mathbf{p}')\psi(\mathbf{p}',t|\mathbf{p_0},0)d\mathbf{p}' \quad (1.49)\end{aligned}$$

We use Eq. (1.48) in Eq. (1.49) to find the desired evolution equation for $\psi(\mathbf{p},t|\mathbf{p_0},0)$:

$$\frac{\partial\psi}{\partial t}=-\lambda\psi+\int_\Omega\lambda K(\mathbf{p},\mathbf{p}')\psi d\mathbf{p}' \quad (1.50)$$

This equation, which represents the evolution equation for the probability density of the stochastic process, has the same form as that previously derived by Stroock [24]

$$\frac{\partial \psi}{\partial t} = -\lambda(\mathbf{x}, \mathbf{p})\psi + \int_{\Omega} \lambda(\mathbf{x}, \mathbf{p}) K(\mathbf{p}, \mathbf{p}')\psi d\mathbf{p}', \tag{1.51}$$

where the tumbling frequency was additionally considered to continuously depend on position. Eq. (1.51) has the same form as Eq. (1.50) because of the Markovian assumption. In addition to the dependence of the tumbling frequency on orientation and position, a dependence on the amount of elapsed time since the last tumble was included in the work by Alt [25], who constructed a more general evolution equation than that obtained in Eq. (1.50). To obtain Stroock's equation from Alt's equations one can just integrate them over the elapsed run time [25, 26].

1.3 Particle extra stress in a dilute suspension of force-free active micro-particles

Consider a volume V enclosed by an imaginary surface S, as shown in Fig. (1.2). We denote by $\Delta\mathbf{F}$ the net force exerted across the surface $\mathbf{\Delta S} = \Delta S\mathbf{n}$ by the material outside on the material inside, where $\mathbf{n}$ corresponds to the outward unit vector normal to ΔS. The average contact force per unit area on ΔS is $\Delta\mathbf{F}/\Delta S$. The Euler-Cauchy stress principle states that the action of the body that is outside on the one that is inside is equivalent to a system of distributed forces on the surface S. According to this principle, the contact force $\mathbf{F}$, as $\Delta S \to 0$ is given by

$$\Delta\mathbf{F} = \mathbf{t}^{(\mathbf{n})}\Delta S, \tag{1.52}$$

where $\mathbf{t}^{(\mathbf{n})}$ is the mean surface traction vector or stress vector. The stress vector depends on its location as well as on the orientation of the plane on which it is acting. Therefore,

$$\mathbf{t}^{(\mathbf{n})}(\mathbf{R}, t) = \lim_{\Delta S \to 0} \frac{\Delta\mathbf{F}}{\Delta S} = \frac{d\mathbf{F}}{dS}, \tag{1.53}$$

From Newton's third law, the surface traction vector acting on opposite sides of the same surface S are equal in magnitude and opposite in direction. Mathematically, this is expressed

as

$$\mathbf{t}^{(\mathbf{n})} = -\mathbf{t}^{(-\mathbf{n})}, \tag{1.54}$$

also known as Cauchy reciprocal theorem. To describe the instantaneous stress at a given point P is necessary to provide the stress vector on three perpendicular planes at the point P at a given time. This is commonly done through a stress dyadic or stress tensor, which we introduce here as $\boldsymbol{\sigma}$. The relation between the traction vector and the stress tensor is:

$$\mathbf{t}^{(\mathbf{n})} = \mathbf{n} \cdot \boldsymbol{\sigma} \tag{1.55}$$

Therefore, the traction vector on any surface element dS is obtained by dotting the unit

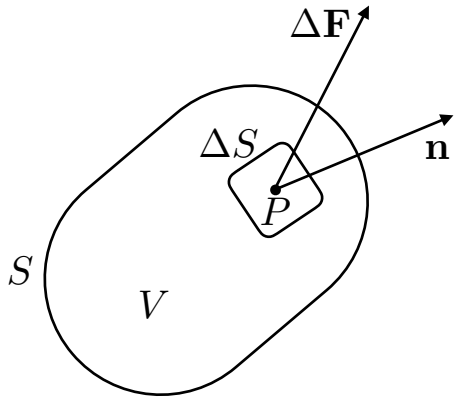

Figure 1.2: Continuum mechanics: Definition of surface traction vector.

normal vector $\mathbf{n}$ into the dyadic tensor. Knowing the instantaneous stress tensor $\boldsymbol{\sigma}$ in space, allows us to determine the net surface force acting on a body, which is equal to the sum of all the traction vectors acting on different elements of the surface area integrated over the whole body, that is:

$$\mathbf{F}_{\mathbf{net}} = \int_S \mathbf{t}^{(\mathbf{n})} dS = \int_S \mathbf{n} \cdot \boldsymbol{\sigma} dS \tag{1.56}$$

One can apply the divergence theorem to Eq. (1.56) to obtain the net force on the body as a volume integral:

$$\mathbf{F}_{\mathbf{net}} = \int_V \nabla \cdot \boldsymbol{\sigma} dV \tag{1.57}$$

The purpose of the next sections is to determine a relation between the macroscopic properties of the bulk stress of a suspension of rigid force-free active particles and its microscopic structure on the particle scale, for some special cases. In a suspension of particles, we define a particle extra stress ($\boldsymbol{\Sigma}^p$), which is a physical quantity that expresses the internal forces

that the particles exert on the surrounding fluid as they move through the medium. The knowledge of the particle extra stress allows one to obtain the force per unit volume (force density) created by the particles on the fluid, whose form ($\nabla \cdot \boldsymbol{\Sigma}^p$) is easily inferred from Eq. (1.57).

1.3.1 The stress system in a suspension of spherical force-free particles subjected to a point torque

We consider spherical particles that rotate under a point torque, and that are dispersed in a Newtonian quiescence fluid of viscosity μ. Neglecting history effects, the stress is obtained from the instantaneous configuration/state of the particles, which in our case mainly depends on the instantaneous orientation of the particles. We take ensemble averages and the bulk stress is defined as a probability ensemble average [27]. These averages are obtained by taking volume integrals of a statistically homogeneous suspension comprised of particles and fluid. By statistically homogeneous, we mean that it is possible to find a length larger than the average interparticle spacing and over which the statistical properties of the suspension barely vary. In the absence of any force or torque, the suspension has an isotropic structure and for sufficiently small strain rates it behaves as a Newtonian fluid. The effect of the particles is just an increase in the shear viscosity of the suspension. An external torque (i.e. magnetic) creates a relative rotational motion of the particle and the ambient fluid, which creates an additional stress contribution to the suspension. The average stress in the suspension is

$$\langle \sigma_{ij} \rangle = \frac{1}{V} \int_V \sigma_{ij} dV. \tag{1.58}$$

We split the volume integral as a sum of two integrals (fluid and particles). The bulk stress becomes

$$\langle \sigma_{ij} \rangle = \frac{1}{V} \sum_\alpha \int_{V_\alpha} \sigma_{ij} dV + \frac{1}{V} \left(\int_{V_f} -p\delta_{ij} + 2\mu E_{ij} \right) dV. \tag{1.59}$$

where we have assumed the well-known Newtonian relation for the fluid stress. For rigid particles, $\int_{V_\alpha} E_{ij} dV$ vanishes and the bulk suspension stress reduces to

$$\langle \sigma_{ij} \rangle = \underbrace{\frac{1}{V} \sum_\alpha \int_{V_\alpha} \sigma_{ij} dV}_{\text{Particle extra stress } \Sigma^p_{ij}} \underbrace{- \frac{1}{V} \int_V p\delta_{ij} dV + \frac{1}{V} \int_V 2\mu E_{ij} dV}_{\text{Newtonian stress}}. \tag{1.60}$$

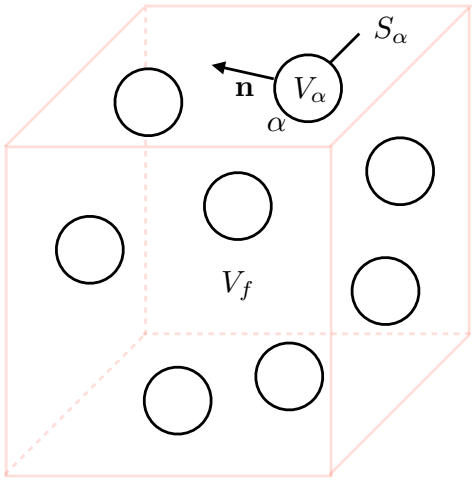

Figure 1.3: Volume of integration V of a statistically homogeneous suspension, comprised of fluid volume V_f and many particles of volume V_α and surface area S_α. Unit vector $\mathbf{n}$ indicates the outward-pointing normal vector on the particle surface.

From the inertialess Cauchy's equation of motion, we have

$$\frac{\partial}{\partial x_k}(\sigma_{kj}x_i) = \frac{\partial \sigma_{kj}}{\partial x_k} + \sigma_{kj}\delta_{ik} = \sigma_{ij}. \tag{1.61}$$

We insert Eq. (1.61) into Eq. (1.60) and, upon the application of Gauss' theorom, the particle extra stress becomes:

$$\Sigma_{ij} = \frac{1}{V}\sum_\alpha \int_{s_\alpha} \underbrace{n_k\sigma_{kj}}_{t_j} x_i dS \tag{1.62}$$

Remember that the vector $\mathbf{n}$ goes from the particle to the fluid. As a consequence, the traction t_j is defined from the fluid to the particle. We can decompose the particle extra stress between a symmetric and an antisymmetric contribution:

$$\Sigma_{ij} = \underbrace{\frac{1}{V}\sum_\alpha \int_{s_\alpha} \frac{1}{2}(x_i t_j + x_j t_i) dS}_{\text{Symmetric contribution}} + \underbrace{\frac{1}{V}\sum_\alpha \int_{s_\alpha} \frac{1}{2}(x_i t_j - x_j t_i) dS}_{\text{Antisymmetric contribution}} \tag{1.63}$$

The torque from particle α to the fluid can be expressed as a function of the traction $\mathbf{t}' = -\mathbf{t}$ as

$$T_k^\alpha = \int_{S_\alpha} \epsilon_{kab} x_a t'_b dS \tag{1.64}$$

A small rearrangement leads to the following equality

$$\epsilon_{ijk} T_k^{\alpha} = \int_{S_\alpha} (x_i t'_j - x_j t'_i) dS \tag{1.65}$$

For spherical particles, the symmetric contribution in Eq. (1.63) vanishes. Direct comparison of Eqs. (1.63) and (1.65) provides a simple expression for the particle extra stress:

$$\Sigma_{ij}^{p} = -\frac{1}{2V} \epsilon_{ijk} T_k \tag{1.66}$$

Therefore, the antisymmetric part of the stress is equal to half the total torque imposed on the particles per unit volume of the suspension. As an example, we can determine the particle extra stress of a suspension of particles with magnetic dipole $\mathbf{M}$, upon the application of a uniform magnetic field $\mathbf{H}$. This particles feel a net magnetic torque $\mathbf{M} \times \mathbf{H}$ which is transmitted to the fluid. The particle extra stress becomes

$$\Sigma_{ij}^{p} = \frac{1}{2V} \left(M_j H_i - M_i H_j \right) \tag{1.67}$$

This expression will be useful in Chapter 7 to investigate the use of uniform magnetic fields to control the effective rheology and self-driven flows of magneto-active suspensions in microfluidic channels as well as in wall-free environments.

1.3.2 Active stresses

An important component of active particle suspensions is the fluid medium. As particles move through the fluid, they exert stresses in the medium that originate due to an exchange of forces between the active parts of the particles and the surrounding fluid molecules. These stresses generate flows that affect the configuration of the particles, which in turn modifies the stress generation. This non-linear effect might lead to collective phenomena effects or hydrodynamic instabilities. Following previous studies [27, 28], we use a mean-field hydrodynamic approach and determine the averaged active particle extra stress. At the continuum level, we account for the effect of the intermolecular forces through the divergence of the continuum stress tensor, which acts as an additional forcing term contribution in the momentum equation. In the absence of particles, the fluid is governed by the Navier-Stokes

equations. Conservation of mass requires

$$\frac{\partial \rho}{\partial t} + \nabla \cdot (\rho \mathbf{u}) = 0, \tag{1.68}$$

where ρ is the fluid density and $\mathbf{u}$ the fluid velocity. Eq. (1.68) can also be expressed as

$$\frac{D\rho}{Dt} + \rho \nabla \cdot \mathbf{u} = 0, \tag{1.69}$$

where D/Dt corresponds to the material derivative. For an incompressible fluid, $\nabla \cdot \mathbf{u} = 0$. The linear momentum conservation equation is

$$\rho \left[\frac{\partial \mathbf{u}}{\partial t} + (\mathbf{u} \cdot \nabla)\mathbf{u} \right] = \nabla \cdot \boldsymbol{\sigma} + \rho \mathbf{f}, \tag{1.70}$$

where $\boldsymbol{\sigma}$ denotes the total stress and $\mathbf{f}$ is the force per unit mass on the fluid. Conservation of angular momentum requires the stress tensor to be symmetric. For a Newtonian fluid, the constitutive relation for the stress is

$$\boldsymbol{\sigma} = -p\mathbf{I} + 2\eta \mathbf{E} \tag{1.71}$$

where p is the pressure, η is the dynamic viscosity of the fluid and $\mathbf{E}$ is the rate-of-strain tensor, defined as

$$\boldsymbol{E} = \frac{1}{2} \left(\nabla \mathbf{u} + \nabla \mathbf{u}^{\dagger} \right) \tag{1.72}$$

Due to the characteristic small length scales, the fluid mechanics of bacterial suspensions are governed by a low Reynolds number hydrodynamics regime, where viscous forces dominate over inertial effects. In this regime, the Navier Stokes' equations reduce to the Stokes' equations:

$$\nabla \cdot \mathbf{u} = 0, \qquad 0 = -\nabla p + \eta \nabla^2 \mathbf{u} + \rho \mathbf{f}, \tag{1.73}$$

We now introduce the Stokeslet $\mathbf{G}$, which is the fundamental solution for the Stokes' equations. Given a point force $\mathbf{F}$ whose point of application is $\mathbf{x_0}$, the fluid velocity at an arbitrary point $\mathbf{x}$ can be obtained as

$$\mathbf{u}(\mathbf{x}) = \mathbf{G}(\mathbf{x} - \mathbf{x_0}) \cdot \mathbf{F}, \tag{1.74}$$

$\mathbf{G}$ represents the Green's function for the Stokes' equations. To determine $\mathbf{G}$, we solve the following system of equations:

$$\nabla \cdot \mathbf{G} = 0, \qquad \mathbf{0} = -\nabla \boldsymbol{\Pi} + \eta \nabla^2 \mathbf{G} + \mathbf{I}\delta(\mathbf{x} - \mathbf{x_0}), \tag{1.75}$$

where $\delta(\mathbf{x} - \mathbf{x_0})$ is the three-dimensional Dirac delta function. The solution of Eq. (1.75) $\mathbf{G}(\mathbf{x} - \mathbf{x_0})$, also called Oseen-Burgers tensor, is given by

$$\mathbf{G}(\mathbf{x}) = \frac{1}{8\pi\eta}\left(\frac{\mathbf{I}}{r} + \frac{\mathbf{x}\,\mathbf{x}}{r^3}\right) \tag{1.76}$$

$\boldsymbol{\Pi}$ is the so-called Green's function for the fluid pressure, given by

$$\boldsymbol{\Pi}(\mathbf{x}) = \frac{1}{4\pi}\frac{\mathbf{x}}{r^3} \tag{1.77}$$

It is related to the fluid pressure by the relation $p(\mathbf{x}) = \boldsymbol{\Pi} \cdot \mathbf{F}$. We are particularly interested in determining an expression for the stress generated by active particles on the surrounding fluid due to its activity. For neutrally buoyant microorganisms with small length scales, we can ignore the inertial and volume force terms on the dynamical equations of the swimmers, and the swimmers will be considered to be force- and torque-free at any instant in time. Consequently, the propulsive force $\mathbf{F_p}$ exerted by the swimmer to advance through the medium is balanced by the drag force $\mathbf{F_d}$:

$$\mathbf{F_p} + \mathbf{F_d} = \mathbf{0} \tag{1.78}$$

Even though the propulsive force is distributed along the motile cilia or flagella appendages

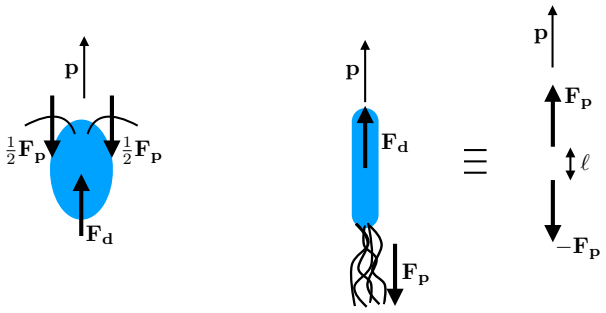

Figure 1.4: Force diagram for front-actuated (modeled as a compressional dipole) and rear-actuated (modeled as an extensional dipole) active cells. Left: puller-particle (i.e. Chlamydomonas reinhardtii). Right: pusher-particle (i.e. Escherichia Coli).

of the microorganism and the drag force is distributed along its body, to leading order the fluid velocity far away from their bodies can be described by the resulting fluid field created by two equal and opposite point forces (refer to Fig. 1.4). The linearity of the Stokes equations permits the use of the Green's function to construct solutions for a distribution of forces. Each of these forces creates a flow. The total flow can be obtained as a superposition of the flow fields created independently by each of these forces. Therefore, the fluid field corresponds to that created by two Stokeslets. Assuming the swimmer is located at $\mathbf{x_0}$, we have

$$\mathbf{u}(\mathbf{x}) = \mathbf{G}(\mathbf{x} - (\mathbf{x_0} + (\ell/2)\mathbf{p})) \cdot \mathbf{F_p} - \mathbf{G}(\mathbf{x} - (\mathbf{x_0} - (\ell/2)\mathbf{p})) \cdot \mathbf{F_p}, \tag{1.79}$$

where ℓ is the distance between the points of application of both Stokeslets. We now introduce the active stresslet $\sigma_0 = \pm F_p \ell$, whose sign depends on the propulsion mechanism: $\sigma_0 < 0$ for pusher swimmers (extensile dipole), whereas $\sigma_0 > 0$ for pullers (contractile dipole). The propulsive force F_p is equal to the drag force $F_d = \zeta v_0$ on the swimmer, where ζ is its drag coefficient scaling as $\zeta \propto \eta\ell$, and v_0 its propulsive velocity. Therefore, the active stresslet coefficient scales as $|\sigma_0| \propto \eta v_0 \ell^2$. The typical small length scales of these microorganisms allows one to expand Eq. (1.79) in Taylor series for small ℓ. To leading order, we get:

$$\mathbf{u}(\mathbf{x}) = \sigma_0 \mathbf{p} \cdot \nabla \mathbf{G}(\mathbf{x} - \mathbf{x_0}) \cdot \mathbf{p} + O(\ell^2) \tag{1.80}$$

where $\nabla\mathbf{G}$ can easily be obtained from Eq. (1.76). We can prove that the fluid field of Eq. (1.80), caused by the active stresslet, satisfies the system of equations [28]:

$$\nabla \cdot \mathbf{u} = 0, \qquad \mathbf{0} = -\nabla p + \eta \nabla^2 \mathbf{u} + \sigma_0 \mathbf{pp} \cdot \nabla \delta(\mathbf{x} - \mathbf{x_0}), \tag{1.81}$$

In the case where there are many particles, we can use the probability distribution $P(\mathbf{x}, \mathbf{p}, t)$ introduced in Section 2.1 to describe the average configuration of the particles. We sum all the dipolar flows created by all the swimmers. Eq. (1.81) becomes

$$\nabla \cdot \mathbf{u} = 0, \qquad \mathbf{0} = -\nabla p + \eta \nabla^2 \mathbf{u} + \int_V \int_\Omega \sigma_0 \mathbf{pp} \cdot \nabla \delta(\mathbf{x} - \mathbf{x_0}) \; P(\mathbf{x_0}, \mathbf{p}, t) d\mathbf{p} d\mathbf{x_0} \tag{1.82}$$

which is equivalent to

$$\nabla \cdot \mathbf{u} = 0, \qquad \mathbf{0} = -\nabla p + \eta \nabla^2 \mathbf{u} + \sigma_0 \nabla \cdot \langle \mathbf{pp} \rangle \tag{1.83}$$

where $\langle \mathbf{pp} \rangle$ corresponds to the local nematic order tensor

$$\langle \mathbf{pp} \rangle = \int_{\Omega} \mathbf{pp}\ P(\mathbf{x}, \mathbf{p}, t) d\mathbf{p} \tag{1.84}$$

To simplify certain mathematical calculations, we can make the tensor $\langle \mathbf{pp} \rangle$ traceless, a manipulation that will modify the fluid pressure but not the fluid velocity. The final expression for the active stress is

$$\boldsymbol{\Sigma}^a(\mathbf{x}, t) = \sigma_0 \langle \mathbf{pp} - \mathbf{I}/3 \rangle \tag{1.85}$$

which suggests that self-generated flows will arise when spatial gradients in nematic alignment develop in the domain. Another way of obtaining the active stress generated by a force-dipole microorganism, is by realizing that the stresslet corresponds to the symmetric first moment of the forces, a result obtained by Batchelor, and previously derived in Eq. (1.63). In the case of two collinear forces, whose point of application is separated by a distance ℓ one recovers Eq. (1.85) [29].

1.4 Thesis overview

The thesis is organized as follows:

In Chapter 2 a mathematical model based on Generalized Taylor Dispersion Theory is developed to study the long-time asymptotic transport of active particles in a two-dimensional periodic porous medium upon the application of a hydrodynamic fluid field, and it is complemented by Langevin simulations. Although it is impossible to anticipate the exact path of an individual particle, the overall behavior of a dilute cloud of cells is predicted, and their net transport is described by a macroscopic advection-diffusion equation. The dependence of the effective mean swimmer velocity vector and dispersivity dyadic on the porous geometry, external shear and swimmer parameters is explored and physical explanations are provided for the trends observed. In addition, the effect of chemical fields on the transport of microbial run-and-tumble communities in heterogeneous media is explored in Chapter 3. Species that respond to both positive and negative gradient of attractants, and strains that only respond to positive gradients are studied, and mathematical expressions for the asymptotic mean bacterial velocity vector and dispersivity dyadic for both species are derived in the limit of vanishing surface fraction of obstacles.

In Chapter 4 a kinetic model based on two probability density functions is proposed

to calculate the mechanical swim pressure exerted by a dilute suspension of athermal run-and-tumble swimmers on the walls of a straight channel. Our model accounts for the finite time spent by the particles at the walls and it is validated against Monte-Carlo simulations. The dependence of pressure on confinement is investigated.

In Chapter 5 the temporal evolution of a three-dimensional bacterial fluid film is analyzed via linear stability analysis. A two-way coupling between the conservation equation for the particles and the fluid equations is used, and active tractions along with fluid pressure, capillary and viscous stresses balance at the air-fluid interface. The base state is derived theoretically, and the small perturbations are calculated numerically. Further normal mode analysis is carried out for inverted bacterial fluid films and bacterial fluid jets. Stability criteria are determined for all the cases.

In Chapter 6 a non-linear mean-field theory is presented to study the configuration and effective rheology of a dilute active suspension in a planar Poiseuille flow. The internal forces between particles and fluid are accounted for through the particle extra stress, where active and passive stresses drive flows and modify the effective suspension rheology. The transition to superfluidity and other rheological trends are captured and further analyzed. In addition, an approximate theory for weak flows and wide channels is derived.

In Chapter 7 a continuum kinetic model is utilized to explore the use of magnetotactic bacterial suspensions as tunable active fluids. The idea of a magnetotactic bacterial suspension behaving as an active ferromagnetic pump is proposed, and its rheological properties are further investigated upon the application of simple external flows in combination with a uniform magnetic field.

In Chapter 8 numerical simulations based on a continuum kinetic model are used together with linear stability analyses to predict and characterize transitions to spontaneous flows and collective motion of suspensions comprised of self-propelled units that lie in several two-dimensional microfluidic geometries. Also, a connection between the onset of spontaneous pumping with the effective rheology of the suspension is proposed.

In Chapter 9 conclusions and review of the contributions of the thesis are provided, and possible directions of future research work are listed.

Chapter 2

Asymptotic transport and dispersion of active particles in periodic porous media

2.1 Introduction

The transport of active self-propelled particles through complex structured media has important consequences in microbial ecology as well as human health. Examples include the spreading of contaminants in soils and groundwater aquifers, bacterial filtering, biodegradation and bioremediation processes, and the transport of various motile cells inside the body. In engineering, applications in areas such as medical diagnostics, chemical analysis and drug delivery also often hinge on the manipulation and control of active micro-particle motions through complex geometries [30], such as particle sorting [31, 32], rectification [33–35], ratcheting [36], jamming [37], trapping [38–40] and hydrodynamic entrapment [41–43].

While the effective transport of passive tracers and particles in various porous media flows has been analyzed in great detail in the past, the case of active particles that can self-propel remains largely unexplored. In free space, a microswimmer with speed v_0 and translational and rotational diffusivities d_t and d_r, performs a spatial random walk with long-time dispersivity $\overline{D} = d_t + v_0^2/2nd_r$ in n dimensions [44]. Experiments with Janus particles accompanied with theory displayed different diffusive behaviors at different times [45]. Different regimes involving inertial, ballistic, anomalous, and diffusive behaviors were found theoretically for active self-phoretic swimmers [46]. Other studies addressed the spreading of constant-speed swimmers using theoretical Langevin calculations in the presence of a linear [47–49] and a parabolic flow [50].

In a porous matrix and in the absence of flow, this *active* dispersion should intuitively be reduced, not only by geometric obstruction but also by the tendency of active particles to accumulate at boundaries [51, 52]. Trapping near obstacles is indeed seen in experiments [42] and is also thought to be enhanced by hydrodynamic interactions [43]. When an external flow is applied, the coupling of particle orientations with the local fluid shear further complicates transport. First, diffusion and swimming across streamlines alter long-time spreading by the classic phenomenon of *shear-induced* Taylor dispersion [53, 54]. Secondly, the rotation of particles in the strong shear near boundaries is expected to result in their alignment against the flow [55, 56]. This could lead to a net reduction in mean transport by an effect similar to upstream swimming in pressure-driven flows in the presence of asymmetric obstacles, where the interaction of microswimmers with boundaries can cause a net directed migration even in the absence of flow [33, 57, 58].

Some of these trends have indeed been confirmed in experiments [56, 59–61] as well as in various computational models [35, 39, 62, 63], yet a general theoretical framework for predicting active transport and dispersion in even simple porous matrices remains lacking. In this chapter, we present a macro-continuum transport model based on generalized Taylor dispersion theory [64] that predicts the asymptotic transport velocity and dispersivity of active Brownian particles in periodic porous media. Starting from the Fokker-Planck equation for the configuration of a single self-propelled particle wandering through the interstices of a periodic lattice, we use a formal averaging procedure to obtain expressions for its long-time mean velocity $\overline{\mathbf{U}} = \lim_{t\to\infty} \frac{d}{dt}\langle \mathbf{R}(t)\rangle$ and dispersivity dyadic $\overline{\mathbf{D}} = \lim_{t\to\infty} \frac{1}{2}\frac{d}{dt}\langle \mathbf{R}(t)\mathbf{R}(t)\rangle$ under the influence of an applied flow, where both quantities simply involve the solution of a boundary-value problem on the pore scale. We also derive a macroscale Eulerian interpretation for these coefficients, and use it to unravel the roles of particle motility, applied fluid flow, and porous lattice geometry on asymptotic transport properties. Our predictions, which show excellent agreement with results from Langevin simulations, provide a simple theoretical framework for analyzing bacterial transport in natural structured environments and for designing engineered porous media in applications involving microswimmers.

2.2 Problem definition

We analyze the long-time asymptotic transport of a dilute collection of self-propelled active particles dispersed in a viscous solvent and moving through the interstices of a doubly-

periodic 2D porous material. The porous medium is modeled as an infinite square lattice comprised of rigid obstacles of characteristic dimension a and generated through the discrete translation of an appropriately chosen geometric unit cell of linear dimension L (Fig. 2.1). The origin O of the coordinate system is chosen as the centroid of an arbitrary cell, and each cell in the lattice is labeled by two integers $(\alpha, \beta) \in \mathbb{Z}^2$ identifying its horizontal and vertical positions, or equivalently by the position $\mathbf{R}_{\alpha\beta} = (X_\alpha, Y_\beta)$ of its centroid where $X_\alpha = \alpha L$ and $Y_\beta = \beta L$. The array is characterized by its porosity $\epsilon_p = S_f/S_t$, or ratio of the interstitial fluid area of the unit cell over its total area. In a dilute system, we may neglect interparticle interactions and thus need only consider the transport of a single swimmer. Its instantaneous configuration is described by its position $\mathbf{R}(t)$ with respect to point O and by its orientation angle $\theta(t) \in \Omega = [0, 2\pi)$ in the plane of motion, which defines its swimming direction $\mathbf{p} = (\cos\theta, \sin\theta)$. The global coordinate $\mathbf{R}$ can be further decomposed as $\mathbf{R} = \mathbf{R}_{\alpha\beta} + \mathbf{r}$, where $\mathbf{R}_{\alpha\beta}$ is the position of the unit cell where the particle is located and $\mathbf{r} = (x, y)$ is a local coordinate with respect to the center of that cell. We assume that the particle is released at $t = 0$ at position $\mathbf{R}_0 = \mathbf{R}_{00} + \mathbf{r}_0$ with orientation $\mathbf{p}_0$. For later use, we introduce a global gradient operator $\nabla_R \equiv \partial/\partial\mathbf{R}$, a local gradient operator $\nabla_r \equiv (\partial/\partial\mathbf{r})_{\mathbf{R}_{\alpha\beta}}$ and an orientational gradient operator $\nabla_p \equiv (\mathbf{I} - \mathbf{pp}) \cdot \partial/\partial\mathbf{p}$.

Particle motion results from self-propulsion with constant speed v_0 in the direction of $\mathbf{p}$, from advection and rotation by fluid flow through the lattice, and from translational and rotational diffusion. Its dynamics can thus be modeled by two Langevin equations

$$\dot{\mathbf{R}} = v_0\mathbf{p} + \mathbf{u}(\mathbf{r}) + \boldsymbol{\eta}_t(t)\,, \tag{2.1}$$

$$\dot{\mathbf{p}} = \boldsymbol{\Omega}(\mathbf{r}) \times \mathbf{p} + \gamma(\mathbf{I} - \mathbf{pp}) \cdot \mathbf{E}(\mathbf{r}) \cdot \mathbf{p} + \boldsymbol{\eta}_r(t)\,. \tag{2.2}$$

The vectors $\boldsymbol{\eta}_t$ and $\boldsymbol{\eta}_r$ are Gaussian random variates with zero mean and with variance $\langle\boldsymbol{\eta}_t(t)\boldsymbol{\eta}_t(t')\rangle = \sqrt{2d_t}\mathbf{I}\delta(t-t')$ and $\langle\boldsymbol{\eta}_r(t)\boldsymbol{\eta}_r(t')\rangle = \sqrt{2d_r}(\mathbf{I} - \mathbf{pp})\delta(t-t')$, respectively, where d_t and d_r denote the constant translational and rotational diffusivities. In two-dimensions, Eq. can be expressed in terms of the polar-director angle θ:

$$\dot{\theta} = \mathbf{p}^\perp \cdot (\gamma\mathbf{E} - \mathbf{W}) \cdot \mathbf{p} + \eta^r(t), \tag{2.3}$$

where $\mathbf{p}^\perp = (-\sin\theta, \cos\theta)$. For most of our Brownian simulations we use $N = 10^5$ particles. The no-flux boundary condition on the surface of the obstacles is ensured by reflecting

boundaries. The Brownian simulations have been validated against the well-known results of passive tracer transport in porous media [65].

The velocity field $\mathbf{u}(\mathbf{r})$ is a two-dimensional viscous flow driven by a macroscopic pressure gradient applied across the array, with uniform speed u_∞ and incoming angle Θ_f upstream of the array; its vorticity $\nabla_r \times \mathbf{u} = 2\,\mathbf{\Omega}(\mathbf{r})$ and rate-of-strain $\mathbf{E}(\mathbf{r}) = \frac{1}{2}[\nabla_r \mathbf{u} + \nabla_r \mathbf{u}^\dagger]$ cause rotation and alignment of the particle in Eq. (2.2) according to Jeffery's equation [7], where the Bretherton constant γ characterizes shape anisotropy ($\gamma = 0$ for a sphere, $\gamma \approx 1$ for a needle). We solve for the fluid field numerically by using a boundary integral formulation. Owing to the periodicity of the lattice we make use of the doubly periodic Green's function of two-dimensional Stokes flow computed using standard Ewald summation techniques. The fluid velocity $\mathbf{u}$ at any point inside the unit cell of the lattice is decomposed into the free-stream component $\mathbf{u}^\infty$ and a disturbance velocity $\mathbf{u}^D$ due to the presence of the obstacles. In the present problem we have assumed $\mathbf{u}^\infty$ to be a uniform (streaming) flow. On the surface of the obstacles ∂S the no-slip condition is satisfied $\mathbf{u} = \mathbf{0}$. We can alternatively write $\mathbf{u}^D = -\mathbf{u}^\infty$. We use a single-layer representation for the velocity to obtain:

$$u_j(\mathbf{x_0}) = u_j^\infty(\mathbf{x_0}) - \frac{1}{4\pi\mu} \sum_{q=0}^{N_p} \int_{C_q} G_{ij}(\mathbf{x}, \mathbf{x_0}) f_i(\mathbf{x}) dl(\mathbf{x}), \tag{2.4}$$

where N_p is the total number of obstacles within the unit cell, C_q is the contour of the q^{th} obstacle, $G_{ij}(\mathbf{x}, \mathbf{x_0})$ is the appropriate Green's function and $f_i(\mathbf{x})$ is the traction. For the hexagonal lattice $q = 5$ while for the square lattice $q = 1$. On enforcing the no-slip boundary condition one is able to solve for the unknown tractions by inverting a dense linear system. Once the tractions are obtained, velocity at any point can be calculated using Eq. 2.4. For all the cases presented here we have used linear elements to discretize the contour of the obstacles and Gauss-Legendre quadrature for evaluating the integrals. Sangani and Acrivos [66] studied the flow past periodic array of circular cylinders using a streamfunction-vorticity formulation and provided the results for drag on a cylinder as a function of volume fraction. Our numerical method has been validated against their results and we find excellent agreement. In order to facilitate fast computation in our Brownian simulations, the velocity is pre-tabulated on a Cartesian mesh and bilinear interpolations are used. We use second order accurate finite difference approximations (FDA) to compute and tabulate gradients on the mesh. Our interpolation results are validated against the boundary

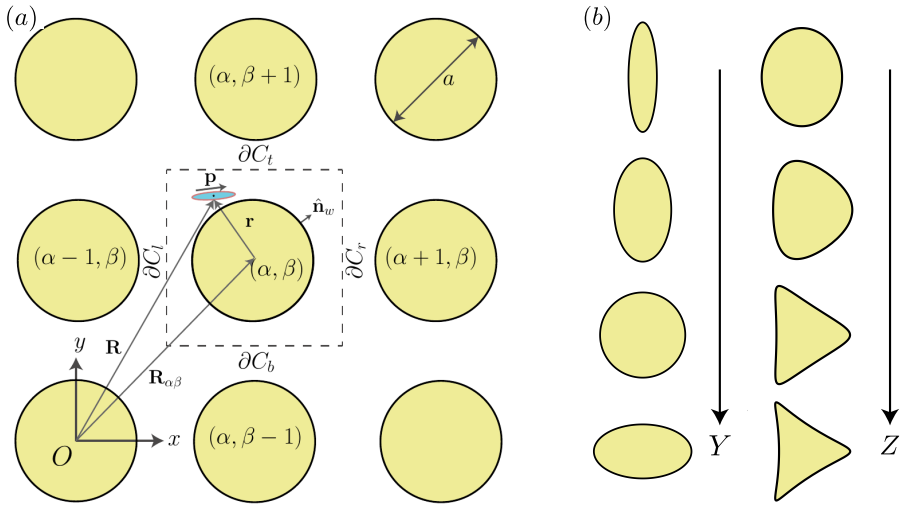

Figure 2.1: (a) Geometry of a representative lattice, unit cell and associated nomenclature. (b) Non-spherical obstacle shapes are generated by conformal mapping of the unit disc [1], where parameters Y and Z control anisotropy and fore-aft asymmetry, respectively.

integral method and the error is always found to be within one percent.

We use conformal mapping on the unit circle to consider different obstacle shapes. The shapes considered are given by the following Riemann map of the unit disc ($|\sigma| < 1$):

$$z(\sigma) = W\sigma + \frac{Y}{\sigma} + \frac{Z}{\sqrt{2}\sigma^2}, \tag{2.5}$$

where $\sigma = e^{i\chi}$, χ varying within $\chi \in [0, 2\pi)$, and $\{W, Y, Z\}$ are three parameters that describe the shape. An identical conformal map was used to study swimming of microorganisms [1]. Avoiding self-intersection of the boundary provides the following constraint on the shape-parameters [1]:

$$W \geq Y \pm \sqrt{2}Z, \quad WY \geq 2Z^2 - W^2. \tag{2.6}$$

For a fixed surface fraction of the porous media we also need to constrain the area of these shapes. It can be shown [1] that the area of any of these obstacle shapes is given by $A = \pi\left(W^2 - Y^2 - Z^2\right)$. Following our non-dimensionalization, we chose the area A to be identical to a circle with unit diameter. The area constraint allows us to vary just the parameters $\{Y, Z\}$ to obtain different shapes of the obstacles.

Our aim in the following is to describe the long-time statistics of $\mathbf{R}$, which we proceed to model within a continuum framework.

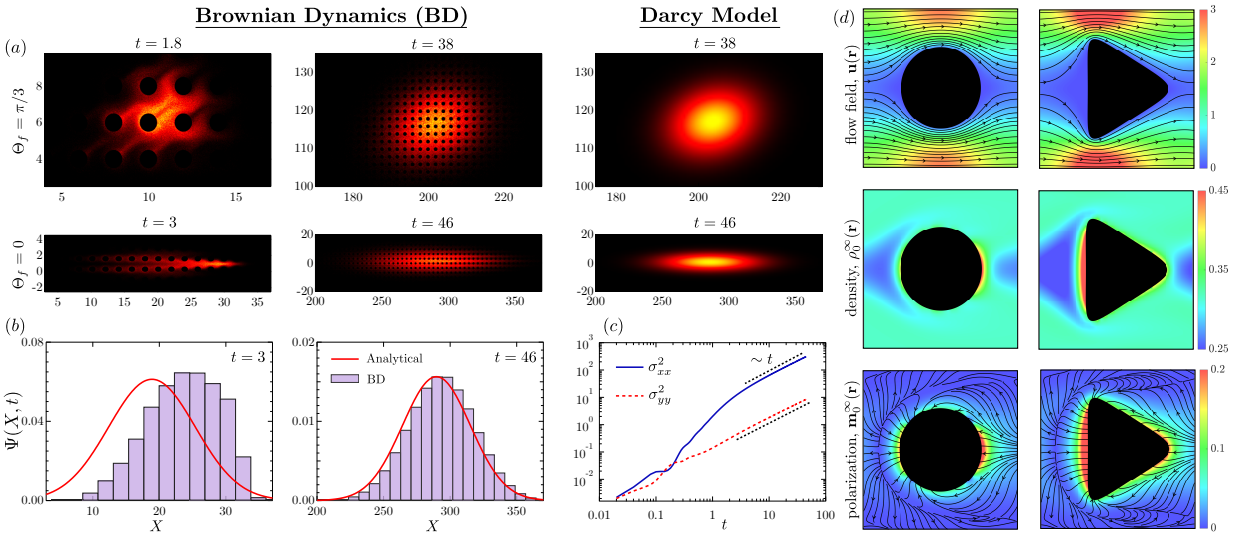

Figure 2.2: (a) Transport and spreading of a cloud of active particles in Brownian dynamics (BD) simulations at two different times (left two columns) compared to the Darcy-scale theoretical prediction obtained by solving Eq. (2.78) (third column). The two rows correspond to two incoming flow angles Θ_f. Results shown are for a square lattice with circular pillars. Parameter values: $\epsilon_p = 0.804$, $\mathrm{Pe}_s = 1$, $\kappa = 0.1$, and $\mathrm{Pe}_f = 5$. (b) Probability density function $\Psi(X,t)$ of the macroscale horizontal position X for the two instantaneous times shown in (a) with $\Theta_f = 0$, where BD results are compared to analytical predictions. (c) Time evolution of the variances σ^2_{xx} and σ^2_{yy} of particle positions, showing convergence to the asymptotic diffusive regime. (d) Asymptotic solutions on the pore scale for two different pillar shapes: flow streamlines and velocity magnitude (*top*), density field $\rho_0^\infty(\mathbf{r}) = \int_\Omega \psi_0^\infty(\mathbf{r},\mathbf{p})d\mathbf{p}$ (*middle*), and polarization field $\mathbf{m}_0^\infty(\mathbf{r}) = \int_\Omega \mathbf{p}\psi_0^\infty(\mathbf{r},\mathbf{p})d\mathbf{p}$ (*bottom*) for the same parameter values as in (a).

2.3 Fokker-Planck description

In order to quantify the likelihood of a certain particle configuration, we define the conditional probability density $\psi(\mathbf{R},\mathbf{p},t|\mathbf{R}_0,\mathbf{p}_0)$ of finding the particle at a position $\mathbf{R}$, with orientation $\mathbf{p}$ at time t, given that it was initially released at a position $\mathbf{R}_0$ with orientation $\mathbf{p}_0$. It satisfies a Fokker-Planck equation

$$\partial_t\psi + \nabla_R\cdot\mathbf{J} + \nabla_p\cdot\mathbf{j} = \delta(\mathbf{R}-\mathbf{R}_0)\delta(\mathbf{p}-\mathbf{p}_0)\delta(t)\,, \tag{2.7}$$

where the initial condition is incorporated by the source term on the right-hand side. The conditional probability is subjected to the pre-initial condition $\psi(t<0)=0$. The spatial and orientational probability fluxes are easily obtained from the Langevin equations (2.1)–(2.2)

as (for more details, we refer the reader to § 1.1.1)

$$\mathbf{J} = [v_0\mathbf{p} + \mathbf{u}(\mathbf{r})]\psi - d_t\nabla_R\psi, \tag{2.8}$$

$$\mathbf{j} = [\boldsymbol{\Omega}(\mathbf{r}) \times \mathbf{p} + \gamma(\mathbf{I} - \mathbf{pp}) \cdot \mathbf{E}(\mathbf{r}) \cdot \mathbf{p}]\,\psi - d_r\nabla_p\psi. \tag{2.9}$$

Noting that ψ only depends on the relative position $\mathbf{X}_{\alpha\beta} = \mathbf{R}_{\alpha\beta} - \mathbf{R}_{00}$, we conveniently rewrite it as $\psi \equiv \psi(\mathbf{X}_{\alpha\beta}, \mathbf{r}, \mathbf{p}, t|\mathbf{r}_0, \mathbf{p}_0)$. For a given cell (α, β), Eq. (2.7) can then be recast in terms of local variables as

$$\partial_t\psi + \nabla_r \cdot \mathbf{J} + \nabla_p \cdot \mathbf{j} = \delta_{\alpha 0}\delta_{\beta 0}\delta(\mathbf{r} - \mathbf{r}_0)\delta(\mathbf{p} - \mathbf{p}_0)\delta(t). \tag{2.10}$$

We normalize the conditional probability distribution, so that at any time after the swimmer is set free in the system, the sum of the probabilities accounting for all possible configurations is one. The normalization condition expressed as an infinite series reads

$$\sum_{\alpha,\beta=-\infty}^{\infty} \int_{S_{\alpha\beta}} \int_{\Omega} \psi \, d\mathbf{p} d^2\mathbf{r} = \begin{cases} 1 & \text{for} \quad t \geq 0\,, \\ 0 & \text{for} \quad t < 0\,, \end{cases} \tag{2.11}$$

Convergence of the previous infinite sum requires that

$$\psi(\mathbf{X}_{\alpha\beta}, \mathbf{r}, \mathbf{p}, t|\mathbf{r_0}, \mathbf{p_0}) \to 0 \quad \text{as} \quad \alpha, \beta \to \pm\infty \tag{2.12}$$

Subsequent convergence of the probability moments requires that for any integer $n \geq 0$

$$|\mathbf{X}_{\alpha\beta}|^n\psi \to \mathbf{0} \qquad \text{and} \qquad |\mathbf{X}_{\alpha\beta}|^n\mathbf{J} \to \mathbf{0} \quad \text{as} \quad \alpha, \beta \to \pm\infty \tag{2.13}$$

We need to specify the boundary conditions satisfied by ψ on the obstacle boundaries as well as on the cell edges. The no-flux condition at the obstacle walls reads

$$\mathbf{n_w} \cdot \mathbf{J} = 0 \quad \text{on} \quad \partial C_w \tag{2.14}$$

where $\mathbf{n_w}$ is the unit vector normal to the wall. Continuity at the edges of the unit cell requires

$$\psi(\mathbf{X}_{\alpha\beta}, \mathbf{r}, \mathbf{p}, t) = \psi(\mathbf{X}_{\alpha+1\beta}, \mathbf{r} - L_x\mathbf{e_x}, \mathbf{p}, t) \quad \text{on} \quad \mathbf{r} \in \partial C_{\alpha^+\beta} \tag{2.15a}$$

$$\psi(\mathbf{X}_{\alpha\beta}, \mathbf{r}, \mathbf{p}, t) = \psi(\mathbf{X}_{\alpha\beta+1}, \mathbf{r} - L_y\mathbf{e_y}, \mathbf{p}, t) \quad \text{on} \quad \mathbf{r} \in \partial C_{\alpha\beta^+} \tag{2.15b}$$

where the initial local position $\mathbf{r_0}$ and orientation $\mathbf{p_0}$ have not been included as dependent variables for simplicity. Likewise, continuity of the bacterial translational flux crossing the cell edges reads:

$$\nabla_r\psi(\mathbf{X}_{\alpha\beta}, \mathbf{r}, \mathbf{p}, t) = \nabla_r\psi(\mathbf{X}_{\alpha+1\beta}, \mathbf{r} - L_x\mathbf{e_x}, \mathbf{p}, t) \quad \text{on} \quad \mathbf{r} \in \partial C_{\alpha^+\beta} \tag{2.16a}$$

$$\nabla_r\psi(\mathbf{X}_{\alpha\beta}, \mathbf{r}, \mathbf{p}, t) = \nabla_r\psi(\mathbf{X}_{\alpha\beta+1}, \mathbf{r} - L_y\mathbf{e_y}, \mathbf{p}, t) \quad \text{on} \quad \mathbf{r} \in \partial C_{\alpha\beta^+} \tag{2.16b}$$

We henceforth use dimensionless equations where we scale variables using a as length scale, d_r^{-1} as time scale, ad_r as velocity scale, and we normalize the conditional probability ψ by $1/a^2$. In addition to ϵ_p and Δ, non-dimensionalization of the governing equations yields the three dimensionless groups $\mathrm{Pe}_s = v_0/ad_r$, $\kappa = \sqrt{d_t/a^2d_r}$, and $\mathrm{Pe}_f = u_\infty/ad_r$.

2.4 Macrotransport model

2.4.1 Local Moments of the Conditional Probability

Following generalized Taylor dispersion theory [64], we seek the mean asymptotic transport properties in terms of the kth-order polyadic local moments of ψ defined as

$$\boldsymbol{\psi}_k(\mathbf{r}, \mathbf{p}, t|\mathbf{r}_0, \mathbf{p}_0) = \sum_{\alpha,\beta=-\infty}^{\infty} \underbrace{\mathbf{X}_{\alpha\beta} \cdots \mathbf{X}_{\alpha\beta}}_{k \text{ times}} \psi\,. \tag{2.17}$$

The local gradient operator ∇_r and the double global sum operator $\sum_{\alpha,\beta=-\infty}^{\infty}$ are commutative. We can use this property and obtain the partial differential equation satisfied by $\boldsymbol{\psi_k}$ by multiplying Eq. 2.10 by the kth-dyadic $\mathbf{X}_{\alpha\beta}^k$ and apply the infinite sum operator over both x and y directions. The result of these operations is:

$$\frac{\partial\boldsymbol{\psi_k}}{\partial t} + \nabla_r \cdot \mathbf{J_k} + \nabla_p \cdot \mathbf{j_k} = \delta_{k0}\delta(\mathbf{r} - \mathbf{r_0})\delta(\mathbf{p} - \mathbf{p_0})\delta(t), \tag{2.18}$$

Here, δ_{k0} is the Kronecker delta operator that satisfies the following condition:

$$\delta_{k0} = \begin{cases} 1 & \text{for} \quad k = 0 \\ 0 & \text{otherwise} \end{cases}$$

$\mathbf{J_k}$ and $\mathbf{j_k}$ are the local moments of the translational and orientational bacterial fluxes, respectively, which in dimensionless form are written as:

$$\mathbf{J_k} = (Pe_s \mathbf{p} + \mathbf{u}(\mathbf{r}))\, \boldsymbol{\psi_k} - \kappa^2 \nabla_r \boldsymbol{\psi_k} \tag{2.19a}$$

$$\mathbf{j_k} = (\mathbf{I} - \mathbf{pp}) \cdot [\gamma \mathbf{E} - \mathbf{W}(\mathbf{r})] \cdot \mathbf{p}\ \boldsymbol{\psi_k} - \nabla_p \boldsymbol{\psi_k} \tag{2.19b}$$

From the pre-initial condition:

$$\boldsymbol{\psi_k} = \mathbf{0} \qquad \text{for} \qquad t < 0. \tag{2.20}$$

According to Eq. (2.14), the local moment $\boldsymbol{\psi_k}$ satisfies the following no-flux condition at the edges of the obstacles:

$$\mathbf{n_w} \cdot \mathbf{J_k} \to 0 \quad \text{on} \quad \partial C_w \tag{2.21}$$

In order to determine the macrotransport coefficients $\overline{\mathbf{U}}$ and $\overline{\mathbf{D}}$, we will see later in the model that we only need the boundary conditions associated to the first three local moments ($k = 0, 1, 2$). To simplify the mathematical expressions, we define the jump operator $[\![\cdot]\!]$ applied to an arbitrary vector $\mathbf{f}$ as:

$$[\![\mathbf{f}]\!] = \begin{cases} [\mathbf{f}(\mathbf{r}, \mathbf{p}, t) - \mathbf{f}(\mathbf{r} - L_x \mathbf{e_x}, \mathbf{p}, t)] \cdot \mathbf{e_x} & \text{for} \quad \mathbf{r} \in \partial C_r \\ [\mathbf{f}(\mathbf{r}, \mathbf{p}, t) - \mathbf{f}(\mathbf{r} - L_y \mathbf{e_y}, \mathbf{p}, t)] \cdot \mathbf{e_y} & \text{for} \quad \mathbf{r} \in \partial C_t \end{cases} \tag{2.22}$$

We now derive the boundary conditions satisfied by $\boldsymbol{\psi_k}$ (k=0,1,2) on both vertical and horizontal edges of the unit cell.

$\underline{\psi_0}$: We take the 0th-order local moment of Eq. (2.15a) by applying the two-direction infinite sum operator:

$$\sum_{\alpha,\beta=-\infty}^{\infty} \psi(\mathbf{X}_{\alpha\beta}, \mathbf{r}, \mathbf{p}, t) = \sum_{\alpha,\beta=-\infty}^{\infty} \psi(\mathbf{X}_{\alpha+1\beta}, \mathbf{r} - L_x \mathbf{e_x}, \mathbf{p}, t) \quad \text{on} \quad \mathbf{r} \in \partial C_{\alpha^+\beta}$$

We apply translational invariance of the dummy index α on the right side and use the definition in Eq. (2.17) to find:

$$\psi_0(\mathbf{r},\mathbf{p},t) = \psi_0(\mathbf{r} - L_x\mathbf{e_x},\mathbf{p},t) \quad \text{on} \quad \mathbf{r} \in \partial C_{\alpha^+\beta} \tag{2.23}$$

Taking the 0th-order local moment of Eq. (2.15b) and following a similar procedure, we obtain the corresponding boundary condition on the horizontal edges:

$$\psi_0(\mathbf{r},\mathbf{p},t) = \psi_0(\mathbf{r} - L_y\mathbf{e_y},\mathbf{p},t) \quad \text{on} \quad \mathbf{r} \in \partial C_{\alpha\beta^+} \tag{2.24}$$

$\underline{\boldsymbol{\psi_1}}$: We multiply Eq. (2.15a) by $\mathbf{X}_{\alpha+1\beta}$ and apply the double infinite sum operator:

$$\sum_{\alpha,\beta=-\infty}^{\infty} \mathbf{X}_{\alpha+1\beta}\,\psi(\mathbf{X}_{\alpha\beta},\mathbf{r},\mathbf{p},t) = \sum_{\alpha,\beta=-\infty}^{\infty} \mathbf{X}_{\alpha+1\beta}\,\psi(\mathbf{X}_{\alpha+1\beta},\mathbf{r} - L_x\mathbf{e_x},\mathbf{p},t) \quad \text{on} \quad \mathbf{r} \in \partial C_{\alpha^+\beta}$$

We insert the identity $\mathbf{X}_{\alpha+1\beta} = \mathbf{X}_{\alpha\beta} + L_x\mathbf{e_x}$ on the left side, apply translational invariance of the dummy index α on the right side and use (2.17) to obtain:

$$\boldsymbol{\psi_1}(\mathbf{r},\mathbf{p},t) - \boldsymbol{\psi_1}(\mathbf{r} - L_x\mathbf{e_x},\mathbf{p},t) = -L_x\mathbf{e_x}\psi_0(\mathbf{r},\mathbf{p},t) \quad \text{on} \quad \mathbf{r} \in \partial C_{\alpha^+\beta} \tag{2.25}$$

We can express the boundary condition in a more elegant form by adding and subtracting the term $\mathbf{r}\psi_0(\mathbf{r},\mathbf{p},t)$ on the right side, and making use of Eq. (2.23) we get:

$$\begin{aligned}&\boldsymbol{\psi_1}(\mathbf{r},\mathbf{p},t) - \boldsymbol{\psi_1}(\mathbf{r} - L_x\mathbf{e_x},\mathbf{p},t) = (\mathbf{r} - L_x\mathbf{e_x})\psi_0(\mathbf{r} - L_x\mathbf{e_x},\mathbf{p},t) - \mathbf{r}\psi_0(\mathbf{r},\mathbf{p},t)\\ &\text{on} \quad \mathbf{r} \in \partial C_{\alpha^+\beta}\end{aligned} \tag{2.26}$$

Similarly, taking the 1st-order local moment of Eq. (2.15b), one finally obtains:

$$\begin{aligned}&\boldsymbol{\psi_1}(\mathbf{r},\mathbf{p},t) - \boldsymbol{\psi_1}(\mathbf{r} - L_y\mathbf{e_y},\mathbf{p},t) = (\mathbf{r} - L_y\mathbf{e_y})\psi_0(\mathbf{r} - L_y\mathbf{e_y},\mathbf{p},t) - \mathbf{r}\psi_0(\mathbf{r},\mathbf{p},t)\\ &\text{on} \quad \mathbf{r} \in \partial C_{\alpha\beta^+}\end{aligned} \tag{2.27}$$

$\underline{\boldsymbol{\psi_2}}$: We multiply Eq. (2.15a) by the second order dyadic $\mathbf{X}_{\alpha+1\beta}\mathbf{X}_{\alpha+1\beta}$ and apply the

double infinite sum operator:

$$\sum_{\alpha,\beta=-\infty}^{\infty} \mathbf{X}_{\alpha+1\beta}\mathbf{X}_{\alpha+1\beta}\,\psi(\mathbf{X}_{\alpha\beta},\mathbf{r},\mathbf{p},t) = \sum_{\alpha,\beta=-\infty}^{\infty} \mathbf{X}_{\alpha+1\beta}\mathbf{X}_{\alpha+1\beta}\,\psi(\mathbf{X}_{\alpha+1\beta},\mathbf{r}-L_x\mathbf{e_x},\mathbf{p},t)$$
$$\text{on} \quad \mathbf{r}\in\partial C_{\alpha^+\beta}$$

We insert the identity $\mathbf{X}_{\alpha+1\beta} = \mathbf{X}_{\alpha\beta} + L_x\mathbf{e_x}$ on the left, and apply translational invariance of the dummy index α on the right side. We use Eq. (2.17) and rearrange terms, to find:

$$\boldsymbol{\psi_2}(\mathbf{r},\mathbf{p},t) - \boldsymbol{\psi_2}(\mathbf{r}-L_x\mathbf{e_x},\mathbf{p},t) = -L_x\mathbf{e_x}\boldsymbol{\psi_1}(\mathbf{r},\mathbf{p},t) - \boldsymbol{\psi_1}(\mathbf{r},\mathbf{p},t)L_x\mathbf{e_x} - L_x^2\mathbf{e_x}\mathbf{e_x}\psi_0(\mathbf{r},\mathbf{p},t)$$
$$\text{on} \quad \mathbf{r}\in\partial C_{\alpha^+\beta}$$

From Eq. (2.25), we can represent the vector $L_x\mathbf{e_x}$ as a function of ψ_0 and $\boldsymbol{\psi_1}$, and insert it in the previous equation to find a more simplified expression:

$$\boldsymbol{\psi_2}(\mathbf{r},\mathbf{p},t) - \boldsymbol{\psi_2}(\mathbf{r}-L_x\mathbf{e_x},\mathbf{p},t) = \frac{\boldsymbol{\psi_1}(\mathbf{r})\boldsymbol{\psi_1}(\mathbf{r})}{\psi_0(\mathbf{r})} - \frac{\boldsymbol{\psi_1}(\mathbf{r}-L_x\mathbf{e_x})\boldsymbol{\psi_1}(\mathbf{r}-L_x\mathbf{e_x})}{\psi_0(\mathbf{r}-L_x\mathbf{e_x})} \tag{2.28}$$
$$\text{on} \quad \mathbf{r}\in\partial C_{\alpha^+\beta}$$

For the boundary condition at the horizontal cell edges, we take the 2nd-order local moment of Eq. (2.15b) and follow a similar procedure. The final result is:

$$\boldsymbol{\psi_2}(\mathbf{r},\mathbf{p},t) - \boldsymbol{\psi_2}(\mathbf{r}-L_y\mathbf{e_y},\mathbf{p},t) = \frac{\boldsymbol{\psi_1}(\mathbf{r})\boldsymbol{\psi_1}(\mathbf{r})}{\psi_0(\mathbf{r})} - \frac{\boldsymbol{\psi_1}(\mathbf{r}-L_y\mathbf{e_y})\boldsymbol{\psi_1}(\mathbf{r}-L_y\mathbf{e_y})}{\psi_0(\mathbf{r}-L_y\mathbf{e_y})} \tag{2.29}$$
$$\text{on} \quad \mathbf{r}\in\partial C_{\alpha\beta^+}$$

Using the jump operator defined in Eq. (2.22), Eqs. (2.23-2.29) summarize as follows:

$$[\![\psi_0]\!] = 0 \tag{2.30a}$$
$$[\![\boldsymbol{\psi_1}]\!] = -[\![\mathbf{r}\psi_0]\!] \tag{2.30b}$$
$$[\![\boldsymbol{\psi_2}]\!] = [\![\boldsymbol{\psi_1}\boldsymbol{\psi_1}/\psi_0]\!] \tag{2.30c}$$

Following a similar procedure, we can obtain the boundary conditions associated to Eqs. (2.16a)

and (2.16b). The final result is:

$$[\![\nabla_r \psi_0]\!] = \mathbf{0} \tag{2.31a}$$

$$[\![\nabla_r \boldsymbol{\psi_1}]\!] = -[\![\nabla_r (\mathbf{r}\psi_0)]\!] \tag{2.31b}$$

$$[\![\nabla_r \boldsymbol{\psi_2}]\!] = [\![\nabla_r (\boldsymbol{\psi_1}\boldsymbol{\psi_1}/\psi_0)]\!] \tag{2.31c}$$

which coincide with those obtained by Brenner [64] for passive particulate systems. Upon taking the asymptotic limits of the local moments, it will be useful to rewrite the 1st-order boundary conditions in the following form:

$$[\![\boldsymbol{\psi_1}]\!] = -[\![\mathbf{r}]\!]\psi_0, \qquad [\![\nabla_r \boldsymbol{\psi_1}]\!] = -\nabla_r \psi_0 [\![\mathbf{r}]\!], \tag{2.32}$$

where we have used the 0th-order boundary conditions.

2.4.2 Global Moments of the Conditional Probability

We define the kth-order dyadic global moment $\mathbf{M_k}$ as the spatial and orientational average of the corresponding local moment $\boldsymbol{\psi_k}$:

$$\mathbf{M_k}(t|\mathbf{r_0}, \mathbf{p_0}) = \int_{S_t}\int_{\Omega} \boldsymbol{\psi_k}(\mathbf{r}, \mathbf{p}, t|\mathbf{r_0}, \mathbf{p_0}) d\mathbf{p} d^2\mathbf{r} \quad k = 0, 1, 2... \tag{2.33}$$

From the normalization condition in Eq. (2.11), we can readily obtain the value for the 0th-order total dyadic:

$$M_0 = \begin{cases} 1 & \text{for} \quad t \geq 0 \\ 0 & \text{for} \quad t < 0 \end{cases} \tag{2.34}$$

We obtain the differential equation satisfied by $\mathbf{M_k}$ by taking the temporal derivative of Eq. (2.33) combined with Eq. (2.18), to give:

$$\frac{d\mathbf{M_k}}{dt} = \int_{S_t}\int_{\Omega} \left[-\nabla_r \cdot \mathbf{J_k} - \nabla_p \cdot \mathbf{j_k} + \delta_{k0}\delta(\mathbf{r} - \mathbf{r_0})\delta(\mathbf{p} - \mathbf{p_0})\delta(t)\right] d\mathbf{p} d^2\mathbf{r}$$

Noticing that the integral of the orientational fluxes vanishes, we apply the divergence theorem to the translational flux contribution, to obtain:

$$\frac{d\mathbf{M_k}}{dt} = -\oint_{\partial C}\int_{\Omega}\mathbf{J_k}d\mathbf{p}\mathbf{d}\mathbf{C} + \delta_{k0}\delta(t) \tag{2.35}$$

where the closed line integral represents the sum of the integrals over all the unit cell edges.

$$\oint_{\partial C} = \left(\int_{\partial C_r} + \int_{\partial C_t} + \int_{\partial C_l} + \int_{\partial C_b}\right)$$

Now we use the jump operator defined in (Eq. 2.22) and rewrite Eq. (2.35) in the form

$$\frac{d\mathbf{M_k}}{dt} = -\int_{\partial C_r+\partial C_t}\int_{\Omega}[\![\mathbf{J_k}]\!]d\mathbf{p}d\mathbf{C} + \delta_{k0}\delta(t) \tag{2.36}$$

2.4.3 Asymptotic Long-Time Limit Analysis

The steady-state 0th-order local moment $\psi_0^\infty(\mathbf{r},\mathbf{p})$ can be obtained by taking the long-time limit of Eq. (2.18) and setting $k = 0$:

$$\nabla_r \cdot \mathbf{J_0^\infty} + \nabla_p \cdot \mathbf{j_0^\infty} = 0 \tag{2.37}$$

where the long-time zeroth-order translational and orientational fluxes are:

$$\mathbf{J_0^\infty} = (Pe_s\mathbf{p} + \mathbf{u}(\mathbf{r}))\,\psi_0^\infty - \kappa^2\nabla_r\psi_0^\infty \tag{2.38a}$$

$$\mathbf{j_0^\infty} = (\mathbf{I} - \mathbf{pp})\cdot[\gamma\mathbf{E} - \mathbf{W}(\mathbf{r})]\cdot\mathbf{p}\;\psi_0^\infty - \nabla_p\psi_0^\infty \tag{2.38b}$$

ψ_0^∞ is subjected to the following boundary conditions and normalization condition:

$$[\![\psi_0^\infty]\!] = 0, \quad [\![\nabla_r\psi_0^\infty]\!] = 0 \qquad \text{on} \quad \partial C_r, \partial C_t \tag{2.39a}$$

$$\mathbf{n_w}\cdot\mathbf{J_0^\infty} = 0 \qquad \text{on} \quad \partial C_w \tag{2.39b}$$

Since the point source term is not appearing in the equations anymore, we need to enforce the normalization condition:

$$\int_{S_t}\int_{\Omega}\psi_0^\infty d\mathbf{p}d^2\mathbf{r} = 1 \tag{2.40}$$

We solve for Ψ_0^∞ by solving numerically Eqs. (2.37-2.40) using a finite volume numerical scheme. The temporal evolution of ψ_0 until it reaches its steady-state can be shown to be exponential [64]:

$$\psi_0(\mathbf{r}, \mathbf{p}, t|\mathbf{r_0}, \mathbf{p_0}) = \psi_0^\infty(\mathbf{r}, \mathbf{p}) + \mathcal{O}(e^{-t}) \tag{2.41}$$

Combining this result with Eq. (2.38a) yields:

$$\mathbf{J_0} = \mathbf{J_0^\infty} + \mathcal{O}(e^{-t}) \tag{2.42}$$

The governing equation satisfied by the 1st-order local moment $\boldsymbol{\psi_1}$ is obtained by setting $k = 1$ in Eq. (2.18):

$$\frac{\partial \boldsymbol{\psi_1}}{\partial t} + \nabla_r \cdot \mathbf{J_1} + \nabla_p \cdot \mathbf{j_1} = 0, \quad \text{for} \quad t > 0 \tag{2.43}$$

where

$$\mathbf{J_1} = (Pe_s\mathbf{p} + \mathbf{u}(\mathbf{r}))\,\boldsymbol{\psi_1} - \kappa^2 \nabla_r \boldsymbol{\psi_1} \tag{2.44a}$$

$$\mathbf{j_1} = (\mathbf{I} - \mathbf{pp}) \cdot [\gamma \mathbf{E} - \mathbf{W}(\mathbf{r})]\,\boldsymbol{\psi_1} - \nabla_p \boldsymbol{\psi_1} \tag{2.44b}$$

We apply the jump operator to Eq. (2.44a), and use the first-order jump boundary conditions in Eq. (2.32) to find the jump relation between the first- and zeroth-order bacterial translational fluxes:

$$[\![\mathbf{J_1}]\!] = -\mathbf{J_0}[\![\mathbf{r}]\!] \tag{2.45}$$

We set $k = 1$ in Eq. (2.36) and use Eq. (2.45) to obtain the temporal evolution of the first global moment:

$$\frac{d\mathbf{M_1}}{dt} = \int_\Omega \int_{\partial C_r + \partial C_t} [\![\mathbf{r}]\!] \mathbf{J_0} \cdot d\mathbf{C} d\mathbf{p} \tag{2.46}$$

The introduction of Eq. (2.42) into Eq. (2.46) yields the following asymptotic relation:

$$\frac{d\mathbf{M_1}}{dt} = \int_\Omega \int_{\partial C_r + \partial C_t} [\![\mathbf{r}]\!] \mathbf{J_0^\infty} \cdot d\mathbf{C} d\mathbf{p} + \mathcal{O}(e^{-t}) \tag{2.47}$$

We are now in the position of determining the long-time mean bacterial velocity vector. We define the mean bacterial displacement vector at time t from its initial position at time $t = 0$ as

$$\overline{\Delta \mathbf{R}}(t) = \overline{\mathbf{R}(t) - \mathbf{R}(0)} = \sum_{\alpha,\beta=-\infty}^{\infty} \int_{S_{\alpha\beta}} \int_\Omega \mathbf{X}_{\alpha\beta} \psi(\mathbf{X}_{\alpha\beta}, \mathbf{r}, \mathbf{p}, t|\mathbf{r_0}, \mathbf{p_0}) d\mathbf{p} d^2\mathbf{r} \tag{2.48}$$

From the definition of global and local moments in Eqs. (2.18, 2.33), the mean bacterial displacement vector is equal to the first global moment $\mathbf{M_1}$:

$$\overline{\Delta \mathbf{R}}(t) = \mathbf{M_1} \tag{2.49}$$

The mean displacement grows linearly with time, where the mean bacterial velocity $\overline{\mathbf{U}}$ is the coefficient of proportionality:

$$\lim_{t\to\infty} \overline{\Delta \mathbf{R}}(t) = \overline{\mathbf{U}} t \tag{2.50}$$

Comparison of the previous two equations allows us to represent the long-time mean bacterial velocity as a function of the first global moment $\mathbf{M_1}$:

$$\overline{\mathbf{U}} = \lim_{t\to\infty} \frac{d\mathbf{M_1}}{dt} \tag{2.51}$$

Substitution of Eq. (2.47) into Eq. (2.51) allows us to obtain the asymptotic mean particle velocity $\overline{\mathbf{U}}$ by simple quadrature:

$$\overline{\mathbf{U}} = \int_{\Omega} \int_{\partial C_r + \partial C_t} [\![\mathbf{r}]\!] \mathbf{J_0^\infty} \cdot d\mathbf{C} d\mathbf{p} \tag{2.52}$$

Therefore, we can simply solve the system of equations involving the long-time 0th-order local moment ψ_0^∞ and then compute $\overline{\mathbf{U}}$ in Eq. (2.52) by just evaluating the integral in orientations and in space along the edges of the unit cell.

Following [64], we define a $\mathbf{B}$-field which allows us to determine the effective dispersivity $\overline{\mathbf{D}}$. We first take the temporal derivative of Eq. (2.47) which gives an expression for the first global moment $\mathbf{M_1}$:

$$\mathbf{M_1}(t) = \overline{\mathbf{U}} t + \overline{\mathbf{B}} + \mathcal{O}(e^{-t}) \tag{2.53}$$

where $\overline{\mathbf{B}}$ is an unknown constant vector. We set $k = 1$ in Eq. (2.33):

$$\mathbf{M_1}(t) = \int_{S_t} \int_{\Omega} \boldsymbol{\psi_1}(\mathbf{r}, \mathbf{p}, t) d\mathbf{p} d^2\mathbf{r} \tag{2.54}$$

Comparison of Eqs. (2.53) and (2.54) suggests the following asymptotic solution for $\boldsymbol{\psi_1}$:

$$\boldsymbol{\psi_1}(\mathbf{r}, \mathbf{p}, t) = \psi_0^\infty(\mathbf{r}, \mathbf{p}) \left[\overline{\mathbf{U}} t + \mathbf{B}(\mathbf{r}, \mathbf{p})\right] + \mathcal{O}(e^{-t}) \tag{2.55}$$

where $\mathbf{B}(\mathbf{r},\mathbf{p})$ is a spatial- and orientational-dependent vector field to be determined. Plugging Eq. (2.55) into Eq. (2.54), using Eq. (2.40) and comparing the subsequent result with Eq. (2.53) allows to obtain a physical interpretation of $\overline{\mathbf{B}}$ as the spatial and orientational average of $\mathbf{B}$ with weighting factor ψ_0^∞:

$$\overline{\mathbf{B}} = \int_{S_t}\int_{\Omega} \psi_0^\infty \mathbf{B}(\mathbf{r},\mathbf{p}) d\mathbf{p} d^2\mathbf{r} \tag{2.56}$$

We now carry out the derivation of the governing equation satisfied by the unknown $\mathbf{B}$-field. Substitution of the first local moment trial solution introduced in Eq. (2.55) into Eqs. (2.44a) and (2.44b) gives

$$\mathbf{J_1} = \mathbf{J_0^\infty}\left[\overline{\mathbf{U}}t + \mathbf{B}\right] - \kappa^2\psi_0^\infty \nabla_r \mathbf{B} + \mathcal{O}(e^{-t}) \tag{2.57a}$$

$$\mathbf{j_1} = \mathbf{j_0^\infty}\left[\overline{\mathbf{U}}t + \mathbf{B}\right] - \psi_0^\infty \nabla_p \mathbf{B} + \mathcal{O}(e^{-t}) \tag{2.57b}$$

We obtain the time-independent governing equation satisfied by the fluctuation field $\mathbf{B}(\mathbf{r},\mathbf{p})$ by inserting Eqs. (2.55), (2.57a) and (2.57b) into Eq. (2.43):

$$-\nabla_r \cdot \left[\mathbf{J_0^\infty}\mathbf{B} - \kappa^2\psi_0^\infty \nabla_r \mathbf{B}\right] - \nabla_p \cdot \left[\mathbf{j_0^\infty}\mathbf{B} - \psi_0^\infty \nabla_p \mathbf{B}\right] = \psi_0^\infty \overline{\mathbf{U}} \tag{2.58}$$

The jump conditions on the edges of the unit cell satisfied by the $\mathbf{B}$-field can be derived by plugging the trial solution in Eq. (2.55) into Eq. (2.32):

$$[\![\mathbf{B}]\!] = -[\![\mathbf{r}]\!], \quad [\![\nabla_r \mathbf{B}]\!] = \mathbf{0} \tag{2.59}$$

The no-flux condition satisfied by the B-field at the obstacle walls can be obtained by setting $k = 1$ in Eq. (2.21) and using the trial solution in Eq. (2.55), one obtains a zero diffusive flux of $\mathbf{B}$ on the obstacle

$$\mathbf{n_w} \cdot \nabla_r \mathbf{B} = 0 \quad \text{on} \quad \partial C_w \tag{2.60}$$

We solve for the time-independent vector field $\mathbf{B}(\mathbf{r},\mathbf{p})$ by solving numerically the vector equation (2.58) subjected to the boundary conditions (2.59-2.60).

We define the mean-square bacterial displacement at time t from its initial position

at time $t = 0$ as

$$\overline{\left(\Delta\mathbf{R}(t) - \overline{\Delta\mathbf{R}}(t)\right)^2} = \sum_{\alpha,\beta=-\infty}^{\infty} \int_{S_{\alpha\beta}} \int_{\Omega} \left(\mathbf{X}_{\alpha\beta} - \overline{\Delta\mathbf{R}}(t)\right)^2 \psi(\mathbf{X}_{\alpha\beta}, \mathbf{r}, \mathbf{p}, t|\mathbf{r_0}, \mathbf{p_0}) d\mathbf{p} d^2\mathbf{r} \quad (2.61)$$

Expanding the dyadic product and making use of the definition of global and local moments in Eqs. (2.18, 2.33), the mean-square displacement can be written in the following form:

$$\overline{\left(\Delta\mathbf{R}(t) - \overline{\Delta\mathbf{R}}(t)\right)^2} = \mathbf{M_2}(t) + \overline{\Delta\mathbf{R}}^2(t) M_0 - \mathbf{M_1}(t)\overline{\Delta\mathbf{R}}(t) - \overline{\Delta\mathbf{R}}(t)\mathbf{M_1}(t) \quad (2.62)$$

Substitution of Eqs. (2.34) and (2.50) into the last expression gives

$$\overline{\left(\Delta\mathbf{R}(t) - \overline{\Delta\mathbf{R}}(t)\right)^2} = \mathbf{M_2}(t) - \mathbf{M_1}(t)\mathbf{M_1}(t) \quad (2.63)$$

From Brownian motion theory, the mean-square displacement grows linearly with time and it is proportional to the mean dispersivity dyadic $\overline{\mathbf{D}}$:

$$\lim_{t\to\infty} \overline{\left(\Delta\mathbf{R}(t) - \overline{\Delta\mathbf{R}}(t)\right)^2} = 2\overline{\mathbf{D}}t \quad (2.64)$$

Comparison of the previous two equations allows us to represent the long-time mean bacterial dispersivity dyadic as a function of the first and second global moments:

$$\overline{\mathbf{D}} = \lim_{t\to\infty} \frac{1}{2}\frac{d}{dt}\left(\mathbf{M_2} - \mathbf{M_1}\mathbf{M_1}\right) \quad (2.65)$$

Plugging the asymptotic value of the first global moment obtained in Eq. (2.53) gives the following expression:

$$\overline{\mathbf{D}} = \lim_{t\to\infty} \frac{1}{2}\frac{d\mathbf{M_2}}{dt} - \overline{\mathbf{U}}\,\overline{\mathbf{U}}t - \frac{1}{2}\left(\overline{\mathbf{U}}\,\overline{\mathbf{B}} + \overline{\mathbf{B}}\,\overline{\mathbf{U}}\right) \quad (2.66)$$

To obtain an expression for $\overline{\mathbf{D}}$, we just need to calculate the long-time temporal derivative of the second global moment, which can be obtained from Eq. (2.36) by setting $k = 2$:

$$\lim_{t\to\infty} \frac{d\mathbf{M_2}}{dt} = -\lim_{t\to\infty} \int_{\partial C_r + \partial C_t} \int_{\Omega} [\![\mathbf{J_2}]\!] d\mathbf{p} d\mathbf{C} \quad (2.67)$$

Applying the jump operator to Eq. (2.38a) and setting $k = 2$, we find that the jump in the

second local moment of the translational flux is

$$\lim_{t\to\infty}[\![\mathbf{J_2}]\!] = (Pe_s\mathbf{p}+\mathbf{u}(\mathbf{r}))\,[\![\boldsymbol{\psi_2}]\!] - \kappa^2[\![\nabla_r\boldsymbol{\psi_2}]\!] \tag{2.68}$$

We now plug the jump boundary conditions that relate the first and second local moments at the edges of the unit cell (see Eqs. (2.30c),(2.31c)) into the previous expression, and substitute the asymptotic solution for $\boldsymbol{\psi_1}$. After a few simplifications, we find:

$$\lim_{t\to\infty}[\![\mathbf{J_2}]\!] = -\mathbf{J_0^\infty}\left(\overline{\mathbf{U}}[\![r]\!]t + [\![r]\!]\overline{\mathbf{U}}t - [\![\mathbf{BB}]\!]\right) - \kappa^2\psi_0^\infty[\![\nabla_r(\mathbf{BB})]\!] \tag{2.69}$$

We insert this expression into Eq. (2.67) and use Eq. (2.52) to find

$$\lim_{t\to\infty}\frac{d\mathbf{M_2}}{dt} = 2\overline{\mathbf{U}}\,\overline{\mathbf{U}}t + \int_{\partial C_r+\partial C_t}\int_\Omega\left[\kappa^2\psi_0^\infty[\![\nabla_r(\mathbf{BB})]\!] - \mathbf{J_0^\infty}[\![\mathbf{BB}]\!]\right]d\mathbf{p}d\mathbf{C} \tag{2.70}$$

Finally, we plug this result into Eq. (2.66) to obtain

$$\overline{\mathbf{D}} = \frac{1}{2}\int_{\partial C_r+\partial C_t}\int_\Omega\left[\kappa^2\psi_0^\infty[\![\nabla_r(\mathbf{BB})]\!] - \mathbf{J_0^\infty}[\![\mathbf{BB}]\!]\right]d\mathbf{p}d\mathbf{C} - \frac{1}{2}\left(\overline{\mathbf{U}}\,\overline{\mathbf{B}}+\overline{\mathbf{B}}\,\overline{\mathbf{U}}\right) \tag{2.71}$$

In order to determine $\overline{\mathbf{D}}$ we can simply evaluate the double integral in Eq. (2.71) numerically. Following a previous dispersion study with tracers [64], we analogously derive an alternative expression for $\overline{\mathbf{D}}$. We use index notation for convenience. We pre-multiply Eq. (2.58) by the vector $\mathbf{B}$:

$$B_i\frac{\partial}{\partial x_k}\left[\kappa^2\psi_0^\infty\frac{\partial B_l}{\partial x_k} - J_{0_k}^\infty B_l\right] + B_i\frac{\partial}{\partial p_k}\left[\psi_0^\infty\frac{\partial B_l}{\partial p_k} - j_{0_k}^\infty B_l\right] = \psi_0^\infty B_i\overline{U}_l \tag{2.72}$$

Note that $\partial/\partial x_i = \nabla_{r_i}$ and $\partial/\partial p_i = \nabla_{p_i}$. We also post-multiply Eq. (2.58) by the vector $\mathbf{B}$ to get:

$$\frac{\partial}{\partial x_k}\left[\kappa^2\psi_0^\infty\frac{\partial B_i}{\partial x_k} - J_{0_k}^\infty B_i\right]B_l + \frac{\partial}{\partial p_k}\left[\psi_0^\infty\frac{\partial B_i}{\partial p_k} - j_{0_k}^\infty B_i\right]B_l = \psi_0^\infty B_l\overline{U}_i \tag{2.73}$$

Summing Eqs. (2.72) and (2.73) we get:

$$\begin{aligned}&B_i\frac{\partial}{\partial x_k}\left[\kappa^2\psi_0^\infty\frac{\partial B_l}{\partial x_k} - J_{0_k}^\infty B_l\right] + \frac{\partial}{\partial x_k}\left[\kappa^2\psi_0^\infty\frac{\partial B_i}{\partial x_k} - J_{0_k}^\infty B_i\right]B_l\\ &+ B_i\frac{\partial}{\partial p_k}\left[\psi_0^\infty\frac{\partial B_l}{\partial p_k} - j_{0_k}^\infty B_l\right] + \frac{\partial}{\partial p_k}\left[\psi_0^\infty\frac{\partial B_i}{\partial p_k} - j_{0_k}^\infty B_i\right]B_l = \psi_0^\infty B_i\overline{U}_l + \psi_0^\infty B_l\overline{U}_i\end{aligned} \tag{2.74}$$

We insert B_i inside the gradients. Rearranging terms, making use of Eq. (2.37) and simplifying, Eq. (2.74) reduces to

$$\frac{\partial}{\partial x_k}\left[\kappa^2\psi_0^\infty\frac{\partial(B_iB_l)}{\partial x_k}-J_{0_k}^\infty B_iB_l\right]=2\kappa^2\psi_0^\infty\frac{\partial B_i}{\partial x_k}\frac{\partial B_l}{\partial x_k}-\frac{\partial}{\partial x_p}\left[\psi_0^\infty\frac{\partial(B_iB_l)}{\partial p_k}-j_{0_k}^\infty B_iB_l\right]$$
$$+2\psi_0^\infty\frac{\partial B_i}{\partial p_k}\frac{\partial B_l}{\partial p_k}+\psi_0^\infty B_i\overline{U}_l+\psi_0^\infty B_l\overline{U}_i \qquad (2.75)$$

We apply the divergence theorem in Eq. (2.71) and use the result obtained in Eq. (2.75). After a few simplifications and with the help of Eq. (2.56), we finally get:

$$\overline{\mathbf{D}}=\int_{S_t}\int_{\Omega}\left[\psi_0^\infty\left(\kappa^2\nabla_r\mathbf{B}\cdot\nabla_r\mathbf{B}^\dagger+\nabla_p\mathbf{B}\cdot\nabla_p\mathbf{B}^\dagger\right)\right]d\mathbf{p}dS \qquad (2.76)$$

where the symbol † denotes the transpose operator, and the surface integral is over the whole unit cell. Therefore, we can use either Eq. (2.71) or Eq. (2.76) to solve for $\overline{\mathbf{D}}$. Due to the simplicity of performing line integrals over surface integrals, we choose to use Eq. (2.71) to numerically solve for $\overline{\mathbf{D}}$.

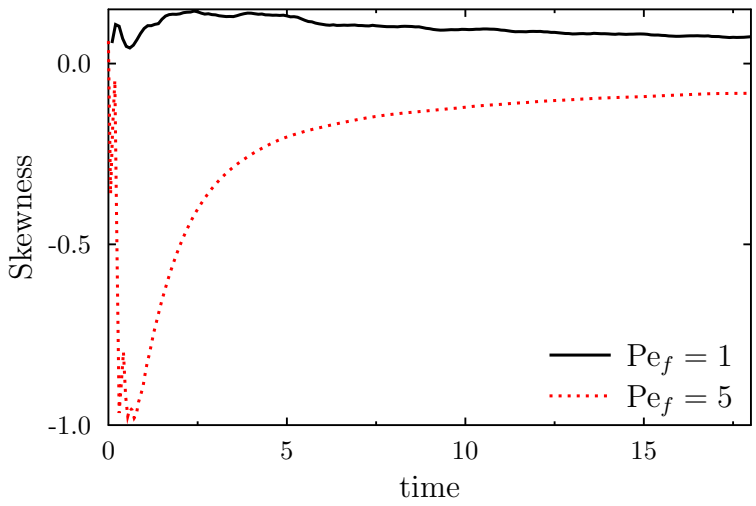

Figure 2.3: Evolution of the skewness of particle distributions moving through a cubic array of circular obstacles over time. Parameter values: $Pe_s = 1$, $\kappa^2 = 1$, $\epsilon_p = 0.804$, $\Theta_f = 0$.

2.4.4 Eulerian interpretation of $\overline{\mathbf{U}}$ and $\overline{\mathbf{D}}$

On long length and time scales, a dilute cloud of particles is thus expected to be transported with mean velocity $\overline{\mathbf{U}}$ and to spread diffusively with dispersivity $\overline{\mathbf{D}}$ as provided

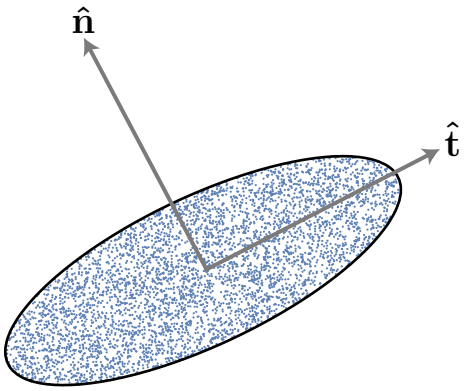

Figure 2.4: A representative distribution of active particles in the asymptotic limit. $\hat{\mathbf{t}}$ and $\hat{\mathbf{n}}$ are the unit vectors aligned with the principal directions of dispersion.

by Eqs. (2.52) and (2.71). This suggests seeking a coarse-grained Eulerian interpretation of $\overline{\mathbf{U}}$ and $\overline{\mathbf{D}}$ at the so-called Darcy scale, where the fluid and solid obstacles that comprise the porous material become indistinguishable and distances shorter than the characteristic size of the unit cell are irrelevant. To this end, we introduce the discrete conditional probability density

$$\Psi(\mathbf{X}_{\alpha\beta}, t|\mathbf{r_0}, \mathbf{p_0}) = \frac{1}{S_t}\int_{\Omega}\int_{S_{\alpha\beta}} \psi(\mathbf{X}_{\alpha\beta}, \mathbf{r}, \mathbf{p}, t|\mathbf{r_0}, \mathbf{p_0}) d^2\mathbf{r}d\mathbf{p}, \tag{2.77}$$

which represents the probability for a particle to be located in the cell labeled by the integers (α, β) at time t, and whose value is assigned to the centroid of the unit cell. On large length scales, we can assimilate $\mathbf{X}_{\alpha\beta}$ to a continuous variable $\mathbf{X}$ and define a corresponding macro-scale gradient operator ∇_X. The Darcy-scale probability density $\Psi(\mathbf{X}, t)$, which is the continuous counterpart of $\psi(\mathbf{X}_{\alpha\beta}, t|\mathbf{r}_0, \mathbf{p}_0)$, can then be shown formally to satisfy the 2D obstacle-free advection-diffusion equation

$$\partial_t\Psi + \nabla_X \cdot \left(\overline{\mathbf{U}}\Psi - \overline{\mathbf{D}} \cdot \nabla_X\Psi\right) = \delta(\mathbf{X} - \mathbf{X}_0)\delta(t)\,, \tag{2.78}$$

thus solidifying the interpretation of $\overline{\mathbf{U}}$ and $\overline{\mathbf{D}}$. In order to prove Eq. (2.78), we first use Eqs. (2.17) and (2.33) to find a relation between the global moments and the discontinuous conditional probability density Ψ:

$$\mathbf{M_k}(t|\mathbf{r_0}, \mathbf{p_0}) = S_t \sum_{\alpha,\beta=-\infty}^{\infty} \mathbf{X}_{\alpha\beta}^k \Psi(\mathbf{X}_{\alpha\beta}, t|\mathbf{r_0}, \mathbf{p_0}) \tag{2.79}$$

The long-time continuous version of Eq. (2.79) becomes:

$$\mathbf{M_k}(t) = \int_{S_\infty} \mathbf{X}^k \, \Psi(\mathbf{X}_{\alpha\beta}, t) d^2\mathbf{X} \tag{2.80}$$

where the infinite double sum operator has been replaced by an integral over the entire surface domain. Notice that we have assumed that at long times, the dependence of the global moments on the initial conditions disappear. We set $k = 1$ in Eq. (2.80) and take the first temporal derivative, that in conjunction with Eq. (2.78) yields at long times:

$$\lim_{t\to\infty} \frac{d\mathbf{M_1}}{dt} = -\int_{S_\infty} \mathbf{X}\nabla_\mathbf{X} \cdot \left(\overline{\mathbf{U}}\Psi - \overline{\mathbf{D}} \cdot \nabla_\mathbf{X}\Psi\right) d^2\mathbf{X} \tag{2.81}$$

We insert Eq. (2.78) into Eq. (2.81), and apply integration by parts that, along with the boundary conditions at infinity gives

$$\lim_{t\to\infty} \frac{d\mathbf{M_1}}{dt} = \overline{\mathbf{U}}, \tag{2.82}$$

which is in agreement with Eq. (2.51). Similarly, we take the first temporal derivative of Eq. (2.80) and set $k = 2$:

$$\lim_{t\to\infty} \frac{d\mathbf{M_2}}{dt} = -\int_{S_\infty} \mathbf{X^2}\nabla_\mathbf{X} \cdot \left(\overline{\mathbf{U}}\Psi - \overline{\mathbf{D}} \cdot \nabla_\mathbf{X}\Psi\right) d^2\mathbf{X} \tag{2.83}$$

We apply integration by parts to Eq. (2.83) that, along with the boundary conditions at infinity gives

$$\lim_{t\to\infty} \frac{d\mathbf{M_2}}{dt} = \overline{\mathbf{U}}\mathbf{M_1} + \mathbf{M_1}\overline{\mathbf{U}} + 2\overline{\mathbf{D}} \tag{2.84}$$

which is in agreement with Eq. (2.65). Therefore, once we obtain the values of $\overline{\mathbf{U}}$ and $\overline{\mathbf{D}}$ from eqs. (2.52) and (2.71), we can describe the long-time transport of a bacterial suspension from a macroscale perspective by just solving a simple unsteady advection-diffusion equation (2.78). For a general streaming flow that is oriented at an angle the dispersivity tensor is non-diagonal, we introduce the principal directions of spreading associated with the principal values of the dispersion tensor. In this general case a bacterial suspensions, initially released as a point source, stretches and takes a form of a translating ellipse (Gaussian) as shown in figure 2.4. The major axis of the ellipse is the principal direction of spreading associated with the maximum eigenvalue. We can obtain the analytical solution of Eq. (2.78) in terms

of the two principal directions and is given by:

$$\psi(\mathbf{X},t) = \frac{1}{4\pi t\sqrt{D_{\hat{\mathbf{t}}\hat{\mathbf{t}}}D_{\hat{\mathbf{n}}\hat{\mathbf{n}}}}} \exp\left[-\frac{(X_{\hat{\mathbf{t}}}-U_{\hat{\mathbf{t}}}t)^2}{4D_{\hat{\mathbf{t}}\hat{\mathbf{t}}}t} - \frac{(X_{\hat{\mathbf{n}}}-U_{\hat{\mathbf{n}}}t)^2}{4D_{\hat{\mathbf{n}}\hat{\mathbf{n}}}t}\right], \tag{2.85}$$

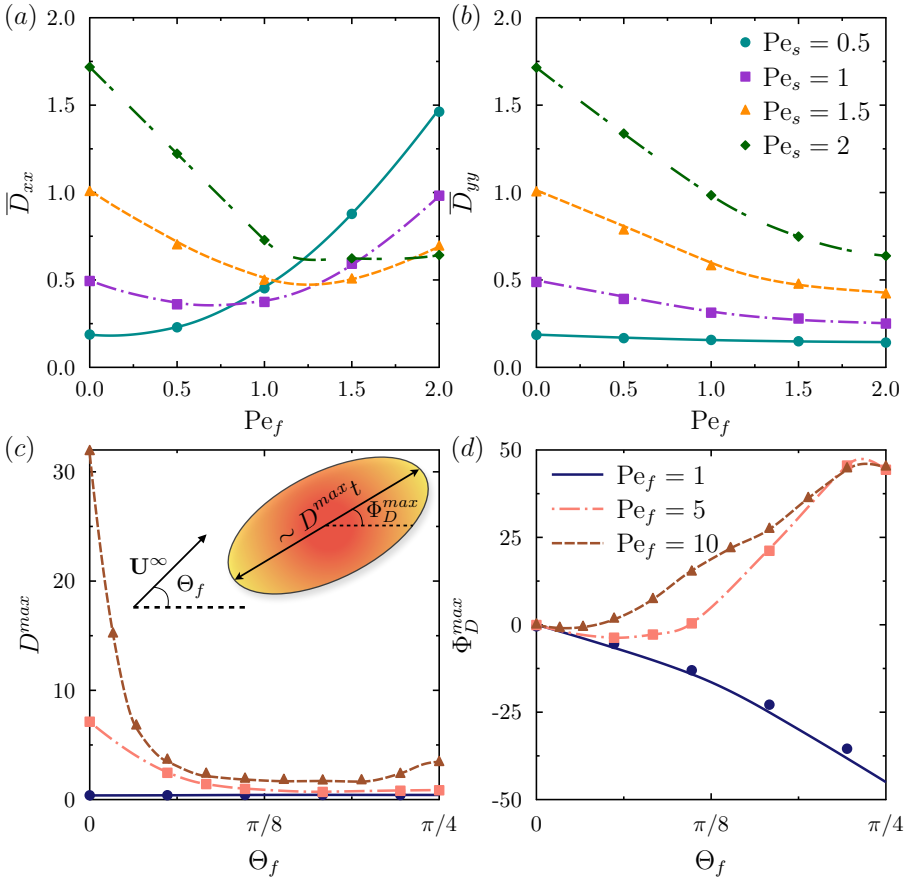

Figure 2.5: Dispersion in an imposed flow. (a)–(b) Dependence of $\overline{D}_{xx}$ and $\overline{D}_{yy}$ on flow Péclet number Pe_f for various values of Pe_s in a square lattice with circular pillars for an external flow applied in the x-direction ($\Theta_f = 0$). (a)–(b) Dependence of $\overline{D}_{xx}$ and $\overline{D}_{yy}$ on flow Péclet number Pe_f for various values of Pe_s in a square lattice with circular pillars for an external flow applied in the x-direction ($\Theta_f = 0$). (c) Maximum eigenvalue D^{max} of the dispersivity dyadic and (d) corresponding polar angle Φ_D^{max} associated to the direction of maximum dispersion as a function of imposed flow direction Θ_f. Parameter values: $\mathrm{Pe}_s = 1$, $\kappa^2 = 0.1$, $\epsilon_p = 0.804$. Symbols: BD simulations; lines: macrotransport model.

where $\hat{\mathbf{t}}$ is the unit vector for the principal direction of spreading associated with the maximum eigenvalue and $\hat{\mathbf{t}}$ is the direction orthogonal to it. The two principal values of the diffusion tensor are $D_{\hat{\mathbf{t}}\hat{\mathbf{t}}}$ and $D_{\hat{\mathbf{n}}\hat{\mathbf{n}}}$. Therefore, the maximum and minimum eigenvalues

of the dispersivity dyadic are denoted as $D^{max} \equiv D_{\hat{\mathbf{t}}\hat{\mathbf{t}}}$ and $D^{min} \equiv D_{\hat{\mathbf{n}}\hat{\mathbf{n}}}$. The coordinates projected along both directions are defined as $X_{\hat{\mathbf{t}}} \equiv \mathbf{X} \cdot \hat{\mathbf{t}}$ and $X_{\hat{\mathbf{n}}} \equiv \mathbf{X} \cdot \hat{\mathbf{n}}$. The mean transport velocities follow identical definitions. This Darcy-scale interpretation of transport and spreading is valid in the asymptotic limit.

2.5 Results and discussion

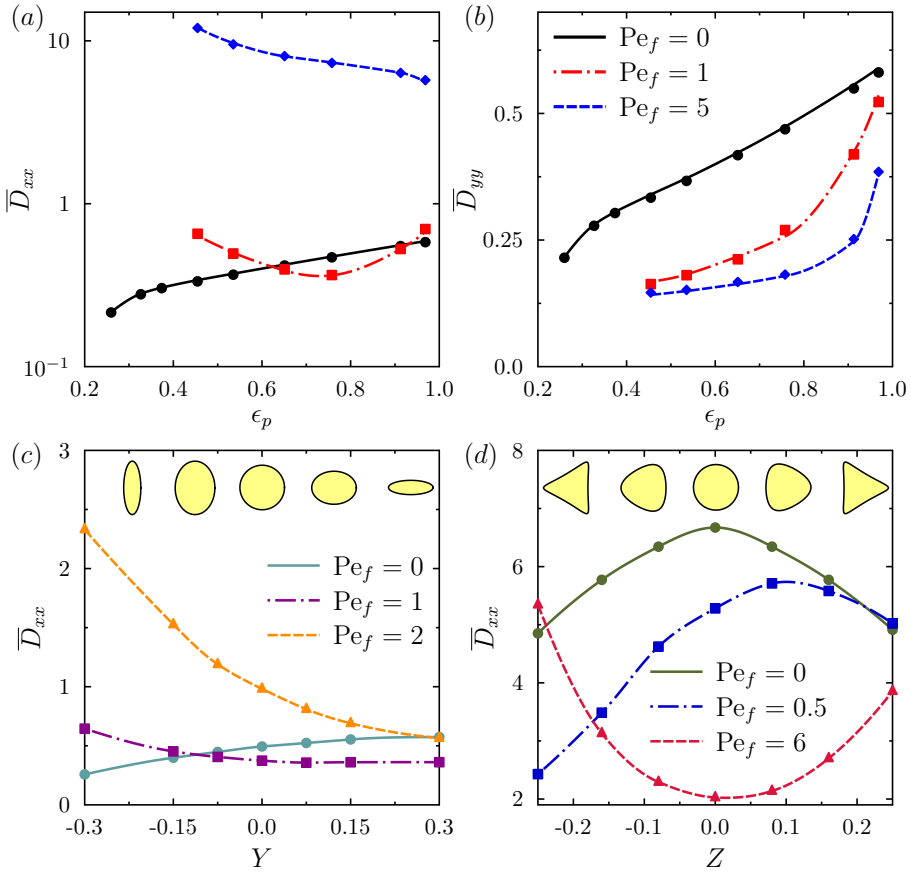

Figure 2.6: Dependence of $\overline{D}_{xx}$ and $\overline{D}_{yy}$ on the porosity of a circular-obstacle-material for various flow strengths Pe_f. Parameter values: $Pe_s = 1$, $\kappa^2 = 0.1$ and $\Theta_f = 0$. $(c) - (d)$ Effect of obstacle shape anisotropy (c) and fore-aft symmetry (d) on $\overline{D}_{xx}$ for different Pe_f. Parameter values: $Pe_s = 4$, $\kappa^2 = 0.1$ and $\Theta_f = 0$. Pillar shapes are shown in the inset.

Results from Brownian Dynamics (BD) simulations of the spreading of a concentrated point source of active swimmers based on Eqs. (2.1)–(2.2) are compared to the analytical solution of Eq. (2.78) in Fig. 2.2. On short time scales, the cloud develops a complex shape that is continually distorted by the pillars and exhibits wakes, boundary layers, and other

features typical of advective-diffusive transport around obstacles. At later times, the cloud shape becomes increasingly smooth and is very well captured by the theoretical model, which predicts spreading into a translating anisotropic Gaussian. This comparison asserts the strength of the Darcy-scale interpretation for describing asymptotic transport, but also highlights key differences. In particular, we observe tailed distributions at pre-asymptotic times in Fig. 2.2(b), a phenomenon also recently reported in experiments using *E. coli* suspensions [56]. The distributions are found to be negatively skewed in the flow direction in strong flows of weakly swimming particles (high Pe_f and low Pe_s), whereas they become positively skewed in the opposite case, as observed in Fig. (2.3). At longer times, the tails are no longer asymmetric and the distributions converge to the asymptotic diffusive solution as shown in Fig. 2.2(c).

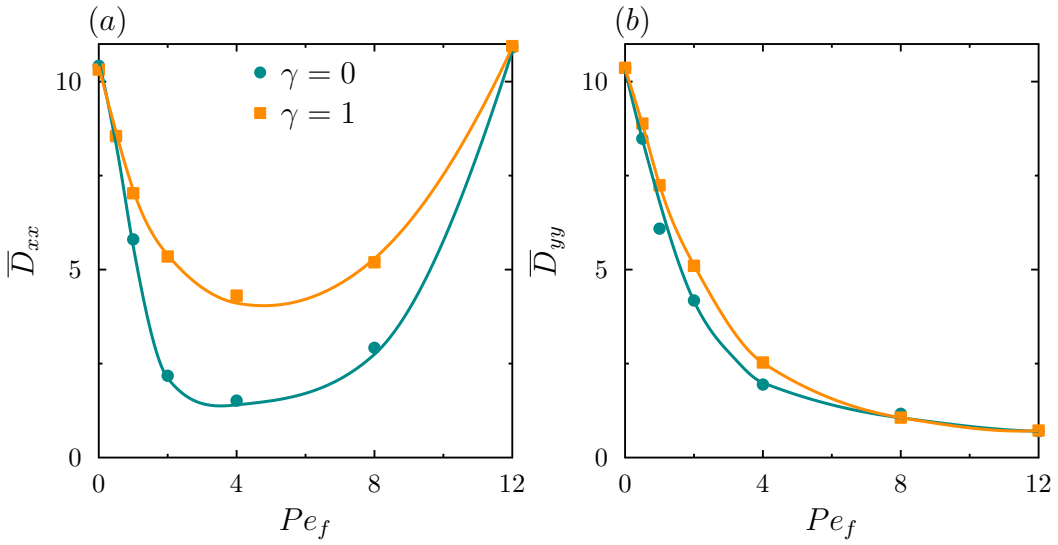

Figure 2.7: Dependence of $\overline{D}_{xx}$ and $\overline{D}_{yy}$ on Pe_f for two particle shapes: Spherical ($\gamma = 0$) and slender ($\gamma = 1$). Symbols: BD simulations; lines: macrotransport model. Paramater values: $Pe_s = 5$, $\kappa^2 = 0.1$, $\epsilon_p = 0.804$, $\Theta_f = 0$

Asymptotic transport characteristics can be attributed to pore-scale features of the fluid flow and of the steady-state zeroth-order moment ψ_0^∞ as illustrated in Fig. 2.2(d). In the absence of flow, the interplay of self-propulsion and translational diffusion near obstacle boundaries creates a net swimmer polarization $\mathbf{m}_0^\infty(\mathbf{r}) = \int_\Omega \mathbf{p}\psi_0^\infty(\mathbf{r},\mathbf{p})d\mathbf{p}$ against the obstacles [51, 52], which vanishes at the cell edges by symmetry. This polarization is accompanied by a net increase in density $\rho_0^\infty(\mathbf{r}) = \int_\Omega \psi_0^\infty(\mathbf{r},\mathbf{p})d\mathbf{p}$, which is azimuthally symmetric near a circular obstacle and enhanced in regions of high curvature for non-circular pillars [67]. When

a flow is applied, the fore-aft symmetry is broken and particles now preferentially accumulate near stagnation points, with a maximum density reached behind the obstacle. Stronger accumulation behind obstacles has been recently observed experimentally in [68], and it is reminiscent of that occurring past funnel constrictions [55]. It results from the combination of advection by the flow and of shear-rotation and swimming in the fast-flowing high-shear regions above and below the pillars. Advection and rotation in the flow also induce a density minimum ahead of the obstacle, with coincides with the position of a stagnation point in the polarization field. As we further explain below, these various features play a crucial role in determining the effective spreading behavior.

The dependence of dispersion coefficients on external flow strength Pe_f and swimming activity Pe_s is shown in Fig. 2.5(a,b) for a lattice comprised of circular pillars. In weak flows, $\overline{D}_{xx}$ and $\overline{D}_{yy}$ are of similar magnitudes, with faster-swimming particles (high Pe_s) spreading more efficiently by active dispersion. Quite remarkably, increasing flow strength Pe_f first causes a decrease in spreading. This decrease is unique to self-propelled particles, and indeed disappears at low values of Pe_s. It is attributed to a reduction in active dispersion by the flow, which prevents particles from sampling all swimming directions freely. At higher values of Pe_f, $\overline{D}_{xx}$ starts increasing again and ultimately exhibits the behavior typical of shear-induced dispersion [53]. This increase is only shown by $\overline{D}_{xx}$; the transverse dispersivity $\overline{D}_{yy}$, on the other hand, monotonically decays with Pe_f as stronger flows cause faster rotations of the swimmers in the local shear and thus hinder their ability to travel in the y-direction.

Dispersion can be further controlled by tuning the direction Θ_f of the imposed flow as shown in Fig. 2.5(c,d). For an arbitrary direction Θ_f, the dispersion tensor $\overline{\mathbf{D}}$ is no longer diagonal and maximum dispersion occurs along the eigendirection Φ_D^{max} associated with its maximum eigenvalue D^{max}. The magnitude of D^{max} is maximum for $\Theta_f \approx 0$, which allows for gliding of the swimmers between rows of pillars with minimal collisions. Other flow directions result in stronger obstruction by the pillars and thus display much weaker values of D^{max}, which reaches its minimum for $\Theta_f \approx \pi/8$ at high flow rates. While in strong flows the direction of maximum dispersion is close to that of the imposed flow (the dominant direction of dispersion becomes aligned with the flow-direction due to shear-dominated dispersion), such is not the case in weak flows where Θ_f and Φ_D^{max} have opposite signs, suggesting significant spreading transverse to the flow (his is a result of active-dispersion as particles swim against the flow around the obstacle causing them to spread more in the transverse direction).

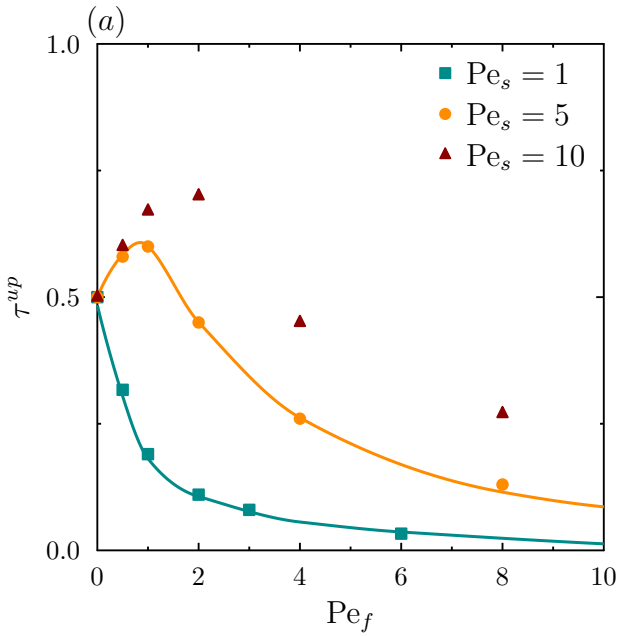

Figure 2.8: Fraction of time during which particles are oriented upstream as a function of Pe_f for different swimming strength. Like before, the symbols correspond to Brownian dynamics and the lines are from the macro-transport theory. Parameter values: $\kappa^2 = 0.1$, $\Theta_f = 0$, $\gamma = 0$, $\epsilon_p = 0.804$.

The effects of lattice porosity and pillar shape are analyzed in Fig. 2.6 and further underscore the subtle interplay of active vs shear-induced dispersion. In the absence of flow and at low porosity, dispersion is weak as the pillars act as entropic barriers that hinder active dispersion [69]. Increasing porosity thus causes a monotonic increase in $\overline{D}_{xx}$ and $\overline{D}_{yy}$ as geometric obstruction plays a lesser role. In a weak flow ($\mathrm{Pe}_f = 1$), $\overline{D}_{xx}$ shows a non-monotonic behavior, with a dispersion enhancement occurring at low ϵ_p due to the strong shear developing between nearby obstacles; as porosity is increased while keeping flow rate constant, axial dispersion first decreases due to a drop in local shear rate, before increasing again at low area fractions to the active swimming. In strong flows ($\mathrm{Pe}_f = 5$), shear-induced dispersion dominates at all area fractions resulting in a monotonic decay in $\overline{D}_{xx}$ with ϵ_p. The limit of $\epsilon_p \to 1$ must approach the case of swimmers in free-space ($\kappa^2 + Pe_s^2/2$). D_{xx} displays an extremely sharp boundary layer at $\epsilon_p = 1$, whose thickness drops drastically as Pe_f increases. Because infinitesimal obstacles still modify the swimmer distribution in their vicinity while also inducing fluid shear in an imposed flow, we would need to run simulations with extremely big unit cells in order to observe the unbounded limit, a regime not explored here.

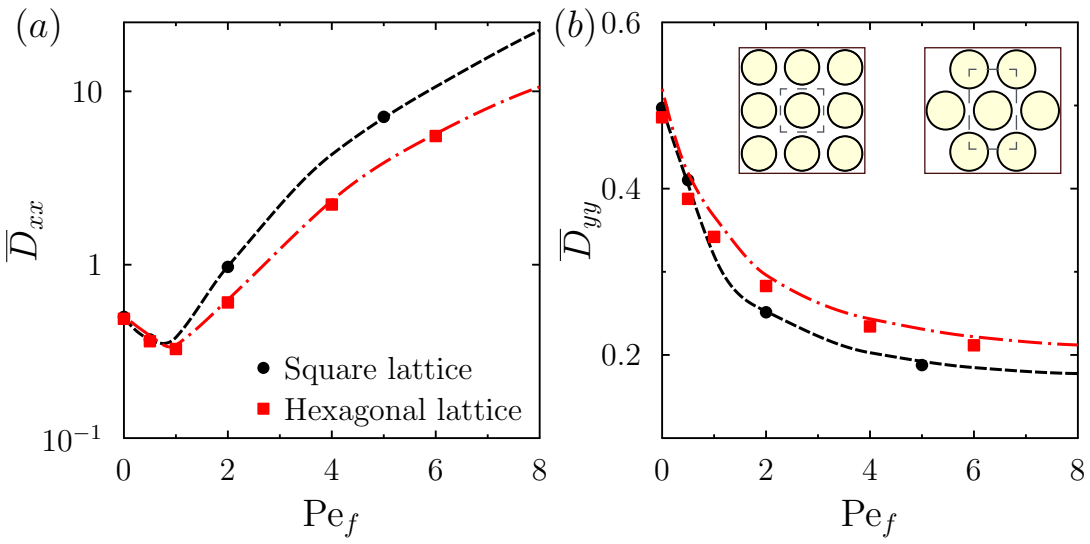

Figure 2.9: Variation of dispersivity as a function of Pe_f for square and hexagonal lattice with circular obstacles at a fixed volume fraction. The lattice arrangement along with the unit cell is shown in the inset. The symbols correspond to Brownian dynamics and the lines are obtained from the macro-transport theory. Parameter values: $\mathrm{Pe}_s = 1$, $\kappa^2 = 0.1$, $\Theta_f = 0$, $\gamma = 0$, $\epsilon_p = 0.804$.

The effect of obstacle shape on $\overline{D}_{xx}$ shows complex trends as analyzed in Fig. 2.6(c) for the case of anisotropic shapes. In weak flows, elliptical obstacles aligned with the flow direction cause higher streamwise dispersion than if aligned perpendicular to the flow, as the former allow swimmers to glide past while the latter act as entropic barriers that obstruct active dispersion in the x-direction [69]. These trends reverse at high flow rates, as perpendicular obstacles induce stronger shear gradients and thus enhance shear-induced dispersion. Fore-aft asymmetric obstacles are also considered in Fig. 2.6(d). In the absence of flow, D_{xx} decreases as the fore-aft-symmetric shape parameter Z deviates from the circular case ($Z = 0$), due to the obstruction mechanism proposed in Fig. 2.6(c). When a flow field is applied, shear enforces particles to swim following the walls and against the flow. For negative values of Z, a particle focusing mechanism occurs along the horizontal cross section where obstacles are located and particle accumulation is enhanced around the obstacles. For positive values of Z, particles swim away from the obstacles and wall accumulation drops. As a consequence, the effects of a decrease in dispersion due to shear-alignment (for weak flows) and an increase in dispersion due to shear-induced-Taylor-dispersion (for strong flows) is magnified for the obstacle-shapes that promote wall accumulation ($Z < 0$), as observed in Fig. 2.6(d).This asymmetry becomes negligible in strong flows. In that regime, the effect

of activity disappears and the magnitude of the shear gradients that govern dispersion is independent of the flow direction by reversibility of Stokes flow.

In Fig. 2.7 we explore the effect of particle shape on the particle dispersion coefficients. Because shape anisotropy favors particle alignment along the streamlines of the flow, slender particles displayed higher effective dispersion coefficients compared with the spherical ones.

The fraction of time τ_{up} spent by the particles swimming upstream is shown in Fig. (2.8). We obtained τ_{up} from the macrotransport theory as

$$\tau^{up} = \int_S \int_\Omega \psi_0^\infty \left(\mathbf{r}, \mathbf{p} \middle| \mathbf{J}_\mathbf{0}^\infty \cdot \hat{\boldsymbol{e}}_{\boldsymbol{x}} < 0 \right) dpdS, \tag{2.86}$$

So far we have mostly restricted ourselves to the discussion of transport in square lattice. Now we consider the effect of different lattice geometries. Fig. (2.9) compares the effect of lattice geometry at a fixed surface fraction of obstacles for streaming flow in the x direction. The axial dispersivity is consistently lower for hexagonal lattice compared to the square lattice while the behavior reverses in the transverse direction. In a hexagonal lattice, active particles are 'effectively' hindered more in the direction of the flow compared to the square lattice, which results in a reduction of axial dispersion. However, the gradients of the vertical fluid velocity are higher in the former case. As a consequence, fluid shear, swimming and the interactions of the particles with the boundaries results in a higher transverse dispersivity compared with the square lattice. The quantitative difference between the lattice geometries is very small, and the qualitative features and mechanism of dispersion for both latices are identical.

For a purely diffusive process in the absence of any flow the particles are equally likely to go downstream or upstream and $\tau^{up} = 0.5$. For weak swimming, particles get washed out by the flow. As Pe_f increases, more particles go downstream due to a strong shear and they eventually behave as passive tracers for sufficiently high Pe_f. For strong swimming, shear-induced rotations promote upstream swimming, which results in an increase in τ_{up}, as observed in Fig. (2.8) for $\mathrm{Pe}_s = 5, 10$. Our results are in good qualitative agreement with recently reported experimental results [56] for the transport of E. Coli under strong flows. In the case of strong swimming steep boundary layers emerge near the boundaries of the obstacles that are difficult to resolve in our finite volume simulations. As a result the macro-transport theory was not used for $\mathrm{Pe}_s = 10$.

2.6 Concluding remarks

Using a simple continuum model based on generalized Taylor dispersion theory, we have predicted the long-time asymptotic behavior of active particles in a two-dimensional porous medium. The asymptotic spreading of a dilute cloud of microswimmers has been shown to obey an obstacle-free advection-diffusion equation. We have elucidated the effects of motility, lattice geometry and applied fluid flow on transport properties. Our model suggests that the interplay of particle self-propulsion, entropic trapping by the obstacles, and shear-induced dispersion in the flow can be exploited for the control and directional transport of active swimmers through micro-structured environments.

Prior to this study, theoretical and experimental progress has been made on controlling and guiding individual bacteria. The macro-continuum theory developed is robust and can be used to study any diffusive spreading process of active particles. An exciting avenue that remains unexplored is the transport in heterogeneous or random lattices that are ubiquitous in nature [70]. We observed that the pore-obstacle configuration does not change the qualitative results, and both hexagonal and square lattices produced similar trends. Because many bacterial colonies that degrade toxic compounds in soils are motile and chemotactic, it would be interesting for bioremediation applications [71, 72] to study the effect of chemotaxis [73, 74] on transport of bacterial suspensions in heterogeneous media (see Chapter 3). Self-generated hydrodynamic interactions [42, 62] have been neglected and they could potentially lead to a subdiffusive behavior. Other effects not considered here are the role played by finite angular time correlations and bacterial velocity fluctuations [75], time-dependent flows, (e.g. intestines [76]), bacterial adhesion [77] and cell size effects [78].

2.7 Acknowledgements

Chapter 2, in part, is a submitted manuscript; authored by R. Alonso-Matilla, B. Chakrabarti and D. Saintillan, "Asymptotic transport and dispersion of active particles in periodic porous media". The dissertation author is the primary author of this work.

2.8 Appendix A: Active dispersion in a straight channel

2.8.1 Problem definition

We make use of Macrotransport Theory to characterize the transport of a dilute suspension of swimming particles in a two-dimensional straight channel when the suspension is subjected to a simple Couette flow and a Poiseuille flow. We develop a coarse-grained description from a microscale constitutive equation and boundary conditions. Upon the application of the Taylor-Aris moment technique, we obtain two steady-state, microscale boundary value problems that we solve in order to determine the mean swimmer velocity $\overline{U}$ and mean swimmer dispersivity $\overline{D}$, which are macroscale coefficients that describe the long-time asymptotic transport of the suspension. Other alternative methods, not addressed here, can be applied to solve the problem, such as homogenization methods, projection-operator techniques or effective medium theories, among others [79].

We base our derivation on the classical Taylor-Aris problem, which analyzes the longitudinal transport of point-size tracer particles that undergo Brownian translations and get advected by a Poiseuille flow [53, 54, 80]. The combination of the spatial inhomogeneous pressure driven fluid field and the lateral Brownian diffusion that allows particles to sample the entire cross section of the channel, results in a net axial particle transport comprised of both a convective and a diffusive contribution.

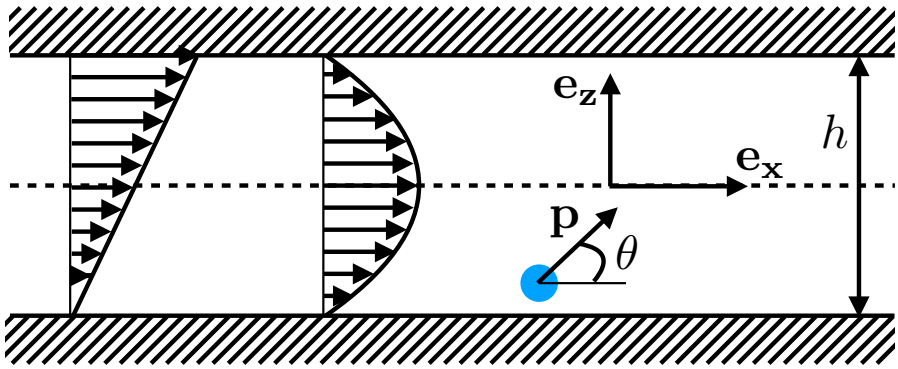

Figure 2.10: Problem definition: Axial transport of a dilute suspension of particles with positions $\mathbf{R} = (x, z)$ and orientations $\mathbf{p} = (\cos\theta, \sin\theta)$ confined between two parallel flat plates ($z = \pm h$) and subject to two different fluid fields: simple Couette flow and parabolic Poiseuille flow.

2.8.2 Macrotransport theory

Our starting point is the microscopic description of the spatial and orientational evolution of a single swimmer suspended in a viscous fluid with viscosity μ. The active micro-particle swims at a constant velocity v_0 in the direction defined by the unit vector $\mathbf{p}$, gets advected and rotated by the fluid velocity $\mathbf{u} = u(z)\mathbf{e_x}$, and undergoes translational and rotational Brownian motion with diffusion coefficients d_t and d_r, respectively. The conditional probability $\psi(x, z, \theta, t|z_0, \theta_0, t)$ of finding the swimmer at a certain position $\mathbf{R} = (x, z)$, with orientation θ at time t satisfies the Fokker-Planck equation (see Eq. (1.23)):

$$\frac{\partial \psi}{\partial t} + \nabla_R \cdot \mathbf{J} + \nabla_p \cdot \mathbf{j} = \delta(\mathbf{R} - \mathbf{R}_0)\delta(\mathbf{p} - \mathbf{p}_0)\delta(t), \tag{2.87}$$

where translational and rotational fluxes are:

$$\mathbf{J} = [v_0\mathbf{p} + \mathbf{u}(z)]\,\psi - d_t\nabla_R\psi, \tag{2.88}$$

$$\mathbf{j} = [\gamma(\mathbf{I} - \mathbf{pp}) \cdot \mathbf{E}(z) \cdot \mathbf{p} - \boldsymbol{W}(z) \cdot \mathbf{p}]\,\psi - d_r\nabla_p\psi. \tag{2.89}$$

The probability density satisfies no-flux conditions at the walls

$$\mathbf{J} \cdot \mathbf{n} = 0 \quad \text{at} \quad z = \pm h/2, \tag{2.90}$$

where $\mathbf{n}$ is the wall-normal unit vector. Additionally, the probability and its axial gradient vanishes at large distances upstream and downstream:

$$|x|^m\psi \to 0, \quad |x|^m\frac{\partial \psi}{\partial x} \to 0 \quad \text{as} \quad x \to \pm\infty, \qquad m = 0, 1, 2... \tag{2.91}$$

Normalization of the conditional probability requires

$$\int_{x=-\infty}^{\infty}\int_{y=-h/2}^{h/2}\int_{\theta=0}^{2\pi}\psi d\theta dy dx = 1 \quad (t \geq 0) \tag{2.92}$$

with pre-initial condition $\psi(t < 0) = 0$.

We non-dimensionalize the problem by selecting h as length scale and d_r as time scale; ψ is non-dimensionalize by the factor $1/h^2$. The resulting dimensionless parameters are $Pe_s = v_0/(hd_r)$, $\kappa = \sqrt{d_t/d_r}/h$ and a dimensionless applied shear Pe_f. For a Couette flow with upper wall velocity u_w, the dimensionless fluid velocity is $u(z) = Pe_f(z + 1/2)$,

where $Pe_f = u_w/(hd_r)$. For a Poiseuille flow with constant imposed gradient dp/dx, $u(z) = Pe_f(1/4 - z^2)$, where $Pe_f = -h^2(dp/dx)/(2\mu)$. We define the kth-order axial moment of ψ as

$$\psi_k(z,\theta,t) = \int_{-\infty}^{\infty} x^k \psi dx \tag{2.93}$$

The 0th and 1st axial moments satisfy the following evolution equations:

$$\begin{aligned}\frac{\partial \psi_0}{\partial t} =& - Pe_s \sin\theta \frac{\partial \psi_0}{\partial z} + \kappa^2 \frac{\partial^2 \psi_0}{\partial z^2} \\ & - \nabla_p \cdot [\gamma(\mathbf{I} - \mathbf{pp}) \cdot \mathbf{E}(z) \cdot \mathbf{p}\psi_0 - \boldsymbol{W}(z) \cdot \mathbf{p}\psi_0 - \nabla_p \psi_0] + \delta(t) \end{aligned} \tag{2.94}$$

$$\begin{aligned}\frac{\partial \psi_1}{\partial t} =& Pe_s \cos\theta \psi_0 + u\psi_0 - Pe_s \sin\theta \frac{\partial \psi_1}{\partial z} + \kappa^2 \frac{\partial^2 \psi_1}{\partial z^2} \\ & - \nabla_p \cdot [\gamma(\mathbf{I} - \mathbf{pp}) \cdot \mathbf{E}(z) \cdot \mathbf{p}\psi_1 - \boldsymbol{W}(z) \cdot \mathbf{p}\psi_1 - \nabla_p \psi_1] \end{aligned} \tag{2.95}$$

subjected to the boundary conditions

$$0 = - Pe_s \sin\theta \psi_0 + \kappa^2 \frac{\partial \psi_0}{\partial z} \quad \text{on} \quad z = \pm\frac{1}{2} \tag{2.96}$$

$$0 = - Pe_s \sin\theta \psi_1 + \kappa^2 \frac{\partial \psi_1}{\partial z} \quad \text{on} \quad z = \pm\frac{1}{2} \tag{2.97}$$

We additionally introduce the 0th, 1st and 2nd orientational moments of the axial moment ψ_k as:

$$c_k(z,t) = \int_\Omega \psi_k d\mathbf{p}, \quad m_k(z,t) = \int_\Omega \psi_k \mathbf{p} d\mathbf{p}, \quad D_k(z,t) = \int_\Omega \psi_k \left(\mathbf{pp} - \mathbf{I}/2\right) d\mathbf{p} \tag{2.98}$$

where Ω corresponds to the unit circle in orientations, $\theta \in [0, 2\pi]$. For convenience, we introduce the k-th order global moments M_k, which are defined as the vertical-averaged of the 0th orientational moments defined in Eq. (2.93). Mathematically:

$$M_k(t) = \int_{-1/2}^{1/2} c_k dz \tag{2.99}$$

The first three global moments satisfy the following partial differential equations:

$$\frac{dM_0}{dt} = 0, \quad \rightarrow M_0 = 1, \tag{2.100}$$

$$\frac{dM_1}{dt} = Pe_s \int_{-1/2}^{1/2} [m_{0_x} + uc_0]\, dy, \tag{2.101}$$

$$\frac{dM_2}{dt} = 2\kappa^2 + 2Pe_s \int_{-1/2}^{1/2} [m_{1_x} + uc_1]\, dy, \tag{2.102}$$

where the normalization condition has been used to determine M_0.

We now proceed to take the asymptotic long-time limits of the axial, orientational and global moments introduced in the previous equations. We will denote them in the same way as before but with an additional $\infty-$subscript (i.e. $\psi_k^\infty = \lim_{t\to\infty} \psi_k$), $c_k^\infty = \lim_{t\to\infty} c_k$)... From the definition of mean displacement $\overline{x}$, the asymptotic long-time mean swimmer velocity $\overline{U}$ can be expressed as a function of the first global moment:

$$\overline{U} = \frac{dM_1^\infty}{dt} = Pe_s \int_{-1/2}^{1/2} \left[m_{0_x}^\infty + uc_0^\infty\right] dz, \tag{2.103}$$

Keeping in mind the definition of mean square displacement $\overline{(x-\overline{x})^2}$, the mean swimmer dispersivity coefficient $\overline{D}$ can be obtained as a function of the first and second global moments as [81]

$$\overline{D} = \frac{1}{2}\frac{dM_2^\infty}{dt} - M_1^\infty \frac{dM_1^\infty}{dt} \tag{2.104}$$

In order to determine M_1, it is common practice to introduce a B-field (see [79]). Here, we avoid that step by subtracting a uniform flow of magnitude $\overline{U}$ to the imposed flow field:

$$u^*(z) = u(z) - \overline{U}, \tag{2.105}$$

a mathematical artifact that does not modify the effective dispersion coefficient. In this way, we do not need to determine M_1^∞. Eq. (2.104) becomes:

$$\overline{D} = \kappa^2 + Pe_s \int_{-1/2}^{1/2} \left[m_{1_x}^\infty + u^* c_1^\infty\right] dz \tag{2.106}$$

Therefore, in order to determine $\overline{U}$ and $\overline{D}$ from Eqs. (2.103) and (2.106), we first need to

solve for ψ_0^∞ and ψ_1^∞. The asymptotic long-time 0th axial moment ψ_0^∞ satisfies

$$\begin{aligned} 0 = &- Pe_s \sin\theta \frac{\partial \psi_0^\infty}{\partial z} + \kappa^2 \frac{\partial^2 \psi_0^\infty}{\partial z^2} \\ &- \nabla_p \cdot [\gamma(\mathbf{I} - \mathbf{pp}) \cdot \mathbf{E}(z) \cdot \mathbf{p}\psi_0^\infty - \boldsymbol{W}(z) \cdot \mathbf{p}\psi_0^\infty - \nabla_p \psi_0^\infty] \end{aligned} \tag{2.107}$$

subject to the no-flux-BC at the walls

$$0 = -Pe_s \sin\theta \psi_0^\infty + \kappa^2 \frac{\partial \psi_0^\infty}{\partial z} \quad \text{on} \quad z = \pm\frac{1}{2} \tag{2.108}$$

and the normalization condition

$$\int_{y=-1/2}^{1/2} \int_{\theta=0}^{2\pi} \psi_0^\infty d\theta dy = 1 \quad (t \geq 0) \tag{2.109}$$

We solve Eqs. (2.107-2.109) using a finite volume numerical scheme; then $\overline{U}$ is readily obtained from Eq. (2.103). Now, we derive the evolution equation for ψ_1^∞. From the definition of M_1^∞, we have

$$M_1^\infty = \int_{-\infty}^{\infty} \int_\Omega \psi_1^\infty d\mathbf{p} dx \tag{2.110}$$

Because we have substracted a uniform flow of magnitude $\overline{U}$ from the external flow field, we know from Eq. (2.103) that $M_1^\infty = \text{constant}$. Using this information and Eq. (2.110), we conclude that ψ_1^∞ is time independent. The evolution equation for the asymptotic long-time 1st axial moment ψ_1^∞ can then be obtained from Eq. (2.95):

$$\begin{aligned} 0 = &Pe_s \cos\theta \psi_0^\infty + u\psi_0^\infty - Pe_s \sin\theta \frac{\partial \psi_1^\infty}{\partial z} + \kappa^2 \frac{\partial^2 \psi_1^\infty}{\partial z^2} \\ &- \nabla_p \cdot [\gamma(\mathbf{I} - \mathbf{pp}) \cdot \mathbf{E}(z) \cdot \mathbf{p}\psi_1^\infty - \boldsymbol{W}(z) \cdot \mathbf{p}\psi_1^\infty - \nabla_p \psi_1^\infty] \end{aligned} \tag{2.111}$$

subject to the no-flux-BC at the walls

$$0 = -Pe_s \sin\theta \psi_1^\infty + \kappa^2 \frac{\partial \psi_1^\infty}{\partial z} \quad \text{on} \quad z = \pm\frac{1}{2} \tag{2.112}$$

We solve Eqs. (2.111,2.112) using a finite volume numerical scheme. We subsequently determine $\overline{D}$ from Eq. (2.106).

2.8.3 Theoretical approximation: Orientational moments

We expand ψ_0^∞ as a function of the first two orientational moments (see § 1.1.2):

$$\psi_0^\infty(z,\theta) = \frac{1}{2\pi}\left[c_0^\infty(z) + 2\mathbf{p}\cdot\mathbf{m_0}(z)\right], \tag{2.113}$$

where we have neglected higher order moments, as done in [51]. The equations for c_0^∞ and $\mathbf{m_0^\infty}$ are obtained by taking the 0th and 1st orientational moments of Eq. (2.107). We get:

$$-Pe_s\frac{dm_{0_z}^\infty}{dz} + \kappa^2\frac{d^2c_0^\infty}{dz^2} = 0 \tag{2.114}$$

$$\kappa^2\frac{d^2m_{0_x}^\infty}{dz^2} - W_{xz}m_{0_z}^\infty - m_{0_x}^\infty = 0 \tag{2.115}$$

$$-\frac{Pe_s}{2}\frac{dc_0^\infty}{dz} + \kappa^2\frac{d^2m_{0_z}^\infty}{dz^2} - W_{zx}m_{0_x}^\infty - m_{0_z}^\infty = 0 \tag{2.116}$$

which are subject to no-flux boundary conditions. This system of equations can be solved in the low-flow asymptotic limit (see [51]), and solved for a Couette flow for any Pe_f. After some math, we get:

$$c_0^\infty = \frac{2Pe_s}{\kappa^2 Pe_f}\left[A_1\frac{1}{\lambda_1}\left(1-\kappa^2\lambda_1^2\right)\cosh(\lambda_1 z) + A_2\frac{1}{\lambda_2}\left(1-\kappa^2\lambda_2^2\right)\cosh(\lambda_2 z)\right] + A_3 \tag{2.117}$$

$$m_{0_x}^\infty = A_1\sinh(\lambda_1 z) + A_2\sinh(\lambda_2 z) \tag{2.118}$$

$$m_{0_z}^\infty = \frac{2}{Pe_f}\left[A_1\left(1-\kappa^2\lambda_1^2\right)\sinh(\lambda_1 z) + A_2\left(1-\kappa^2\lambda_2^2\right)\sinh(\lambda_2 z)\right] \tag{2.119}$$

where λ_1 and λ_2 are

$$\lambda_1 = \left[\frac{1}{2\kappa^2}\left(2 + \frac{Pe_s^2}{2\kappa^2} + \sqrt{\frac{Pe_s^4}{4\kappa^4} - Pe_f^2}\right)\right]^{1/2} \tag{2.120}$$

$$\lambda_2 = \left[\frac{1}{2\kappa^2}\left(2 + \frac{Pe_s^2}{2\kappa^2} - \sqrt{\frac{Pe_s^4}{4\kappa^4} - Pe_f^2}\right)\right]^{1/2} \tag{2.121}$$

Notice that there is a critical fluid Peclet number $Pe_{f_c} = Pe_s^2/(2\kappa^2)$, beyond which the behavior of the solution changes. A_1, A_2 and A_3 are constants that we obtain from the

wall-conditions:

$$A_1 = \frac{1}{2}\frac{Pe_s}{A_4 + A_5} \tag{2.122}$$

$$A_2 = -\frac{\lambda_1 \cosh(\lambda_1/2)}{\lambda_2 \cosh(\lambda_2/2)} A_1 \tag{2.123}$$

$$A_3 = 1 - \frac{4Pe_s}{\kappa^2 Pe_f}\left[\frac{A_1}{\lambda_1^2}(1-\kappa^2\lambda_1^2)\sinh(\lambda_1/2) + \frac{A_2}{\lambda_2^2}(1-\kappa^2\lambda_2^2)\sinh(\lambda_2/2)\right] \tag{2.124}$$

where A_4 and A_5 take the value

$$A_4 = (1-\kappa^2\lambda_1^2)\left[\cosh\left(\frac{\lambda_1}{2}\right)\left(\frac{2\kappa^2\lambda_1}{Pe_f} - \frac{Pe_s^2}{\kappa^2 Pe_f \lambda_1}\right) + \frac{2Pe_s^2}{\kappa^2 Pe_f \lambda_1^2}\sinh\left(\frac{\lambda_1}{2}\right)\right] \tag{2.125}$$

$$\begin{aligned} A_5 = &-\frac{\lambda_1}{\lambda_2}(1-\kappa^2\lambda_2^2)\left[\cosh\left(\frac{\lambda_1}{2}\right)\left(\frac{2\kappa^2\lambda_2}{Pe_f} - \frac{Pe_s^2}{\kappa^2 Pe_f \lambda_2}\right)\right. \\ &\left. + \frac{2Pe_s^2}{\kappa^2 Pe_f \lambda_2^2}\cosh\left(\frac{\lambda_1}{2}\right)\tanh\left(\frac{\lambda_2}{2}\right)\right] \end{aligned} \tag{2.126}$$

In the same way, we expand ψ_1^∞ as a function of the first two orientational moments:

$$\psi_1^\infty(z,\theta) = \frac{1}{2\pi}\left[c_1^\infty(z) + 2\mathbf{p}\cdot\mathbf{m_1}(z)\right], \tag{2.127}$$

where we have neglected higher order moments. The equations for c_1^∞ and $\mathbf{m_1^\infty}$ are obtained by taking the 0th and 1st orientational moments of Eq. (2.111). We get:

$$-Pe_s\frac{dm_{1_z}^\infty}{dz} + \kappa^2\frac{d^2c_1^\infty}{dz^2} = -Pe_s m_{0_x}^\infty - u^* c_0^\infty \tag{2.128}$$

$$\kappa^2\frac{d^2m_{1_x}^\infty}{dz^2} - W_{xz}m_{1_z}^\infty - m_{1_x}^\infty = -\frac{Pe_s}{2}c_0^\infty - u^* m_{0_x}^\infty \tag{2.129}$$

$$-\frac{Pe_s}{2}\frac{dc_1^\infty}{dz} + \kappa^2\frac{d^2m_{1_z}^\infty}{dz^2} - W_{zx}m_{1_x}^\infty - m_{1_z}^\infty = -u^* m_{0_z}^\infty \tag{2.130}$$

which are subject to no-flux boundary conditions. Analytical solutions for a parabolic pressure-driven flow are rather complicated. Upon the application of a Couette flow, the system of Eqs. (2.128-2.130) is a 2nd order, non-homogeneous and linear system. We can easily solve this set of equations by converting the system into a 1st order system of equations. The general solution can be decomposed into a linear combination of the homogeneous solution and a particular solution. The homogenous solution can be obtained by determining the exponential of the system matrix, and the particular solution can be obtained by inspection,

or any other procedure. Here, we do not provide the solutions because the mathematical expressions are rather complicated.

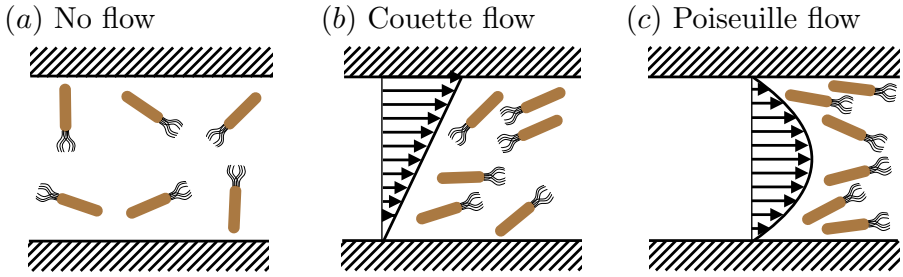

Figure 2.11: Bacterial orientational distribution for three different flow conditions. (a) No flow: Particles point towards the walls on average and swim equally in both x-directions. (b) Couette flow: Swimmers orient along the flow close to the top wall and against the flow close to the bottom wall. The fluid field enhances active dispersion. (c) Poiseuille flow: The orientation of the particles is biased towards the negative x-direction. The fluid field reduces active dispersion.

We obatined the low and high Pe_f asymptotic solutions.

In the absence of flow, the mean swimmer drift velocity vanishes ($\overline{U}(Pe_f = 0) = 0$) and the dispersion coefficient is the sum of molecular diffusion and wall-free active dispersion $\overline{D}(Pe_f = 0) = \kappa^2 + Pe_s^2/2$ [44]. For high external flows, mean swimmer velocity and dispersivity asymptote to $\overline{U} = Pe_f/2$ (solution valid at any flow regime and independent of Pe_s) and $\overline{D}(Pe_f \to \infty) = Pe_f^2/(120\kappa^2)$ for Couette flow, and $\overline{U}(Pe_f \to \infty) = Pe_f/6$ and $\overline{D}(Pe_f \to \infty) = Pe_f^2/(7560\kappa^2)$ for Poiseuille flow, this latter result is in agreement with previous derivations for tracer particles [82]. Our numerical solutions approach the low- and high- Pe_f asymptotic regimes, as observed in Figs. (2.13,2.12).

2.8.4 Numerical results

We solve numerically Eqs. (2.107) and (2.111), and determine $\overline{U}$ and $\overline{D}$ from Eqs. (2.103) and (2.106). In the absence of an external flow, particles swim equally in both horizontal directions, and the dispersion coefficient is that of active particles in an unbounded domain [44]. They also accumulate at the boundaries increasing the wall-normal polarization [51]. The flow conditions modify the orientational and spatial configurations of the swimmers, which affects the axial transport of swimmers along the channel.

Upon the application of a Poiseuille flow, shear alignment reduces the mean swimmer

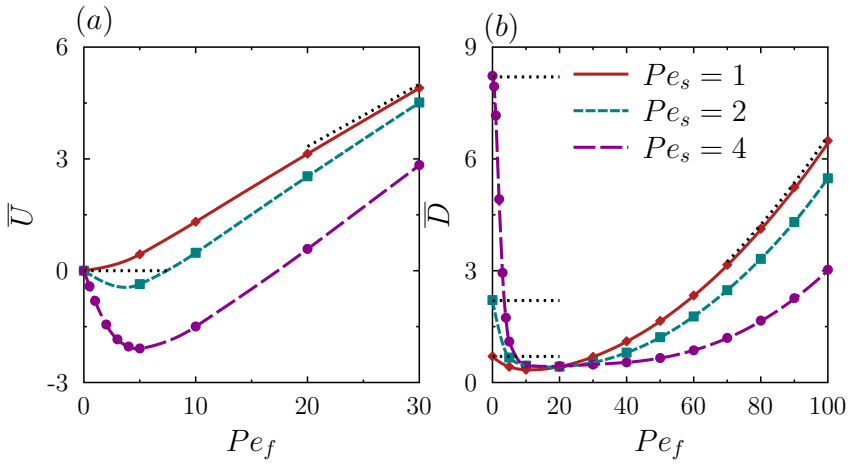

Figure 2.12: Poiseuille flow. Long-time mean swimmer velocity $\overline{U}$ (left) and mean swimmer dispersion coefficient $\overline{D}$ (right) as a function of the dimensionless external shear Pe_f, for three different swimming Peclet numbers. Lines correspond to the numerical solution, symbols correspond to Brownian dynamic simulations, and dot lines in black correspond to the low and high Pe_f asymptotes. Parameter values: $\kappa^2 = 0.2$, $\gamma = 0$.

velocity below that of the fluid molecules, and it can become negative for low external flows and high-motility particles. This biased motion, characterized by particles swimming longer against the flow, not only decreases the mean swimmer velocity but also the active dispersion, as shown in Fig. (2.12). This phenomenon was observed previously in a recent numerical study [83]. For low shears, the decrease in active dispersion dominates the increase in shear-dispersion, and the net axial dispersion coefficient decreases. Therefore, the application of a small parabolic flow can be used to attain a reduction in microbial dispersion. At a critical Pe_f, $\overline{D}$ reaches a minimum, beyond which shear-dispersion becomes dominant and $\overline{D}$ keeps growing with Pe_f. We see from Fig. (2.12) that activity increases the axial dispersion for low external shears and decreases it for higher external shears. This is a very interesting result. How is it possible that in a high-shear regime a suspension of passive particles disperses more than its active counterpart? Obtaining a physical explanation for this phenomenon requires the understanding of the conventional Taylor dispersion. In the case of tracer particles, vertical molecular diffusion enables the particles to sample different cross sections, hence different fluid velocities. The time spent by the particles at every vertical position in the channel is not the same for every particle at the same instantaneous time. This effect combined with vertical velocity gradients results in a net axial particle dispersion. As cross-stream migrations decrease (lower Brownian motion), the variance of

the time distribution for all the particles spending at every vertical location is enhanced, which leads to an increase of particle mean-square displacement and axial particle dispersion increases. In the limiting case of an athermal suspension, particles do not cross streamlines and the system becomes deterministic. In this special case, the mean square displacement is maximized, but the suspension is not diffusive anymore. A similar reasoning can be used to study how self-propulsion affects particle dispersion. Particles with higher propulsive speed that undergo lower Brownian rotations experience more vertical migrations; hence particles with higher run-lengths (higher Pe_s) will disperse less under intermediate-high flow conditions, as visualized in Fig. (2.12). Activity hinders shear-induced Taylor dispersion. At extremely high external shears (not studied here), particles rotate extremely fast with the flow and the effect of self-propulsion is cancelled. The effect of self-propulsion decreasing the variance of axial particle positions is also observed for Couette flows, as seen in Fig. (2.13). Upon the application of a Couette flow (top wall moving), particles drift with the mean fluid velocity for any Pe_s, a phenomenon that arises due to the symmetry of the problem. Particles located in the upper mid-plane additionally reorient, on average, in the direction of the flow, and particles in the lower mid-plane reorient against the flow. The result is an increase in active dispersion, even at low external shears, as shown in Fig. (2.13).

A few simulations have been carried out for different particle shapes (not shown here). At any particle shape, the qualitative features explained above remain present. Particles with higher Bretherton constant disperse more due to particle alignment along the streamlines of the fluid flow. For a similar reason, they also drift at lower velocities. A more detailed analysis of the effect of particle shape on particle transport has been carried out for the porous problem.

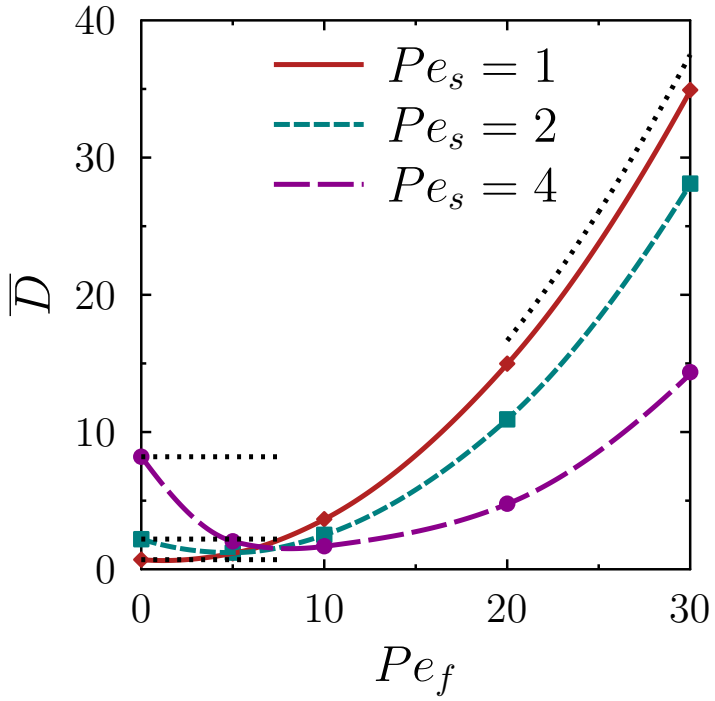

Figure 2.13: Couette flow. Long-time mean swimmer dispersion coefficient $\overline{D}$ (right) as a function of the dimensionless external shear Pe_f, for three different swimming Peclet numbers. Lines correspond to the numerical solution, symbols correspond to Brownian dynamic simulations, and dot lines in black correspond to the low and high Pe_f asymptotes. Parameter values: $\kappa^2 = 0.2$, $\gamma = 0$.

Chapter 3

Effect of chemical fields on the transport and spreading of active particles in periodic porous media

3.1 Introduction

Chemical fields play a key role on the behavior and transport of living matter. Examples include the motion of human spermatozoa [15], the migration of white blood cells [16] or the locomotion of bacteria [17, 18]. Chemotaxis, the cell movement in response to a chemical gradient resulting in a net drift up a chemoattractant gradient or down a chemorepellent gradient, was first discovered in the 1880s by Theodor W. Engelmann, who first reported the aggregation of an oxygen-sensing organism in the vicinity of an oxygen source [84]. He took advantage of the special ability of this aerotactic bacteria to quantify the oxygen production of photosynthetic processes of plants and algae [85]. In a posterior study, Pfeffer observed bacterial accumulation near the tip of a capillary filled up with a chemoattractant [86]. This work became the basis of a wide variety of techniques developed to evaluate chemotactic ability in cells. After half a century of a lack of scientific research in the field of chemotaxis, the burgeoning interest in this phenomenon reemerged with several experimental studies with Rhodospirillum rubrum exhibiting positive chemotaxis toward a great variety of chemical compounds [87] and different strains of Pseudomonas exhibiting aerotaxis [88, 89]. More quantitative studies were carried out by Adler [90, 91], who provided an explanation for the formation of Escherichia coli bands and rings appearing inside

capillary tubes and agar plates, respectively, due to their chemotactic behavior toward oxygen and energy sources. These migrating bands were first observed by Beyerinck (1893), subsequently modeled by Keller and Segel following a phenomenological analysis [92], and further observed in experimental studies in semi-solid agar gels [93–96] and numerical studies [95]. Other studies investigated the effect of fluid shear on chemotaxis [97], and the role of chemotaxis on collective swimming [98–101].

Chemotaxis and bacterial motility studies have been highly concentrated on Escherichia coli and Salmonella Typhimurium, both present in the mammalian gastrointestinal tract [102]. Due to their small size ($3\mu m$ long), they do not have much flexibility to adjust to a change in environmental conditions. For this reason, they continuously migrate from environment to environment in search for an optimum habitat by sensing gradients of certain physicochemical properties. In order to propel themselves through the environment they rotate their flagella, mostly counterclockwise. These flagella are slender threadlike structures, distributed around the cell, and each filament is driven by a motor, which uses a proton-motive force [103] as energy source, and is embedded in the cell wall and the cytoplasmic membrane [104]. The flagellar motor switches the direction of rotation either spontaneously or in response to signals received from their receptors. These chemoreceptors are located at the cell surface, and they get stimulated through binding/dissociation of molecules to/from the receptor. The transmission of molecular signals from the cell-surface receptors to its intracellular sensors allows the cell to ensure an appropriate response. Their complex switch element, comprised of self-interacting proteins, is in charged of receiving the signal and determine the probability of the motor to rotate in a certain direction [105]. In the case of Escherichia coli, they use transmembrane methyl-accepting chemotaxis sensor proteins (MCPs) that allow bacteria to detect concentration gradients in the environment. The external chemotactic stimuli can either bind directly to chemotactic-specific receptors or bind to a primary receptor which then communicates with a chemotaxis-specific receptor [105]. The ligand/molecule produces a signal when binding to a site on an MCP, which leads to conformational changes of the receptor, resulting in the rearrangement of most of its constituents. The information about the receptor occupancy is transmitted across the cytoplasmic membrane and protein-protein interactions (via chemical reactions) subsequently transduces the chemotactic signal from the receptor supramolecular complex to the flagellar-motor supramolecular complex by the messenger protein CheY. This signaling involves other cytoplasmic proteins such as CheW, CheA and CheZ. The result is an alternation between

fairly straight-line runs with brief intermissions of clockwise rotation and pauses (tumbles) [17, 106]. During the runs, deviations from a straight line arise due to rotational Brownian motion [17], and tumbles occur provided that a minimum number of flagella rotate clockwise [107, 108]. In the absence of any stimuli, the time duration between consecutive tumbles follows an exponential distribution [17]. When they experience a gradient of a chemical species, the final outcome is a decrease in frequency of tumbling in response to a favorable signal originally received from the receptor [106]. The changes in direction from the end of one run to the beginning of the next one for the wild type E.coli strain were found to be correlated and biased in the forward direction, with a distribution with mean of 68^o and standard deviation of 36^o [17]. No correlation between the length of the run and the change in direction was found.

In the present work, we model chemotaxis through a spatially varying particle tumbling frequency, which is an approximation, in the limit of weak fields, to the actual mechanism adopted by real bacteria. Because of their tiny size, they sense spatial concentration gradients that are comparable to the statistical noise. In order to overcome this problem, they make temporal comparisons as they swim through the environment [109, 110], and remember local concentrations for a memory time comparable to the mean duration of a single run, in order for the effect of chemotaxis to remain effective [110]. An adaptation model involving proportional control [20] was proposed to mimic the behavior of cells upon the application of different chemoattractant fields. The actuation of the flagellar motors depended on an error signal proportional to the difference between the current chemoreceptor occupancy and the occupancy averaged over the recent past. In a subsequent study by Segall et al. [21], a suspension comprised of tethered wild-type E. coli cells were subject to an impulse stimulus of aspartate. The cells were found to make temporal comparisons of the concentrations experienced during the last 4 seconds, and integrate the inputs coming from their receptors during that amount of time. More precisely, they were found to compare the concentration experienced during the past second with that experienced during the previous 3 seconds. The cells integrated this biphasic signal and responded to a weighted difference integral (refer to Fig. 1 in [21]). Mutants lacking the genes CheR and CheB were found to miss the second lobe of the response [104]. These long-time integrations are striking knowing that the amount of time it takes for a small molecule to cross the cell via diffusion is about 1 ms [104].

In this study, motivated by the necessity of understanding the effect of chemotaxis

on the transport of microbial communities in heterogeneous media [73, 74], we use a macro-continuum model based on generalized Taylor dispersion theory, introduced in Chapter 2, to get insights about the drift and spreading of run-and-tumble bacterial suspensions in complex geometries. In our analysis, we distinguish between species that respond to any chemical gradient (positive-negative chemotaxis) and strains that only modify the tumbling frequency when moving towards favorable directions (positive chemotaxis). We use a Lagrangian perspective and start from a micro-continuum level approach, where we track the spatial and orientational configuration of a single bacterium as it moves through the medium. We obtain analytical expressions for the asymptotic long-time mean bacterial velocity vector $\overline{\mathbf{U}}$ and mean bacterial dispersivity dyadic $\overline{\mathbf{D}}$ in the limit of vanishing surface fraction of obstacles, and explore numerically their dependence on medium porosity. On the one hand, from a microscopic point of view $\overline{\mathbf{U}}$ denotes the temporal rate of change of the swimmer's displacement relative to a fixed point of view and $\overline{\mathbf{D}}$ represents the linear temporal growth of the swimmer's mean square displacement. On the other hand, from a macroscopic perspective $\overline{\mathbf{U}}$ and $\overline{\mathbf{D}}$ also characterize the net convective and dispersive particle flux (see Chapter 2). We explore the effect of chemotactic field strength and analyze the bacterial distribution around the obstacles. We compare our macro-continuum model results with discrete Brownian particle simulations and find a good agreement between both approaches.

3.2 Problem definition. Langevin equations and modeling of bacterial tumbling frequency

We analyze the long-time asymptotic transport of a dilute suspension of chemotactic run-and-tumble particles that move through a two-dimensional granular medium. The fluid is quiescent and particles are subjected to a macroscopic linear chemical field gradient along the direction defined by the unit vector $\hat{\mathbf{s}}$, whose chemical concentration is denoted by the variable s. The periodic discontinuous medium is comprised of a repetitive arrangement of rigid obstacles of characteristic length a organized in a square-lattice, with unit cell of length L. The swimmer runs at constant speed v_0 along the direction defined by the unit vector $\mathbf{p}$, and undergoes translational and rotational diffusion. The Langevin equations that describe

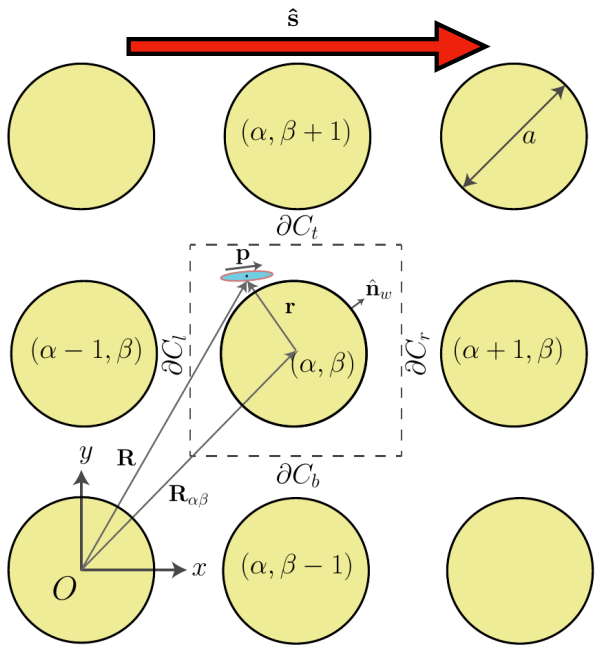

Figure 3.1: Sketch of the porous geometry and nomenclature used in the model. The origin O of the coordinate system is chosen as the centroid of an arbitrary cell, and each cell in the lattice is labeled by two integers $(\alpha, \beta) \in \mathbb{Z}^2$ identifying its horizontal and vertical positions, or equivalently by the position $\mathbf{R}_{\alpha\beta} = (X_\alpha, Y_\beta)$ of its centroid where $X_\alpha = \alpha L$ and $Y_\beta = \beta L$. The array is characterized by its porosity $\epsilon_p = S_f/S_t$. The instantaneous position of the swimmer is denoted by $\mathbf{R}(t)$ with respect to point O and its orientation angle by $\theta(t) \in \Omega = [0, 2\pi)$, whose swimming direction is denoted by the unit vector $\mathbf{p} = (\cos\theta, \sin\theta)$. The global coordinate $\mathbf{R}$ can be further decomposed as $\mathbf{R} = \mathbf{R}_{\alpha\beta} + \mathbf{r}$, where $\mathbf{R}_{\alpha\beta}$ is the position of the unit cell where the particle is located and $\mathbf{r} = (x, y)$ is a local coordinate with respect to the center of that cell.

the swimmer motion are

$$\dot{\mathbf{R}} = v_0\mathbf{p} + \boldsymbol{\eta}_t(t), \qquad \dot{\mathbf{p}} = \boldsymbol{\eta}_r(t) \ + \ \text{tumble events} \tag{3.1}$$

Apart from Brownian rotations, changes in direction also occur due to instantaneous tumble events, where the number of tumbles in a fixed period of time follows a Poisson process (see § 1.2.1). When spatial gradients are small, the locomotion of the cells can be approximated by a Markovian process, where the bacterial mean tumbling frequency λ depends only on their instantaneous position and orientation. Denoting the fraction of bounded cell surface receptors as $P_b = \chi s/(k_d + s)$, where χ is a scaling constant factor that represents the total number of receptors for the ligand and k_d is the dissociation constant between the chemical substance and its receptor on the cell surface, the regulation of the tumbling frequency

depends on the temporal changes of P_b as the cells swim through the medium [110, 111]:

$$\lambda = \lambda_0 e^{-DP_b/Dt}, \tag{3.2}$$

where λ_0 corresponds to the mean tumbling frequency in the absence of chemical fields, and $D/Dt = \partial/\partial t + v_0 \mathbf{p} \cdot \nabla_r$ is the material derivative following the cell. Assuming small spatial chemical gradients, we can approximate Eq. (3.2) by truncating its Taylor series and keeping the first two terms in the expansion

$$\lambda(\mathbf{r}, \mathbf{p}) \approx \lambda_0 - \xi v_0 \mathbf{p} \cdot \nabla_r s, \tag{3.3}$$

where we have assumed a time independent chemical field ($\partial s/\partial t = 0$) and a dissociation constant much greater than the chemoattractant concentration ($k_d \gg s$). We have introduced the new dimensionless variable $\xi = \lambda_0 \chi / k_d$, which denotes the strength of the external chemotactic field. We distinguish between $\xi > 0$ for chemoattractant chemical species and $\xi < 0$ for chemorepellent species. The chemical concentration gradient $\nabla_r s$ is periodic along the unit cells that form the porous material, which justifies the dependence of λ on the local variable $\mathbf{r}$.

In order to carry out the Brownian dynamic simulations we advance position and orientation of the swimmers according to Eq. (3.1). We determine if a tumbling event takes place in a time step Δt by generating a random number $N_{rand} \in [0, 1]$. Then,

$$\begin{cases} \text{If } N_{rand} < 1 - e^{-\lambda(\mathbf{r},\mathbf{p})\Delta t} & \rightarrow \text{ Tumble occurs.} \\ \text{If } N_{rand} > 1 - e^{-\lambda(\mathbf{r},\mathbf{p})\Delta t} & \rightarrow \text{ No tumble occurs.} \end{cases} \tag{3.4}$$

In the present study, we have taken $\Delta t = 10^{-3}$. For more details, refer to § 1.2.1. In the next section we describe the long-time statistics of the bacterial position $\mathbf{R}$ using a macroscopic framework.

3.3 Macroscopic framework

3.3.1 Discontinuous medium

We describe the long-time statistics of the bacterial position $\mathbf{R}$ using a macroscopic mathematical framework introduced in Chapter 2 and define a swimmer conditional probability density $\psi(\mathbf{R}, \mathbf{p}, t|\mathbf{R_0}, \mathbf{p_0})$. The probability density satisfies a similar equation to the Boltzmann equation, where the tumbling of the bacterium is modeled as a Markov process. It satisfies the Fokker-Planck equation (see § 1.2.2)

$$\partial_t \psi + \nabla_R \cdot \mathbf{J} + \nabla_p \cdot \mathbf{j} = -\lambda(\mathbf{r}, \mathbf{p})\psi + \int_\Omega K(\mathbf{p}|\mathbf{p}')\psi(\mathbf{R}, \mathbf{p}', t)\lambda(\mathbf{r}, \mathbf{p}')d\mathbf{p}', \tag{3.5}$$

subjected to the initial position $\mathbf{R_0}$ and orientation $\mathbf{p_0}$. From the Langevin equation in (3.1), the spatial bacterial flux $\mathbf{J}$ is the sum of swimming and Brownian translational diffusion, and the rotational bacterial flux $\mathbf{j}$ accounts for simply Brownian rotational diffusion

$$\mathbf{J} = v_0\mathbf{p}\ \psi - d_t\nabla_R\psi, \qquad \mathbf{j} = -d_r\nabla_p\psi \tag{3.6}$$

The first two terms on the right-hand-side of Eq. (3.5) represent run-and-tumble processes (see Appendix for more details). The first term represents the local rate at which the swimmer located at position $\mathbf{r}$ tumbles away from orientation $\mathbf{p}$, and the second term represents the rate at which the swimmer at position $\mathbf{r}$ tumbles to orientation $\mathbf{p}$ accounting for all possible pre-tumble orientations $\mathbf{p}'$. The tumbling kernel or angular correlation function, $K(\mathbf{p}, \mathbf{p}')$, captures correlations between the direction of motion before and after tumble events. We use a two-dimensional angular correlation function [112, 113]

$$K(\mathbf{p}|\mathbf{p}') = \frac{1}{2\pi I_0(\Upsilon)} e^{\Upsilon(\mathbf{p}\cdot\mathbf{p}')}, \tag{3.7}$$

where Υ is a controlled parameter. Perfect isotropic tumbles occur when $\Upsilon \to 0$, whereas no changes in direction occur when $\Upsilon \to \infty$. The factor in front of the exponential enforces normalization ($\int K d\mathbf{p} = 1$), and the function I_0 corresponds to the 0th-order modified Bessel function of the first kind. In order to include correlations between the pre- and post- tumbling directions in the Brownian dynamic simulations, we numerically obtain a density distribution according to Eq. (3.7) through the method of inverse transform sampling.

Because we numerically find that $\overline{\mathbf{U}}$ and $\overline{\mathbf{D}}$ are independent of the parameter Υ, we take the isotropic kernel $K(\mathbf{p},\mathbf{p}') = 1/2\pi$ in our analysis to simplify the calculations. The fact that angular correlations do not affect the drift velocity has been studied in previous studies (e.g. [114]). Because the mean cosine of the turning angle is independent of the factor Υ, angular correlations do not affect the diffusion coefficient neither [115]. This is a consequence of using the kernel introduced in Eq. (3.7).

We non-dimensionalize the equations by choosing $1/\lambda_0$ as time-scale and a as length scale. In addition to the porosity of the medium ϵ_p and the chemotactic field strength ξ, non-dimensionalization yields three additional dimensionless groups: $Pe_s = v_0/(\lambda_0 a)$, $\kappa = \sqrt{d_t/\lambda_0}/a$, and $\tau = d_r/\lambda_0$. The swimming Peclet number Pe_s compares the ratio of two time scales: the reorientation time scale due to tumbling events over the characteristic time to swim a distance equal to the obstacle diameter, κ^2 represents the dimensionless translational diffusivity of the swimmer, and τ compares the importance of Brownian rotations over tumbling reorientations; for E. Coli, $\tau \ll 1$. We use dimensionless variables in the proceeding discussions.

The mean asymptotic transport velocity $\overline{\mathbf{U}}$ can be obtained from the steady-state zeroth-order local moment $\psi_0^\infty(\mathbf{r},\mathbf{p})$, which describes the long-time probability of finding the particle at a certain local position $\mathbf{r}$ with orientation $\mathbf{p}$ irrespective of which unit cell it is traversing. It satisfies the simplified steady Fokker-Planck equation

$$\nabla_r \cdot \mathbf{J}_\mathbf{0}^\infty + \nabla_p \cdot \mathbf{j}_\mathbf{0}^\infty = -\lambda(\mathbf{r},\mathbf{p})\psi_0^\infty(\mathbf{r},\mathbf{p}) + \int_\Omega K(\mathbf{p},\mathbf{p}')\psi_0^\infty(\mathbf{r},\mathbf{p}')\lambda(\mathbf{r},\mathbf{p}')d\mathbf{p}', \tag{3.8}$$

with translational and rotational fluxes

$$\mathbf{J}_\mathbf{0}^\infty = Pe_s\mathbf{p}\ \psi_0^\infty - \kappa^2\nabla_r\psi_0^\infty, \qquad \mathbf{j}_\mathbf{0}^\infty = -\tau\nabla_p\psi_0^\infty \tag{3.9}$$

subject to normalization condition $\int_S\int_\Omega \psi_0^\infty d\mathbf{p}d^2\mathbf{r} = 1$, to the no-flux condition $\mathbf{n}_w \cdot \mathbf{J}_0^\infty = 0$ on the surface of the pillar, and to jump conditions $[\![\psi_0^\infty]\!] = 0$ and $[\![\nabla_r\psi_0^\infty]\!] = \mathbf{0}$ on the edges ∂C_r and ∂C_t of the unit cell. The dimensionless mean tumbling frequency becomes

$$\lambda(\mathbf{r},\mathbf{p}) = 1 - \xi Pe_s\mathbf{p}\cdot\nabla_r s, \tag{3.10}$$

for strains undergoing positive-negative chemotaxis, and

$$\lambda(\mathbf{r},\mathbf{p}) = \begin{cases} 1 - \xi Pe_s \mathbf{p}\cdot\nabla_r s, & \text{if } \mathbf{p}\cdot\nabla_r s > 0 \\ 1, & \text{if } \mathbf{p}\cdot\nabla_r s < 0 \end{cases} \tag{3.11}$$

for strains undergoing positive chemotaxis. In the work by Macnab & Koshland [109], Salmonella typhimurium responded to both positive and negative gradient of attractants (approximated by Eq. 3.10). A different behavior was observed by Brown & Berg [110, 116], where E.coli responded to favorable spatial gradients, and the tumbling probability remained to the value equal to that in the absence of any chemical gradient when moving towards unfavorable conditions (approximated by Eq. 3.11).

We solve for ψ_0^∞ numerically using a finite-volume method. The asymptotic mean particle velocity is then obtained by simple integration as

$$\overline{\mathbf{U}} = \int_\Omega \int_{\partial C_{\mathrm{r+t}}} [\![\mathbf{r}]\!]\, \mathbf{J}_0^\infty \cdot d\mathbf{C} d\mathbf{p}\,. \tag{3.12}$$

Determining the long-time dispersivity tensor $\overline{\mathbf{D}}$ requires consideration of the first-order moment $\boldsymbol{\psi_1}$. It takes the asymptotic form

$$\boldsymbol{\psi_1}(\mathbf{r},\mathbf{p},t) = \psi_0^\infty(\mathbf{r},\mathbf{p})\left[\overline{\mathbf{U}}t + \mathbf{B}(\mathbf{r},\mathbf{p})\right] + \mathcal{O}(\mathrm{e}^{-t}). \tag{3.13}$$

The fluctuation field $\mathbf{B}(\mathbf{r},\mathbf{p})$ contains information about dispersion and obeys the steady problem

$$\begin{aligned} &\nabla_r\cdot\left[\mathbf{J}_0^\infty\mathbf{B} - \kappa^2\psi_0^\infty\nabla_r\mathbf{B}\right] + \nabla_p\cdot\left[\mathbf{j}_0^\infty\mathbf{B} - \kappa^2\psi_0^\infty\nabla_p\mathbf{B}\right] + \lambda\psi_0^\infty\mathbf{B} - \frac{1}{2\pi}\int_\Omega \psi_0^\infty\mathbf{B}\lambda d\mathbf{p}' \\ &= -\psi_0^\infty\overline{\mathbf{U}}\,, \end{aligned} \tag{3.14}$$

subject once again to the no-flux condition $\mathbf{n}_w\cdot\nabla_r\mathbf{B} = \mathbf{0}$ at the obstacle walls, and to jump conditions $[\![\mathbf{B}]\!] = -[\![\mathbf{r}]\!]$, $[\![\nabla_r\mathbf{B}]\!] = \mathbf{0}$ on ∂C_{r} and ∂C_{t}. We solve numerically for $\mathbf{B}$, and its knowledge provides the asymptotic dispersivity dyadic $\overline{\mathbf{D}}$ as

$$\overline{\mathbf{D}} = \frac{1}{2}\int_\Omega\int_{\partial C_{\mathrm{r+t}}} \left\{\kappa^2\psi_0^\infty[\![\nabla_r(\mathbf{BB})]\!] - \mathbf{J}_0^\infty[\![\mathbf{BB}]\!]\right\}\cdot d\mathbf{C}d\mathbf{p} - \frac{1}{2}\left(\overline{\mathbf{U}}\,\overline{\mathbf{B}} + \overline{\mathbf{B}}\,\overline{\mathbf{U}}\right), \tag{3.15}$$

where $\overline{\mathbf{B}}$ denotes the spatial and orientational average of $\mathbf{B}$ with weighting factor ψ_0^∞.

3.3.2 Analytical solutions in the limit of $\epsilon_p \to 1$

We derive analytical expressions for $\overline{\mathbf{U}}$ and $\overline{\mathbf{D}}$ in the limit of low surface fraction of obstacles, and neglect rotational fluctuations ($\tau = 0$). Due to the negligible effect of the obstacle boundaries ($\epsilon_p \to 1$), we use a continuum analysis and solve the unbounded problem. In this continuum limit, the local spatial variable $\mathbf{r}$ disappears and only the global variable $\mathbf{R}$ remains in the analysis. If we were to include rotational Brownian motion, the effective tumbling rate of the particles would increase, and the drift velocity would decrease, but the qualitative behavior would remain the same. We explore two different chemotactic behaviors: a species that displays positive-negative chemotaxis, and a species that displays only positive chemotaxis.

Positive-negative chemotaxis

The configuration of the swimmer is described by its position vector $\mathbf{R}$ and orientation $\mathbf{p}$. To simplify the analytical calculation, we assume that the swimmer orientation angle θ is measured with respect to the direction of increasing chemoattractant concentration, denoted by the unit vector $\hat{\mathbf{s}}$. Under this convention, $\mathbf{p} \cdot \hat{\mathbf{s}} = \cos\theta$, and the swimmer mean tumbling frequency is described by

$$\lambda(\theta) = 1 - \xi Pe_s \cos\theta \tag{3.16}$$

We define the mth-order polyadic local moment of $\psi(\mathbf{R}, \mathbf{p}, t|\mathbf{R}_0, \theta_0)$ as

$$\boldsymbol{\Psi}_{\boldsymbol{k}}(\theta, t|\mathbf{R}_0, \theta_0) = \iint_{-\infty}^{\infty} \underbrace{\mathbf{R} \cdots \mathbf{R}}_{k \text{ times}} \Psi d\mathbf{R} \qquad k = 0, 1, 2... \tag{3.17}$$

where $\iint_{-\infty}^{\infty}$ corresponds to a double spatial definite integral over the infinite domain. In addition, we define the global moments of $\psi(\mathbf{R}, \mathbf{p}, t|\mathbf{R}_0, \theta_0)$ as

$$\boldsymbol{M}_{\boldsymbol{k}}(t|\mathbf{R}_0, \theta_0) = \int_{\Omega} \boldsymbol{\Psi}_{\boldsymbol{k}} d\mathbf{p} \qquad k = 0, 1, 2... \tag{3.18}$$

From the normalization condition, $M_0 = 1$. We can relate the long-time mean bacterial velocity $\overline{\mathbf{U}}$ and mean bacterial dispersivity dyadic $\overline{\mathbf{D}}$ to the temporal rate of change of the

global moments as

$$\overline{\mathbf{U}} = \lim_{t\to\infty} \frac{d\boldsymbol{M_1}}{dt}, \tag{3.19}$$

$$\overline{\mathbf{D}} = \lim_{t\to\infty} \frac{1}{2}\frac{d}{dt}\left(\boldsymbol{M_2} - \boldsymbol{M_1 M_1}\right) \tag{3.20}$$

We set $k = 0, 1, 2$ in Eq. (3.17), take the temporal derivative on both sides, make use of Eq. (3.5) and apply integration by parts to find the temporal evolution of the 0th-, 1st- and 2nd- local moments of Ψ:

$$\frac{\partial \Psi_0}{\partial t} = -\lambda\Psi_0 + \frac{1}{2\pi}\int_\Omega \lambda\Psi_0 d\mathbf{p}', \tag{3.21}$$

$$\frac{\partial \boldsymbol{\Psi_1}}{\partial t} = Pe_s\Psi_0\mathbf{p} - \lambda\boldsymbol{\Psi_1} + \frac{1}{2\pi}\int_\Omega \lambda\boldsymbol{\Psi_1} d\mathbf{p}', \tag{3.22}$$

$$\frac{\partial \boldsymbol{\Psi_2}}{\partial t} = 2\kappa^2\Psi_0\mathbf{I} + Pe_s\left(\mathbf{p}\boldsymbol{\Psi_1} + \boldsymbol{\Psi_1}\mathbf{p}\right) - \lambda\boldsymbol{\Psi_2} + \frac{1}{2\pi}\int_\Omega \lambda\boldsymbol{\Psi_2} d\mathbf{p}'. \tag{3.23}$$

We now focus on the asymptotic long-time solution of the system of equations (3.21- 3.23). At steady state, Eq. (3.21) becomes

$$\lambda(\theta)\Psi_0^\infty(\theta) = \frac{1}{2\pi}\int_{-\pi}^{\pi} \lambda(\theta')\Psi_0^\infty(\theta')d\theta', \tag{3.24}$$

where $\Psi_0^\infty(\theta) = \lim_{t\to\infty}\Psi_0(\theta, t)$. The RHS is independent of the polar angle θ, which suggests the following solution for Ψ_0^∞:

$$\Psi_0^\infty(\theta) = \frac{C_1}{\lambda(\theta)}, \tag{3.25}$$

where C_1 is a constant easily obtained from the normalization condition $\int_{-\pi}^{\pi}\Psi_0^\infty d\theta = 1$:

$$C_1 = \frac{1}{2\pi}(1 + \xi Pe_s)^{1/2}(1 - \xi Pe_s)^{1/2}. \tag{3.26}$$

Hence,

$$\Psi_0^\infty(\theta) = \frac{1}{2\pi}\frac{(1 + \xi Pe_s)^{1/2}(1 - \xi Pe_s)^{1/2}}{1 - \xi Pe_s\cos\theta}. \tag{3.27}$$

The long-time mean bacterial velocity $\overline{\mathbf{U}}$ can be determined by taking the temporal derivative of Eq. (3.18), use Eq. (3.22) and substitute the result in Eq. (3.19). We get

$$\overline{\mathbf{U}} = Pe_s\int_\Omega \mathbf{p}\Psi_0^\infty d\mathbf{p} \tag{3.28}$$

After a simple integration the components of $\overline{\mathbf{U}}$, parallel and perpendicular to the chemical field direction, are obtained:

$$\overline{U}_{\parallel} = \frac{1}{\xi}\left[1 - (1+\xi Pe_s)^{1/2}(1-\xi Pe_s)^{1/2}\right], \tag{3.29}$$

$$\overline{U}_{\perp} = 0. \tag{3.30}$$

We set $k = 1$ in Eq. (3.18) and integrate Eq. (3.19) in time to get:

$$\mathbf{M_1} = \int_{\Omega} \boldsymbol{\Psi_1} d\mathbf{p} = \overline{\mathbf{U}} t + \overline{\mathbf{B}} + \mathcal{O}(e^{-t}), \tag{3.31}$$

where $\overline{\mathbf{B}} = \int_{\Omega} \Psi_0^{\infty} \mathbf{B} d\mathbf{p}$. The vector $\mathbf{B}$ satisfies the integral equation

$$\lambda \Psi_0^{\infty} \mathbf{B} - \frac{1}{2\pi} \int_{-\pi}^{\pi} \lambda \Psi_0^{\infty} \mathbf{B} d\theta' = (Pe_s \mathbf{p} - \overline{\mathbf{U}}) \Psi_0^{\infty}. \tag{3.32}$$

We insert Eq. (3.27) into Eq. (3.32) to get

$$\mathbf{B}(\theta) = \frac{Pe_s \mathbf{p} - \overline{\mathbf{U}}}{1 - \xi Pe_s \cos\theta} + \int_{-\pi}^{\pi} \mathbf{B} d\theta'. \tag{3.33}$$

The last term on the right-hand side is a constant vector. The addition of a constant vector to $\mathbf{B}$ does not modify $\overline{\mathbf{D}}$. Therefore, we assume that $\int_{-\pi}^{\pi} \mathbf{B} d\theta' = 0$. The components of $\mathbf{B}$ parallel and perpendicular to the chemoattractant concentration gradient direction are

$$B_{\parallel} = \frac{Pe_s \cos\theta - \overline{U}_{\parallel}}{\lambda(\theta)}, \tag{3.34}$$

$$B_{\perp} = \frac{Pe_s \sin\theta}{\lambda(\theta)}. \tag{3.35}$$

The weighted averages $\overline{B}_{\parallel}$ and $\overline{B}_{\perp}$ are

$$\overline{B}_{\parallel} = \frac{Pe_s \xi - \overline{U}_{\parallel}}{(1+\xi Pe_s)(1-\xi Pe_s)}, \tag{3.36}$$

$$\overline{B}_{\perp} = 0. \tag{3.37}$$

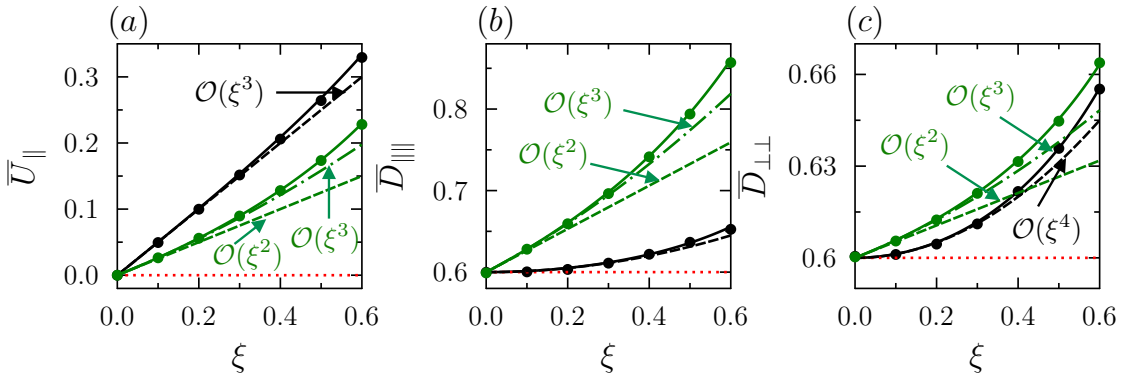

Figure 3.2: Analytical solutions for the long-time mean particle velocity and dispersivity dyadic in the limit of $\epsilon_p \to 1$. Solid lines are the exact solutions, whereas dashed lines are the low chemotactic strength asymptotic solutions (all of them obtained in S.M.). Black color corresponds to positive-negative chemotaxis, green color corresponds to positive chemotaxis, and red color corresponds to the values in the absence of chemical fields ($\xi = 0$). Symbols correspond to Brownian dynamic simulations and they perfectly match with the exact solution. Parameter values: $Pe_s = 1$, $\kappa^2 = 0.1$, $\tau = 0$ and $\epsilon_p = 1$.

We express the long-time asymptotic dyadic $\overline{\mathbf{D}}$ as

$$\overline{\mathbf{D}} = \kappa^2 \mathbf{I} + \frac{Pe_s}{2} \int_{\Omega} \Psi_0^{\infty} (\mathbf{pB} + \mathbf{Bp}) d\mathbf{p} - \frac{1}{2} \left(\overline{\mathbf{U}}\, \overline{\mathbf{B}} + \overline{\mathbf{B}}\, \overline{\mathbf{U}} \right), \tag{3.38}$$

and perform a simple integration. The final results are

$$\overline{D} = \kappa^2 + \frac{1}{\xi^2} \left[1 - (1 + \xi Pe_s)^{1/2} (1 - \xi Pe_s)^{1/2} \right], \tag{3.39}$$

where $\overline{D}_{\parallel\parallel} = \overline{D}_{\perp\perp} = \overline{D}$, and $\overline{D}_{\parallel\perp} = \overline{D}_{\perp\parallel} = 0$. This effect is not observed in three dimensions, where the dispersivity tensor is anisotropic: Bacterial dispersion decreases along the chemical field gradient and increases along the other two directions [117].

Positive chemotaxis.

For particles lacking negative chemotaxis, the spatial- and orientational-dependent mean tumbling frequency has the form:

$$\lambda(\theta) = \begin{cases} \lambda^{\uparrow} = 1 - \xi Pe_s \cos\theta, & \text{if } \cos\theta > 0 \\ \lambda^{\downarrow} = 1, & \text{if } \cos\theta < 0 \end{cases} \tag{3.40}$$

In order to make analytical progress and to account for the jump discontinuity in the tumbling frequency, we define two probability distribution functions

$$\Psi(\mathbf{R},\theta,t)=\begin{cases}\Psi^{\uparrow}(\mathbf{R},\theta^{\uparrow},t), & \theta^{\uparrow}\in[-\pi/2,\pi/2]\\ \Psi^{\downarrow}(\mathbf{R},\theta^{\downarrow},t), & \theta^{\downarrow}\in[\pi/2,3\pi/2]\end{cases} \tag{3.41}$$

$\Psi^{\uparrow}$ and $\Psi^{\downarrow}$ represent the conditional probability of the swimmer traveling in the same and opposite directions as that of growing chemoattractant concentration, respectively. They satisfy the following governing equations:

$$\partial_t\Psi^{\uparrow}+\nabla_R\cdot\left[Pe_s\mathbf{p}\Psi^{\uparrow}-\kappa\nabla_R\Psi^{\uparrow}\right]=-\lambda^{\uparrow}\Psi^{\uparrow}+\frac{1}{2\pi}\left[\int_{-\pi/2}^{\pi/2}\Psi^{\uparrow}\lambda^{\uparrow}d\alpha+\int_{\pi/2}^{3\pi/2}\Psi^{\downarrow}d\alpha\right] \tag{3.42}$$

$$\partial_t\Psi^{\downarrow}+\nabla_R\cdot\left[Pe_s\mathbf{p}\Psi^{\downarrow}-\kappa\nabla_R\Psi^{\downarrow}\right]=-\Psi^{\downarrow}+\frac{1}{2\pi}\left[\int_{-\pi/2}^{\pi/2}\Psi^{\uparrow}\lambda^{\uparrow}d\alpha+\int_{\pi/2}^{3\pi/2}\Psi^{\downarrow}d\alpha\right] \tag{3.43}$$

where α is a dummy integration variable. We define the m-th order polyadic local moments of $\Psi^{\uparrow}$ and $\Psi^{\downarrow}$ as

$$\boldsymbol{\Psi}_{\boldsymbol{k}}^{\uparrow}\ (\theta^{\uparrow},t|\mathbf{R}_0,\theta_0)=\iint_{-\infty}^{\infty}\underbrace{\mathbf{R}\cdots\mathbf{R}}_{k\text{ times}}\,\Psi^{\uparrow}d\mathbf{R}, \tag{3.44}$$

$$\boldsymbol{\Psi}_{\boldsymbol{k}}^{\downarrow}(\theta^{\downarrow},t|\mathbf{R}_0,\theta_0)=\iint_{-\infty}^{\infty}\underbrace{\mathbf{R}\cdots\mathbf{R}}_{k\text{ times}}\,\Psi^{\downarrow}d\mathbf{R} \tag{3.45}$$

for $k=0,1,2...$ The global moments $\mathbf{M_k}$ are obtained as the sum of both contributions $\mathbf{M}_{\mathbf{k}}^{\uparrow}$ and $\mathbf{M}_{\mathbf{k}}^{\downarrow}$

$$\mathbf{M_k}(t)=\mathbf{M}_{\mathbf{k}}^{\uparrow}(t)+\mathbf{M}_{\mathbf{k}}^{\downarrow}(t)=\int_{-\pi/2}^{\pi/2}\boldsymbol{\Psi}_{\boldsymbol{k}}^{\uparrow}\ d\theta^{\uparrow}+\int_{\pi/2}^{3\pi/2}\boldsymbol{\Psi}_{\boldsymbol{k}}^{\downarrow}d\theta^{\downarrow} \tag{3.46}$$

The integro-differential equations satisfied by the long-time 0th-order local moments of $\Psi^{\uparrow}$ and $\Psi^{\downarrow}$ are

$$\lambda^{\uparrow}\Psi_0^{\uparrow^{\infty}}=\frac{1}{2\pi}\left[\int_{-\pi/2}^{\pi/2}\Psi_0^{\uparrow^{\infty}}\lambda^{\uparrow}d\alpha+\int_{\pi/2}^{3\pi/2}\Psi_0^{\downarrow^{\infty}}d\alpha\right] \tag{3.47}$$

$$\Psi_0^{\downarrow^{\infty}}=\frac{1}{2\pi}\left[\int_{-\pi/2}^{\pi/2}\Psi_0^{\uparrow^{\infty}}\lambda^{\uparrow}d\alpha+\int_{\pi/2}^{3\pi/2}\Psi_0^{\downarrow^{\infty}}d\alpha\right] \tag{3.48}$$

subjected to the normalization condition $c_0^{\uparrow\infty} + c_0^{\downarrow\infty} = 1$:

$$\int_{-\pi/2}^{\pi/2} \Psi_0^{\uparrow\infty} d\theta^{\uparrow} + \int_{\pi/2}^{3\pi/2} \Psi_0^{\downarrow\infty} d\theta^{\downarrow} = 1 \tag{3.49}$$

Here, $c_0^{\uparrow\infty}$ and $c_0^{\downarrow\infty}$ represent the fraction of time the swimmer is moving up and down the chemoattractant gradient, respectively. We solve the system of Eqs. (3.47-3.49). After some math, we get

$$\Psi_0^{\uparrow\infty} = \frac{1}{\pi} \frac{c_0^{\downarrow\infty}}{\lambda^{\uparrow}}, \tag{3.50}$$

$$\Psi_0^{\downarrow\infty} = \frac{1}{\pi} c_0^{\downarrow\infty}, \tag{3.51}$$

$$c_0^{\downarrow\infty} = \left[1 + \frac{4 \tan^{-1}\left(\sqrt{\frac{1+\xi Pe_s}{1-\xi Pe_s}} \right)}{\pi \sqrt{1 - \xi^2 Pe_s^2}} \right]^{-1}. \tag{3.52}$$

The long-time mean swimmer velocity can be obtained as

$$\overline{\mathbf{U}} = Pe_s \left[\int_{-\pi/2}^{\pi/2} \mathbf{p} \Psi_0^{\uparrow\infty} d\theta^{\uparrow} + \int_{\pi/2}^{3\pi/2} \mathbf{p} \Psi_0^{\downarrow\infty} d\theta^{\downarrow} \right] \tag{3.53}$$

We insert Eqs. (3.50-3.52) into Eq. (3.53) to determine the swimmer velocity components parallel and perpendicular to the chemical field:

$$\overline{U}_{\parallel} = \frac{Pe_s c_0^{\downarrow\infty}}{\pi} \left[4 \frac{\tan^{-1}\left(\frac{1+\xi Pe_s}{1-\xi Pe_s} \right)}{\xi Pe_s \sqrt{1 - \xi^2 Pe_s^2}} - \frac{\pi}{\xi Pe_s} - 2 \right], \tag{3.54}$$

$$\overline{U}_{\perp} = 0. \tag{3.55}$$

We know that $d\mathbf{M_1}/dt = \overline{\mathbf{U}}$. Temporal integration yields $\mathbf{M_1} = \overline{\mathbf{U}} t + \overline{\mathbf{B}}$, where

$$\mathbf{M_1}(t) = \int_{-\pi/2}^{\pi/2} \boldsymbol{\Psi}_{\mathbf{1}}^{\uparrow} \, d\theta^{\uparrow} + \int_{\pi/2}^{3\pi/2} \boldsymbol{\Psi}_{\mathbf{1}}^{\downarrow} d\theta^{\downarrow} \tag{3.56}$$

We try asymptotic solutions of the form

$$\boldsymbol{\Psi}_{\mathbf{1}}^{\uparrow} = \Psi_0^{\uparrow\infty} \left(\overline{\mathbf{U}} t + \mathbf{B}^{\uparrow} \right) + \mathcal{O}(e^{-t}), \tag{3.57}$$

$$\boldsymbol{\Psi}_{\mathbf{1}}^{\downarrow} = \Psi_0^{\downarrow\infty} \left(\overline{\mathbf{U}} t + \mathbf{B}^{\downarrow} \right) + \mathcal{O}(e^{-t}). \tag{3.58}$$

The value of the constant vector $\overline{\mathbf{B}}$ is:

$$\overline{\mathbf{B}} = \int_{-\pi/2}^{\pi/2} \Psi_0^{\uparrow\infty} \mathbf{B}^{\uparrow} d\theta^{\uparrow} + \int_{\pi/2}^{3\pi/2} \Psi_0^{\downarrow\infty} \mathbf{B}^{\downarrow} d\theta^{\downarrow}, \tag{3.59}$$

and the governing equations satisfied by the vector fields $\mathbf{B}^{\uparrow}$ and $\mathbf{B}^{\downarrow}$ are

$$\frac{1}{2\pi}\left[\int_{-\pi/2}^{\pi/2} \Psi_0^{\uparrow\infty} \mathbf{B}^{\uparrow} \lambda^{\uparrow} d\alpha + \int_{\pi/2}^{3\pi/2} \Psi_0^{\downarrow\infty} \mathbf{B}^{\downarrow} d\alpha\right] = \lambda^{\uparrow} \Psi_0^{\uparrow\infty} \mathbf{B}^{\uparrow} + \left(\overline{\mathbf{U}} - Pe_s \mathbf{p}\right) \Psi_0^{\uparrow\infty} \tag{3.60}$$

$$\frac{1}{2\pi}\left[\int_{-\pi/2}^{\pi/2} \Psi_0^{\uparrow\infty} \mathbf{B}^{\uparrow} \lambda^{\uparrow} d\alpha + \int_{\pi/2}^{3\pi/2} \Psi_0^{\downarrow\infty} \mathbf{B}^{\downarrow} d\alpha\right] = \Psi_0^{\downarrow\infty} \mathbf{B}^{\downarrow} + \left(\overline{\mathbf{U}} - Pe_s \mathbf{p}\right) \Psi_0^{\downarrow\infty} \tag{3.61}$$

We plug Eqs. (3.50)-(3.52) into Eqs. (3.60) and (3.61). After simplification, we get

$$\begin{aligned} \mathbf{B}^{\uparrow} =& \frac{Pe_s \mathbf{p} - \overline{\mathbf{U}}}{1 - \xi Pe_s \cos\theta^{\uparrow}} + A_3, \\ \mathbf{B}^{\downarrow} =& Pe_s \mathbf{p} - \overline{\mathbf{U}} + A_3 \end{aligned} \tag{3.62}$$

where A_3 is an unknown constant with value

$$A_3 = \frac{1}{2\pi}\left[\int_{-\pi/2}^{\pi/2} \mathbf{B}^{\uparrow} d\theta^{\uparrow} + \int_{\pi/2}^{3\pi/2} \mathbf{B}^{\downarrow} d\theta^{\downarrow}\right]. \tag{3.63}$$

In order to determine the mean swimmer dispersivity dyadic, we can set arbitrarily $A_3 = 0$. We prove later on that this assumption is valid. We calculate the components of the constant vector $\overline{\mathbf{B}}$. We get

$$\begin{aligned} \overline{B}_{\parallel} =& \frac{4c_0^{\downarrow\infty}}{\pi}\left(\xi Pe_s^2 - \overline{U}_{\parallel}\right) \frac{\tan^{-1}\left(\frac{1+\xi Pe_s}{\sqrt{1-\xi^2 Pe_s^2}}\right)}{\left(1-\xi^2 Pe_s^2\right)^{3/2}} + \frac{2\xi^2 Pe_s^3 c_0^{\downarrow\infty}}{\pi(1-\xi^2 Pe_s^2)} \\ & - \frac{\overline{U}_{\parallel} c_0^{\downarrow\infty}}{\pi}\left(\frac{2\xi Pe_s}{1-\xi^2 Pe_s^2} + \pi\right) \end{aligned} \tag{3.64}$$

$$\overline{B}_{\perp} = 0. \tag{3.65}$$

The long-time mean swimmer dispersivity dyadic $\overline{\mathbf{D}}$ is expressed as

$$\overline{\mathbf{D}} = \kappa^2\mathbf{I} + \frac{Pe_s}{2}\left[\int_{-\pi/2}^{\pi/2} \Psi_0^{\uparrow\infty}\left(\mathbf{pB}^{\uparrow} + \mathbf{B}^{\uparrow}\mathbf{p}\right) d\theta^{\uparrow} + \int_{\pi/2}^{3\pi/2} \Psi_0^{\downarrow\infty}\left(\mathbf{pB}^{\downarrow} + \mathbf{B}^{\downarrow}\mathbf{p}\right) d\theta^{\uparrow}\right] - \frac{1}{2}\left(\overline{\mathbf{U}}\,\overline{\mathbf{B}} + \overline{\mathbf{B}}\,\overline{\mathbf{U}}\right) \tag{3.66}$$

The first term corresponds to pure Brownian dispersion and the remaining terms correspond to active dispersion due to self-propulsion. Let $\mathbf{B} = \mathbf{b} + \mathbf{C}$, where $\mathbf{C}$ is a constant vector. We can easily check that the expression for the dispersivity does not depend on the vector $\mathbf{C}$ (not shown here). Therefore, we can always add a constant $\mathbf{C}$ to the fluctuating vector $\mathbf{B}$ such that $A_3 = 0$, which is the assumption we made in our derivation. Finally, we compute the non-zero components of $\overline{\mathbf{D}}$. After performing the integrals in Eq. (3.66) we get:

$$\overline{D}_{\parallel\parallel} = \kappa^2 + \frac{4c_0^{\downarrow\infty}}{\pi}\frac{Pe_s^2(2-\xi\overline{U}_{\parallel}) - 1/\xi^2}{(1-\xi^2Pe_s^2)^{3/2}} \times \tan^{-1}\left(\frac{1+Pe_s\xi}{\sqrt{1-Pe_s^2\xi^2}}\right) - \frac{2\xi^2Pe_s^3c_0^{\downarrow\infty}\overline{U}_{\parallel}}{\pi\left(1-\xi^2Pe_s^2\right)} + c_0^{\downarrow\infty}\left[\frac{1}{\xi^2} + \frac{Pe_s^2}{2} + \frac{2Pe_s}{\pi\xi(1-\xi^2Pe_s^2)}\right] - \overline{U}_{\parallel}\overline{B}_{\parallel} \tag{3.67}$$

$$\overline{D}_{\perp\perp} = \kappa^2 + \frac{c_0^{\downarrow\infty}}{\pi\xi^2}\left[\frac{Pe_s^2\xi^2\pi}{2} - 2Pe_s\xi - \pi + \frac{4}{\sqrt{1-Pe_s^2\xi^2}}\tan^{-1}\left(\frac{1+Pe_s\xi}{\sqrt{1-Pe_s^2\xi^2}}\right)\right] \tag{3.68}$$

Low chemotactic strength asymptotic limits ($\xi \to 0$)

We take the weak chemotactic strength asymptotic limits $\xi \to 0$ of Eqs. (3.29) and (3.54) and find the asymptotic behavior of the mean bacterial velocity vector $\overline{\mathbf{U}}$ for microorganisms undergoing positive-negative chemotaxis

$$\overline{U}_{\parallel} = \frac{Pe_s^2}{2}\xi + \frac{Pe_s^4}{8}\xi^3 + \mathcal{O}(\xi^5), \tag{3.69}$$

and for those undergoing just positive chemotaxis

$$\overline{U}_{\parallel} = \frac{Pe_s^2}{4}\xi + \frac{5Pe_s^3}{12\pi}\xi^2 + \mathcal{O}(\xi^3). \tag{3.70}$$

We additionally calculate the weak chemotactic asymptotic behavior of the mean bacterial dispersivity dyadic $\overline{\mathbf{D}}$. We take the corresponding limits of Eqs. (3.39), (3.67) and (3.68).

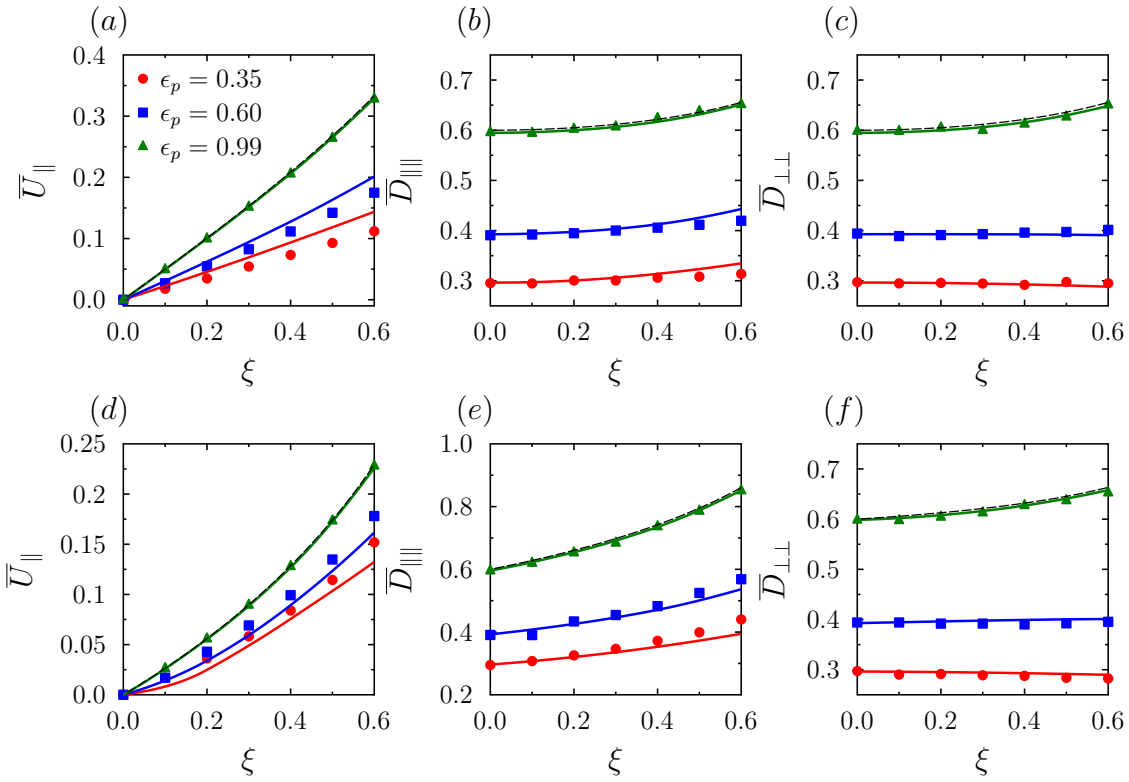

Figure 3.3: Dependence of the long-time mean particle velocity component $\overline{U}_{\parallel}$ and of the dispersivity dyadic components $\overline{D}_{\parallel\parallel}$ and $\overline{D}_{\perp\perp}$ on the chemotactic field strength ξ, for different material porosities ϵ_p, and for microorganisms undergoing positive-negative chemotaxis (*a-c*) and only positive chemotaxis (*d-f*). Parameter values: $Pe_s = 1$, $\kappa^2 = 0.1$ and $\tau = 0$. Black dashed lines correspond to the exact analytical solutions obtained in S.M. for $\epsilon_p = 1$.

After some tedious math, for positive-negative chemotactic bacteria we get

$$\overline{D}_{\parallel\parallel} = \overline{D}_{\perp\perp} = \kappa^2 + \frac{Pe_s^2}{2} + \frac{Pe_s^4}{8}\xi^2 + \mathcal{O}(\xi^4), \tag{3.71}$$

and for positive chemotactic bacteria

$$\overline{D}_{\parallel\parallel} = \kappa^2 + \frac{Pe_s^2}{2} + \frac{5Pe_s^3}{6\pi}\xi + \left(\frac{1}{4} - \frac{5}{6\pi^2}\right) Pe_s^4\xi^2 + \mathcal{O}(\xi^3), \tag{3.72}$$

$$\overline{D}_{\perp\perp} = \kappa^2 + \frac{Pe_s^2}{2} + \frac{Pe_s^3}{6\pi}\xi + \frac{3\pi^2 - 8}{48\pi^2} Pe_s^4\xi^2 + \mathcal{O}(\xi^3). \tag{3.73}$$

Results are summarized in Fig. (3.2).

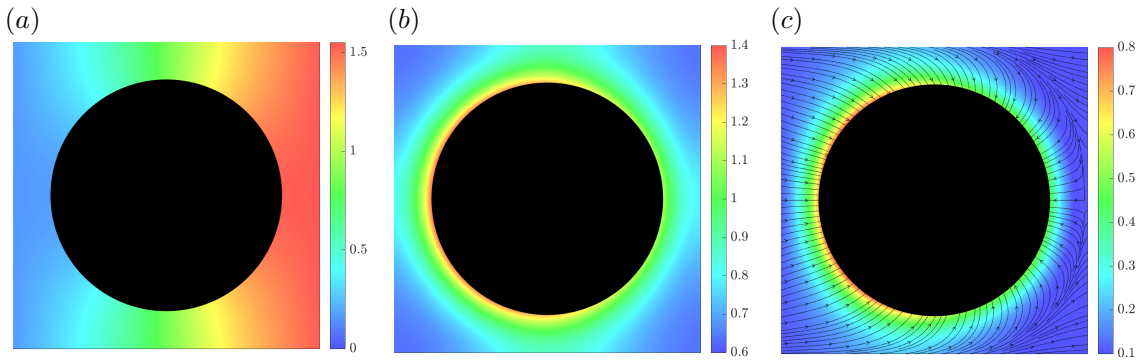

Figure 3.4: Distribution profiles under the application of a horizontal positive chemical gradient. (a) Chemical field, (b) bacterial concentration c_0^∞ and (c) bacterial polarization $\mathbf{m_0^\infty}$. Parameter values: $Pe_s = 1$, $\kappa^2 = 0.1$, $\tau = 0$, $\xi = 0.6$ and $\epsilon_p = 0.60$.

3.4 Numerical Results

Regardless of medium porosity, the particle mean transport velocity in the direction of increasing chemoattractant is higher for those cells that experience positive-negative chemotaxis than for those that experience solely positive chemotaxis. Unlike cells that lack negative chemotaxis, which reorient as if the chemical field were not present, positive-negative chemotactic cells reorient at a higher frequency when they are swimming in the wrong direction (down the chemoattractant gradient/up the chemorepellent gradient), which manifests in the enhancement of the biased transport towards regions of high chemoattractant concentration. Also, because positive-negative chemotactic particles have a stronger preferred swimming direction than strains that lack negative chemotaxis, they do disperse less along the chemical field direction. They also disperse less along the direction perpendicular to the chemoattractant field, but the difference in dispersion between both strains is minimal. Not physical explanation has been found for this phenomenon.

The numerical results that explore the dependence of the medium porosity on the coefficients $\overline{\mathbf{U}}$ and $\overline{\mathbf{D}}$ are shown in Fig. (3.3). The strength of the chemical field enhances $\overline{U}_{\parallel}$ and $\overline{D}_{\parallel\parallel}$ regardless of the material porosity, whereas $\overline{D}_{\perp\perp}$ increases with ξ for high porosity mediums and decreases for low porosity mediums. Fig. (3.4) shows the chemical field as well as bacterial concentration and polarization fields around the obstacles when a horizontal chemical field is applied. Because of the no-flux condition on the obstacle boundaries and the drift towards favorable conditions, particles tend to accumulate more in front of the obstacle than in the rear part. This imbalance creates a net active force on the obstacles in the direction of increasing chemoattractant (decreasing chemorepellent) concentration. Particles

get polarized longer along the chemoattarctant direction, whose maximum magnitude seems to occur at the obstacle walls at $\sim 135^o$ and $\sim 225^o$ with respect to the horizontal direction, as observed in Fig. (3.4c).

3.5 Acknowledgements

Chapter 3, in part, is a manuscript in preparation; authored by R. Alonso-Matilla and D. Saintillan, "Effect of chemical fields on the transport and spreading of active particles in periodic porous media". The dissertation author is the primary author of this work.

Chapter 4

On the distribution and swim pressure of run-and-tumble particles in confinement

4.1 Introduction

The propensity of confined self-propelled particles to accumulate at boundaries is a trademark of active matter and has been reported in many experiments on bacterial suspensions [41, 118, 119] as well as simulations based on various models [120–122]. Several disparate mechanisms have been proposed in explanation, including wall hydrodynamic interactions [41] and scattering due to collisions with the walls [123], though recent theoretical efforts have shown that the mere interplay of self-propulsion, stochastic processes and confinement is sufficient to explain accumulation [51, 124, 125]. With few exceptions, however, these models have necessitated particle diffusion, which in reality is nearly negligible in bacterial suspensions where stochasticity in the dynamics takes instead the form of run-and-tumble random walks [44].

Understanding the distribution of active particles in confinement is especially critical for determining the mechanical force per unit area exerted by the suspension on the boundaries, or so-called 'swim pressure'. This novel concept, which has received much scrutiny recently, is similar to the ideal pressure in a gas due to the random motion of the gas molecules or to the osmotic pressure present in a colloidal solution. It describes the force per unit area that the particles exert on confining osmotic boundaries. Action-reaction implies that the swim pressure can also be defined as the force per unit area that must be applied on the containing walls to keep self-propelled particles confined. Models based on the virial

theorem [126–128] and on direct calculations of the wall mechanical pressure [129] in infinite or semi-infinite collections of spherical swimmers have all arrived at a simple ideal-gas law Π_i for the swim pressure in the limit of infinite dilution:

$$\Pi_i = n\zeta D_t = n\zeta \frac{v_0^2}{3\lambda}, \tag{4.1}$$

where n is the mean number density, ζ is the viscous drag coefficient of a particle and $D_t = v_0^2/3\lambda$ is the long-time translational diffusivity of an unconfined run-and-tumble swimmer expressed in terms of its speed v_0 and mean tumbling rate λ [44]. Equation (4.1) and its extension to finite concentrations have proven useful to explain motility-induced phase separation in suspensions of self-propelled colloids [126, 130], though its general validity as a thermodynamic equation of state for the pressure of active matter remains controversial [131–133] and appears to be limited to unconfined spherical particles [127, 129, 134]. A recent study [135] addressed the contribution of hydrodynamic interactions on the pressure of an active suspension on a non-osmotic boundary, where they found an increase in the swim pressure due to hydrodynamic effects.

In this work, we analyze the simple case of a dilute suspension of athermal run-and-tumble spherical swimmers confined between two parallel flat plates. Because the particles are athermal, they spend a finite time touching the wall. In order to quantify this effect, we propose in § 4.2 a kinetic model based on two probability density functions describing the spatial and orientational distribution of the particles inside the gap and at the walls, which are coupled via flux conditions and only account for the effects of swimming and orientation decorrelation by tumbling. Further, our model implicitly captures hard-wall steric interactions without resorting to a soft potential to describe wall collisions as in previous theories [129, 134]. A semi-analytical solution method is outlined in § 4.3, which provides the full probability density functions and allows for a direct calculation of the mechanical swim pressure exerted on the walls in terms of the polarization of the surface distributions. Results for the distributions and swim pressure are presented in § 4.4, where they are shown to compare very favorably with Monte-Carlo simulations. The swim pressure in the system approaches the previously proposed ideal-gas behavior in wide channels but, keeping the mean number density of particles in the system, it is found to decrease in narrow channels as a result of confinement.

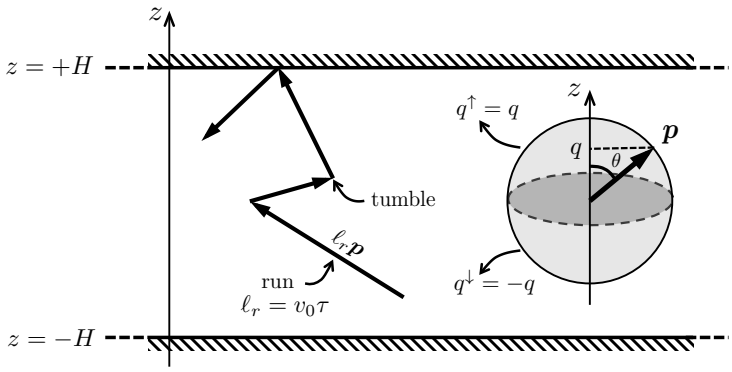

Figure 4.1: Problem definition: run-and-tumble particles are confined between two flat plates separated by $2H$. The distribution of particles is a function of z and $q = \mathbf{p} \cdot \hat{\boldsymbol{z}} = \cos\theta \in (-1, 1)$. Orientations pointing towards the top and bottom walls are parametrized by $q^\uparrow = q$ and $q^\downarrow = -q$, respectively, both defined in $(0, 1)$.

4.2 Problem definition and theoretical model

4.2.1 Problem formulation

As a minimal model for an active suspension in confinement, we consider a dilute collection of self-propelled spherical particles confined between two infinite parallel plates separated by a distance $2H$ (see figure 4.1). The swimmers are non-Brownian and simply perform a run-and-tumble random walk: straight runs of duration τ at constant velocity v_0 along the unit director $\mathbf{p}$ alternate with instantaneous tumbling events causing random and uncorrelated reorientations of $\mathbf{p}$. The time τ between tumbles is an exponentially distributed random variate with mean λ^{-1}, where the tumbling rate λ is assumed to be independent of position and orientation. To elucidate the interplay between run-and-tumble dynamics and confinement, we focus on the dilute limit and entirely neglect interparticle interactions. Particle-wall interactions are purely steric: as a swimmer meets one of the two surfaces, the normal component of its swimming motion is cancelled by a hard-core repulsive force causing it to stay at and push against the wall until a subsequent tumbling event reorients it into the bulk. Tumbling events occurring at the walls can lead to reorientation into the wall or into the bulk, so that a particle at a surface may need to undergo more than one tumble before it is able to escape.

There are only two length scales in the problem: the mean run length $\ell_r = v_0\lambda^{-1}$ and the channel width $2H$. We define their ratio as the Péclet number $Pe = \ell_r/2H =$

$v_0/(2\lambda H)$, where the two limits $Pe \to 0$ and $Pe \to \infty$ describe weak and strong confinement, respectively. Pe also represents a ratio of time scales: the characteristic time for a particle to travel from wall to wall over the average particle reorientation time. Due to the symmetry of the problem, the distribution of particles in the channel only depends on two degrees of freedom: the wall-normal coordinate $z \in (-H, H)$ and the wall-normal component of the particle director $q = \mathbf{p} \cdot \hat{\mathbf{z}} = \cos\theta \in (-1, 1)$. It is convenient to distinguish particles pointing towards the top and bottom walls, and to this end we divide the unit sphere of orientations into two hemispheres and define two distinct orientation coordinates $q^{\uparrow} = q \in (0, 1)$ and $q^{\downarrow} = -q \in (0, 1)$ for particles pointing up or down, respectively, as depicted in figure 4.1.

The distribution of particles in the channel is then fully described by a bulk probability density function $P(z, q)$ and by two surface probability density functions $P_s^{\uparrow}(q^{\uparrow})$ and $P_s^{\downarrow}(q^{\downarrow})$, which are only defined over half of the orientations since the surfaces cannot sustain a concentration of particles pointing towards the bulk. By symmetry, we expect

$$P(z, -q) = P(-z, q), \quad P(z, q^{\uparrow}) = P(-z, q^{\downarrow}) \quad \text{and} \quad P_s^{\uparrow}(q^{\uparrow}) = P_s^{\downarrow}(q^{\downarrow}) \tag{4.2}$$

for $q^{\uparrow} = q^{\downarrow}$. Next, we describe the coupled bulk/surface conservation equations satisfied by these distributions, together with the appropriate boundary conditions.

4.2.2 Bulk conservation equation

Assuming that the number of tumbling events follows a Poisson distribution, the steady bulk probability density function $P(z, q)$ satisfies the conservation equation

$$v_0\, q\, \frac{\partial}{\partial z} P\,(z, q) = -\lambda\, P\,(z, q) + \frac{1}{2} \int_{-1}^{1} \lambda\, P\,(z, q')\, \mathrm{d}q'. \tag{4.3}$$

The left-hand side describes transport along z due to self-propulsion. Run-and-tumble dynamics is captured by the right-hand side, where the first term accounts for depletion due to swimmers tumbling away from orientation q, and the second term for restoration due to swimmers tumbling from orientations q' into q. It is also useful to define the orientational moments of order j of the bulk probability density function on the full sphere and on the

upper/lower hemispheres of orientations as

$$M_j(z) = \int_{-1}^{1} q^j \, P\,(z,q)\, \mathrm{d}q \quad \text{and} \quad M_j^{\uparrow\downarrow}(z) = \int_0^1 (q^{\uparrow\downarrow})^j \, P(z,q^{\uparrow\downarrow})\, \mathrm{d}q^{\uparrow\downarrow}, \tag{4.4}$$

and we note that the zeroth, first and second moments correspond to the concentration, polarization, and nematic alignment fields:

$$c(z) = M_0(z), \qquad m(z) = M_1(z), \qquad S(z) = M_2(z), \tag{4.5}$$

$$c^{\uparrow\downarrow}(z) = M_0^{\uparrow\downarrow}(z), \qquad m^{\uparrow\downarrow}(z) = M_1^{\uparrow\downarrow}(z), \qquad S^{\uparrow\downarrow}(z) = M_2^{\uparrow\downarrow}(z). \tag{4.6}$$

By symmetry, it is straightforward to see that full moments of even order are even functions of z whereas those of odd order are odd functions. With these notations, the bulk conservation equation (4.3) simplifies to

$$\ell_r \, q \, \frac{\partial}{\partial z} P\,(z,q) = -P(z,q) + \tfrac{1}{2} c(z). \tag{4.7}$$

We take the zeroth and first orientational moments of Eq. (4.7)

$$\frac{dm}{dz} = 0, \quad \frac{dS}{dz} = 0 \tag{4.8}$$

and apply symmetry conditions to show that the polarization vanishes and the nematic alignment is uniform across the channel:

$$m(z) = 0 \quad \text{and} \quad S(z) = S_0 \quad \forall z \in (-H, H), \tag{4.9}$$

where S_0 is a constant independent of z.

4.2.3 Surface conservation equations

Similarly, conservation equations for the steady surface probability density functions at the walls can be written. We first define the surface concentration and polarization as

$$c_s = \int_0^1 P_s^{\uparrow\downarrow}(q^{\uparrow\downarrow})\, \mathrm{d}q^{\uparrow\downarrow} \quad \text{and} \quad m_s = \int_0^1 q^{\uparrow\downarrow} \, P_s^{\uparrow\downarrow}(q^{\uparrow\downarrow})\, \mathrm{d}q^{\uparrow\downarrow}, \tag{4.10}$$

and note that the values of c_s and m_s are the same at both walls. With these notations, the conservation equation at the upper wall ($z = +H$) reads

$$v_0\, q^{\uparrow}\, P(H, q^{\uparrow}) = \lambda \left[P_s^{\uparrow}(q^{\uparrow}) - \tfrac{1}{2} c_s \right], \tag{4.11}$$

and a similar equation holds at $z = -H$. The right-hand side in Eq. (4.11) describes tumbling processes at the wall. The left-hand side, on the other hand, captures the flux of particles that enter the surface from the bulk by self-propulsion, and is therefore proportional to the bulk probability density function $P(H, q^{\uparrow})$ next to the wall. Evaluating the zeroth and first moments of Eq. (4.11) yields simple relations between c_s and m_s and the values of the bulk moments in the vicinity of the wall:

$$c_s = 2\ell_r m^{\uparrow}(H), \qquad m_s - \tfrac{1}{4} c_s = \ell_r S^{\uparrow}(H). \tag{4.12a, b}$$

4.2.4 Boundary condition and particle number conservation

Equation (4.11) can be interpreted as a boundary condition for orientations pointing into the wall. For orientations pointing away from the wall, the swimming flux away from the wall must be balanced by tumbling of particles from the surface towards the bulk. Simply stated, particles on the surface that tumble to an orientation pointing into the bulk are transported away by self-propulsion. This leads to the additional condition

$$v_0\, q^{\downarrow}\, P(H, q^{\downarrow}) = \tfrac{1}{2} \lambda\, c_s \qquad \text{or} \qquad \ell_r\, q^{\downarrow}\, P(H, q^{\downarrow}) = \tfrac{1}{2} c_s. \tag{4.13}$$

As c_s is constant and finite, this condition suggests divergence and discontinuity of the bulk probability density function for orientations parallel to the wall ($q^{\downarrow} \to 0$), as will indeed be verified in our analytical solution and stochastic simulations. Taking the zeroth and first moments of Eq. (4.13) provides the two additional relations

$$c_s = 2\ell_r m^{\downarrow}(H), \qquad c_s = 4\ell_r S^{\downarrow}(H). \tag{4.14a, b}$$

Finally, the above system of equations for the bulk and surface distributions is supplemented by a constraint on the total number of particles in the channel:

$$2\,c_s + \int_{-H}^{H} c(z)\,\mathrm{d}z = N, \tag{4.15}$$

where N is the particle number in a vertical slice of unit horizontal cross-section.

4.3 Method of solution and swim pressure calculation

4.3.1 Integral equation for the moments

We now outline a solution method for the system described in §4.2.1. As a first step, we derive an integral equation relating the bulk orientational moments to the concentration field. The bulk concentration equation (4.7) can be viewed as a linear inhomogeneous ordinary differential equation for $P(z,q)$ where q is a parameter. We solve it by the method of variation of constants, treating orientations $q^{\uparrow}$ and $q^{\downarrow}$ separately. From the bulk conservation equation (4.7):

$$\ell_r\, q^{\uparrow}\,\frac{\partial}{\partial z}P^{\uparrow}\left(z,q^{\uparrow}\right) = -P^{\uparrow}(z,q^{\uparrow}) + \tfrac{1}{2}c(z), \qquad \ell_r\, q^{\downarrow}\,\frac{\partial}{\partial z}P^{\downarrow}\left(z,q^{\downarrow}\right) = -P^{\downarrow}(z,q^{\downarrow}) + \tfrac{1}{2}c(z) \tag{4.16}$$

Note that $c(z) = c^{\uparrow}(z) + c^{\downarrow}(z) = \int_0^1 \psi(z,q^{\uparrow})dq + \int_{-1}^0 \psi(z,q^{\downarrow})dq$. From Eq. (4.11), we obtain the surface conservation equations

$$\ell_r\, q^{\uparrow}\, P(H,q^{\uparrow}) = -P_s^{\uparrow}(q^{\uparrow}) + \tfrac{1}{2}c_s, \qquad \ell_r\, q^{\downarrow}\, P(H,q^{\downarrow}) = P_s^{\downarrow}(q^{\downarrow}) - \tfrac{1}{2}c_s \tag{4.17}$$

and from Eq. (4.13) the boundary conditions:

$$P(-H,q^{\uparrow}) = \frac{c_s}{2\ell_r q^{\uparrow}}, \qquad P(H,q^{\downarrow}) = -\frac{c_s}{2\ell_r q^{\downarrow}}. \tag{4.18}$$

We apply the method of variation of parameters to solve Eq. (4.16). After applying the boundary condition (4.18), we obtain a general expression for the bulk density function:

$$P(z,q^{\uparrow\downarrow}) = \frac{c_s}{2\ell_r\, q^{\uparrow\downarrow}}\exp\left[-\frac{(H\pm z)}{\ell_r\, q^{\uparrow\downarrow}}\right] \pm \int_{\mp H}^{z} \frac{c(z')}{2\ell_r\, q^{\uparrow\downarrow}}\exp\left[\mp\frac{(z-z')}{\ell_r\, q^{\uparrow\downarrow}}\right]\,\mathrm{d}z'. \tag{4.19}$$

Note that the bulk and surface concentrations $c(z)$ and c_s both appear on the right-hand side and are still unknown. However, Eq. (4.19) shows that their knowledge entirely specifies the bulk distribution $P(z,q)$. The bulk moments of order j on both hemispheres of orientations

are immediately obtained by integration:

$$M_j^{\uparrow\downarrow}(z) = \frac{c_s}{2\ell_r}\mathcal{E}_{j+1}\left[\frac{H \pm z}{\ell_r}\right] \pm \int_{\mp H}^{z} \frac{c(z')}{2\ell_r}\,\mathcal{E}_{j+1}\left[\pm\frac{(z-z')}{\ell_r}\right]\,\mathrm{d}z', \tag{4.20}$$

where $\mathcal{E}_j$ is the exponential integral function defined as

$$\mathcal{E}_j(z) = \int_0^1 u^{j-2}\exp\left(-\frac{z}{u}\right)\,\mathrm{d}u. \tag{4.21}$$

Finally, the moment of order j on the full sphere of orientations can be shown to be

$$M_j(z) = \frac{c_s}{2\ell_r}\left(\mathcal{E}_{j+1}\left[\frac{H+z}{\ell_r}\right] + \mathcal{E}_{j+1}\left[\frac{H-z}{\ell_r}\right]\right) + \int_{-H}^{H}\frac{c(z')}{2\ell_r}\mathcal{E}_{j+1}\left[\left|\frac{z-z'}{\ell_r}\right|\right]\,\mathrm{d}z'. \tag{4.22}$$

4.3.2 Concentration field and solution procedure

Setting $j = 0$ in Eq. (4.22) immediately provides an integral equation for the yet unknown concentration profile:

$$c(z) = \frac{c_s}{2\ell_r}\left(\mathcal{E}_1\left[\frac{H+z}{\ell_r}\right] + \mathcal{E}_1\left[\frac{H-z}{\ell_r}\right]\right) + \int_{-H}^{H}\frac{c(z')}{2\ell_r}\mathcal{E}_1\left[\left|\frac{z-z'}{\ell_r}\right|\right]\,\mathrm{d}z'. \tag{4.23}$$

Dividing through by c_s, we obtain an equation for $c(z)/c_s$ that can be solved numerically. For finite ℓ_r, we find that an approximate solution is easily obtained iteratively by casting Eq. (4.23) in the form $c_{k+1}(z)/c_s = f[c_k(z)/c_s]$, starting with an initial guess which we take to be $c_0(z) = 0$. In strong confinement ($Pe \gtrsim 10$), the solution converges in $O(20)$ iterations, though more iterations are required in wider channels.

To complete the solution for the concentration field, the value of the surface concentration c_s must be calculated. Having previously obtained $c(z)/c_s$, it is easily evaluated by recasting the constraint (4.15) as

$$c_s = N\left[2 + \int_{-H}^{H}\frac{c(z)}{c_s}\,\mathrm{d}z\right]^{-1}. \tag{4.24}$$

Knowledge of $c(z)$ and c_s then directly provides all the remaining variables. The bulk probability density function is given by Eq. (4.19), while the bulk partial and full moments can be calculated using Eqs. (4.20) and (4.22). Finally, the surface orientation distribution is provided by Eq. (4.11) and the surface polarization by Eq. (4.12*b*). Solutions obtained by

this method are presented in § 4.4, where excellent agreement with results from Monte-Carlo simulations will be shown.

4.3.3 Swim pressure calculation

The above formulation provides a direct way of estimating the swim pressure in the system, which is simply the force per unit area exerted by the particles at the walls as they push on the surface. Specifically, the normal component of the motion of each particle at the upper wall is resisted by a force $\zeta v_0 q^{\uparrow}$, where ζ is the viscous drag coefficient of one particle [126]. Knowing the surface probability density function $P_s^{\uparrow}$, an expression for the swim pressure is then easily found as

$$\Pi_s = \int_0^1 \zeta v_0 q^{\uparrow} P_s^{\uparrow}(q^{\uparrow})\, \mathrm{d}q^{\uparrow} = \zeta v_0 m_s, \tag{4.25}$$

where m_s is the surface polarization. Combining Eqs. (4.12b) and (4.14b) to solve for m_s yields a simple relation between the swim pressure and the second moment S_0 of the bulk distribution function:

$$\Pi_s = \zeta v_0 \ell_r \left[S^{\uparrow}(H) + S^{\downarrow}(H)\right] = \zeta \frac{v_0^2}{\lambda} S(H) = \zeta \frac{v_0^2}{\lambda} S_0. \tag{4.26}$$

A similar result was obtained by [129]. In bulk unconfined systems, previous models have led to the ideal-gas pressure Π_i of Eq. (4.1), which contains no information on particle orientations due to isotropy but follows the same scaling as Eq. (4.26). To compare both predictions, we define a dimensionless pressure as the ratio of Eqs. (4.26) and (4.1):

$$\mathcal{P} = \frac{\Pi_s}{\Pi_i} = \frac{3 m_s}{n \ell_r} = \frac{3 S_0}{n}, \tag{4.27}$$

where $n = N/2H$ is the mean number density in our system. $\mathcal{P} - 1$ quantifies the departure from the ideal-gas swim pressure. In an infinitely wide channel ($Pe \to 0$), the bulk distribution at the centerline is expected to be isotropic, implying $S_0 = n/3$ and therefore $\mathcal{P} \to 1$. This will be confirmed in our numerical results in § 4.4, where we also show that $\mathcal{P}$ deviates from 1 when $Pe > 0$ as a result of confinement.

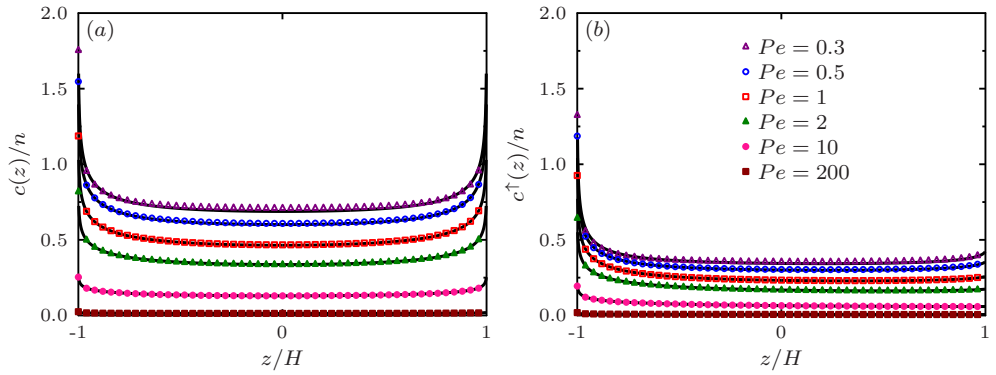

Figure 4.2: Concentration profiles across the channel for various values of $Pe = \ell_r/2H$: (a) full concentration $c(z)$, and (b) partial 'up' concentration $c^{\uparrow}(z)$. Solid lines show the semi-analytical solution of §4.3, and symbols are Monte-Carlo simulation results.

4.4 Results and comparison to simulations

4.4.1 Simulation method

To validate our model, we also perform Markov-chain Monte-Carlo simulations of run-and-tumble swimmers between two hard walls. During a run of duration τ, the swimmer trajectory simply evolves as $\mathbf{x}(t + \Delta t) = \mathbf{x}(t) + v_0\mathbf{p}\,\Delta t$ where Δt is a short time step. Each run is then followed by a tumbling event, where the new orientation vector $\mathbf{p}$ is picked randomly on the unit sphere. The time τ between two consecutive tumbles is drawn from an exponential distribution with cumulative distribution function $F(\tau) = 1 - \exp[-\lambda\tau]$. When a swimmer meets a wall, it remains there and continues to tumble until it reorients towards the bulk and swims away. Time-averaged bulk and surface probability density functions were extracted from orientational and spatial histograms, and convergence was checked with respect to Δt and to the duration of the simulation.

4.4.2 Theoretical and numerical results

Solutions for the bulk concentration profile are depicted in figure 4.2, where both the full concentration $c(z)$ and the partial 'up' concentration $c^{\uparrow}(z)$ are plotted for various values of the Péclet number, which measures the degree of confinement. The full concentration profiles in figure 4.2(a) show significant accumulation at the walls, with wall boundary layers whose thickness scales with ℓ_r. An interesting and unique feature of non-interacting and non-aligning spherical run-and-tumble particles is that accumulation occurs in the absence

of polarization, and $m(z)$ is found to be strictly zero throughout the channel as already derived in Eq. (4.9). A non-zero polarization would indeed lead to a net flux of particles in the wall-normal direction, which cannot happen in a confined athermal system, unlike in Brownian suspensions where this flux can be balanced by diffusion [51]. The profiles also show the presence of a singularity in $c(z)$ at the walls, which is a direct consequence of the boundary condition (4.13) and is also obvious from the solution (4.23) where $\mathcal{E}_1(0)$ diverges. Concentration singularities were also predicted by [125], though their model did not capture orientation distributions. As confinement becomes significant and Pe increases, the bulk concentration decreases throughout the channel to reach nearly zero at $Pe = 200$, indicating that strongly confined particles spend most of their time at the boundaries. Excellent quantitative agreement is obtained between theory and Monte-Carlo simulations.

Figure 4.2(b) also shows the partial 'up' concentration obtained by only counting particles pointing towards the top wall. The asymmetry of the profiles and the singularity at the bottom wall indicates that on average there are more particles pointing away from the wall than towards it inside the wall accumulation layers. However, in order to satisfy no net polarization in the bulk, this implies that those particles pointing towards the wall are more strongly polarized than those pointing away. This point is confirmed in figure 4.3(a–b), showing the orientation distributions in the bulk in the vicinity of the top wall for orientations pointing away from and towards the wall. Figure 4.3(a) confirms the divergence of the bulk probability density in the neighborhood of orientations parallel to the wall ($q^{\downarrow} \to 0$) as expected from boundary condition (4.13), which is also captured by the simulations. The presence of this discontinuity can be rationalized as follows: particles that leave the surface at an orientation $q^{\downarrow} \gtrsim 0$ swim nearly parallel to the surface and therefore remain there much longer than particles leaving in other orientations. The distribution of particles pointing towards the wall in figure 4.3(b) shows no such singularity, but exhibits a weak finite peak at a critical value of $q^{\uparrow}$ for an intermediate range of Péclet numbers between 5 and 50, whose physical origin remains unclear. The orientation distribution $P_s^{\uparrow}(q^{\uparrow})$ of particles on the top wall is shown in figure 4.3(c) and shows a preferential alignment normal to the wall rather than parallel to it. However, this distribution becomes nearly isotropic under very strong confinement ($Pe = 1000$), for reasons that we elucidate below.

Taking moments of $P_s^{\uparrow}(q^{\uparrow})$ provides the surface concentration c_s and surface polarization m_s, which are plotted versus Péclet number in figure 4.4(a–b). Both quantities increase with increasing confinement, but asymptote as $Pe \to \infty$. The asymptote for c_s is $N/2$,

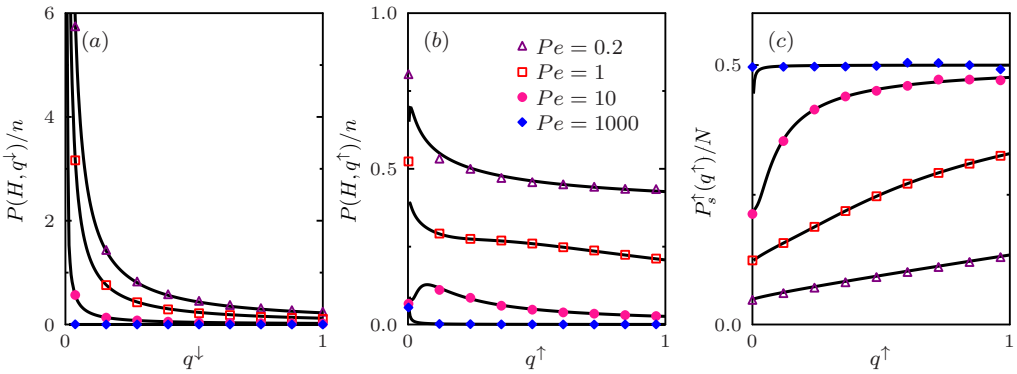

Figure 4.3: Bulk probability density at the top wall for (a) orientations pointing away from the wall and (b) orientations pointing towards it. (c) Surface probability density at the top wall as a function of $q^{\uparrow}$. Solid lines show the semi-analytical solution of § 4.4.1, and symbols are Monte-Carlo simulation results.

meaning that in very narrow channels the particles spend all their time at the boundaries; indeed, the time $2H/v_0$ it takes them to cross the gap is infinitesimal compared to the mean run time λ^{-1}. This is also consistent with the decrease in the bulk concentration seen in figure 4.2(a). In this limit, particles tumbling away from one wall reach the other wall nearly instantaneously, leading to an isotropic surface orientation distribution in agreement with figure 4.3(c), hence the asymptote of $N/4$ for the wall polarization.

Lastly, the dependence of the dimensionless swim pressure $\mathcal{P}$ on the degree of confinement is illustrated in figure 4.4(c). In the limit of weak confinement ($H \gg \ell_r$ or $Pe \to 0$), the swim pressure is seen to tend to the ideal-gas law of Eq. (4.1) in both our model and simulations: $\mathcal{P} \to 1$ or $\Pi_s \to \Pi_i$. This corresponds to the limit of a single wall where the gap width $2H$ plays no role, and validates the results of previous studies in infinite or semi-infinite systems for which the expression for Π_i was first derived [126, 129]. Confinement, however, causes a decrease in the swim pressure, which in fact tends to zero for fixed n in very narrow gaps. The high-Pe asymptote for m_s describes the limiting behavior:

$$\mathcal{P} \to \frac{3}{4} Pe^{-1}, \quad \text{i.e.} \quad \Pi_s \to \frac{3}{4} Pe^{-1} \Pi_i = \frac{nH\zeta v_0}{2} = \frac{N\zeta v_0}{4} \tag{4.28}$$

as $Pe \to \infty$ (or $H \to 0$), which corresponds to $N/2$ particles pushing with an average force of $\zeta v_0/2$ against each wall. The decrease in pressure and the details of the asymptote agree with the previous two-dimensional results of [127], who also verified them in numerical simulations of self-propelled disks. They are also consistent with the study of [131], who

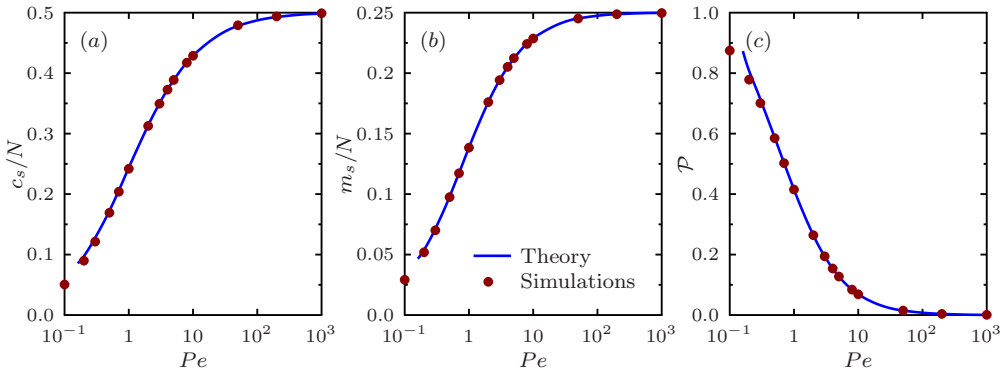

Figure 4.4: (a) Surface concentration c_s, (b) surface polarization m_s, and (c) dimensionless pressure $\mathcal{P}$ as functions of Péclet number $Pe = \ell_r/2H$. Solid lines show the semi-analytical solution of § 4.4.1, and symbols are Monte-Carlo simulation results.

analyzed the force on two nearby parallel plates in an active particle bath and proposed that the pressure inside the gap in a one-dimensional system with constant run length varies as $\Pi_i/(1 + Pe)$.

4.4.3 Summary and discussion

We have presented a simple continuum model for a dilute suspension of spherical run-and-tumble particles confined between two hard walls and interacting via purely steric forces with the walls. The model improves upon our previous theory for confined Brownian suspensions [51] by allowing us to address the limit of zero temperature within a continuum framework and by incorporating a more realistic treatment of surface interactions and exchange processes between surfaces and the bulk. This description also provides a direct and simple way of calculating the mechanical swim pressure exerted on the walls and serves as a complementary approach to the work of [129], where a continuous description of the same problem using a soft potential for wall interactions was used to calculate the pressure. We have outlined an elegant approach to derive a semi-analytical solution for the probability density functions, and demonstrated excellent quantitative agreement between our model and results from discrete Monte-Carlo simulations.

Our theoretical predictions and simulation results have highlighted several striking features of confined suspensions of run-and-tumble particles, namely the presence of a singularity and discontinuity in the bulk probability density function for orientations nearly parallel to the walls in the near-wall region, and the existence of a concentration boundary layer of thickness of the order of ℓ_r that actually diverges at the walls. Our pressure calcula-

tions were shown to match the recently proposed ideal-gas equation of state of active matter in wide channels, thus further validating this ideal-gas law and confirming the prediction that the precise nature of particle-wall steric interactions has no impact on the wall mechanical pressure for spherical particles [129]. We demonstrated, however, that confinement leads to departures from this ideal behavior and specifically to a decrease in the swim pressure, which in fact vanishes in the limit of an infinitely narrow gap when the mean number density is held fixed. In this case, we found that swimmers spend all their time at the boundaries, which provides the basis for previous models of strongly confined systems that only account for the surface distribution of swimmers [136].

While capturing the salient features of confined active suspensions, the problem under consideration remained minimal. Yet, the kinetic model presented here could be further modified to incorporate other effects and provide a more realistic description of biological or synthetic active systems. In particular, many active particles are rod-shaped and therefore also incur an aligning torque as they interact with boundaries. Recent theoretical work has shown that the wall pressure is modified in that case and becomes dependent upon the details of particle-wall interactions [134, 137]. In addition, experiments show that the surface-to-bulk tumbling of biological swimmers as well as certain types of synthetic swimmers is not uncorrelated but rather results in the preferential release of the particles near a specific angle [31, 138, 139]. Incorporating such details in our model is straightforward and would modify the distribution of particles near the walls with unexpected consequences for the mechanical pressure. Our basic model, validated here in the dilute limit, could also be modified to account for hydrodynamic couplings and to study the structure of the self-generated flows and collective dynamics of interacting active particles in confinement. In more complicated problems such as the ones described above, a complete solution for the bulk and surface probability density functions may not be tractable semi-analytically. Orientational moment equations with a suitable closure model [51, 140] likely would not perform well either because of the near-wall singularities in the bulk probability density function as well as complications arising from having to develop governing equations and closure approximations for the partial moments as opposed to the full ones. Therefore, in order to approximate the probability distribution function as a linear combination of its moments, we would need an infinite series in the spherical harmonic expansion to accurately resolve the singularities in the bulk probability distribution function and because of this, a truncation approximation using a closure would fail to give good quantitative agreement. Extending the present model to

non-planar boundaries, whether concave or convex, is not straightforward either but would be of great interest for the theoretical description of active particle transport in complex geometries or of their interaction with and transport of passive payloads. This rich avenue is the focus of our current work.

4.5 Acknowledgements

Chapter 4, in part, is a manuscript published in *J. Fluid Mech.*; authored by B. Ezhilan, R. Alonso-Matilla and D. Saintillan, "On the distribution and swim pressure of run-and-tumble particles in confinement". The dissertation author is the co-first author of this work. We thank J. F. Brady for seminal discussions and A. Solon for insightful comments.

Chapter 5

Stability of active fluid films

5.1 Introduction

The properties of confined dynamical active matter systems have been widely analyzed in many recent publications [41, 51, 120, 123, 139, 141–153], where the interplay between hydrodynamics and boundary effects has been shown to give rise to very interesting dynamics. Instabilities and non-linear dynamics have been observed in suspensions of active microorganisms, with the appearance of coherent structures and the generation of large-scale flows [5, 98, 99, 154–163]. The instabilities driven by these bacterial organisms has been shown to lead to spontaneous flows in confinement [13, 112], such as the formation of steady counter-rotating vortices in circular domains [13, 164, 165] and the manifestation of unidirectional fluid pumping states in periodic geometries [13, 166], a phenomenon resulting from a reduction in the effective suspension viscosity [2, 118, 167–172]. Control and regulation of these internally-driven flows could be extremely useful for the design of microfluidic pumps and flow actuation devices, where the chemical energy introduced into the system could be converted into a net mechanical energy in a controlled manner [173].

Lately, the scientific community has made an effort to understand the forces exchanged by active matter species with their surroundings. Understanding the generated force exerted by these systems on confined boundaries is crucial in numerous biological processes, such as cell migration during the formation of cancer metastasis [174, 175], embryogenesis [176] and wound healing processes [177–180]. Inspired by cellular dynamics, T. Sanchez et al. (2012) [181] observed experimentally spontaneous motion of active drops in solution containing extensile microtubules networks. Using numerical simulations, L. Giomi and A.

DeSimone (2014) [182] showed spontaneous division and self-propulsion of active droplets in solution caused by the interplay between activity and polarization-boundary effects. F. C. Keber et al. (2014) [183] used a theoretical description to model the evolution of active nematics encapsulated in a deformable lipid vesicle. Oscillatory patterns were observed in their analysis. Similarly, recent experimental [184, 185], numerical [186] and theoretical [187–189] studies analyzed the evolution of active drops on top of rigid substrates. In addition, the dynamics of nematic fluid films and its possible instabilities have been explored in previous works [190–193].

In the present study, we focus on the understanding of the forces exerted by a suspension of swimming microorganisms on deformable boundaries. More specifically, we analyze the stability of a suspension of Brownian self-propelled particles confined in a viscous fluid film with an air-fluid interface at the top of the film. We use a continuum model for the particle configuration, coupled with the Stokes equations for the fluid. Linear stability analysis is used to understand the dynamics of the film. In our model, there is a two-way coupling between the conservation equation for the particles and the fluid equations. The active stresses exerted by bacteria into the fluid create disturbance flows that are particle orientation dependent. These self-generated flows not only can drive the interface out-of equilibrium, but also can change the orientation of microorganisms, which in turn modifies the flows. Fluid pressure, capillary, viscous and active stresses are taken into account on the air-fluid interface. In most existing studies, the calculation of the force exerted on a boundary by a suspension of microorganisms has been done by neglecting the presence of the fluid [14, 126–128]. A recent study [135] addressed the contribution of hydrodynamics on the pressure of an active suspension on a hard boundary. A varying particle drag coefficient was added to include the hydrodynamic effect with the wall and a fixed particle speed was prescribed. An increase in the swim pressure for constant-speed swimmers was observed due to hydrodynamic effects. In the case of a free boundary, satisfaction of Newton's third law prevents a reaction force from occurring and the direct contact force is considered to be zero. Steric interactions between swimmers have been neglected in this model, an assumption that is valid for dilute suspensions. The main effect of swimmer-swimmer steric interactions is enhancing the local nematic alignment of elongated microswimmers, which can enhance the disturbance flows, making the initial perturbation of the system grow in time for lower levels of activity.

We first carry out a 1-D stability analysis and compare our fluid film results with

that of a straight channel with two rigid walls. The system is found to be unstable only for suspensions of pushers, provided that the activity parameter is higher than a certain threshold. We find that in the case of two rigid walls, higher activity is necessary to overcome dissipation at both walls, and drive the system out-of-equilibrium, resulting in a unidirectional fluid flow. We then analyze the 2-D stability analysis. Again, suspensions of pushers are found to be destabilizing, whereas suspensions of pullers play a stabilizing role. In addition, we address the stability of inverted bacterial fluid films. We find that suspensions of contractile swimmers can stabilize the film by damping the effect of the destabilizing gravitational field, thus hindering the well-known Rayleigh-Taylor instability. Finally, we show that rear-actuated cells (pushers) can stabilize fluid jets (Rayleigh-Plateau instability). The instabilities addressed in this work can be relevant to the understanding of active forces at free boundaries.

5.2 Theoretical model

We consider a 3-D bacterial film suspended in a Newtonian fluid of density ρ and dynamic viscosity μ that is resting over an infinite planar rigid wall. On top of the bacterial viscous film, there is an air-fluid interface with characteristic surface tension Γ, and a conservative gravitational field is considered, whose gravitational potential is represented by $\phi^g = -\rho g z$. The swimmers are oriented along the direction defined by the unit vector $\mathbf{p}$ and they self-propel along the same direction with constant velocity v_0. Particles undergo translational and rotational Brownian motion with constant translational and rotational diffusivities d_t and d_r, respectively. Particles are force-free as they swim through the suspending medium, and they are modeled as dynamical force dipoles that exert active stresses in the surrounding fluid with dipole strength σ_0. Following the natural distinction of swimmer microorganisms, we distinguish between pushers ($\sigma_0 < 0$), pullers ($\sigma_0 > 0$) and movers ($\sigma_0 = 0$). The biofilm thickness $h(x,t)$ evolves in time due to the flow generated by activity, where h_0 corresponds to its initial thickness. After carrying out dimensional analysis of the governing equations and boundary conditions, we find the following dimensionless groups:

$$Re = \frac{\rho h_0^2 d_r}{\mu}, \quad \alpha = \frac{\sigma_0 n}{\mu d_r}, \quad G = \frac{\rho g h_0}{\mu d_r}, \quad Ca_{act} = \frac{|\sigma_0| n h_0}{\Gamma}, \quad Pe_s = \frac{v_0}{d_r h_0}, \quad \Lambda = \frac{d_t d_r}{v_0^2} \tag{5.1}$$

The Reynolds number Re, which is set to zero in our stability analysis, quantifies the

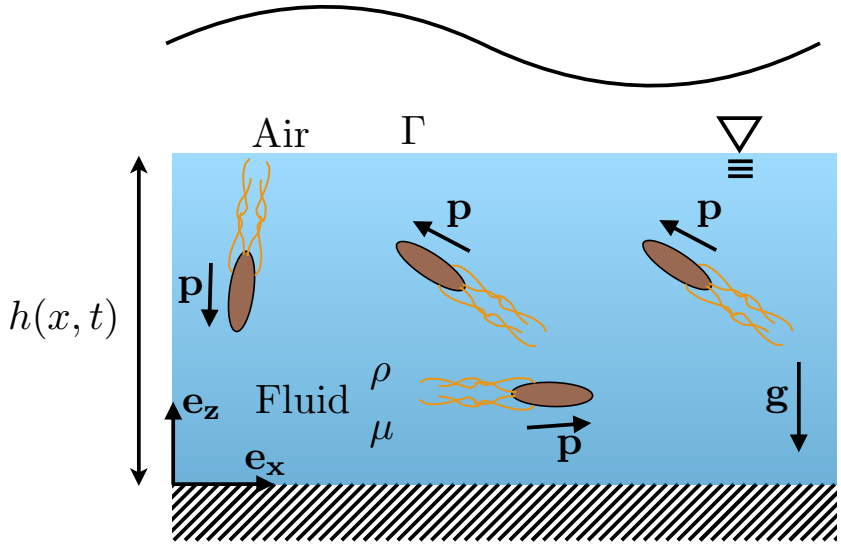

Figure 5.1: Sketch of the 3-D bacterial fluid film. The evolution of the film thickness h(x,t) is analyzed via linear stability analysis.

importance of inertial forces over viscous forces, the dimensionless dipole strength α compares active stresses with respect to viscous dissipation, the gravitational number G represents the ratio of gravitational forces to viscous forces, the active capillary number Ca_{act} represents the ratio of active forces to capillary forces, the Peclet number Pe_s, which quantifies the level of confinement, compares the persistence length of the swimmers with respect to the thickness film, and the parameter Λ, which only depends on the characteristics of the swimmers, compares Brownian diffusion to self-propulsion. We find two additional dimensionless numbers after carrying out linear stability analysis: the dimensionless wavenumber and growth rate of the perturbation, $K = kh_0$ and $S = s/d_r$ respectively. K defines the wavelength of the perturbation and S defines how fast the initial perturbation decays or grows in time. For convenience, we also define a viscous capillary number $Ca_{vis} = Ca_{act}/|\alpha| = \mu d_r h_0/\Gamma$, which quantifies viscous forces over capillary forces, and it will be useful later on when comparing our results with situations where no active stresses are exerted into the fluid. We describe the spacial and orientational distribution of particles by defining a probability distribution function $P(\mathbf{x}, \mathbf{p}, t)$ of finding a particle at position $\mathbf{x}$, with orientation $\mathbf{p}$ and at time t. For convenience, we take orientational moments of the probability distribution function over the unit sphere of orientations Ω:

$$c(\mathbf{x},t) = \int_\Omega P d\mathbf{p}, \qquad \mathbf{m}(\mathbf{x},t) = \int_\Omega P\mathbf{p} d\mathbf{p}, \qquad \mathbf{D}(\mathbf{x},t) = \int_\Omega P\left(\mathbf{pp} - \frac{\mathbf{I}}{3}\right) d\mathbf{p} \tag{5.2}$$

Here, c, $\mathbf{m}$ and $\mathbf{D}$ are local variables that correspond, respectively, to concentration, polarization and nematic order parameter. See § 1.1.2 for more details. Using a continuum kinetic model based on the Smoluchowski equation, these variables satisfy the following moment equations:

$$\partial_t c = -\nabla_x \cdot \mathbf{F_c}, \tag{5.3}$$

$$\partial_t \mathbf{m} = -\nabla_x \cdot \mathbf{F_m} + \left(\frac{3\gamma}{5}\mathbf{E} - \mathbf{W}\right) \cdot \mathbf{m} - 2d_r\mathbf{m}, \tag{5.4}$$

$$\partial_t \mathbf{D} = -\nabla_x \cdot \mathbf{F_D} + \gamma\left[\frac{2c\mathbf{E}}{5} + \frac{3}{7}\left[\mathbf{E}\cdot\mathbf{D} + \mathbf{D}\cdot\mathbf{E}\right] - \frac{2}{7}\left(\mathbf{D}:\mathbf{E}\right)\mathbf{I}\right] + \left(\mathbf{D}\cdot\mathbf{W} - \mathbf{W}\cdot\mathbf{D}\right) - 6d_r\mathbf{D} \tag{5.5}$$

where $\mathbf{F_c}$, $\mathbf{F_m}$ and $\mathbf{F_D}$ are respectively, the 0^{th}, 1^{st} and 2^{nd} moments of the translational bacterial flux:

$$\mathbf{F_c} = v_0\mathbf{m} + \mathbf{v}c - d_t\nabla_x c, \tag{5.6}$$

$$\mathbf{F_m} = v_0\left(\mathbf{D} + \frac{c}{3}\mathbf{I}\right) + \mathbf{v}\mathbf{m} - d_t\nabla_x\mathbf{m} \tag{5.7}$$

$$\mathbf{F_D} = v_0\left(\langle\mathbf{ppp}\rangle - \frac{\mathbf{mI}}{3}\right) + \mathbf{v}\mathbf{D} - d_t\nabla_x\mathbf{D} \tag{5.8}$$

Here $\mathbf{v}$ is the fluid velocity, $\mathbf{E} = (\nabla\mathbf{v} + \nabla\mathbf{v}^T)/2$ and $\mathbf{W} = (\nabla\mathbf{v} - \nabla\mathbf{v}^T)/2$ are the strain and vorticity tensors respectively, and γ is the so-called Bretherton constant [194], which is a swimmer shape parameter whose bounding limits are 0 for spherical swimmers and 1 for slender swimmers. The third orientational moment $\langle\mathbf{ppp}\rangle$ is related to the polarization vector according to the following closure approximation:

$$\langle p_i p_j p_k\rangle = \frac{1}{5}\left[m_i\delta_{jk} + m_j\delta_{ik} + m_k\delta_{ij}\right] \tag{5.9}$$

We enforce a no-translational-flux boundary condition for the distribution of particles at both solid-fluid and air-fluid interfaces. The bottom wall is stationary and it satisfies no-slip. The top interface is moving with the fluid, where both air-fluid interface and swimmers are advected equally by the flow. As a result, only the relative velocity between the boundaries and the swimmers enters into this boundary condition. As a consequence, we can generalize

the no-flux boundary condition at both interfaces as follows:

$$\mathbf{n}\cdot(\mathbf{F_c}-\mathbf{v}c)=\mathbf{n}\cdot(\mathbf{F_m}-\mathbf{vm})=\mathbf{n}\cdot(\mathbf{F_D}-\mathbf{vD})=0 \qquad \text{at} \quad z=0,\ \ z=h(x,t) \tag{5.10}$$

, which represents a balance between self-propulsion and translational diffusion. Here $\mathbf{n}$ is the local unit normal.

The fluid velocity field $\mathbf{v}$ created by the swimmers satisfies the incompressible Navier-Stokes equations forced by the active stress contribution $\sigma_0\nabla\cdot\mathbf{D}$:

$$\nabla\cdot\mathbf{v}=0, \qquad \rho\left(\partial_t\mathbf{v}+\mathbf{v}\cdot\nabla\mathbf{v}\right)=-\nabla p+\mu\nabla^2\mathbf{v}+\nabla\phi^g+\sigma_0\nabla\cdot\mathbf{D} \tag{5.11}$$

In our model, the fluid velocity $\mathbf{v}$ satisfies a no-slip boundary condition at the bottom wall. We also enforce both a kinematic and a dynamic boundary condition at the air-fluid interface. The kinematic boundary condition ensures that no mass is transferred through the interface. We define a function $g(x,z,t)=z-h(x,t)$ that moves with the fluid. Therefore, its material derivative vanishes leading to the following condition:

$$\partial_t h+u\partial_x h=w \qquad \text{at} \quad z=h(x,t) \tag{5.12}$$

Neglecting viscous effects in the air, the dynamic boundary condition at the interface is given by

$$-\left(\mathbf{T}+\sigma_0\mathbf{D}\right)\cdot\mathbf{n}=\mathit{\Gamma}\kappa\mathbf{n} \qquad \text{at} \quad z=h(x,t) \tag{5.13}$$

which is a surface balance of pressure, viscous, active and capillary forces. Here, the fluid stress tensor $\mathbf{T}$ can be expressed in terms of a fluid-static and a fluid-dynamic contribution $\mathbf{T}=-p\mathbf{I}+\mu\left[\nabla\mathbf{v}+\nabla\mathbf{v}^T\right]$, and the curvature of the interface κ can be expressed as $\kappa=\nabla\cdot\mathbf{n}$. It will be useful later on to express the unit normal vector $\mathbf{n}$ and the tangential vector $\mathbf{t}$ as a function of the film thickness $h(x,t)$. The normal vector $\mathbf{n}$ satisfies the following condition: $\mathbf{n}=\nabla g/|\nabla g|$, and both $\mathbf{n}$ and $\mathbf{t}$ are orthogonal vectors; thus:

$$\mathbf{n}=\frac{(-\partial_x h,0,1)}{\sqrt{1+(\partial_x h)^2}}, \quad \mathbf{t}=\frac{(1,0,\partial_x h)}{\sqrt{1+(\partial_x h)^2}} \tag{5.14}$$

5.3 Non-dimensionalization

We now proceed to non-dimensionalize both governing equations and boundary conditions. We scale all the variables using time scale d_r^{-1}, length scale h_0, velocity scale $h_0 d_r$ and pressure scale μd_r. The probability distribution function P is also scaled by the mean number density n. From now on, all the variables, unless otherwise specified, will be dimensionless. The non-dimensional moment equations (5.3-5.5) are given by:

$$\partial_t c = -\nabla_x \cdot \left[Pe_s \mathbf{m} + \mathbf{v}c - \Lambda Pe_s^2 \nabla_x c \right], \tag{5.15}$$

$$\partial_t \mathbf{m} = -\nabla_x \cdot \left[Pe_s \left(\mathbf{D} + \frac{c}{3}\mathbf{I} \right) + \mathbf{v}\mathbf{m} - \Lambda Pe_s^2 \nabla_x \mathbf{m} \right] + \left(\frac{3\gamma}{5}\mathbf{E} - \mathbf{W} \right) \cdot \mathbf{m} - 2\mathbf{m}, \tag{5.16}$$

$$\begin{aligned} \partial_t \mathbf{D} = &-\nabla_x \cdot \left[Pe_s \left(\langle \mathbf{ppp} \rangle - \frac{\mathbf{m}\mathbf{I}}{3} \right) + \mathbf{v}\mathbf{D} - \Lambda Pe_s^2 \nabla_x \mathbf{D} \right] \\ &+ \gamma \left[\frac{2c\mathbf{E}}{5} + \frac{3}{7} \left[\mathbf{E} \cdot \mathbf{D} + \mathbf{D} \cdot \mathbf{E} \right] - \frac{2}{7} \left(\mathbf{D} : \mathbf{E} \right) \mathbf{I} \right] + \left(\mathbf{D} \cdot \mathbf{W} - \mathbf{W} \cdot \mathbf{D} \right) - 6\mathbf{D} \end{aligned} \tag{5.17}$$

We also write down the NS-equations in dimensionless form:

$$\partial_x u + \partial_z w = 0 \tag{5.18}$$

$$Re \left[\partial_t u + u\partial_x u + w\partial_z u \right] = -\partial_x p + \left[\partial_x^2 u + \partial_z^2 u \right] + \alpha \left[\partial_x D_{xx} + \partial_z D_{xz} \right] \tag{5.19}$$

$$Re \left[\partial_t w + u\partial_x w + w\partial_z w \right] = -\partial_z p + \left[\partial_x^2 w + \partial_z^2 w \right] + \alpha \left[\partial_x D_{xz} + \partial_z D_{zz} \right] - G \tag{5.20}$$

The no-slip boundary condition at the bottom wall is represented in dimensionless form as

$$u = 0, \quad w = 0 \qquad \text{at} \quad z = 0 \tag{5.21}$$

and the kinematic boundary condition (eq. 5.12) is expressed as

$$\partial_t h + u\partial_x h = w \qquad \text{at} \quad z = h(x,t) \tag{5.22}$$

Finally, the dynamic boundary condition (eq. 5.13) projected along both tangential and normal to the interface reads:

$$[\alpha(D_{zz} - D_{xx}) + 4\partial_z w]\,\partial_x h + [\alpha D_{xz} + \partial_z u + \partial_x w]\left(1 - (\partial_x h)^2\right) = 0 \quad \text{at} \quad z = h(x,t) \tag{5.23}$$

$$\begin{aligned} &- p - \frac{2\partial_x h}{1 + (\partial_x h)^2}\left[\partial_z u + \partial_x w + \alpha D_{xz}\right] + \frac{(\partial_x h)^2}{1 + (\partial_x h)^2}\left[2\partial_x u + \alpha D_{xx}\right] + \\ &+ \frac{1}{1 + (\partial_x h)^2}\left[2\partial_z w + \alpha D_{zz}\right] = |\alpha| Ca_{act}^{-1} \frac{\partial_{xx} h}{\left[1 + (\partial_x h)^2\right]^{3/2}} \quad \text{at} \quad z = h(x,t) \end{aligned} \tag{5.24}$$

5.4 Linear Stability Analysis

Linear stability analysis of fluid films

In this section we carry out a linear stability analysis of a fluid film, where no bacteria are present. We derive an analytical solution for the growth rate of the instability. We start by taking the divergence of the Stokes' equations, which allows us to find a general expression for the pressure:

$$\hat{p} = C_{p1}\mathrm{e}^{Kz} + C_{p2}\mathrm{e}^{-Kz} \tag{5.25}$$

where C_{p1} and C_{p2} are constants of integration. Plugging this solution into the Stokes' equations and solving two non-homogeneous ODEs we find a general expression for both velocity eigenfunctions $\hat{u}$ and $\hat{w}$:

$$\hat{u} = C_{u1}\mathrm{e}^{Kz} + C_{u2}\mathrm{e}^{-Kz} + C_{u3} z\mathrm{e}^{Kz} + C_{u4} z\mathrm{e}^{-Kz} \tag{5.26}$$

$$\hat{w} = C_{w1}\mathrm{e}^{Kz} + C_{w2}\mathrm{e}^{-Kz} + C_{w3} z\mathrm{e}^{Kz} + C_{w4} z\mathrm{e}^{-Kz} \tag{5.27}$$

where

$$C_{u3} = \frac{\mathrm{i}C_{p1}}{2K}, \quad C_{u4} = -\frac{\mathrm{i}C_{p2}}{2K} \quad C_{w3} = \frac{C_{p1}}{2K^2}, \quad C_{w4} = \frac{C_{p2}}{2K^2} \tag{5.28}$$

Combining continuity and the no-slip boundary condition at the bottom wall we get four additional relationships:

$$C_{u1} = \frac{\mathrm{i}(C_{p1} - C_{p2})}{4K^2}, \;\; C_{u2} = -\frac{\mathrm{i}(C_{p1} - C_{p2})}{4K^2}, \;\; C_{w1} = -\frac{C_{p1} + C_{p2}}{4K^3}, \;\; C_{w2} = \frac{C_{p1} + C_{p2}}{4K^3} \quad (5.29)$$

Now we apply the kinematic boundary condition and both tangential and normal dynamic boundary conditions at the air-fluid interface, and using eqs. (5.28, 5.29) we get an algebraic system of three equations and four unknowns ($C_{p1}, C_{p2}, \hat{h}$ and S):

$$\left[\frac{\mathrm{e}^K}{2K^2} - \frac{\sinh K}{2K^3}\right] C_{p1} + \left[-\frac{\sinh K}{2K^3} + \frac{\mathrm{e}^{-K}}{2K^2}\right] C_{p2} = s\hat{h} \quad (5.30)$$

$$\left[\mathrm{e}^K + \frac{\cosh K}{K}\right] C_{p1} + \left[\mathrm{e}^{-K} - \frac{\cosh K}{K}\right] C_{p2} = 0 \quad (5.31)$$

$$\left[K\mathrm{e}^K - \cosh K\right] C_{p1} + \left[-K\mathrm{e}^{-K} - \cosh K\right] C_{p2} = -\left[GK^2 + Ca_{vis}^{-1}K^4\right] \hat{h} \quad (5.32)$$

From eq. (5.31), we can express C_{p1} as a function of C_{p2} and substitute this result into eqs. (5.30) and (5.32). Finally, dividing these two equations and simplifying, we get a dispersion relation for the growth rate S as a function of the parameters of the problem K, Ca_{vis} and G:

$$S = \frac{2K - \sinh(2K)}{4K(K^2 + \cosh^2 K)} \left(G + K^2 Ca_{vis}^{-1}\right) \quad (5.33)$$

This expression is in agreement with the previous result obtained by S. G. Yiantsios and B. G. Higgins (1989) [195] for the special case of zero-air viscosity and zero-air density. The pre-factor of this expression is always negative for any value of K. Therefore, the only way this fluid problem can be unstable is if gravity becomes negative, which is the case for an inverted film (wall on top and free surface at the bottom). For this case, the critical Capillary number Ca_c for the fluid instability to happen is $Ca_c = K^2/G$. In the limits of $K \to 0$ and $K \to \infty$, we get:

$$S(K \to 0) = -\frac{K^2}{3}\left(G + K^2 Ca_{vis}^{-1}\right), \qquad S(K \to \infty) = -\frac{1}{2K}(G + K^2 Ca_{vis}^{-1}) \quad (5.34)$$

We now proceed to use temporal linear stability analysis to extend the understanding of instabilities of fluid films when a dilute bacterial suspension is added to the film.

5.4.1 Base state

The base state is characterized by no-flow and a flat interface. We derive analytically the equilibrium configuration of the bacterial film. In the base state, $u^0 = w^0 = m_x^0 = D_{xz}^0 = D_{zx}^0 = 0$. In addition, only vertical spatial variations are allowed. In the base state, the total pressure will be the sum of two contributions: the hydrostatic pressure and the pressure due to active stresses. One can obtain the pressure gradient at equilibrium from the z-momentum conservation equation. In dimensionless form:

$$\frac{dp^0}{dz} = \alpha \frac{dD_{zz}^0}{dz} - G \tag{5.35}$$

To simplify the derivation of the orientational moment in the base state, the origin of the reference system will be placed along the centerline of the film, and as a result we will be able to apply symmetries when calculating the constants of integration. The moment equations read:

$$-Pe_s \frac{dm_z^0}{dz} + \Lambda Pe_s^2 \frac{d^2c^0}{dz^2} = 0, \tag{5.36}$$

$$-Pe_s \left(\frac{dD_{zz}^0}{dz} + \frac{1}{3}\frac{dc^0}{dz} \right) + \Lambda Pe_s^2 \frac{d^2m_z^0}{dz^2} - 2m_z^0 = 0, \tag{5.37}$$

$$-\frac{4Pe_s}{15}\frac{dm_z^0}{dz} + \Lambda Pe_s^2 \frac{d^2D_{zz}^0}{dz^2} - 6D_{zz}^0 = 0, \tag{5.38}$$

No translational flux is considered on both solid-fluid and air-fluid interfaces:

$$-Pe_s m_z^0 + \Lambda Pe_s^2 \frac{dc^0}{dz} = 0, \qquad \text{at} \quad z = \pm\frac{1}{2} \tag{5.39}$$

$$-Pe_s \left(D_{zz}^0 + \frac{1}{3}c^0 \right) + \Lambda Pe_s^2 \frac{dm_z^0}{dz} = 0, \qquad \text{at} \quad z = \pm\frac{1}{2} \tag{5.40}$$

$$-\frac{4Pe_s}{15} m_z^0 + \Lambda Pe_s^2 \frac{dD_{zz}^0}{dz} = 0, \qquad \text{at} \quad z = \pm\frac{1}{2} \tag{5.41}$$

To close the system, we impose a normalization condition:

$$\int_{-1/2}^{1/2} c(z) dz = 1 \tag{5.42}$$

Integrating Eq. (5.36), and using Eq. (5.39) to compute the integrating constant, we get:

$$m_z^0(z) = \Lambda Pe_s \frac{dc^0}{dz} \tag{5.43}$$

Plugging this result into Eq. (5.37) and integrating again yields:

$$D_{zz}^0(z) = \Lambda^2 Pe_s^2 \frac{d^2c^0}{dz^2} - \left(2\Lambda + \frac{1}{3}\right) c^0 - A_1 \tag{5.44}$$

where A_1 is a constant of integration. We have expressed both wall-normal polarization (m_z) and the zz-diagonal component of the nematic order parameter (D_{zz}) as a function of the concentration (c). Therefore, plugging eqs. (5.43) and (5.44) into eq. (5.38) and rearranging terms we get a 4^{th} order non homogeneous ODE for c:

$$\frac{d^4c^0}{dz^4} - \left(\zeta^2 + \nu^2\right) \frac{d^2c^0}{dz^2} + \zeta^2\nu^2 c^0 = -\frac{6A_1}{\Lambda^3 Pe_s^4} \tag{5.45}$$

where

$$\zeta = \frac{\left(8\Lambda + 3/5 + \sqrt{16\Lambda^2 + 8\Lambda/5 + 9/25}\right)^{1/2}}{\sqrt{2}\Lambda Pe_s} \tag{5.46}$$

$$\nu = \frac{\left(8\Lambda + 3/5 - \sqrt{16\Lambda^2 + 8\Lambda/5 + 9/25}\right)^{1/2}}{\sqrt{2}\Lambda Pe_s} \tag{5.47}$$

Taking into account the symmetry of the problem, the general solution of Eq. (5.45) can be simplified as follows:

$$c^0(z) = c_p + A_2 \cosh \zeta z + A_3 \cosh \nu z \tag{5.48}$$

where c_p is the particular solution of the ODE and A_2 and A_3 are constants of integration to be determined. The general solution for m_z and D_{zz} are respectively:

$$m_z^0(z) = A_2 \Lambda Pe_s \zeta \sinh \zeta z + A_3 \Lambda Pe_s \nu \sinh \nu z \tag{5.49}$$

$$D_{zz}^0(z) = A_2 \left(\Lambda^2 Pe_s^2 \zeta^2 - 2\Lambda - 1/3\right) \cosh \zeta z + A_3 \left(\Lambda^2 Pe_s^2 \nu^2 - 2\Lambda - 1/3\right) \cosh \nu z \tag{5.50}$$

One can determine the constants c_p, A_2 and A_3 by using eqs. (5.40 – 5.42):

$$A_2 = \frac{\nu \sinh\frac{\nu}{2}\left(\Lambda^2 Pe_s^2\nu^2 - 2\Lambda - 3/5\right)}{\Omega_1 - \Omega_2}, \qquad A_3 = -\frac{\zeta \sinh\frac{\zeta}{2}\left(\Lambda^2 Pe_s^2\zeta^2 - 2\Lambda - 3/5\right)}{\Omega_1 - \Omega_2}$$
$$c_p = \frac{6\Lambda\left[\nu\cosh\frac{\zeta}{2}\sinh\frac{\nu}{2}\left(\Lambda^2 Pe_s^2\nu^2 - 2\Lambda - 3/5\right) - \zeta\cosh\frac{\nu}{2}\sinh\frac{\zeta}{2}\left(\Lambda^2 Pe_s^2\zeta^2 - 2\Lambda - 3/5\right)\right]}{\Omega_1 - \Omega_2} \tag{5.51}$$

where

$$\Omega_1 = \nu\sinh\frac{\nu}{2}\left(6\Lambda\cosh\frac{\zeta}{2} + \frac{2}{\zeta}\sinh\frac{\zeta}{2}\right)\left[\Lambda^2 Pe_s^2\nu^2 - 2\Lambda - 3/5\right] \tag{5.52}$$

$$\Omega_2 = \zeta\sinh\frac{\zeta}{2}\left(6\Lambda\cosh\frac{\nu}{2} + \frac{2}{\nu}\sinh\frac{\nu}{2}\right)\left[\Lambda^2 Pe_s^2\zeta^2 - 2\Lambda - 3/5\right] \tag{5.53}$$

We found perfect agreement of the analytical solution for the concentration, polarization and nematic order parameter (eqs. 5.48 -5.50) with the numerical solution (not shown here).

5.4.2 Perturbation from the base state

We perturb the shape of the interface around the base state using normal mode analysis $h = 1 + \epsilon\hat{h}\mathrm{e}^{\mathrm{i}Kx+St}$, ϵ being very small, and perturb both the probability distribution function and fluid velocity in the same way: $P = P_0 + \epsilon\hat{P}(z)\mathrm{e}^{\mathrm{i}Kx+St}$, $\mathbf{v} = \epsilon\hat{\mathbf{v}}(z)\mathrm{e}^{\mathrm{i}Kx+St}$. In our analysis we take the limit of $Re \to 0$. We linearize the moment equations, only keeping terms of order ϵ, but for clarity we do not include them in the manuscript. The resulting linearized moment equations along with the linearized kinematic boundary condition

$$S\hat{h} = \hat{w} \qquad \text{at} \quad z = 1 \tag{5.54}$$

form a set of Ordinary Differential Equations (ODE's) in z, that after discretization take the following form:

$$S\mathbf{r} = \mathbf{M}_1 \cdot \mathbf{q} \quad \rightarrow \quad \begin{cases} \mathbf{r} = [\hat{c}, \hat{m}_x, \hat{m}_z, \hat{D}_{xx}, \hat{D}_{xz}, \hat{D}_{zz}, \hat{h}]^T \\ \mathbf{q} = [\hat{c}, \hat{m}_x, \hat{m}_z, \hat{D}_{xx}, \hat{D}_{xz}, \hat{D}_{zz}, \hat{h}, \hat{u}, \hat{w}]^T \end{cases} \tag{5.55}$$

, where $\mathbf{M}_1$ is a matrix defined by the governing equations and boundary conditions, and $\mathbf{r}$ and $\mathbf{q}$ are both vectors of variables that are discretized in space. Note that the non-diagonal components of the nematic order tensor $\hat{D}_{xy}$ and $\hat{D}_{yz}$ are in general non-zero, but they only

appear in the problem as non-linear contributions. $\hat{D}_{yy}$ is non-zero but it can be obtained easily by noticing that the nematic order tensor $\hat{\mathbf{D}}$ is trace-free. We can transform this system of equations into an eigenvalue problem by expressing both $\hat{u}$ and $\hat{w}$ as a function of the rest of variables as shown below. From continuity (Eq. 5.18):

$$\hat{u} = \frac{\mathrm{i}}{K}\frac{d\hat{w}}{dz} \tag{5.56}$$

and plugging it into the linearized version of the x-momentum equation (obtained from Eq. 5.19), one obtains:

$$\hat{p} = \frac{1}{K^2}\frac{d^3\hat{w}}{dz^3} - \frac{d\hat{w}}{dz} + \alpha\hat{D}_{xx} - \frac{\mathrm{i}\alpha}{K}\frac{d\hat{D}_{xz}}{dz} \tag{5.57}$$

After substituting the previous two equations into the linearized z-momentum equation (obtained from Eq. (5.20)), we get a non-homogeneous 4^{th} order ODE for the vertical velocity $\hat{w}$ only as a function of the components of the nematic order tensor:

$$\frac{d^4\hat{w}}{dz^4} - 2K^2\frac{d^2\hat{w}}{dz^2} + K^4\hat{w} = \alpha K^2\left[\frac{d\hat{D}_{zz}}{dz} - \frac{d\hat{D}_{xx}}{dz}\right] + \mathrm{i}\alpha K\frac{d^2\hat{D}_{xz}}{dz^2} + \mathrm{i}\alpha K^3\hat{D}_{xz} \tag{5.58}$$

No slip at the bottom wall translates into:

$$\hat{w} = \frac{d\hat{w}}{dz} = 0 \qquad \text{at} \quad z = 0 \tag{5.59}$$

and both tangential and normal dynamic boundary conditions at the free surface become:

$$\frac{d^2\hat{w}}{dz^2} + K^2\hat{w} = \mathrm{i}\alpha K\hat{D}_{xz} + \alpha K^2(D^0_{xx} - D^0_{zz})\hat{h} \qquad \text{at} \quad z = 1 \tag{5.60}$$

$$-\frac{d^3\hat{w}}{dz^3} + 3K^2\frac{d\hat{w}}{dz} = \alpha K^2(\hat{D}_{xx} - \hat{D}_{zz}) - \mathrm{i}\alpha K\frac{d\hat{D}_{xz}}{dz} - \left(GK^2 + |\alpha|Ca^{-1}_{act}K^4\right)\hat{h}$$

$$\text{at} \quad z = 1 \tag{5.61}$$

The system of equations (5.55) can then be transformed into an eigenvalue problem of the form $S\mathbf{r} = \mathbf{M}_2 \cdot \mathbf{r}$, where $\mathbf{r}$ has been previously defined in Eq. (5.55) and $\mathbf{M}_2$ is a matrix of dimensions $(6N_z+1)\times(6N_z+1)$, where N_z is the number of points used for the discretization of the domain in the vertical direction z. This eigenvalue problem is solved numerically.

5.5 Results

5.5.1 1-D perturbation

We first analyze 1-D perturbations of bacterial fluid films ($K = 0$). This special case has been solved separately, where now the boundary condition at the free interface simplifies to a balance between viscous stresses and active stresses. After linearizing the moment equations, we find that the only non-zero eigenfunctions that remain in the problem to order ϵ in the perturbation are the horizontal velocity $\hat{u}$, the streamwise polarization $\hat{m}_x$ and the XZ-component of the nematic order tensor $\hat{D}_{xz}$. The rest of eigenfunctions are found to be of order ϵ^2, and thus they vanish in our 1-D analysis. In the base state, there is no flow, particles accumulate at the boundaries as a consequence of the interplay between self-propulsion, translational diffusion and no penetration at the boundaries and, on average, the wall-normal polarization is antisymmetric with respect to the mid-plane, particles being polarized towards the bottom wall and air-fluid interface respectively. Any small perturbation will induce a flow along any arbitrary direction, which in turn will foster nematic alignment of the swimmers, as depicted in Fig. (5.2c). For sufficiently thick films and sufficiently high levels of activity, viscous dissipation is overcome, vertical gradients in nematic alignment generate additional flows that, in the case of pushers, reinforce the original perturbation, and a unidirectional fluid flow arises, as seen in Fig. (5.2a). Fluid shear is minimum in the mid-section of the film, being maximum and around the same order of magnitude at both interfaces (hard wall and free interface). The fact that the fluid shear does not vanish at the air-fluid interface is counter-intuitive, this phenomenon arising due to the fact that viscous stresses must balance the tangential active stresses exerted by bacteria on the interface. Because the shear velocity is positive across the entire film, the horizontal velocity reaches its maximum value at the interface. Due to this monotonous shear profile and taking into account how particles are polarized against both interfaces, shear-alignment makes particles reorient against the flow near the bottom wall and in the same direction of the flow near the top interface, as seen in Fig. (5.2b). Close to both interfaces, the gradients in velocity increase as the swimmer parameter Λ decreases (not shown here), which is a consequence of steep bacterial boundary layers in the ground state, characteristic of low diffusive systems. The net velocity of bacteria will be dictated by the competition between self-propulsion and advection by the flow. Close to the free surface, the synergy between

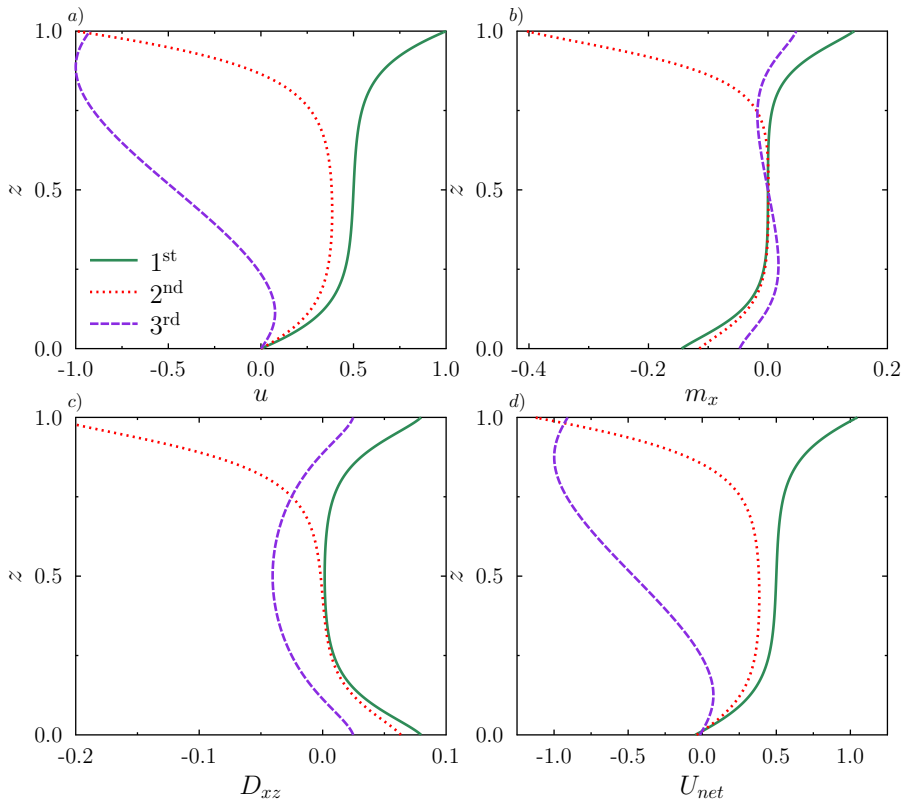

Figure 5.2: Unstable modes corresponding to the normalized eigenfunctions for 1-D perturbations $K = 0$ and a set of parameters characteristic of an unstable system $Pe_s = 0.5$, $\Lambda = 0.2$ and $\alpha = -50$. The only non-zero eigenfunctions of this linear problem to order ϵ are the horizontal velocity $\hat{u}$ (top left), horizontal polarization $\hat{m}_x$ (top right) and the off-diagonal component of the nematic order tensor $\hat{D}_{xz}$ (bottom left). The net bacterial horizontal velocity $\hat{U}_{net} = Pe_s\,\hat{m}_x/c + \hat{u}$, defined as the sum of self-propulsion and advection, is also shown (bottom right).

advection and self-propulsion enhances the net bacterial velocity. Away from this interface, there is a competition between advection and self-propulsion, and only near the bottom wall, the no-slip BC allows self-propulsion to overcome advection, where the fluid velocity is small compared with the self-propelled velocity of the swimmers. Only in these regions, the corresponding net bacterial velocity becomes slightly negative (see Fig. (5.2d)).

In Fig. (5.3), marginal stability was used to compare the onset of spontaneous flows in two different configurations: two rigid-wall straight channel and a film with one rigid wall and an air-fluid interface on top. We found that the critical level of activity for the instability to happen increases in both geometries for more confined channels/films. More interesting is the fact that spontaneous flows arise for lower levels of activity for the case of the fluid

film. In the case of two rigid walls, the swimmers have to inject more mechanical energy via active stresses into the system in order to drive the system unstable, due to the higher viscous dissipation happening at both walls compared with the air-fluid interface case.

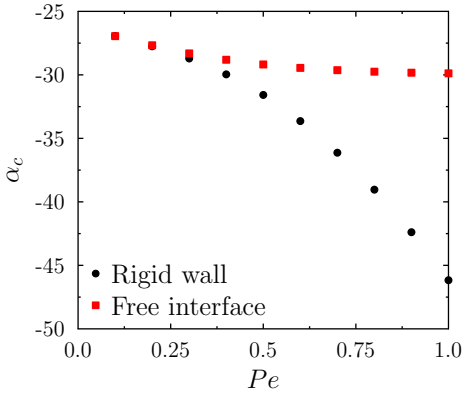

Figure 5.3: One-dimensional marginal stability for the critical activity parameter α_c as a function of the swimming Peclet number Pe_s for two different cases: a straight channel with two rigid walls and a fluid film with rigid wall at the bottom and a free interface on top. Parameter values: $\Lambda = 0.5$, $\gamma = 1$. Results confirm that spontaneous flows are more energetically favorable in fluid films than in hard-wall channels.

5.5.2 2D perturbation

Here we analyze 2-D perturbations. We validate our model by comparing the analytical solution for inverted fluid films free of bacteria where gravity is the destabilizing mechanism (Eq. 5.33) and its corresponding numerical solution. To compare both solutions, we set in our numerical solution the activity parameter α to 0 and the swimmer parameter Λ to ∞ ($\alpha = 0, \Lambda \to \infty$), which is the equivalent system as that of a free-bacteria system, characterized by an isotropic distribution with no active stresses exerted into the fluid. Both solutions perfectly match (not shown here). After our numerical validation, we analyze the mechanism responsible for the fluid bacterial film instability. Figs. (5.4, 5.5) show the eigenfunctions corresponding to concentration, vector polarization, direction and magnitude of the active forcing term in the Stokes' equations, and fluid velocity profile with the corresponding streamlines for $\alpha = -1$ and $\alpha = -100$ respectively. Under a small perturbation of the interface, particles get squeezed at the valleys of the air-fluid region fostering accumulation of particles within these regions, whereas depletion of particles manifest at the crests. The coupling of self-propulsion and the shape of the perturbed interface along with

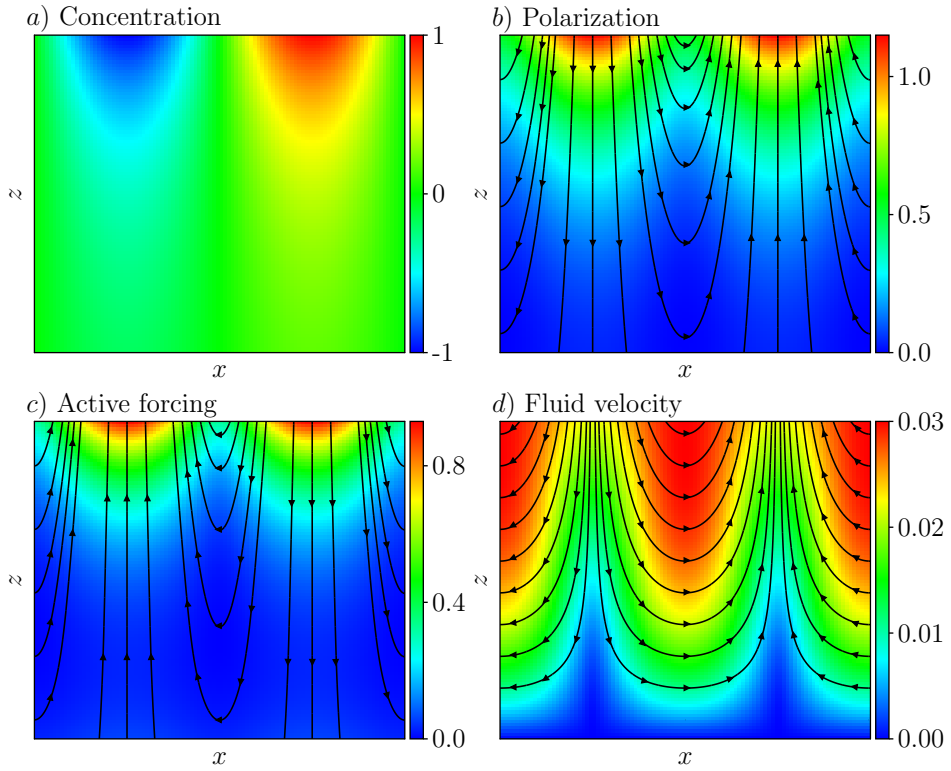

Figure 5.4: Perturbation of the first two orientational moments of the probability density $\hat{P}$, perturbation of the active forcing and fluid velocity profiles for $\alpha = -1$ and the following parameter values: $G = 0$, $Ca_{act} = 10$, $K = 1$, $Pe_s = 1$, $\Lambda = 0.5$, $\gamma = 1$. a) Concentration ($\hat{c}(x, z)$). Color (blue to red) indicates the magnitude of the concentration. b) Vector polarization ($\hat{\mathbf{m}}(x, z)$). Color (blue to red) indicates the magnitude of the polarization. c) Active forcing term in the Stokes' equations ($\alpha \nabla \cdot \hat{\mathbf{D}}$). Color (blue to red) indicates its corresponding magnitude. d) Streamlines of the flow. Color (blue to red) indicates the magnitude of the fluid velocity (low to high). The horizontal x-values correspond to a perturbation of the air-fluid interface fo that shown in Fig. (5.1)

base state gradients of the orientational moments promotes a decrease in the wall-normal polarization near the peaks of the free interface and an increase near its valleys, whereas the streamwise polarization increases near the intermediate regions (nodes). For $\alpha = -1$, nematic alignment is found to be very small compared with both concentration and polarization levels, and it creates an stabilizing active forcing, as seen in Fig. (5.4c). The interface is forced to move to the original flat configuration due to the effect of surface tension and activity and as a result the system is stable. For the case of $\alpha = -100$, shear flows reinforce nematic alignment and micro-swimmers tend to align parallel to the free surface near its valleys and perpendicular to the free surface near its peaks. Subsequently the disturbance flows

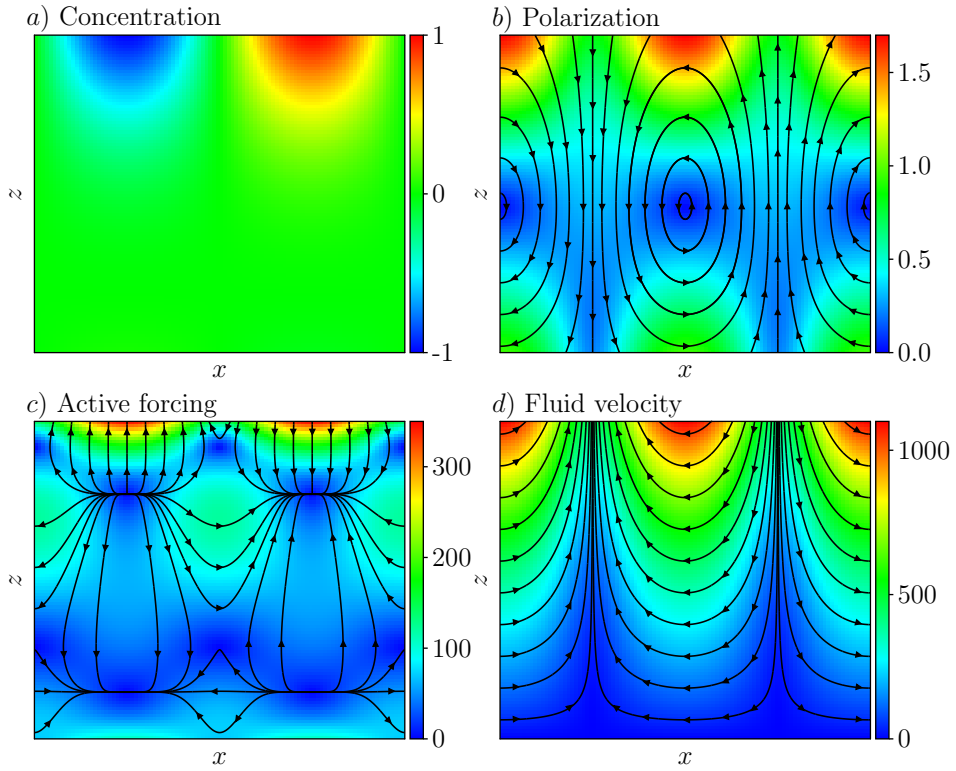

Figure 5.5: Same subplots and parameter values depicted in Fig. (5.4) for $\alpha = -100$.

created by pushers will drive the peaks and the valleys upwards and downwards respectively. Whereas suspensions of pullers are found to be always stable, the stability of suspensions of pushers is found to depend on the remaining dimensionless parameters. Fig. (5.6) shows the eigenvalue S associated to the most rapidly growing mode as a function of the level of activity for different microswimmer shapes. Nematic alignment can be attributed to reorientations induced by self-generated shear flows. For spherical swimmers ($\gamma = 0$), the only self-generated-flow contribution that reorient microswimmers comes from vorticity. As a consequence, nematic alignement is weak, being only caused by the shape of the perturbed interface, leading to weak flows and as a consequence the fluid film filled with spherical swimmers is stable regardless of the activity of the swimmers α (see Fig. (5.6)). Departures from spherical shape lead to reorientation of the swimmers by both vorticity and strain rate of the ambient flow, and as a result the system becomes unstable for high enough levels of activity. The straining field nematically aligns the particles, which results in stronger flows that destabilize the perturbed interface. For the same reason, as the shape of the swimmer becomes more slender-like, the initial perturbation grows faster in time. The stability of the

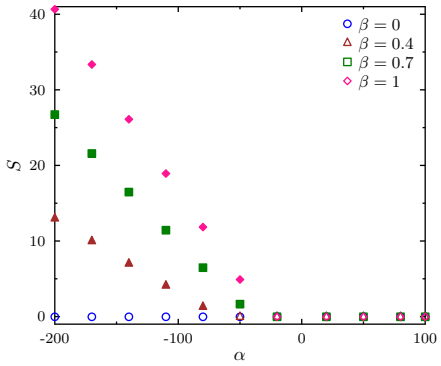

Figure 5.6: Dependence of the growth rate of the perturbation of the bacterial fluid film on the level of activity α for different values of the Bretherton constant γ. Parameter values: $Ca_{act} = 100$, $G = 0$, $K = 1$, $Pe_s = 0.2$, $\Lambda = 0.5$. Solid symbols and empty symbols represent respectively unstable and stable systems.

film as a function of the remaining dimensionless parameters of the problem is explored in Fig. (5.7). The effect of the dimensionless wavenumber of the linear perturbation on the stability of the film is analyzed in Fig. (5.7a). Surface tension stabilizes short wavelength perturbations. As the wavelength of the perturbation increases, the rate at which the initial perturbation decays in time drops. Only at long wavelengths, active forces overcome capillary and viscous forces leading to the growth of the initial perturbation, provided that the level of activity is above a certain threshold, whose magnitude depends on the remaining parameters of the problem. Fig. (5.7b) explores the effect of both active capillary number Ca_{act} and Peclet number Pe_s on the temporal growth rate of the perturbation. Ca_{act} can be viewed as the comparison of destabilizing forces over stabilizing forces. Then, it is evident that as Ca_{act} increases, the growthrate of the perturbation S increases. More interesting and less obvious is the effect of confinement on the stability of the film. As confinement increases, both boundary layers merge and Brownian effects become more dominant. This results in a smoothing of the gradients of concentration, polarization, and nematic alignment in the base state. Specifically, gradients in nematic alignment are responsible for active flows. As a consequence, confinement will decrease the strength of these flows and stabilize the system. Similar arguments can be used in Fig. (5.7d), where we show the critical level of activity below which the system becomes unstable as a function of the Peclet number Pe_s for different values of the swimmer parameter Λ. With an increase in the values of either Λ or Pe_s, Brownian effects become dominant and the spatial gradients of nematic alignment smooth out, hence the critical level of activity for the instability increases in absolute value. Finally,

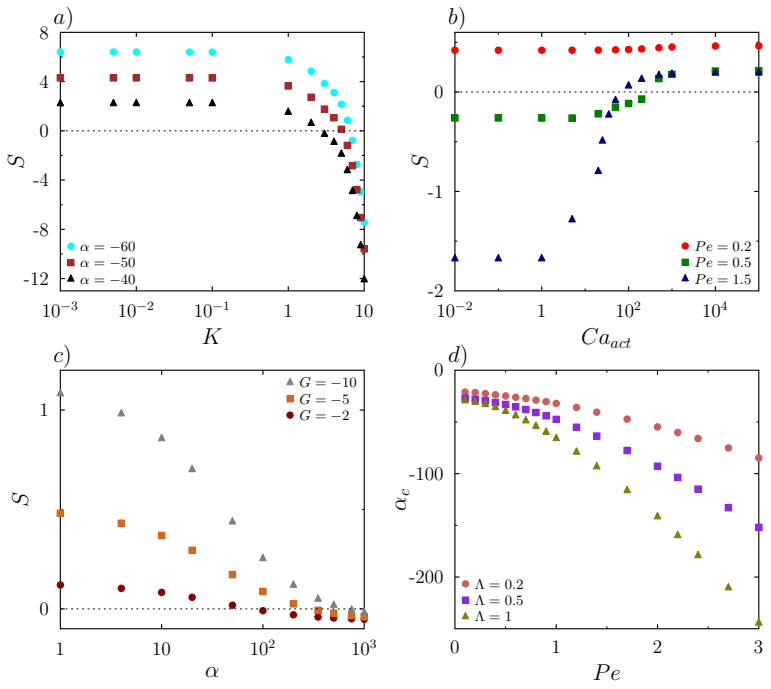

Figure 5.7: Stability of the bacterial fluid film as a function of the dimensionless numbers of the problem. (a) Growth rate S as a function of the wavenumber of the perturbation K for three different values of the activity parameter α. Parameter values: $G = 0$, $Ca_{act} = 10$, $Pe_s = 0.5$, $\Lambda = 0.5$, $\gamma = 1$. (b) Growth rate S as a function of the active capillary number Ca_{act} for three different values of the Peclet number Pe_s. Parameter values: $G = 0$, $\alpha = -30$, $K = 1$, $\Lambda = 0.5$, $\gamma = 1$. (c) Growth rate S as a function of the activity parameter α for three different values of the gravitational number G. Note that we are studying the stability of an inverted film (negative gravity). In this case, activity tends to stabilize the film for pullers. Parameter values: $Ca_{vis} = 1$, $K = 1$, $Pe_s = 1$, $\Lambda = 0.5$, $\gamma = 1$. (d) Marginal stability for the critical level of activity α_c as a function of Peclet number Pe_s for three different values of the swimmer parameter Λ. Parameter values: $G = 0$, $Ca_{act} = 0.1$, $K = 1$, $\gamma = 1$.

we would like to address the case of inverted films, where a heavier fluid is on top of a lighter fluid. We can use the same framework used so far, where we take the gravitational number G to be negative. We would like to answer the following question: Is it possible to stabilize an inverted fluid film by adding micro-organisms? It turns out that suspensions of pullers will stabilize the film for high enough levels of the activity parameter as shown in Fig. (5.7c).

Bacterial fluid jet

We briefly analyzed the stability of a bacterial fluid viscous cylindrical jet. The instability of a jet of a heavy fluid into air has been previously investigated by Plateau.

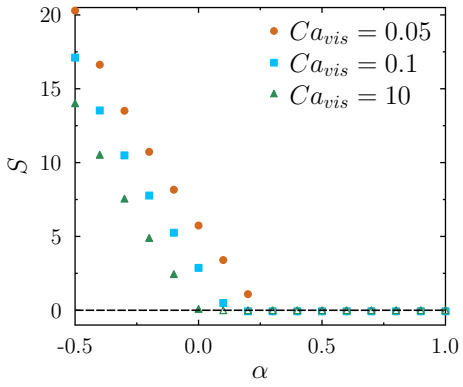

Figure 5.8: Instability of a bacterial fluid jet. Dependence of the growth rate on the level of activity α for different values of the viscous capillary number. Parameter values: $Pe_s = 0.5$, $\Lambda = 0.1$, $K = 1$, $\gamma = 1$. Solid symbols and empty symbols represent respectively unstable and stable systems.

Surface tension renders the cylindrical jet unstable by disintegrating it into smaller fluid masses. Here, we show that even if surface tension plays a destabilizing mechanism, a suspension of pullers can also stabilize the jet. Similarly as in the inverted bacterial film, suspensions of pullers tend to stabilize the jet (see Figs. (5.8) and (5.9).

5.6 Conclusion remarks

The temporal evolution of a 3-D bacterial fluid film has been analyzed. The distribution of particles is described by means of a continuum kinetic model, which is solved along with the Stokes' equations for the fluid. The stability of the film is carried out via normal mode analysis. The base state is derived theoretically, which is characterized by no flow and only non-zero vertical gradients. We perturbed the system, linearized the equations for small perturbations and applied normal mode analysis. The active stresses exerted by the microorganisms into the fluid create fluid flows that can destabilize the air-fluid interface. We found that the film is always stable for suspensions of pullers, whereas the instability arises above a critical level of activity for suspensions of pushers. Low wavenumbers of the perturbation, high capillary numbers, high bacterial confinement and high Brownian effects prevent the instability from happening. Additionally, we addressed the stability of inverted bacterial fluid films (Rayleigh Taylor instability) and bacterial fluid jets (Rayleigh Plateau instability). We found that sufficiently concentrated suspensions of contractile swimmers

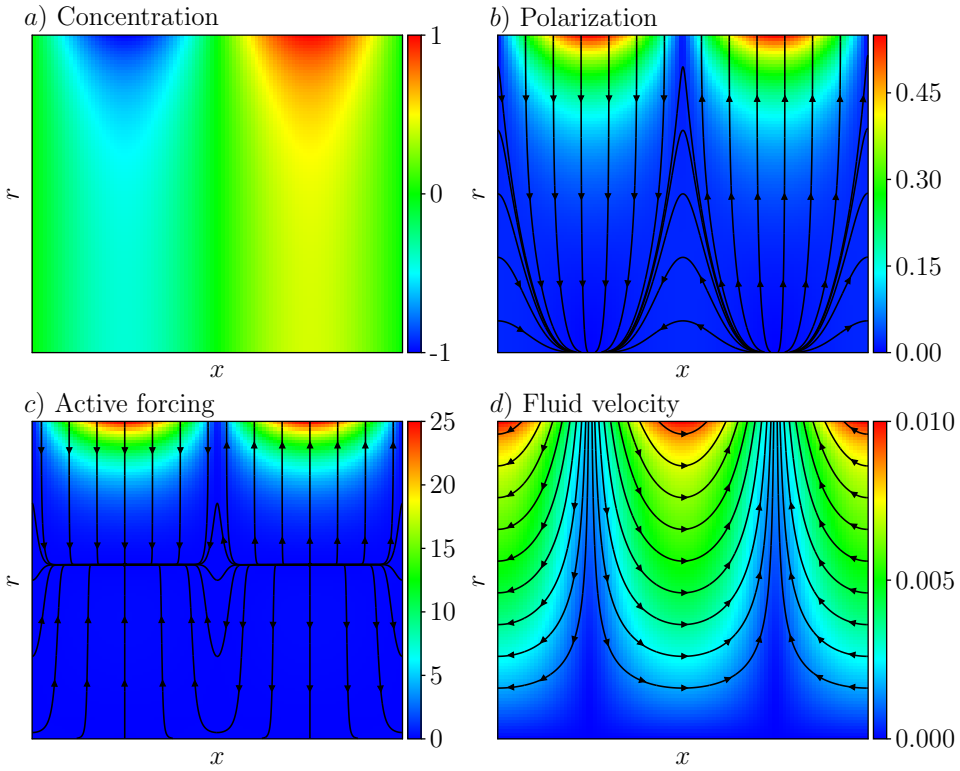

Figure 5.9: Instability of a bacterial fluid jet. Parameters correspond to a stable jet (suspensions of pullers). $Pe_s = 0.3$, $\Lambda = 0.3$, $\alpha = 10$, $K = 1$, $Ca_{vis} = 0.1$, $\gamma = 1$. Note: the fluid velocity is multiplied by $2\pi r$. Note: Active forcing has two points of zero forcing.

can stabilize both instabilities.

5.7 Acknowledgements

Chapter 5, in part, is a manuscript in preparation; authored by R. Alonso-Matilla and D. Saintillan, "Stability of active fluid films". The dissertation author is the primary author of this work.

Chapter 6

Microfluidic rheology of active particle suspensions: Kinetic theory

6.1 Introduction

The transport of motile cells and other self-propelled swimmers through small-scale microfluidic devices has received much scrutiny over the last decade, in part due to its relevance to biological processes such as reproduction[196–198] and its use in engineering applications such as cell sorting and cell concentration.[33, 55, 199, 200] Unlike passive particles whose transport is largely dictated by the imposed flow, the case of active swimmers is significantly more complex due to their self-propulsion, which enables them to swim across streamlines and can cause them to accumulate at boundaries.[41, 123, 150] In the presence of shear, the coupling of self-propulsion and alignment of slender swimmers with the flow has also been shown to result in unexpected transport phenomena such as upstream swimming[138, 201, 202] and migration from low-shear towards high-shear regions in pressure-driven channel flows.[203] Such effects occur even in very dilute suspensions when interparticle interactions are negligible.

As a result of their swimming kinematics, microorganisms also exert active stresses on the carrying fluid, thereby driving local disturbance flows that have been characterized experimentally.[204–206] Many microorganisms are nearly neutrally buoyant, so that the leading-order disturbance that they drive in the surrounding medium is a dipole flow, which can be interpreted as resulting from the equal and opposite thrust and drag forces exerted by the flagella and cell body on the fluid, respectively. When placed in an external flow,

these disturbances can either facilitate or hinder the flow depending on the sign of the dipole strength σ_0 and on its orientation relative to the flow, potentially leading to unusual rheologies. This was first noted in a theoretical study by Hatwalne *et al.*,[167] who argued that extensile particles or so-called pushers for which $\sigma_0 < 0$ should have a negative intrinsic viscosity $[\eta] < 0$, whereas contractile particles or pullers for which $\sigma_0 > 0$ should have $[\eta] > 0$. A number of more sophisticated models have been proposed since,[169, 207–214] which usually extend theories for the rheology of passive rod suspensions[215–217] to account for this active dipole and have led to similar predictions. Of particular relevance to the present study is the model of Saintillan,[209] which calculated the effective viscosity and normal stress differences in a dilute active suspension in uniform shear flow as functions of shear rate. The model showed that the effects of activity are strongest in weak flows, where a reduction in viscosity occurs in pusher suspensions; in stronger flows, dissipative viscous stresses were shown to overtake active stresses and lead to a positive intrinsic viscosity followed by shear-thinning.

Experiments aimed at testing these predictions have been relatively scarce, in part owing to technical difficulties: firstly, the effects of activity on the rheology are strongest at very low shear rates, which are not accessible to standard rheometers; secondly, the viscosity of dilute suspensions is typically close to that of water, whereas rheometers work best with more viscous fluids. Nonetheless, a few experimental techniques have been devised to overcome these challenges. In the case of suspensions of pusher particles, Sokolov and Aranson[168] were the first to estimate the viscosity of thin liquid films containing swimming *B. subtitlis* by measuring the angular velocity of a rotating particle subject to a constant imposed magnetic torque. They indeed reported a viscosity reduction due to activity, which initially became stronger with increasing volume fraction. However, the unusual nature of their experimental setup rendered quantitative comparisons with bulk models difficult. Very recently, Lopez *et al.*[170] performed experiments in a circular Couette cell specially designed to measure torques at very low shear rates, and confirmed the existence of a negative intrinsic viscosity in suspensions of *E. coli*. In the low-shear-rate plateau, they found that the total viscosity could even decrease to zero in sufficiently concentrated suspensions, suggesting that active pusher suspensions can behave as superfluids. The possibility of a negative total viscosity is consistent with other experiments[166, 218] as well as theories[13, 219, 220] that have reported spontaneous unidirectional flows in confined active suspensions; in the case of bulk suspensions, the predicted decrease of the intrinsic zero-shear-rate viscosity towards

zero has also been shown to the driver of hydrodynamic instabilities leading to collective motion.[112]

The case of puller particles was considered by Rafaï *et al.*,[221] who studied suspensions of the micro alga *C. reinhardtii*. They used concentrated suspensions in a cone-plate rheometer, and measured higher shear viscosities in suspensions of live cells than in suspensions of dead cells as predicted by models. The extensional rheology of both pusher and puller suspensions was also recently studied by McDonnell *et al.*[222] using an acoustically-driven microfluidic capillary-breakup extensional rheometer. In agreement with studies in shear flows and with theoretical predictions in extensional flows,[209] they observed a decrease in viscosity in bacterial and sperm suspensions but an increase in algae suspensions.

The present study is primarily motivated by the experiments of Gachelin *et al.*,[118] who devised a microfluidic rheometer based on the deflection of streamlines in the co-flow of a bacterial suspension of *E. coli* and of clear fluid in a rectangular Hele-Shaw geometry. At equal flow rates between the two streams, this deflection is proportional to the viscosity ratio between the two fluids. They also reported a negative particle viscosity in weak flows, followed by an increase to a positive value and eventual shear thinning with increasing flow rate. While these trends agree qualitatively with predictions for bulk suspensions in uniform shear,[169] a direct comparison is difficult owing to the non-uniform distribution achieved by self-propelled particles in confinement: in particular, the tendency of swimmers to spend time in the near-wall high-shear regions in a pressure-driven flow is expected to amplify the effect of activity on the rheology in ways that are not easily anticipated.

In this study, we analyze the effective rheology of a dilute active suspension of self-propelled particles confined between two flat plates and subject to an imposed pressure-driven flow. The theory extends the previous work of Ezhilan and Saintillan,[51] who studied the distribution and transport of self-propelled particles in the same geometry using a continuum model[12, 160] but neglected the effect of the hydrodynamic disturbances induced by the swimmers. Here, this effect is taken into account and the modification of the background flow by the particles is used to obtain estimates for the suspension viscosity as a function of flow rate and concentration. Details of the theoretical model are presented in Sec. 6.2, where we also derive an approximate theory for weak flows and wide channels. Numerical results are discussed in Sec. 6.3 where good agreement with experiments is demonstrated. Our results are also in agreement with previous bulk models, and in particular demonstrate that the effect of activity is strongest at low flow rates, where pushers tend to decrease

the suspension viscosity whereas pullers enhance it. In stronger flows, dissipative stresses overcome the effects of activity leading to increased viscosities followed by shear-thinning. The effects of confinement and number density are also analyzed, and our results confirm the apparent transition to superfluidity reported in recent experiments on pusher suspensions at intermediate densities. We also derive an approximate analytical expression for the effective viscosity in the limit of weak flows and wide channels, and demonstrate good agreement between theory and numerical calculations.

6.2 Theoretical model

6.2.1 Problem definition and Fokker-Planck description

We analyze the effective rheology of a dilute suspension of self-propelled slender particles of length ℓ and aspect ratio r placed between two planar parallel walls in a Newtonian fluid with shear viscosity μ (Fig. 7.1). The suspension is subject to an imposed pressure-driven Poiseuille flow, whose velocity field in the absence of particles is given by

$$\mathbf{U}(z) = U_m \left[1 - (z/H)^2\right] \hat{\mathbf{y}}, \tag{6.1}$$

where $2H$ denotes the gap width and U_m is the maximum velocity at the centerline ($z = 0$). The corresponding shear rate profile is linear across the channel:

$$\dot{\Gamma}(z) = -\frac{2U_m}{H^2} z. \tag{6.2}$$

We also introduce the characteristic shear rate $\overline{\dot{\Gamma}} = U_m/H$, and note that the maximum shear rate at the walls is $2\overline{\dot{\Gamma}}$. The particles have high aspect ratio ($r \gg 1$), and their length ℓ is assumed to be small compared to the channel dimensions so that it can be effectively neglected: $\ell \ll H$. The distribution of particles inside the channel is described according to classic models[12, 160, 223] by the probability density function $P(\mathbf{R}, \mathbf{p}, t)$ of finding a particle at position $\mathbf{R}$ with unit director $\mathbf{p}$ at time t. It satisfies a Fokker-Planck equation

$$\frac{\partial P}{\partial t} + \nabla_R \cdot \mathbf{J} + \nabla_p \cdot \mathbf{j} = 0, \tag{6.3}$$

where $\mathbf{J}$ and $\mathbf{j}$ denote the translational and angular particle fluxes and are modeled as

$$\mathbf{J} = (v_0\mathbf{p} + \mathbf{u})P - d_t\nabla_R P, \tag{6.4}$$

$$\mathbf{j} = (\gamma(\mathbf{I} - \mathbf{pp}) \cdot \mathbf{E} \cdot \mathbf{p} + \tfrac{1}{2}\boldsymbol{\Omega} \times \mathbf{p})P - d_r\nabla_p P. \tag{6.5}$$

Here, v_0 is the swimming velocity of an isolated particle, and d_t and d_r denote the translational and rotational Brownian diffusion coefficients, which are assumed to be constant and isotropic. The velocity $\mathbf{u}$ entering the fluxes is the total fluid velocity, which is the sum of the imposed flow $\mathbf{U}(\mathbf{x})$ of Eq. (6.1) and of the disturbance velocity $\mathbf{u}^d(\mathbf{x}, t)$ due to the presence of the particles, whose calculation is detailed in §. 6.2.2. The angular flux arises due to the rate-of-strain tensor $\mathbf{E} = (\nabla\mathbf{u} + \nabla\mathbf{u}^t)/2$ and vorticity $\boldsymbol{\Omega} = \nabla \times \mathbf{u}$; it involves the Bretherton constant γ,[194] which for a spheroidal particle is given by $\gamma = (r^2 - 1)/(r^2 + 1)$.

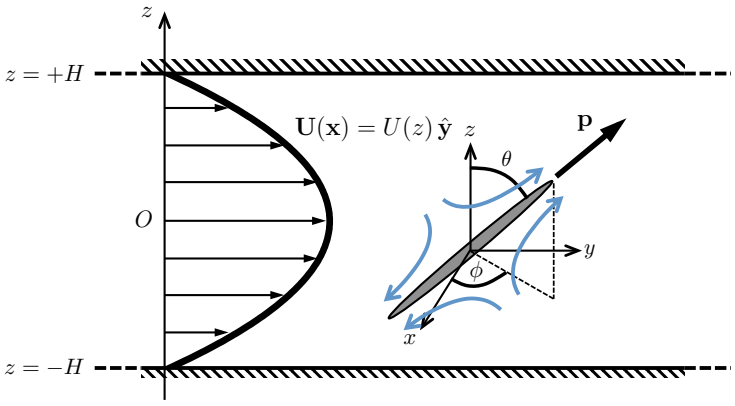

Figure 6.1: Problem definition: a dilute suspension of self-propelled particles (with swimming director $\mathbf{p}$) is placed in a plane Poiseuille flow with velocity $\mathbf{U}(\mathbf{x})$ between two parallel flat plates separated by $2H$. The arrows surrounding the particle show the direction of the disturbance flow for a pusher ($\sigma_0 < 0$).

We focus here on the case of a dilute suspension, defined as $n\ell^3 \ll 1$ where n is the mean number density. In this limit, the distribution of particles is expected to be homogeneous in the x and y directions, and the disturbance velocity simplifies to $\mathbf{u}^d(\mathbf{x}, t) = u^d(z, t)\hat{\mathbf{y}}$. At steady state, Eqs. (6.3)–(6.5) can then be rewritten as

$$v_0 \cos\theta \frac{\partial P}{\partial z} - d_t \frac{\partial^2 P}{\partial z^2} + \gamma S(z)\nabla_p \cdot [(\mathbf{I} - \mathbf{pp}) \cdot \hat{\mathbf{y}} \cos\theta P] = d_r \nabla_p^2 P, \tag{6.6}$$

where $S(z) = \Gamma(z) + du^d/dz$ is the total shear rate. Eq. (6.6) expresses the balance of self-propulsion and translational diffusion in the z direction, shear alignment by the local

flow, and rotational diffusion. It is subject to a no-flux boundary condition at both channel walls:[51]

$$\mathbf{J} \cdot \hat{\mathbf{z}} = 0 \quad \text{i.e.} \quad d_t \frac{\partial P}{\partial z} = v_0 \cos\theta \, P \quad \text{at} \quad z = \pm H. \tag{6.7}$$

Finally, the probability density function P is normalized as

$$\frac{1}{2H} \int_{-H}^{H} \int_{\Omega} P(z, \mathbf{p}) \, d\mathbf{p} \, dz = n, \tag{6.8}$$

where Ω denotes the unit sphere of orientation.

6.2.2 Particle extra stress and disturbance flow

The calculation of the disturbance flow and of effective rheological properties requires modeling of the particle extra stress, which includes contributions from active dipolar stresses due to self-propulsion, from Brownian motion, and from the imposed flow: $\mathbf{\Sigma}^p(z) = \mathbf{\Sigma}^a + \mathbf{\Sigma}^b + \mathbf{\Sigma}^f$. Following Saintillan,[169] each term is modeled as

$$\mathbf{\Sigma}^a(z) = n\sigma_0 \left[\langle \mathbf{pp} \rangle - \frac{\langle \mathbf{I} \rangle}{3} \right], \tag{6.9}$$

$$\mathbf{\Sigma}^b(z) = 3nk_BT \left[\langle \mathbf{pp} \rangle - \frac{\langle \mathbf{I} \rangle}{3} \right], \tag{6.10}$$

$$\mathbf{\Sigma}^f(z) = n\ell^3 A\mu S(z) \left[\langle \mathbf{pppp} \rangle - \frac{\mathbf{I}}{3} \langle \mathbf{pp} \rangle \right] : \hat{\mathbf{y}}\hat{\mathbf{z}}, \tag{6.11}$$

where angle brackets $\langle \cdot \rangle$ denote the orientational average:

$$\langle h(\mathbf{p}) \rangle = \frac{1}{n} \int_{\Omega} h(\mathbf{p}) P(z, \mathbf{p}) \, d\mathbf{p}. \tag{6.12}$$

The active stress $\mathbf{\Sigma}^a$ arises from the force dipoles that neutrally buoyant self-propelled particles exert on the fluid[167] and involves the stresslet strength σ_0, which is negative for pushers[206] such as *E. coli* and *B. subtilis* and positive for pullers[204, 205] such as *C. reinhardtii*. The case of $\sigma_0 = 0$ describes hypothetical particles known as movers that swim but do not exert active stresses. The Brownian stress $\mathbf{\Sigma}^b$ arises from Brownian rotations of the particles and involves the thermal energy unit k_BT. Finally, $\mathbf{\Sigma}^f$ is a passive dissipative stress resulting from the inextensibility of the particles in the local strain field $\mathbf{E} = S(z)\hat{\mathbf{y}}\hat{\mathbf{z}}$ that they experience.[217] The dimensionless constant A depends on the shape of the particles;

for high-aspect-ratio particles ($r \gg 1$), it is obtained from slender-body theory [215, 224] as $A = \pi/6 \log(2r)$.

Knowledge of the stress distribution across the channel allows one to solve for the disturbance fluid velocity, which satisfies the Stokes equations: $-\mu\nabla^2\mathbf{u}^d + \nabla q^d = \nabla \cdot \boldsymbol{\Sigma}^p$, $\nabla \cdot \mathbf{u}^d = 0$, where q^d is the disturbance pressure. Straightforward integration provides an expression for the velocity in terms of the particle shear stress as

$$u^d(z) = -\frac{1}{\mu}\int_{-H}^{z} \Sigma^p_{yz}(z')\, dz', \tag{6.13}$$

which scales linearly with $n\ell^3$ in the dilute limit. As a result, inclusion of the mean-field disturbance velocity into the Smoluchowski equation for the particle distribution ensures asymptotic accuracy of our model to order $(n\ell^3)^2$. In addition to the flow field, a disturbance pressure gradient is also established in the cross-stream direction as a result of normal stresses: $q^d(z) = \Sigma^p_{zz}(z) + q^d_0$.

Equations (6.9)–(6.11) can also be used to estimate the modification of the solvent viscosity by the particles. First, we define a local particle viscosity $\eta_p(z)$ based on a generalized Newtonian model as

$$\eta_p(z) = \frac{\Sigma^p_{yz}(z)}{S(z)} = \frac{n(3k_BT + \sigma_0)\langle p_y p_z\rangle}{\Gamma(z) + du^d/dz} + \mu n\ell^3 A\langle p_y^2 p_z^2\rangle. \tag{6.14}$$

For convenient comparison with the experiments, it is also useful to introduce a global measure of the particle viscosity that is independent of z. To this end, we follow the approach of Gachelin *et al.*[118] and consider the modification of the net flow rate in the channel by the particles. The imposed flow rate per unit width in the absence of particles is given by

$$\dot{Q}_i = \int_{-H}^{H} U(z)\, dz = \frac{4}{3}U_m H, \tag{6.15}$$

whereas the disturbance flow rate due the presence of the particles is

$$\dot{Q}_d = \int_{-H}^{H} u^d(z)\, dz. \tag{6.16}$$

Assuming a Poiseuille law of the form $\dot{Q} = \kappa/\eta$ for the flow rate per unit width, where $\kappa = -(2H^3/3)dq/dy$, and dq/dy is the imposed pressure gradient, we can define a dimensionless

relative Newtonian viscosity as the ratio

$$\eta_r = \frac{\dot{Q}_i}{\dot{Q}_i + \dot{Q}_d} = \left[1 + \frac{3}{4U_m H}\int_{-H}^{H} u^d(z)\, dz\right]^{-1}. \tag{6.17}$$

Clearly, $\eta_r = 1$ in the case of pure solvent ($n\ell^3 = 0$), and departures from this value quantify the effect of the particles on the net viscosity. The effective intrinsic viscosity is then given by

$$[\eta] = \eta_r - 1 = -\frac{\dot{Q}_d}{\dot{Q}_i + \dot{Q}_d}. \tag{6.18}$$

From this last expression, it becomes obvious that $[\eta] < 0$ corresponds to a positive disturbance flow rate, i.e. a suspension in which particles enhance the imposed flow.

6.2.3 Non-dimensionalization

In the following, we scale all variables using time scale d_r^{-1}, length scale H, and velocity scale Hd_r. The probability density function P is also scaled by the number density n. Upon non-dimensionalization, the Fokker-Planck equation (6.6) becomes

$$Pe_s \cos\theta \frac{\partial P}{\partial z} - 2\Lambda Pe_s^2 \frac{\partial^2 P}{\partial z^2} + \frac{1}{2}\gamma S(z)\nabla_p \cdot [(\mathbf{I} - \mathbf{pp}) \cdot \hat{\mathbf{y}} \cos\theta P] = \frac{1}{2}\nabla_p^2 P, \tag{6.19}$$

with $S(z) = -Pe_f\, z + du^d/dz$, subject to the boundary conditions

$$\frac{\partial P}{\partial z} = \frac{\cos\theta}{2\Lambda Pe_s} P \quad \text{at} \quad z = \pm 1. \tag{6.20}$$

We have introduced three-dimensionless groups: [51]

$$Pe_s = \frac{v_0}{2d_r H}, \quad Pe_f = \frac{2\overline{\Gamma}}{d_r}, \quad \Lambda = \frac{d_t d_r}{v_0^2}. \tag{6.21}$$

The swimming Péclet number Pe_s is the ratio of the persistence length of swimmer trajectories over the channel width and is a measure of confinement. The flow Péclet number Pe_f is the ratio of the imposed wall shear rate over the rotational diffusivity of the swimmers; equivalently, it is also the ratio of the correlation time d_r^{-1} of swimmer orientations over the characteristic time $(2\overline{\Gamma})^{-1}$ for alignment by the flow. Finally, Λ is a swimmer-specific parameter characterizing the relative magnitude of Brownian diffusion over deterministic swimming. In particular, the boundary condition (6.20) is only valid for positive values, i.e.

in the presence of translational diffusion; the limit of $\Lambda = 0$, which involves a singularity in the distribution of particles at the channel boundaries, is therefore not considered in this work but could be addressed using a different model such as that proposed in our recent work. [14]

Non-dimensionalization of the particle shear stress leads to the simple form

$$\Sigma^p_{yz}(z) = \alpha\langle p_y p_z\rangle + \beta S(z)\langle p_y^2 p_z^2\rangle, \tag{6.22}$$

where we have introduced the dimensionless groups

$$\alpha = \frac{n}{\mu d_r}(\sigma_0 + 3k_BT) \qquad \text{and} \qquad \beta = n\ell^3 A. \tag{6.23}$$

Noting that $k_BT \ll |\sigma_0|$ for typical biological swimmers, $\alpha \approx n\sigma_0/\mu d_r$ describes the relative magnitude of active stresses with respect to dissipative processes. Expressions for the dimensionless disturbance velocity $u^d(z)$, local particle viscosity $\eta_p(z)$, and relative viscosity η_r are then easily obtained as

$$u^d(z) = -\int_{-1}^{z} \Sigma^p_{yz}(z')\, dz', \tag{6.24}$$

and

$$\eta_p(z) = \frac{\alpha\langle p_y p_z\rangle}{-Pe_f\, z + du^d/dz} + \beta\langle p_y^2 p_z^2\rangle, \quad \eta_r = \left[1 + \frac{3}{2Pe_f}\int_{-1}^{1} u^d(z)\, dz\right]^{-1}. \tag{6.25}$$

6.2.4 Approximate theory for weak flows and wide channels

Before proceeding to solve the governing equations numerically, we derive an approximate theory for the viscosities $\eta_p(z)$ and η_r in the limits of weak flows ($Pe_f \to 0$) and wide channels ($Pe_s \to 0$). If the channel is wide, spatial gradients in orientational moments are weak, and we can approximate the distribution function in the form

$$P(z, \mathbf{p}) \approx c(z)P(\mathbf{p}; z), \tag{6.26}$$

where $c(z) = \langle 1\rangle$ is the concentration profile and where the orientation distribution function $P(\mathbf{p}; z)$ is that for an unbounded suspension in uniform simple shear with shear rate $S(z)$. An approximate expression for the concentration in weak flows was previously found by

Ezhilan and Saintillan, [51] as

$$c(z) \approx \frac{B[6\Lambda \cosh B + \cosh Bz]}{6\Lambda B \cosh B + \sinh B} \qquad \text{with} \qquad B^{-1} = \Lambda Pe_s \sqrt{\frac{12}{1+6\Lambda}}. \tag{6.27}$$

In the limit of weak flow, the orientation distribution $P(\mathbf{p}; z)$ can be also calculated asymptotically as a regular expansion in powers of shear rate, [216] leading to the approximation

$$P(\mathbf{p}; z) \approx \frac{1}{4\pi} + \frac{\gamma}{8\pi} S(z) p_y p_z + ... \tag{6.28}$$

The orientational moments are then readily obtained as

$$\langle p_y p_z \rangle \approx \frac{\gamma}{30} S(z) c(z), \qquad \langle p_y^2 p_z^2 \rangle \approx \frac{1}{15} c(z). \tag{6.29}$$

Using Eqs. (6.27) and (6.29), it is then straightforward to estimate the dimensionless particle shear stress and local viscosity as

$$\Sigma_{yz}^p(z) \approx \frac{1}{30} \left(\alpha\gamma + 2\beta\right) c(z) S(z), \qquad \eta_p(z) \approx \frac{1}{30} \left(\alpha\gamma + 2\beta\right) c(z). \tag{6.30}$$

In very wide channels and away from walls we have $c(z) \approx 1$, and η_p simplifies to the low-shear-rate asymptote previously derived by Saintillan [169] for a bulk suspension in uniform shear. If we further assume that $S(z) \approx -Pe_f z$, which is valid in very dilute systems, we can also derive an analytical expression for the relative viscosity as

$$\eta_r \approx \left[1 - \frac{1}{10} \left(\alpha\gamma + 2\beta\right) \frac{2\sinh B - 2B\cosh B + B^2 \sinh B + 2B^3 \Lambda \cosh B}{B^2 (6\Lambda B \cosh B + \sinh B)}\right]^{-1}. \tag{6.31}$$

In very wide channels ($B \to \infty$) and dilute systems ($n\ell^3 \to 0$):

$$\eta_r \to \left[1 - \frac{1}{30} \left(\alpha\gamma + 2\beta\right)\right]^{-1} \approx 1 + \frac{1}{30} \left(\alpha\gamma + 2\beta\right), \tag{6.32}$$

which again matches the low-shear-rate asymptote in a bulk suspension. [169] As shown below in Sec. 6.3, Eq. (6.31) indeed captures the relative viscosity quantitatively at low concentrations and in wide channels.

6.2.5 Numerical solution and parameter selection

Equation (6.19) subject to boundary conditions (6.20) was solved numerically for a range of parameter values using a finite-volume numerical algorithm previously developed by Ezhilan and Saintillan. [51] The algorithm solves for the full distribution function in the three-dimensional space $\Omega \times [-1, 1]$ and satisfies the normalization condition of Eq. (6.8) to machine precision. Due to the nonlinearity of the governing equations, the unsteady version of Eq. (6.19) was marched explicitly in time to steady state, coupled to a semi-analytical solution for the fluid velocity based on Eq. (6.24).

Simulation parameters were estimated based on the experiments of Gachelin *et al.*, [118] Rusconi *et al.* [203] and Lopez *et al.* [170] These studies used *E. coli* bacteria, with body length $\ell \approx 2\,\mu$m, swimming speed $v_0 \approx 20\,\mu\text{m.s}^{-1}$, and dipole strength $\sigma_0 \approx -9.46 \times 10^{-19}\,\text{N.m}$. The translational and rotational diffusivities were estimated as $d_t \approx 1.6 \times 10^{-11}\,\text{m}^2\text{.s}^{-1}$ and $d_r \approx 0.5\,\text{s}^{-1}$ (based on the tumbling rate of the bacteria). The number density is varied in the range of $n \approx 10^{14}$ to $10^{16}\,\text{m}^{-3}$, which is consistent with typical experiments, and the mean shear rate is varied between 0 and $250\,\text{s}^{-1}$. Based on these estimates, the activity parameter α ranges from 1 to 10 in absolute value; we focus in this study on the case of pushers for which $\alpha < 0$, though a few results are also shown for pullers ($\alpha > 0$) as well as movers ($\alpha = 0$). Finally, we set $\gamma = 1$ in all of our calculations, as is appropriate for slender swimmers, and most of the results presented here are for channel half widths of $H = 10\,\mu$m and smaller, which is on the lower end of typical experimental values.

6.3 Results and discussion

6.3.1 Particle distributions

We first analyze steady-state particle distributions across the channel, with special focus on the orientational moments governing the effective rheology. Some of these results echo those presented in our previous work, [51] but also extend them to higher-order moments and differ slightly due to the inclusion of the disturbance velocity u_d, which was neglected in that prior study. Concentration profiles $c(z) = \langle 1 \rangle$ are illustrated in Fig. 6.2 and show strong accumulation of particles at the channel walls in agreement with experiments, [41, 118, 123, 150] numerical simulations, [120, 225–227] and theoretical models. [14, 51, 124, 125] As explained in previous studies, this accumulation is to leading order simply the result of

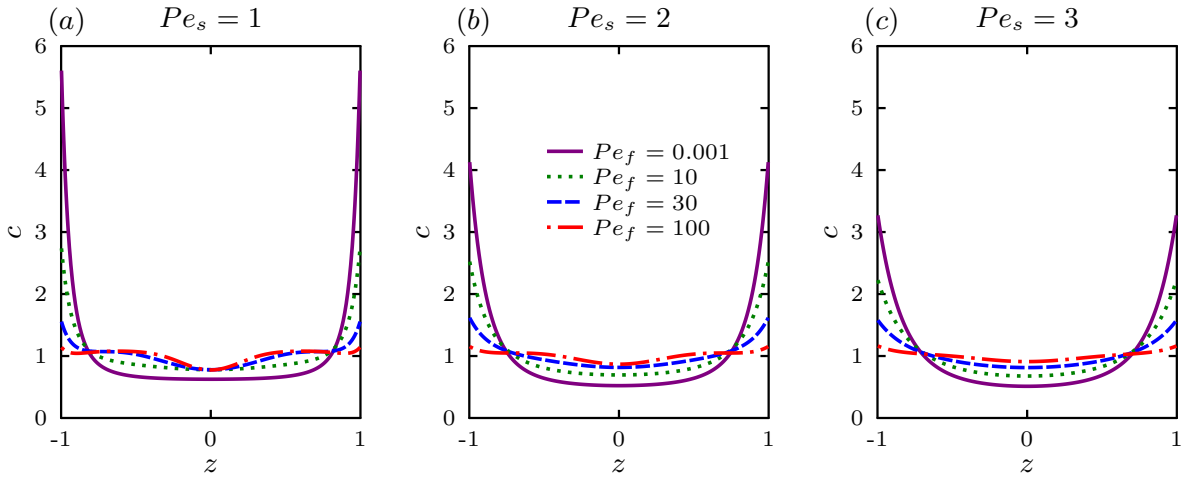

Figure 6.2: Concentration profiles for $\Lambda = 0.02$, $\alpha = -5$, $\beta = 1$, different values of Pe_f, and increasing levels of confinement: (a) $Pe_s = 1$, (b) $Pe_s = 2$, and (c) $Pe_s = 3$.

self-propulsion and confinement, [51] and is also amplified by hydrodynamic interactions in the case of pusher particles. [41] The influence of the flow and swimming Péclet numbers is also as expected. In particular, increasing Pe_s is equivalent to decreasing the channel width, which results in the interaction and eventual merging of the two accumulation layers. Increasing Pe_f also causes a decrease in accumulation due to the reorientation of the particles by the shear, which limits their ability to swim towards boundaries by reducing the wall-normal polarization. [51] This effect of flow strength was also recently observed in the microfluidic experiments of Figueroa-Morales *et al.* [119] Another effect of increasing Pe_f is the appearance of a weak depletion near the channel centerline, which is also observed in experiments [203] and results from the preferential trapping of the particles in high-shear near-wall regions due to their nematic alignment with the flow. This depletion is most notable in wide channels ($Pe_s = 1$) as rationalized by previous theoretical models. [51, 228] The reader is referred to our previous modeling work [51] for a more thorough analysis of these various effects, including the derivation of scaling laws for the thickness of the wall accumulation layer and centerline depletion, as well as their relation to the polarization and nematic parameter fields.

We first plot the second moment $\langle p_z^2 \rangle$ in Fig. (6.3), which quantifies particle alignment along the z-direction, and decreases with shear. Walls foster both wall-normal polarization and vertical alignment. As Pe_f increases, the value of $\langle p_z^2 \rangle$ drops near high shear regions, becoming maximum at the center of the channel. In anticipation of the rheology results

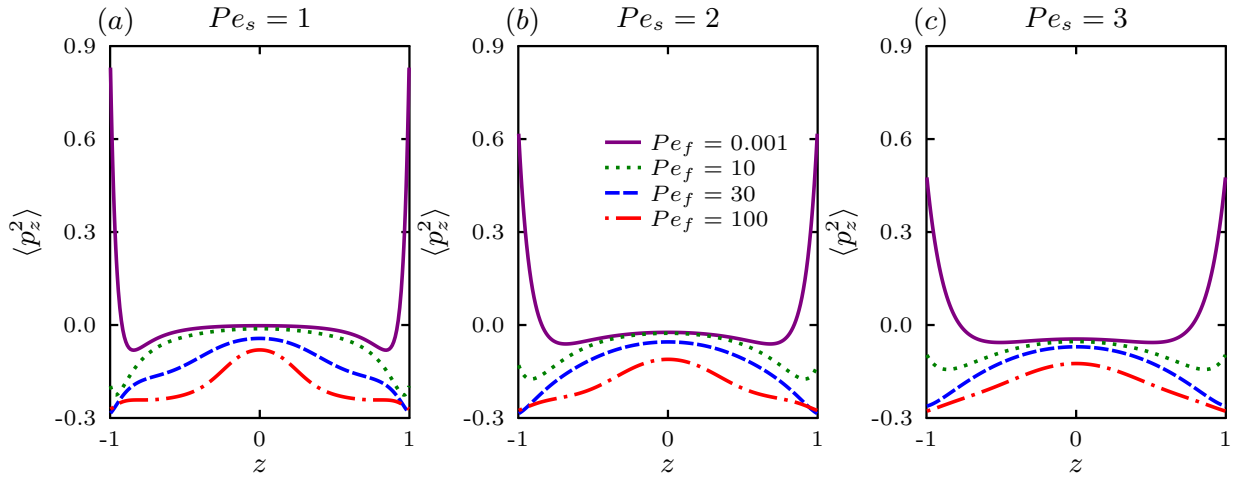

Figure 6.3: Profiles of the diagonal component $\langle p_z p_z \rangle$ of the nematic order parameter tensor for $\Lambda = 0.02$, $\alpha = -5$, $\beta = 1$, different values of Pe_f, and increasing levels of confinement: (a) $Pe_s = 1$, (b) $Pe_s = 2$, and (c) $Pe_s = 3$.

discussed earlier, we turn our attention to the second and fourth orientational moments, which are known to affect the particle shear stress and effective viscosity via Eqs. (6.22) and (6.25). The off-diagonal component $\langle p_y p_z \rangle$ of the nematic order parameter tensor, which enters the active contribution to the particle stress, is plotted in Fig. 6.4 for the same parameters as in Fig. 6.2. Unsurprisingly, we find that the particles align under the local shear, leading to a net shear nematic alignment across the channel. Upon increasing flow rate, $\langle p_y p_z \rangle$ first increases strongly near the walls, since the concentration and shear rate are both highest there. As Pe_f keeps increasing, the weakening of wall accumulation becomes evident, causing the maximum in shear alignment to shift away from the walls towards the shear-trapping region where the particle concentration is the highest. Corresponding data for the fourth moment $\langle p_y^2 p_z^2 \rangle$, which enters the dissipative contribution to the particle stress, is shown in Fig. 6.5. This fourth moment, which is always positive, follows trends very similar to the concentration profiles of Fig. 6.2, in agreement with the weak flow estimate of Eq. (6.29). In particular, it is sharply peaked near the walls in weak flows but becomes nearly uniform in stronger flows.

6.3.2 Particle shear stress and disturbance flow

Both moments $\langle p_y p_z \rangle$ and $\langle p_y^2 p_z^2 \rangle$ calculated above enter the particle shear stress Σ_{yz}^p in Eq. (6.22), which is plotted in Fig. 6.6 for pushers, movers, and pullers at different flow

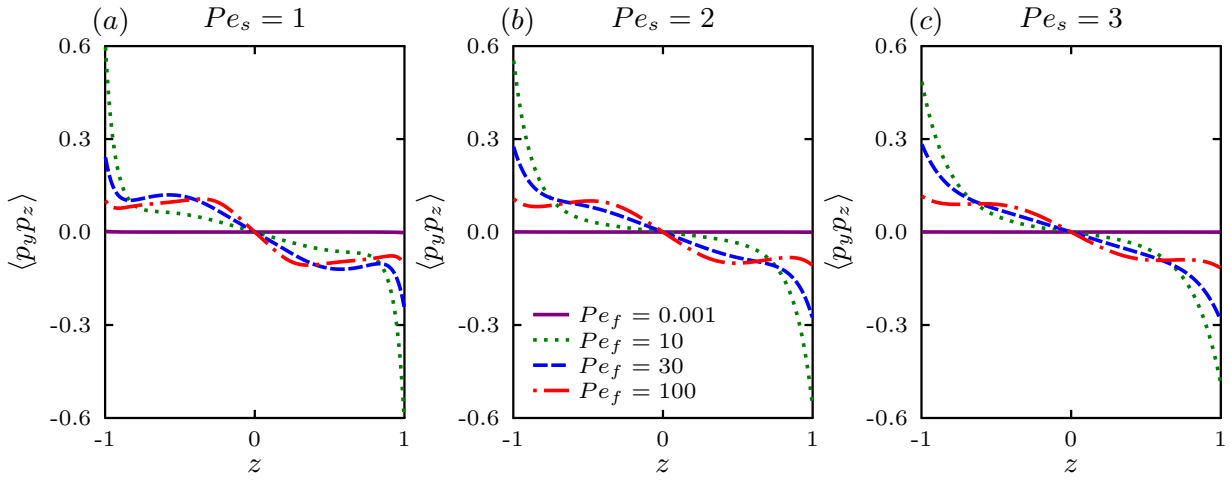

Figure 6.4: Profiles of the off-diagonal component $\langle p_y p_z \rangle$ of the nematic order parameter tensor for $\Lambda = 0.02$, $\alpha = -5$, $\beta = 1$, different values of Pe_f, and increasing levels of confinement: (a) $Pe_s = 1$, (b) $Pe_s = 2$, and (c) $Pe_s = 3$.

strengths. In all cases, the particle shear stress is an odd function of z as expected from symmetry considerations, and its magnitude tends to increase with flow strength as a result of the passive stress $\boldsymbol{\Sigma}^f$, which scales linearly with the local shear rate. The trends in the case of pushers, however, are more complex: we find that the sign of the shear stress changes at a critical flow strength, indicating a change in rheological behavior. This reversal results from the competition between active and dissipative stresses, which are of opposite signs for pushers, and will be discussed in more detail below. Movers and pullers, however, do not exhibit this reversal and behave in a qualitatively similar way.

These trends on the particle stress are easier to interpret in terms of the disturbance flow profiles, which are obtained by integration of Σ^p_{yz} according to Eq. (6.24) and plotted in Fig. 6.7. In the case of movers and pullers in Figs. 6.7(b-c), the disturbance velocity is always negative across the entire channel and has a roughly parabolic profile, indicating that the effects of the particles is to slow down the imposed pressure-driven flow, as would be expected in the case of passive rodlike particles. [216, 229] This effect, which becomes stronger with increasing Pe_f, can be interpreted as an increase in the effective shear viscosity due to the particles, which results from both passive stresses and active stresses in the case of pullers. This explains, in particular, why the disturbance flow is stronger for pullers than movers. The case of pushers in Fig. 6.7(a), however, is more complex and interesting. In weak flows, the disturbance velocity is positive suggesting an enhancement of the flow rate with respect to

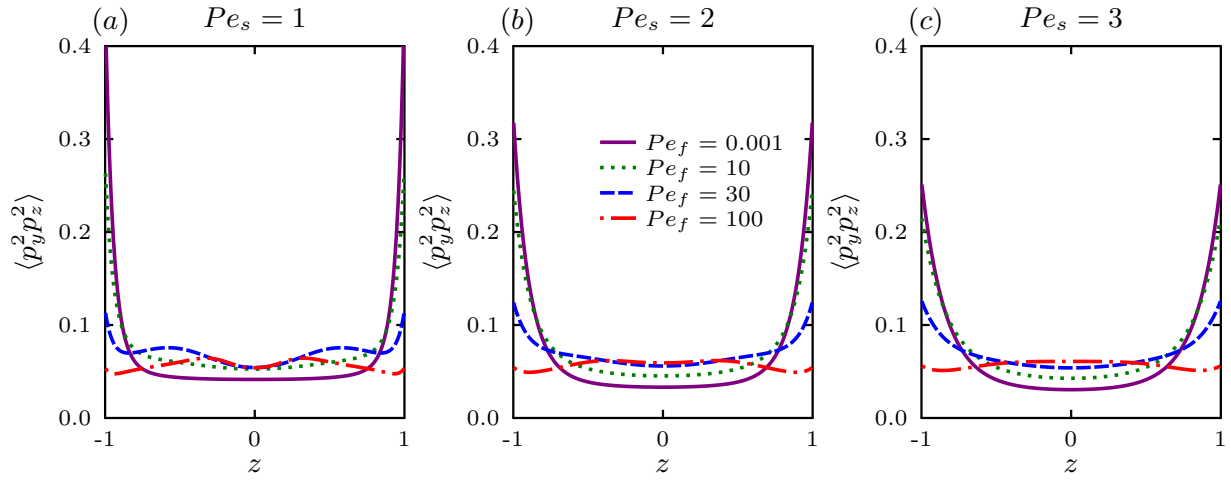

Figure 6.5: Profiles of the component $\langle p_y^2 p_z^2 \rangle$ of the fourth-order orientational moment for $\Lambda = 0.02$, $\alpha = -5$, $\beta = 1$, different values of Pe_f, and increasing levels of confinement: (a) $Pe_s = 1$, (b) $Pe_s = 2$, and (c) $Pe_s = 3$.

the imposed flow; this will be confirmed in Sec. **??** where we report relative viscosities below one. This enhancement is the result of active stresses, which are strongest in the near-wall accumulation layer in weak flows as shown in Fig. 6.4; consequently, the profiles are nearly flat in the bulk of the channels with sharp gradients near the walls. Above a certain flow strength, the disturbance velocity decreases to become negative as active stresses become weaker and the effect of dissipative stresses is more significant; this non-monotonic trend will be reflected in the viscosity data below. The profile shape also becomes more parabolic in strong flows owing to the nearly linear particle shear stress distribution in this case.

6.3.3 Effective rheology

We now turn to the effective rheology of the suspension, first considering the local particle viscosity $\eta_p(z)$, which is plotted in Fig. 6.8. Unsurprisingly, the local viscosity varies across the channel due to the combined effects of confinement and non-uniform shear rate, both of which affect the local orientation distribution. In suspensions of movers and pullers in Figs. 6.8(b-c), the particle viscosity is found to be positive everywhere in the channel. In weak flows, it is maximum near the walls due to the strong particle accumulation and strong shear rate there. As the flow strength increases, shear-thinning is observed as in the classic case of passive rod-like particles [216] though it occurs predominantly near the walls, eventually leading to a weak maximum in the viscosity near the centerline at high values of

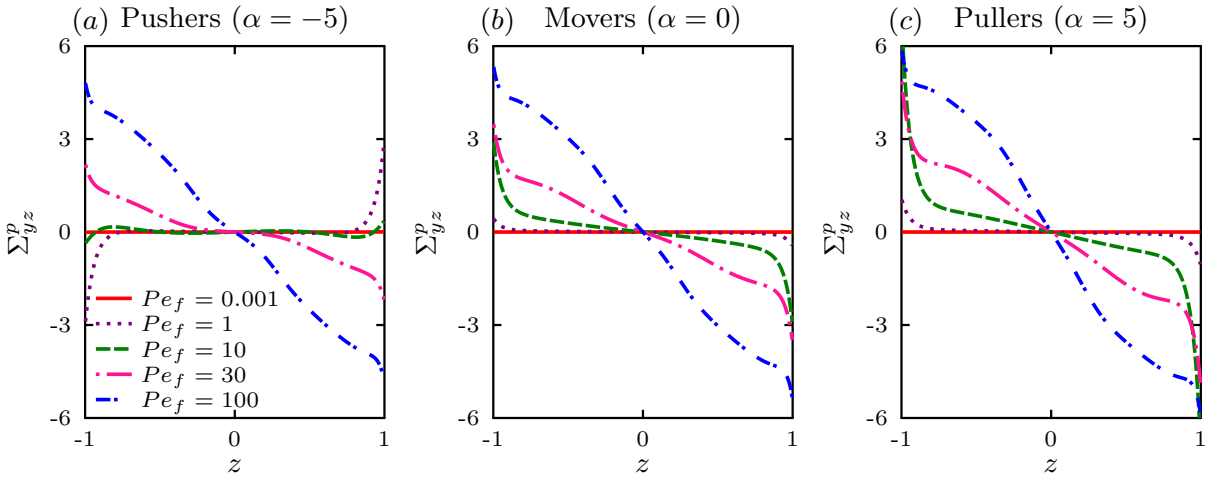

Figure 6.6: Particle shear stress profiles $\Sigma^p_{yz}(z)$ for $Pe_s = 1$, $\Lambda = 0.02$, $\beta = 1$ and for different flow strengths Pe_f in the case of: (a) pushers ($\alpha < 0$), (b) movers ($\alpha = 0$), and (c) pullers ($\alpha > 0$).

Pe_f; this is consistent with the standard explanation of shear-thinning in rod suspensions due to the nematic alignment of the particles with the flow, which is strongest in the high-shear near-wall regions but negligible at the centerline where the shear rate vanishes. The case of pushers is illustrated in Fig. 6.8(a). In weak flows, the particle viscosity is strongly negative close to the boundaries but slightly positive in the low-shear regions close to the centerline; this explains the enhancement of the flow and the plug-like disturbance velocity profiles observed in Fig. 6.7(a). At intermediate Pe_f, the viscosity becomes positive near the channel walls due to the strong nematic alignment of the particles there, which causes the passive contribution to the stress to dominate the active contribution in Eq. (6.22), though it remains negative near the centerline where the shear rate is weak. This change in sign explains the non-monotonicity of the velocity profiles in Fig. 6.7(a): for a given pressure gradient, the flow is hindered near the walls where $\eta_p > 0$, whereas it is enhanced near the centerline where $\eta_p < 0$ (see the curve for $Pe_f = 10$). In strong flows, the local viscosity becomes positive throughout the channel due to passive stresses and reaches its maximum at the centerline.

The net effect of these results on the flow rate in summarized in Fig. 6.9, showing the relative viscosity η_r as a function of the various parameters. Fig. 6.9(a) illustrates the effect of flow strength and activity: in suspensions of movers and pullers, shear-thinning is observed with increasing flow rate as occurs in passive rod suspensions; the relative viscosity,

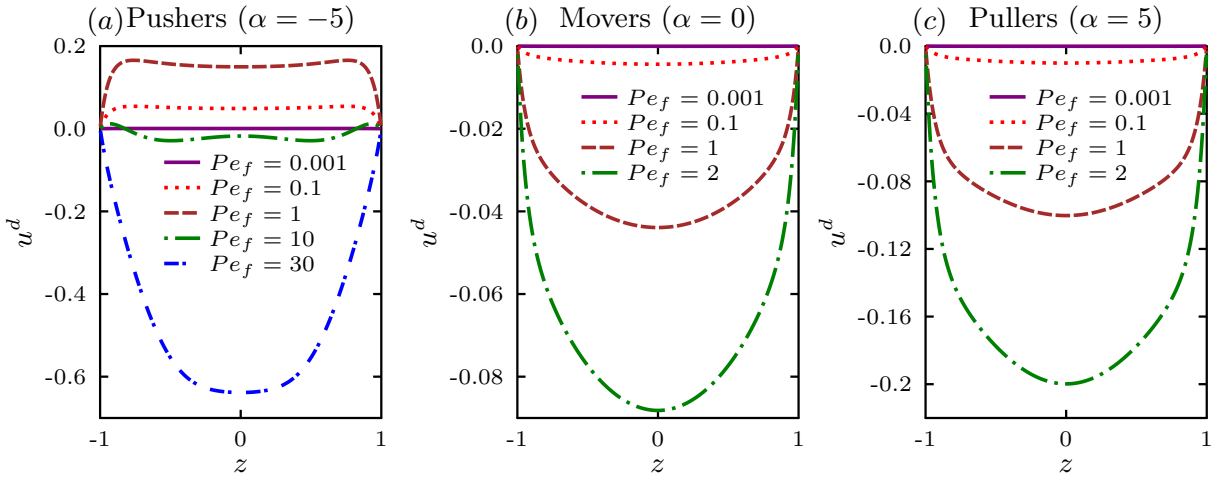

Figure 6.7: Disturbance velocity profiles $u^d(z)$ for $Pe_s = 1$, $\Lambda = 0.02$, $\beta = 1$ and for different flow strengths Pe_f in the case of: (a) pushers ($\alpha < 0$), (b) movers ($\alpha = 0$), and (c) pullers ($\alpha > 0$).

however, is enhanced by activity in the case of pullers as known from previous models [169] and experiments. [221, 222] The case of pushers shows a non-monotonic dependence on flow rate: in weak flows, active stresses dominate resulting in a relative viscosity below one; as flow rate increases, the dissipative stresses become stronger leading to an increase in η_r, which becomes greater than one and eventually shear-thins in very strong flows. These trends are all consistent with the experiments of Gachelin *et al.* [118] and Lopez *et al.* [170], and also agree qualitatively with previous bulk models. [169] Confinement, however, has a quantitative effect as depicted in Fig. 6.9(b) showing the same results in the case of pushers but for different values of Pe_s. The effect is found to be stronger in weak flows, where increasing confinement reduces the effect of activity: this is primarily the consequence of the merging of the accumulation layers and flattening of the concentration profile, which drives more particles towards the center of the channel where the shear rate is weaker.

The effect of number density n is described in Figs. 6.9(c-d), with the caveat that our model is based on a dilute assumption and is therefore likely inaccurate at high concentrations. In Fig. 6.9(c), the number density n is varied while keeping the ratio of the two parameters α and β constant. As expected, increasing density enhances the effect of both active stresses (at low flow rates) and passive stresses (at high flow rates), leading to more pronounced departures from case of pure solvent ($\eta_r = 1$). The transition from $\eta_r < 1$ to $\eta_r > 1$, however, always occurs at a fixed flow rate of $Pe_f \approx 10$ for this choice of parameters,

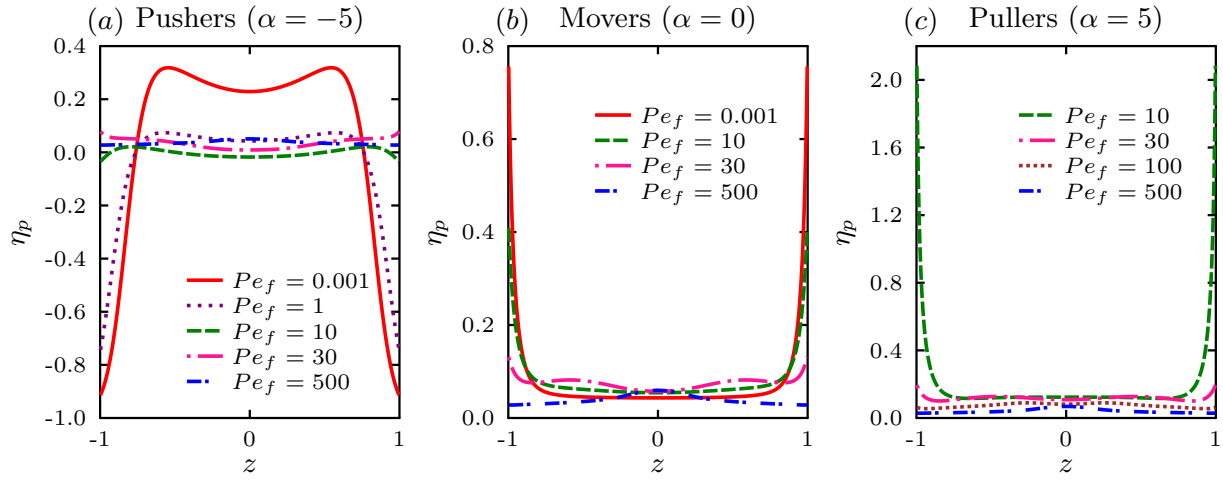

Figure 6.8: Local particle viscosity profiles $\eta_p(z)$ for $Pe_s = 1, \Lambda = 0.02, \beta = 1$ and different values of Pe_f for: (a) pushers, (b) movers, and (c) pullers.

regarding of density. In the low-Pe_f regime, we find that the Newtonian plateau for η_r decreases monotonically with n in the case of pushers, eventually reaching zero at high concentrations. Both of these observations are consistent with the recent experiments of Lopez *et al.* [170] in a cylindrical Couette flow, who measured very similar trends as in Fig. 6.9(c) and also reported an apparent transition to superfluidity at high densities. This transition to negative total viscosities is expected to lead to instabilities and is related to the previously reported emergence of unidirectional flows in confined active suspensions. [13, 166, 218–220] In the experiments of Lopez *et al.* [170], the transition to superfluidity occurred at a number density $n \approx 8 \times 10^{15}\,\mathrm{m}^{-3}$, from which we can estimate the value of the ratio n/n_0 for the transition as

$$\left(\frac{n}{n_0}\right)_{\eta_r=0} \approx \frac{|\sigma_0|n}{\mu d_r} = \frac{7.98 \times 10^{-19} \times 8 \times 10^{15}}{1.4 \times 10^{-3} \times 0.5} \approx 9.1, \tag{6.33}$$

which is reasonably close to the value of 8 predicted by our model. Fig. 6.9(d) shows more details on the dependence of the low-Pe_f viscosity plateau on number density, and also compares the numerical results to the theoretical estimate of Eq. (6.31). This estimate captures the initial decrease in viscosity quite well, especially in wider channels ($Pe_s = 1$) as anticipated; however, significant quantitative departures are observed at higher number densities.

6.4 Concluding remarks

We have developed a nonlinear mean-field kinetic theory for the configuration and effective rheology of a dilute active suspension in planar Poiseuille flow that accounts for the hydrodynamic disturbance driven by the particles as a result of both active and passive stresses. This model links together our previous theories for the rheology of bulk active suspensions in uniform shear [169] and for the distribution of particles in Poiseuille flow in the absence of hydrodynamic disturbances. [51] The rheological trends we predicted agree qualitatively with prior bulk models as well as experiments on bacterial suspensions, both in the bulk [170] and in microfluidic geometries.[118] In particular, we have confirmed that the effect of activity are predominant in weak flows, where pushers tend to decrease the viscosity whereas pullers increase it; in strong flows, activity becomes negligible and the suspension behavior is similar to that of passive rodlike particles. Confinement, however, has a nontrivial quantitative influence on the viscosity as results of two main effects: the non-homogeneous distribution of particles across the channel with strong accumulation near the walls in weak flows, and the non-uniform shear profile of the imposed pressure-driven flow controlling particle alignment. Notably, this tends to enhance the impact of the particles on the flow in weak flows compared to a bulk system. Finally, our dilute model was able to capture the decrease in viscosity in pusher suspensions with increasing volume fraction, which led to the transition to superfluidity in the experiments of Lopez *et al.* [170]: a more quantitative description of this transition, however, is beyond the range of applicability of the present theory and may require more realistic particle simulations such as those of Saintillan and Shelley, [159, 163] whose validity extends into the semi-dilute regime.

In the next chapter, we explore the possibility of using a magnetotactic bacterial suspension as a microfluidic pump, and study its rheological properties upon the application of a uniform magnetic field.

6.5 Acknowledgements

Chapter 6, in part, is a manuscript published in *Biomicrofluidics*; authored by R. Alonso-Matilla, B. Ezhilan and D. Saintillan, "Microfluidic rheology of active particle suspensions: Kinetic theory". The dissertation author is the primary author of this work. We thank Anke Lindner and Eric Clément for useful conversations.

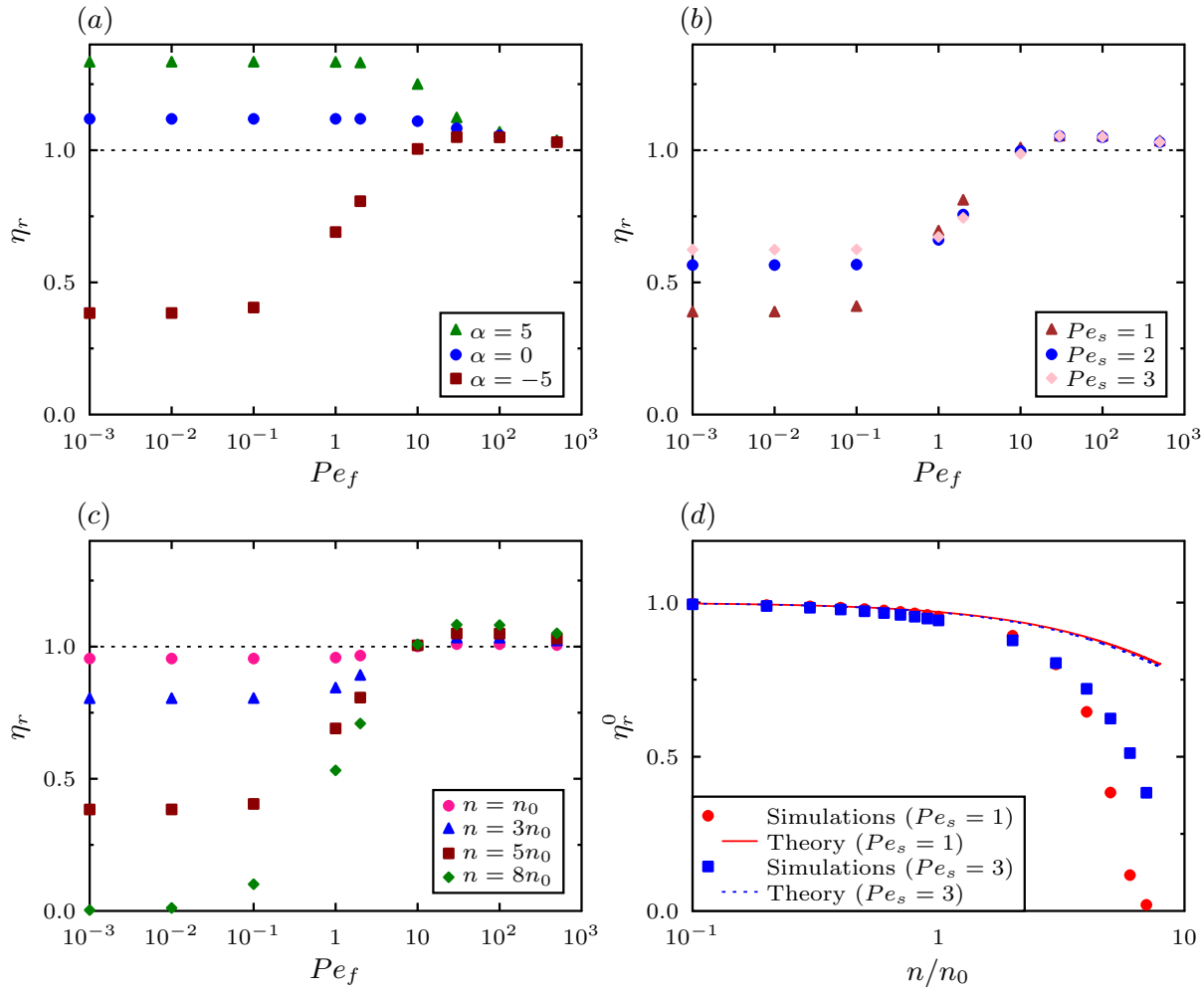

Figure 6.9: (a) Relative viscosity η_r for $Pe_s = 1$, $\Lambda = 0.02$ and $\beta = 1$ as a function of flow rate Pe_f for pullers, movers, and pushers. (b) Effect of confinement on η_r in the case of pushers ($\alpha = -5$). (c) Effect of number density n on η_r in the case of pushers. In this plot, the ratio $\alpha/\beta = -5$ is kept fixed while varying n; the reference number density n_0 corresponds to $\alpha = -1$. (d) Effect of number density n on the low-Pe_f Newtonian asymptote η_r^0, and comparison to the theoretical estimate of Eq. (6.31).

Chapter 7

Microfluidic flow actuation using magnetoactive suspensions

7.1 Introduction

Suspensions of active particles, such as motile microorganisms, synthetic microswimmers, or externally actuated colloids, exhibit unusual rheological properties that are unlike those of classical complex fluids [230]. While the additional viscous dissipation incurred by flow around suspended particles typically enhances viscosity in passive systems [231], such is not the case in active suspensions, where mechanical stresses generated on the microscale as a result of activity can have the opposite effect of reducing flow resistance [167]. This curious trend has been characterized in detail in the case of swimming bacteria [118, 170], where the coupling of particle reorientations by the applied flow and of dipolar stresses exerted during self-propulsion indeed causes a decrease in viscosity in weak flows [169]. In sufficiently concentrated systems, the apparent viscosity can in fact reach zero [2, 170], indicating a transition to a superfluid-like state where internal activity exactly compensates viscous dissipation. A dramatic manifestation of this transition is the emergence of spontaneous directed motions in confined systems [166, 218], which has been explained as a linear instability driven by active stresses [13]. The ability to harness these flows for applications, however, remains limited due to the lack of external control on particle configurations, which instead emerge spontaneously from internal mechanical couplings.

Tunable rheological properties are typically achieved in passive systems by applying external electric or magnetic fields [232, 233], which drive particle rearrangements or re-

orientations and thus affect resistance to flow. The viscous properties of passive magnetic fluids have been extensively studied, with experiments [234] showing an increase in the viscosity of ferromagnetic fluids when a constant magnetic field is applied. This effect is well understood theoretically [235–239] as a consequence of the magnetic torque acting on the particles, which hinders their rotation by the applied vorticity and results in an additional stress contribution.

In this work, we investigate the use of magnetic fields as a means to control the effective rheology and internally-driven flows of active suspensions in microfluidic channels. The system of choice for this problem is magnetotactic bacteria, which are motile prokaryotes mostly present in marine habitats that synthesize intracellular magnetic membrane-bound crystals known as magnetosomes. These bacteria, which swim by similar mechanisms as other flagellated bacteria, behave as self-propelled permanent magnetic dipoles that orient and migrate along the local magnetic field lines [240]. Magnetotactic suspensions thus behave as magnetic fluids with additional complexities arising from self-propulsion, which causes particle accumulation at walls in confined systems [14, 51], and from active stresses, which modify the rheology [2, 169, 230]. Although the active nature of magnetotactic bacteria has not been characterized in detail experimentally, it has been suggested that the strain MC-1 of *Magnetococcus marinus* behaves as a puller [3]. The ability to manufacture magnetotactic pusher-like particles using engineered flagellar motors of *Escherichia coli* bacteria tethered to magnetic beads has also been demonstrated [241].

The complex dynamics of magnetoactive suspensions in microfluidic flows have recently been studied in experiments [3], where the interplay of magnetic alignment and rotation in shear was shown to cause flow-focusing in pressure-driven flow [242]. In semi-dilute systems, a pearling instability was observed [3], though it remains unclear whether it is caused by hydrodynamic [243] or magnetic [244] interactions. These experiments hint at an unusual rheology, which we analyze in this Letter. In both unbounded and confined geometries, the response of these suspensions under simple external flows can be controlled by applying a magnetic field and hinges in a subtle way on the interplay of magnetic alignment, rotation under shear, and wall-induced accumulation. By tuning magnetic field strength and direction, the apparent viscosity can either be enhanced or reduced, and the mechanisms for these trends are elucidated. We show that, when placed in an external uniform magnetic field, a confined magnetotactic suspension can behave as an active ferromagnetic pump. When the direction of the field and the magnetization of the microorganisms are

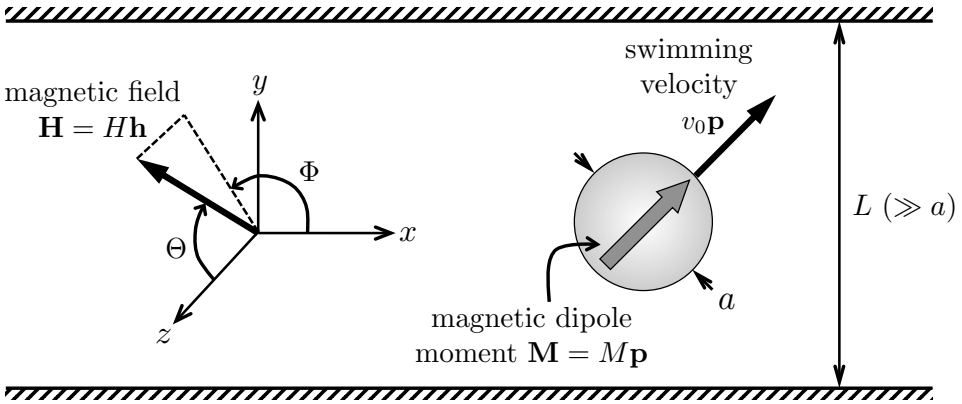

Figure 7.1: Problem definition: a dilute suspension of spherical magnetotactic swimmers (velocity $v_0\mathbf{p}$, magnetic dipole $\mathbf{M} = M\mathbf{p}$) is subject to an externally applied magnetic field $\mathbf{H}$.

not collinear, bacteria feel a net magnetic torque which is transmitted to the surrounding fluid, and can give rise to a net unidirectional fluid flow in a planar channel, with a flow rate and direction that can be controlled by adjusting both the magnitude and orientation of the field. Using a kinetic theory [2, 169], we provide a physical explanation for these flows, and suggest novel avenues for the design of microfluidic pumps and flow actuation devices

7.2 Continuum kinetic model

We consider a suspension of rigid spherical magnetotactic motile bacteria of radius a dispersed in an incompressible Newtonian solvent with dynamic viscosity η_s. The suspension is assumed to be dilute, with mean number density n and corresponding volume fraction $\phi_v = \frac{4}{3}\pi a^3 n \ll 1$. We study both unbounded and confined systems, where the confining geometry is a Hele-Shaw cell comprised of two infinite parallel plates separated by a distance $L \gg a$. We adopt the coordinate system shown in Fig. 7.1, where x is the flow direction, y the wall-normal coordinate, and z the vorticity direction. A spatially uniform magnetic field $\mathbf{H} = H\mathbf{h}$ is applied along the unit vector $\mathbf{h}$, which we parametrize in spherical coordinates as $\mathbf{h} = (\sin\Theta\cos\Phi, \sin\Theta\sin\Phi, \cos\Theta)$. Bacteria are assumed to swim at constant speed v_0 along their unit director $\mathbf{p}$, similarly expressed as $\mathbf{p} = (\sin\theta\cos\varphi, \sin\theta\sin\varphi, \cos\theta)$. They carry a permanent magnetic dipole modeling the presence of the magnetosome chains that longitudinally traverse the cell body of magnetobacteria [245]: $\mathbf{M} = M\mathbf{p} + \boldsymbol{\vartheta}$, where $\boldsymbol{\vartheta}$ corresponds to the induced polarization tensor, which we neglect in our study, hence $\boldsymbol{\vartheta} = \mathbf{0}$.

We additionally neglect magnetic interactions between particles. Here, the Neel relaxation time of the magnetic moment is considered to be much greater than the relaxation time associated to the rotation of the particles in the fluid due to Brownian or external fluid effects. Therefore, we neglect the rotation of the magnetic vector within the particle, and thus assume that $\mathbf{M}$ is constant and rotates rigidly with each cell body. When placed in a uniform external field, the bacteria are subject to a net magnetic torque $\mathbf{M} \times \mathbf{H}$ that generates an additional suspension stress.

7.2.1 Fokker-Planck description

Following previous kinetic models for dilute active fluids [2, 51, 140, 169, 246], we describe the configuration of the suspension in terms of the probability density function $P(\mathbf{R}, \mathbf{p}, t)$ of finding a particle at position $\mathbf{R}$ with orientation $\mathbf{p}$ at time t, where the mean value of P over all positions and orientations defines the number density. At steady state, the density function satisfies the Fokker-Planck equation [247]

$$\nabla_R \cdot \mathbf{J} + \nabla_p \cdot \mathbf{j} = 0, \tag{7.1}$$

where $\mathbf{J}$ and $\mathbf{j}$ capture translational and rotational particle fluxes, respectively. The translational flux is obtained from a force balance on a swimmer,

$$6\pi\eta_s a \left[\mathbf{J}/P - v_0\mathbf{p} - \mathbf{u}(\mathbf{R})\right] + k_\mathrm{B}T\nabla_R \ln P = \mathbf{0}, \tag{7.2}$$

where the viscous drag force on the spherical particle balances the Brownian force scaling with thermal energy $k_\mathrm{B}T$. In writing eq. (7.2), we have used the fact that $a \ll L$, so that advection of the particle by the flow simply occurs with the local fluid velocity $\mathbf{u}(\mathbf{R})$ [248]. Introducing the translational diffusivity $d_t = k_\mathrm{B}T/6\pi\eta_s a$, eq. (7.2) yields

$$\mathbf{J} = (v_0\mathbf{p} + \mathbf{u}(\mathbf{R}))P - d_t\nabla_R P. \tag{7.3}$$

Similarly, we obtain the rotational flux from an angular momentum balance, where the viscous, magnetic, and Brownian torques on a swimmer sum up to zero:

$$8\pi\eta_s a^3 \left[\tfrac{1}{2}\boldsymbol{\omega}(\mathbf{R}) - \boldsymbol{\Omega}\right] + \mathbf{M} \times \mathbf{H} - k_\mathrm{B}T\mathbf{p} \times \nabla_p \ln P = \mathbf{0}. \tag{7.4}$$

Here, $\boldsymbol{\omega}(\mathbf{x}) = \nabla_R \times \mathbf{u}(\mathbf{x})$ is the ambient fluid vorticity, while $\boldsymbol{\Omega}$ denotes the bacterium angular velocity. $\mathbf{p}$ is a constant vector in the coordinate frame attached to the particle, which rotates with angular velocity $\boldsymbol{\Omega}$. We denote the change of the vector $\mathbf{p}$ with respect to the stationary framework as $\dot{\mathbf{p}}$. Using the kinematic relation $\mathbf{j}/P = \dot{\mathbf{p}} = \boldsymbol{\Omega} \times \mathbf{p}$, eq. (7.4) provides an expression for the rotational flux,

$$\mathbf{j} = \left(\tfrac{1}{2}\boldsymbol{\omega}(\mathbf{R}) \times \mathbf{p} + \frac{MH}{8\pi\eta_s a^3}\mathbf{h}^{\perp} \right) P - d_r \nabla_p P, \tag{7.5}$$

where $d_r = k_{\mathrm{B}}T/8\pi\eta_s a^3$ is the rotational diffusivity of a spherical particle, and $\mathbf{h}^{\perp} \equiv (\mathbf{I} - \mathbf{pp}) \cdot \mathbf{h}$.

7.2.2 Fluid flow and suspension stress

The suspension of bacteria exchanges both linear and angular momentum with its surroundings, thus affecting the rheology of the system. In the low-Reynolds-number limit relevant to microscopic swimmers, the fluid velocity $\mathbf{u}$ and corresponding pressure q satisfy the incompressible Stokes equations:

$$\nabla_R \cdot \mathbf{u} = 0, \quad -\nabla_R q + \nabla_R \cdot \boldsymbol{\Sigma} = \mathbf{0}, \tag{7.6}$$

where the deviatoric stress $\boldsymbol{\Sigma}$ includes contributions from the solvent as well as from the particles. Following standard methods [2, 27, 169, 230, 235], we model the stress as

$$\boldsymbol{\Sigma} = 2\eta_s \left(1 + \tfrac{10}{3}\pi a^3 c\right) \mathbf{E} + \tfrac{1}{2} MH \left(\mathbf{hm} - \mathbf{mh}\right) + \sigma_0 \mathbf{D}, \tag{7.7}$$

where $\mathbf{E} = \frac{1}{2}\left(\nabla_R \mathbf{u} + \nabla_R \mathbf{u}^T\right)$ is the rate-of-strain tensor, and c, $\mathbf{m}$ and $\mathbf{D}$ denote the zeroth, first, and second orientational moments of the distribution function:

$$c(\mathbf{x}) = \langle 1 \rangle, \quad \mathbf{m}(\mathbf{x}) = \langle \mathbf{p} \rangle, \quad \mathbf{D}(\mathbf{x}) = \langle \mathbf{pp} - \mathbf{I}/3 \rangle, \tag{7.8}$$

where $\langle \cdot \rangle = \int \cdot \, P(\mathbf{x}, \mathbf{p}) \, \mathrm{d}\mathbf{p}$ is the orientational average. Upon normalization by c, the two moments $\mathbf{m}$ and $\mathbf{D}$ describe local polar and nematic alignment, respectively.

The first term in eq. (7.7) is a viscous contribution arising from the flow, and involves the usual Newtonian stress corrected for particle concentration according to Einstein's for-

mula [231]. The second term, which is antisymmetric, captures the effect of magnetic torques and vanishes for a suspension aligned with the applied field ($\mathbf{m} \propto \mathbf{h}$) [235, 249, 250]. Finally, the last term accounts for active stresses arising from self-propulsion and involves the active stresslet σ_0, whose sign depends on the propulsion mechanism [167, 169, 230]: $\sigma_0 < 0$ for so-called *pusher* swimmers, whereas $\sigma_0 > 0$ for *pullers*. While σ_0 has been measured for certain types of microorganisms [204, 206], it is still unknown for common magnetotactic bacteria.

7.2.3 Dimensional analysis

We nondimensionalize the governing equations using time scale d_r^{-1}, length scale L, velocity scale Ld_r, and pressure scale $\eta_s d_r$. The distribution function P is normalized by the number density n. In addition to the volume fraction ϕ_v, scaling of the equations in the absence of an external flow yields four independent dimensionless groups, which we define as

$$\mathrm{Pe}_s = \frac{v_0}{Ld_r}, \quad \epsilon = \frac{\sqrt{d_t/d_r}}{L}, \quad \alpha = \frac{\sigma_0}{k_\mathrm{B}T}, \quad \beta = \frac{MH}{k_\mathrm{B}T}. \tag{7.9}$$

The swimming Péclet number Pe_s represents the ratio of the persistence length $\ell = v_0/d_r$ of swimmer trajectories over the channel width L, and can be viewed as a measure of confinement. The parameter ϵ is the ratio of the diffusive length scale $\delta = \sqrt{d_t/d_r}$ over L; for a Brownian spherical particle, $\delta = \sqrt{4/3}\,a$, so that $\epsilon \ll 1$ for the case of interest where $a \ll L$. Finally, α and β compare the magnitudes of active and magnetic stresses to the thermal energy unit $k_\mathrm{B}T$. With these scalings, the steady Fokker-Planck eq. (7.1) simplifies to

$$\nabla_R \cdot \left[\left(\mathrm{Pe}_s \mathbf{p} + \mathbf{u}\right) P\right] - \epsilon^2 \nabla_R^2 P + \nabla_p \cdot \left[\left(\tfrac{1}{2}\boldsymbol{\omega} \times \mathbf{p} + \beta \mathbf{h}^\perp\right) P\right] - \nabla_p^2 P = 0, \tag{7.10}$$

subject to a no-flux boundary condition at domain boundaries: $\hat{\mathbf{n}} \cdot (\mathrm{Pe}_s \mathbf{p} P - \epsilon^2 \nabla_R P) = 0$. The scaling of translational diffusion with ϵ^2 underscores the weak role it plays in moderately wide channels outside of near-wall accumulation layers [51]. Similarly, the dimensionless linear momentum conservation equation becomes

$$-\nabla_R q + \left(1 + \tfrac{5}{2}\phi_v c\right) \nabla_R^2 \mathbf{u} + 5\phi_v \mathbf{E} \cdot \nabla_R c + 6\alpha\phi_v \nabla_R \cdot \mathbf{D} + 3\beta\phi_v \left[\mathbf{h} \cdot \nabla_R \mathbf{m} - (\nabla_R \cdot \mathbf{m})\,\mathbf{h}\right] = \mathbf{0}, \tag{7.11}$$

where the linear dependence of particle stresses on ϕ_v in the dilute limit is apparent. In the event that an external flow is applied to the system, we also introduce a flow Péclet number defined as $\mathrm{Pe}_f = \dot{\gamma}/d_r$ in an imposed shear flow with shear rate $\dot{\gamma}$, and as $\mathrm{Pe}_f = \Delta q L/\eta_s d_r$ in a pressure-driven flow with pressure gradient Δq.

7.3 Results and discussion

The governing equations (7.10)–(7.11) are solved numerically using a finite-volume algorithm described in our previous work [2, 51]. In unbounded domains, we further check our results using a spectral method based on spherical harmonics [169]. In all results shown here, we assume that the magnetic field lies in the x-y plane ($\Theta = \pi/2$), and we choose the values $\epsilon^2 = 0.025$ and $\phi_v = 0.01$.

7.3.1 Unbounded simple shear flow

We first gain intuition by discussing the simple case of an unbounded suspension in an imposed linear shear flow ($\mathbf{u} = \mathrm{Pe}_f y\,\hat{\mathbf{x}}$, $\boldsymbol{\omega} = \mathrm{Pe}_f \hat{\mathbf{z}}$), a situation also recently analyzed by Vincenti *et al.* [251]. In this case, we define the intrinsic shear viscosity as

$$[\eta] = \lim_{\phi_v \to 0} \frac{\Sigma_{yx} - \mathrm{Pe}_f}{\phi_v \mathrm{Pe}_f}, \tag{7.12}$$

which takes on the simple form

$$[\eta] = \frac{5}{2} + \frac{3\beta}{\mathrm{Pe}_f}(\sin\Phi\, m_x - \cos\Phi\, m_y) + \frac{6\alpha}{\mathrm{Pe}_f} D_{yx}. \tag{7.13}$$

It is straightforward to realize that $[\eta](\Phi + \pi) = [\eta](\Phi)$, and therefore we only consider field orientations $\Phi \in [0, \pi]$. We also focus on the case of pushers for which $\alpha < 0$.

Results for the intrinsic viscosity are presented in Fig. 2. In the absence of magnetic or active stresses, $[\eta] = 5/2$ due to the passive stresslet resulting from the enhanced dissipation around the particles [231]. When a magnetic field is applied, magnetic stresses can either enhance or decrease this value depending on the sign of $(\mathbf{m} \times \mathbf{h})_z = \sin\Phi\, m_x - \cos\Phi\, m_y$. Defining an angle $\Upsilon = \tan^{-1}(m_y/m_x)$, which captures the mean swimmer orientation, we see that $[\eta]$ is reduced by magnetic stresses whenever $\Phi < \Upsilon < \Phi + \pi$, and enhanced otherwise. In an applied shear flow, the applied field always resists particle rotations resulting

in $\Phi - \pi < \Upsilon < \Phi$, and therefore $[\eta]$ monotonically increases with β as shown by the dashed lines in Fig. 2(a). Active stresses, however, qualitatively modify this trend through the last term in eq. (7.13), which depends on the sign of D_{yx}. For fields nearly aligned with the flow direction ($\Phi \gtrsim 0$), particles tends to point in the fourth quadrant $-\pi/2 < \Upsilon < 0$ so that $D_{yx} < 0$ and $[\eta]$ is slightly enhanced for pushers ($\alpha < 0$). As Φ increases towards $\pi/2$, Υ enters the first extensional quadrant resulting in $D_{yx} > 0$ and in a decrease in viscosity, which reaches a minimum for a value of $\Phi \approx \pi/4$ in weak flows. Further increasing Φ beyond $\pi/2$ causes particles to align in the second compressional quadrant, and thus $[\eta]$ is enhanced again. In stronger flows, similar trends are observed but require larger values of Φ to resist rotation in the applied flow. For the purpose of decreasing the intrinsic viscosity, Fig. 2 suggests that an optimum field direction Φ_{opt} exists, which is also that maximizing D_{yx} in the case of pushers.

We seek analytical expressions for $[\eta]$ and Φ_{opt} by taking orientational moments of eq. (7.10) and applying a closure approximation for the third-order moment [51, 140]. In an unbounded homogeneous suspension, this transformation reduces the conservation equation to a system of coupled algebraic equations for $\mathbf{m}$ and $\mathbf{D}$:

$$\begin{aligned} -\mathbf{W}\cdot\mathbf{m} + \beta\left(\tfrac{2}{3}\mathbf{h} - \mathbf{D}\cdot\mathbf{h}\right) &= 2\mathbf{m}, \\ \mathbf{D}\cdot\mathbf{W} - \mathbf{W}\cdot\mathbf{D} + \beta\left[\tfrac{3}{5}(\mathbf{m}\mathbf{h} + \mathbf{h}\mathbf{m}) - \tfrac{2}{5}(\mathbf{m}\cdot\mathbf{h})\mathbf{I}\right] &= 6\mathbf{D}. \end{aligned}$$

Inverting this system and inserting the solution into eq. (7.13) yields an expression for the intrinsic viscosity:

$$[\eta](\mathrm{Pe}_f, \alpha, \beta, \Phi) = P/Q, \tag{7.14}$$

where P and Q are polynomial functions:

$$\begin{aligned} P &= \tfrac{375}{2}\left(\mathrm{Pe}_f^4 + 52\mathrm{Pe}_f^2 + 576\right) - 100\beta^2\left(\mathrm{Pe}_f^2 - 234\right) \\ &+ 24\tfrac{\alpha\beta^2}{\mathrm{Pe}_f}\left[\left(3\beta^2 - \tfrac{5}{2}\mathrm{Pe}_f^2 + 60\right)\sin 2\Phi - 25\mathrm{Pe}_f\cos 2\Phi\right], \qquad (7.15) \\ Q &= 75\left(\mathrm{Pe}_f^4 + 52\mathrm{Pe}_f^2 + 576\right) - 80\beta^2\left(2\mathrm{Pe}_f^2 - 63\right) + 144\beta^4. \qquad (7.16) \end{aligned}$$

This prediction perfectly matches the numerical results of Fig. 7.2(b,c). The optimum field

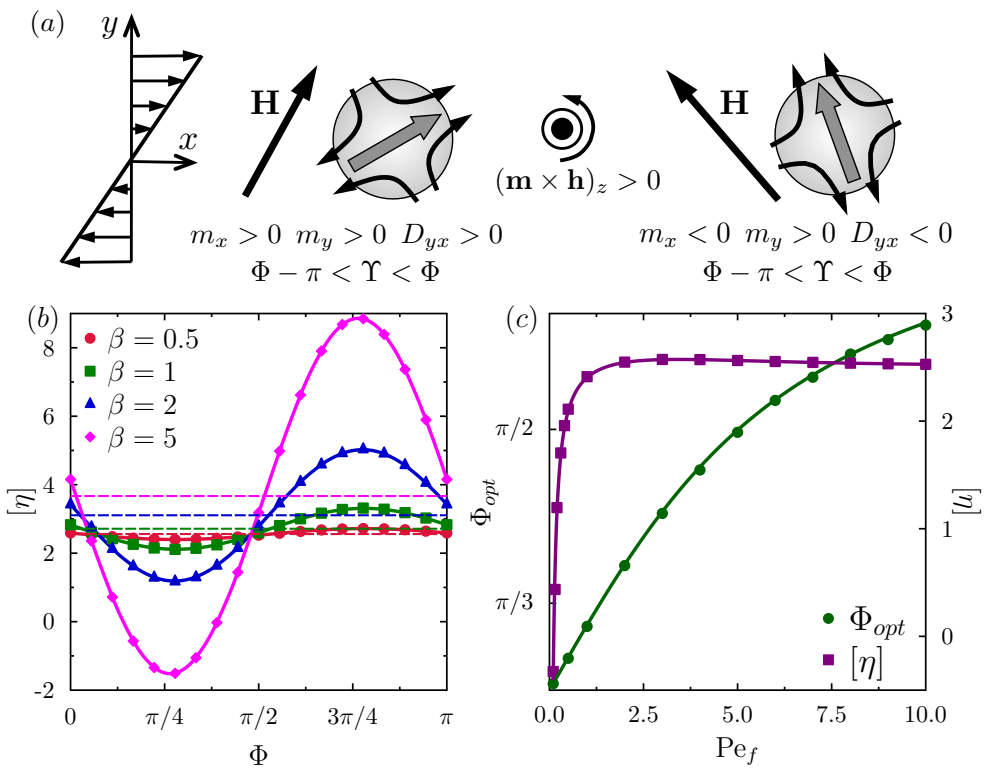

Figure 7.2: (a) Mean particle orientation and mechanism for viscosity modification in unbounded simple shear flow for two magnetic field orientations. Disturbance flow fields are shown for pushers and have the opposite direction for pullers. (b) Intrinsic viscosity $[\eta]$ for $\mathrm{Pe}_f = 0.5$ as a function of magnetic field direction Φ for varying field strengths β. Dashed lines: movers (no active stress, $\alpha = 0$). Solid lines: pushers ($\alpha = -5/3$), where the solution is also checked using spherical harmonics (symbols). (c) Optimum field direction Φ_{opt} (left axis), in a suspension of pushers, that minimizes $[\eta]$ (right axis) as a function of the flow Péclet number Pe_f. Results for pullers are obtained by noting $\Phi_{opt}(\alpha) = \Phi_{opt}(-\alpha) + \pi/2$. Solid line: analytical prediction of eq. (7.17). Symbols: numerical solution.

direction Φ_{opt} can then be obtained by straightforward minimization as

$$\Phi_{opt} = \tfrac{1}{2}\tan^{-1}\left[\frac{\frac{5}{2}\mathrm{Pe}_f^2 - 3\beta^2 - 60}{25\mathrm{Pe}_f}\right], \tag{7.17}$$

which increases from $\pi/4$ as flow strength increases and also matches numerical calculations in Fig. 2(c). Eq. (7.17) also provides the dependence of Φ_{opt} on magnetic field strength: for a given flow strength Pe_f, the optimum angle decreases as β increases. In the limit of strong fields and moderate flows, particles orient approximately along the field direction, yielding an optimum angle of $\Phi_{opt} \gtrsim \pi/4$.

7.3.2 Magnetoactive pumping in confinement

We now turn to the effects of confinement and first analyze the dynamics in the absence of any imposed flow ($\mathrm{Pe}_f = 0$). In this case, fluid motion is solely the result of magnetic and active stresses which can produce a net non-zero volumetric flow rate $\dot{Q}_v = \int_0^1 u_x(y)\,\mathrm{d}y$ by a mechanism summarized in Fig. 7.3(a). Symmetry of the problem allows us to only consider $\Phi \in [0, \pi/2]$. When $\beta = 0$ (no magnetic field), particles accumulate equally at both boundaries with a net polarization towards them [14, 51], and no flow is generated ($\dot{Q}_v = 0$). Applying a magnetic field ($\beta > 0$) in any direction other than $\Phi = \pi/2$ results in a net torque on the particles, which competes against wall-induced polarization and is transmitted to the fluid via viscous drag. For a longitudinally applied field ($\Phi = 0$), the magnetic torque is clockwise $(\mathbf{m} \times \mathbf{h})_z < 0$ near the top wall and counter-clockwise near the bottom wall, and corresponding magnetic shear stresses drive a flow in the negative x-direction ($\dot{Q}_v < 0$). This is evident in Fig. 7.3(b), showing $\dot{Q}_v$ as a function of β for movers ($\alpha = 0$). In weak to moderate fields, $|\dot{Q}_v|$ increases with β as longitudinal polarization m_x progressively increases from zero. In strong fields, however, magnetic alignment overcomes wall-induced polarization, leading to $m_y \to 0$ and therefore to a drop in magnetic stresses and flow rate. In this limit, wall accumulation becomes negligible as particles primarily swim in the field direction. The transition between the two regimes is marked by a maximum in flow rate occurring for $\beta \sim 2.0 - 3.0$. The coupling of wall-normal polarization with field alignment also results in nematic alignment [51] with $D_{yx} > 0$ near the top wall and < 0 near the bottom wall. In the case of pushers in Fig. 7.3(c), the resulting active stress profile further promotes retrograde flow ($\dot{Q}_v < 0$) by a mechanism similar to that for the viscosity decrease observed in pressure-driven flows [2]. In the case of pullers, however, active stresses have the opposite sign and can dominate magnetic stresses to drive a net flow in the positive x-direction ($\dot{Q}_v > 0$) as seen in Fig. 7.3(d).

These basic trends on flow rate remain valid for non-parallel field directions ($\Phi > 0$). As Φ increases from zero, particle distributions become asymmetric with a stronger accumulation at the top wall; in sufficiently strong fields, accumulation at the lower boundary can be suppressed entirely, resulting in $m_y > 0$ throughout the channel. While the magnetically-driven flow rate monotonically decreases towards zero as Φ increases from 0 to $\pi/2$, as observed in Fig. 7.3(a), activity-driven flows in both pusher and puller suspensions show a non-monotonic dependence, with a maximum $|\dot{Q}_v|$ attained for $\Phi \approx \pi/4$. Therefore, a tran-

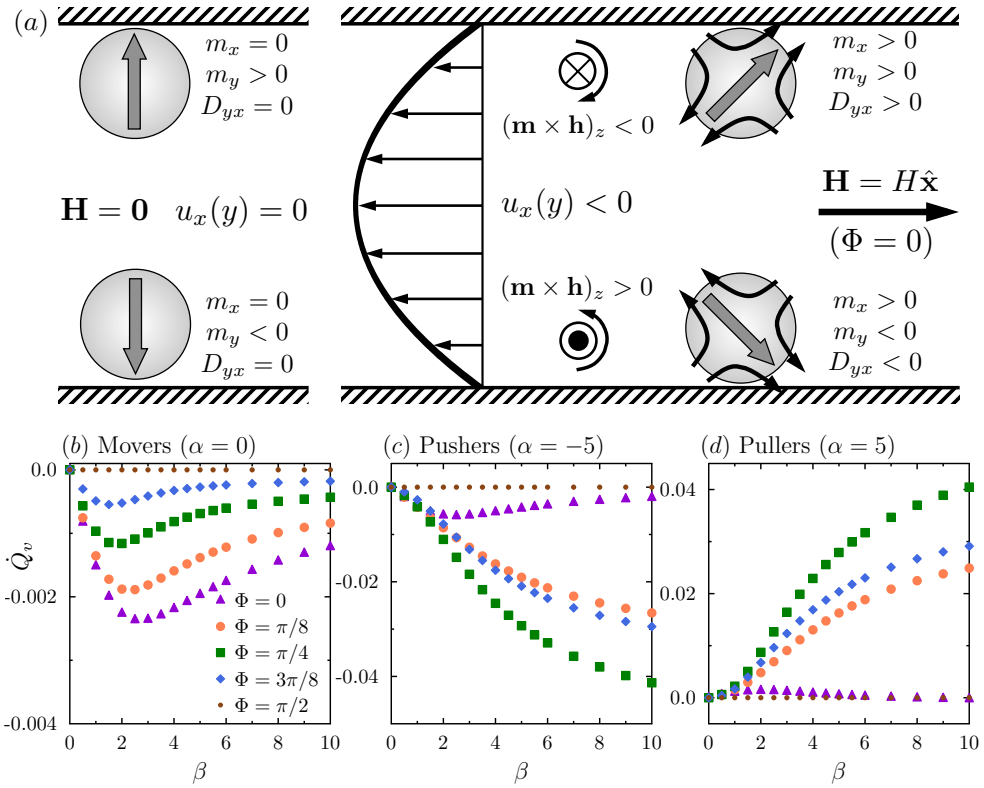

Figure 7.3: (a) Mechanism for magnetoactive pumping in a planar channel with no imposed flow ($\mathrm{Pe}_f = 0$). Left: Average particle configuration in the absence of a magnetic field. Right: Disturbance flow created by the synergistic effect of magnetic and active stresses in a suspension of pushers under a uniform magnetic field. In the case of pullers, magnetic stresses remain the same while active disturbance flows change sign. (*b*)–(*d*) Volumetric flow rate $\dot{Q}_v$ as a function of magnetic field strength β for $\mathrm{Pe}_s = 0.5$ and for different swimmer types: movers ($\alpha = 0$), pushers and pullers ($\alpha = \mp 5$).

sition between magnetically-dominated flows to activity-dominated flows manifests itself as $|\alpha|$ increases from zero. In the case of $\mathrm{Pe}_s = 0.5$ and $\beta = 2$, the transition occurs at a critical level of activity of $|\alpha_c| \approx 1$.

While these internally-driven active flows are reminiscent of the spontaneous unidirectional flows known to arise in confined suspensions of elongated pushers [13, 166, 218], a fundamental difference lies in the ability to turn flows on and off and control their strength and direction by tuning the magnetic field strength β and orientation Φ. We also note that particle accumulation at the boundaries as a result of swimming plays a crucial role in the mechanism of Fig. 7.3(*a*): it is this very accumulation that induces polarization in the system, which upon application of the field generates both magnetic and active stress gradients.

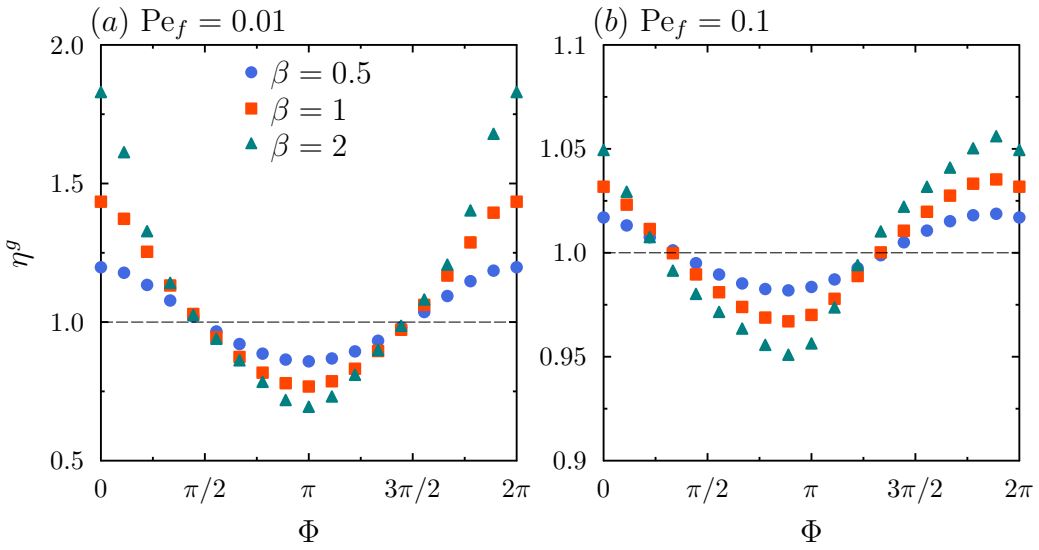

Figure 7.4: Dependence of the generalized Newtonian viscosity η^g on magnetic field direction Φ in a confined suspension of movers ($\alpha = 0$) subject to a linear shear flow: (a) Pe$_f = 0.01$, (b) Pe$_f = 0.1$. In both cases, Pe$_s = 0.5$.

7.3.3 Simple shear flow in confinement

Our understanding of unconfined rheology and of magnetoactive pumping in confinement provides the basis for analyzing the response in imposed confined flows. We first discuss the case of a linear shear flow between two planar walls, where the upper wall translates with constant velocity $u_w = \mathrm{Pe}_f$. Here, we define a generalized Newtonian viscosity

$$\eta^g = \frac{\mathrm{Pe}_f}{2\dot{Q}_v}, \tag{7.18}$$

which quantifies the change in volumetric flow rate $\dot{Q}_v$ due to the bacteria and reduces to 1 in the passive case.

Results for η^g in a weak imposed flow (Pe$_f = 0.01$) are shown in Fig. 7.4(a) for a suspension of movers ($\alpha = 0$). In this case, the flow has only a weak effect on particle configurations, which instead are controlled primarily by the interplay of magnetic alignment and wall-induced accumulation and polarization as was the case in Fig. 7.3(a). Following the reasoning of the previous section, the resulting magnetic stress profile induces a disturbance flow in the direction opposite to the horizontal field component. It follows that magnetic stresses enhance the imposed flow for $\Phi \in [\pi/2, 3\pi/2]$ but impede it otherwise, resulting in an effective reduction in η^g in the latter case and increase otherwise, with a magnitude that

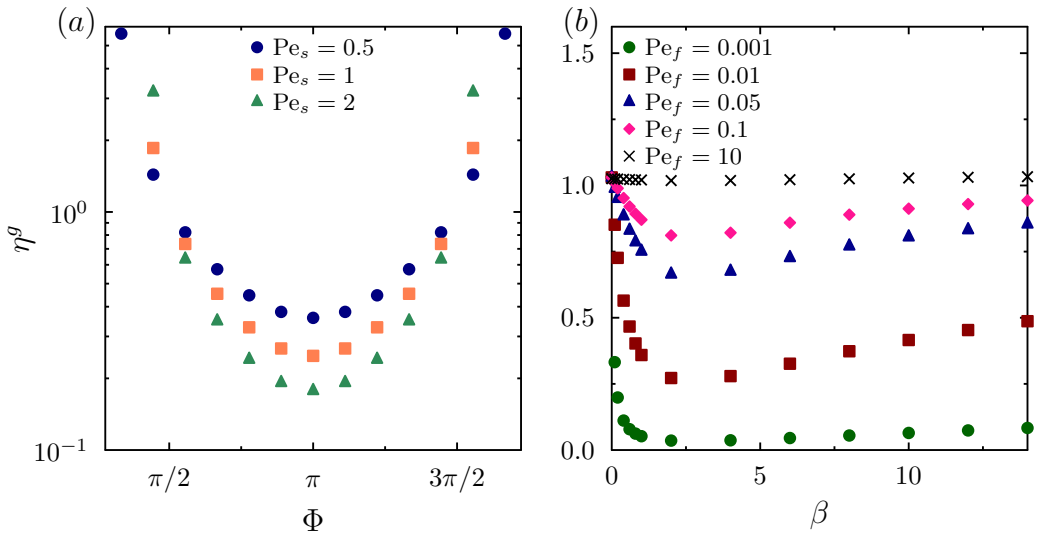

Figure 7.5: (a) Generalized viscosity η^g in a pressure-driven flow of movers ($\alpha = 0$) as a function of Φ for different values of Pe$_s$. Parameter values: Pe$_f = 0.01$, $\beta = 1$. (b) Dependence of η^g on magnetic field strength β for $\Phi = \pi$ and different values of Pe$_f$. Parameter values: Pe$_s = 0.5$, $\alpha = 0$.

increases with β. Pushers/pullers further enhance/mitigate this effect, respectively, as can be anticipated from Fig. 7.3(cd).

In stronger flows, the applied shear affects the particle distribution more significantly and breaks the horizontal symmetry. This is illustrated in Fig. 7.4(b) for Pe$_f = 0.1$, where the leading effect of the flow is to substantially reduce departures of the generalized viscosity from unity. The hydrodynamic torque experienced by the particles acts in the clockwise direction across the entire channel; in a magnetic field, the mean particle orientation is position-dependent but tends to be such that $\Phi - \pi < \Upsilon < \Phi$ so that hydrodynamic and magnetic torques counteract each other. For small Φ, particles thus tend to swim towards and accumulate at the bottom wall, where the magnetic torque then acts to slow down the flow and therefore enhance viscosity. In order for η^g to be reduced, particle accumulation must be forced towards the upper wall where counterclockwise magnetic torques near the no-slip boundary tend to enhance the applied flow: this occurs for magnetic field orientations $\pi/4 \lesssim \Phi \lesssim 5\pi/4$ as seen in Fig. 7.4(b). For yet higher angles Φ, particle accumulation returns to the lower wall and the effective viscosity η^g raises again above 1.

7.3.4 Pressure-driven flow in confinement

As a final example, we consider the effective rheology in a Poiseuille flow driven by a constant pressure gradient, which drives the flow from left to right. Here, we also introduce a generalized Newtonian viscosity

$$\eta^g = \frac{\mathrm{Pe}_f}{12\dot{Q}_v}, \tag{7.19}$$

which again reduces to 1 in the passive case. Results for η^g and its dependence on magnetic field direction are shown in Fig. 7.5(a), where η^g is found to be reduced whenever $\pi/2 < \Phi < 3\pi/2$ and reaches a minimum for $\Phi = \pi$. This direction indeed maximizes the angle between $\mathbf{h}$ and $\mathbf{m}$, which directly controls the magnitude of magnetic stresses. The dependence of η^g on field strength for $\Phi = \pi$ is non-monotonic as shown in Fig. 7.5(b), which is a result of changes in the distribution of particles across the channel. In weak fields, particles pointing towards the top/bottom walls feel a magnetic torque in the counterclockwise/clockwise directions, respectively, which is transmitted to the fluid and enhances the applied flow. This effective decrease in η^g becomes stronger with increasing β, up to a point where wall accumulation is suppressed as particle orientations become slaved to the field. This strong field alignment has two competing effects on the rheology. On the one hand, the weakening of accumulation causes a decrease in the passive viscous contribution to the stress, as fewer particles occupy the high-shear near-wall regions; this reduction in passive stress causes a further decrease of η^g. On the other hand, stronger alignment with the field also decreases magnetic stresses, which enhances the apparent viscosity. As β is increased, the second effect tends to dominate, which explains the eventual increase of η^g towards 1 in Fig. 7.5(b). In very strong flows ($\mathrm{Pe}_f = 10$), a qualitative change in particle configurations is also observed, whereby particles now migrate towards the centerline of the channel (Fig. 7.6). This magnetic focusing, which has previously been reported in experiments [3] and explained theoretically [242], causes a change in the sign of magnetic stresses as polarization now points towards the centerline; this has the effect of enhancing η^g and in fact causes it to exceed 1. The effect of varying flow strength is also illustrated in Fig. 7.5(b), where shear-thickening is observed for all values of β, primarily as a consequence of passive stresses which become dominant in strong flows.

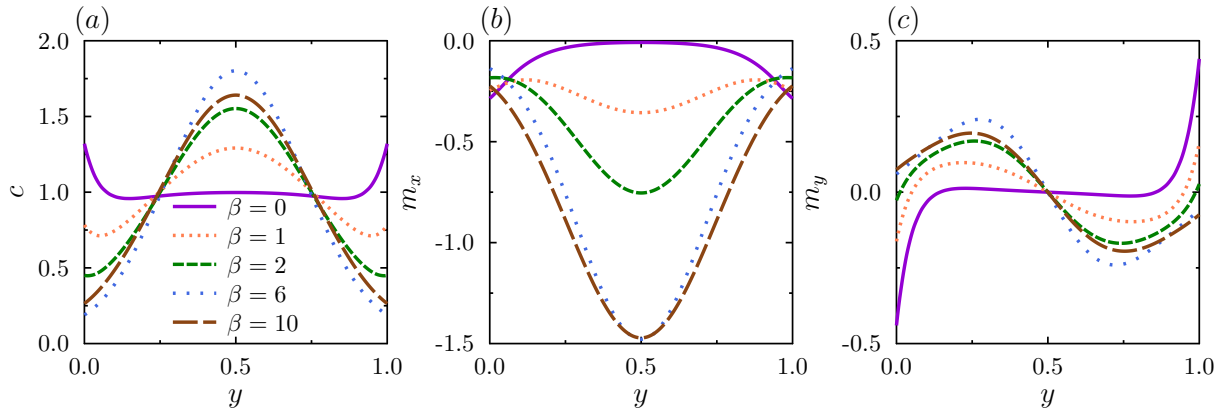

Figure 7.6: (a) Concentration, (b) streamwise and (c) transverse polarization in pressure-driven flow for a magnetic field oriented against the flow ($\Phi = \pi$). Parameter values: $\mathrm{Pe}_s = 0.5$, $\alpha = 0$, $\mathrm{Pe}_f = 10$.

7.4 Experimental estimates

We finish by providing numerical estimates for the magnitude of magnetically-actuated flows based on typical experimental parameters such as those of Waisbord *et al.* [3], who used *M. marinus* bacteria with radius $a \approx 1\,\mu$m, swimming speed $v_0 \approx 140\,\mu$m/s, rotational diffusivity $d_r \approx 0.5\,\mathrm{s}^{-1}$, and magnetic moment $M \approx 10^{-16}\,\mathrm{A.m}^2$. The value of σ_0 is unknown; we use the estimate of $\sigma_0 \approx 8 \times 10^{-19}\,\mathrm{N.m}$ obtained for *E. coli* [206] but consider puller swimmers which *M. marinus* is thought to be [3]. The channel width is taken to be $L = 50\,\mu$m. The corresponding dimensionless groups are $\mathrm{Pe}_s = 5.6$, $\alpha = 200$ and $\epsilon^2 = 5 \times 10^{-4}$. This value of ϵ^2 results in exceedingly thin accumulation layers that are challenging to resolve

Table 7.1: Cross-sectionally averaged fluid velocity u (μm/s) in magnetically-actuated flows, estimated based on typical experimental parameters [3].

		$\phi_v = 0.01$		$\phi_v = 0.1$	
Φ	α \ β	30	60	30	60
0	10	-0.05	-0.04	-0.35	-0.36
	100	0.66	0.15	4.96	1.20
	200	1.43	0.37	10.85	2.93
$\frac{\pi}{4}$	10	1.90	1.99	4.45	4.49
	100	19.04	19.91	42.10	43.04
	200	38.07	39.83	83.93	85.88

numerically; we use $\epsilon^2 = 0.01$ instead in our calculations, which only weakly affects flow rate and viscosity. Finally, we consider two volume fractions $\phi_v = 0.01$ and 0.1, and two magnetic field strengths of $H = 1.75\,\mathrm{mT}$ and $H = 3.5\,\mathrm{mT}$ corresponding to $\beta = 30$ and 60. Estimates for the cross-sectionally averaged fluid velocity u for these cases are provided in Table 7.1. For weak levels of activity ($\alpha = 10$), the flow is dominated by magnetic stresses resulting in fairly weak negative velocities. As α increases, active stresses in puller suspensions change the flow direction and result in significantly larger velocities, especially for $\phi = \pi/4$. Velocity magnitudes in these cases are on the order of tens of μm/s, which makes them relevant for microfluidic applications.

7.5 Concluding remarks

We have used a continuum kinetic model to explore the use of magnetotactic bacterial suspensions as tunable active fluids whose rheological response in an external flow can be controlled by an applied magnetic field. In confined systems, we also demonstrated the ability of these fluids to internally drive steady unidirectional flows, whose strength and direction are easily adjusted by tuning the applied field. The role of particle activity in these systems was found to be two-fold: (i) firstly, active stresses generated by self-propulsion directly modify the rheology and can be harnessed in various ways by controlling particle orientations using the external field; (ii) perhaps yet more interestingly, the wall accumulation resulting from self-propulsion in confined geometries induces local polarization, which under the action of the field gives rise to magnetic stresses whose sign can again be controlled. The richness of behaviors exhibited by these systems and the ability to externally control their rheological response and even to drive flows internally hold great promise for microfluidic and lab-on-a-chip applications requiring local flow actuation without moving parts. For such applications, the design of artificial suspensions of self-propelled nano-magnetic units may be desirable. Our study also paves the way for analyzing the dynamics of more complex systems, such as semi-dilute suspensions where the role of active and magnetic stresses in driving large-scale instabilities [3] has yet to be elucidated.

7.6 Acknowledgements

Chapter 7, in part, is a manuscript published in *Europhysics Letters*; authored by R. Alonso-Matilla and D. Saintillan, "Microfluidic flow actuation using magnetoactive suspensions". The dissertation author is the primary author of this work. We thank C. Cottin-Bizonne, I. Frankel, and C. Rinaldi for useful conversations.

Chapter 8

Geometric control of active collective motion

8.1 Introduction

A common feature of many active matter systems is their ability to spontaneously self-organize into complex dynamic mesoscale structures above a certain density. [140, 246, 252] Such is the case of suspensions of motile bacteria, [253–256] cellular extracts, [181, 257, 258] collections of colloidal rollers, [259, 260] shaken grains, [261, 262] among many others. Particle-particle interactions, whether long-ranged such as hydrodynamic or electrostatic interactions, or short-ranged such as direct contact forces, are the drivers of self-organization. [252] The symmetries of these interactions along with their coupling with system geometry dictates the structure and morphology of the emerging patterns, which include: steady vortices, [260, 263] asters, [257] traveling bands, [258, 259] density shocks, [264, 265] as well as more complex spatiotemporal chaotic patterns composed of unsteady jets and vortices. [253]

Of interest to us in this work is the case of suspensions of hydrodynamically interacting slender self-propelled particles such as swimming bacteria.[266] In these suspensions, particles exert dipolar stresses on the surrounding medium and also align in shear due to their elongated shape. The interplay between these two effects has been known to lead to hydrodynamic instabilities in the case of extensile particles or so-called pushers, which are thought to be responsible for the emergence of collective motion above a critical density. [112, 160, 223, 267] In large unconfined systems, the collective dynamics in the nonlinear

regime takes the form of unsteady chaotic motions reminiscent of high-Reynolds-number turbulence, characterized by strong jets and vortices, enhanced swimming speeds and diffusivities, and efficient fluid mixing. [163]

Only recently have interactions with boundaries and dynamics in confined geometries gained attention in experiments. In dilute systems, it is well known that self-propelled particles accumulate at boundaries [41, 119, 150, 268] as a result of both kinematic [14, 51, 121, 125, 150] and hydrodynamic mechanisms. [41, 269, 270] In complex geometries, transport of the particles along curved boundaries has also been exploited to design ratchets for concentrating microswimmers or directing their motion. [33, 36, 55, 199, 200] The case of semi-dilute to concentrated suspensions in confinement, however, has largely been unexplored but in a few studies. Wioland *et al.* [164] first analyzed the flow inside small droplets of a dense bacterial suspension squeezed between two flat plates. Rather than observing chaotic motion as in bulk systems, they reported the emergence of a steady vortex; detailed observation of the bacterial velocity field in fact revealed a more complex structure with a counter-rotating boundary layer surrounding the vortex core. This vortex was subsequently captured by Lushi *et al.* [165] in discrete particle simulations using a basic model accounting for dipolar hydrodynamic interactions as well as steric forces, where it was found that including hydrodynamic interactions is critical in order to correctly capture the counter-rotating boundary layer. Interactions between such vortices were also considered recently using a microfluidic lattice of circular chambers each containing one vortex and connected by junctions: [271] in this case, hydrodynamic coupling was shown to produce synchronization on the scale of the lattice, with adjacent vortices rotating either in the same or opposite direction depending on the geometry of the junctions between chambers.

The case of periodic geometries such as circular channels and racetracks has also been studied, where spontaneous flows have been reported in both bacterial [166] and sperm [218] suspensions above a critical density. In the case of bacteria, Wioland *et al.* [166] systematically studied the effect of geometry by varying the channel width. In very narrow channels, unidirectional flow takes place with a nearly parabolic velocity profile. Upon increasing channel width, flow patterns start exhibiting longitudinal oscillations leading to sinusoidal trajectories and eventually take the form of arrays of counter-rotating vortices. Longitudinal density waves were also reported in the case of dense semen. [218] The observed transition to directed motion has been predicted in a number of models for active nematics, [219, 220] where extensile stresses were found to be the destabilizing factor leading to spontaneous

flows. These models, however, neglected polarization, which plays an important role in setting the structure of the suspension in confined systems of self-propelled particles; [51] they also assumed anchoring boundary conditions for the nematic order parameter field at the channel boundaries, whereas the distribution of particle orientations near the walls appears to be dependent on flow conditions in experiments. [164, 166] A qualitative explanation for the transition can also be gleaned from recent studies on the effective rheology of active suspensions, [2, 118, 169, 170] where a decrease of the effective viscosity due to activity can lead at sufficiently high densities to a superfluid-like behavior in weak flows; this connection will be made clearer below.

In this paper, we use numerical simulations based on a continuum kinetic model together with linear stability analyses to predict and characterize transitions to spontaneous flows and collective motion in various two-dimensional microfluidic geometries, with the aim of explaining the experimental observations discussed above. In circular domains, a systematic exploration of the parameter space casts light on three distinct states: equilibrium with no flow, stable vortex, and chaotic motion, and the transitions between these are explained and predicted quantitatively using a linearized theory. In periodic racetracks, similar transitions from equilibrium to net pumping to traveling waves to chaos are observed in agreement with experimental observations and are also explained theoretically. Our results underscore the subtle effects of geometry on the morphology and dynamics of emerging patterns in active suspensions and pave the way for the control of active collective motion in microfluidic devices. The governing equations are presented in section 2 and consist of evolution equations for the concentration, polarization and nematic order parameter, which are coupled to the Navier-Stokes equations for the mean-field flow induced by the swimmers. Results from simulations and theory are then discussed in section 3, where both circular domains and periodic racetracks are considered. We conclude in section 4.

8.2 Model and simulation method

8.2.1 Continuum model

We consider a collection of active Brownian particles suspended in a Newtonian fluid of density ρ and shear viscosity μ. The particles swim with velocity v_0 and have constant translational and rotational diffusivities d_t and d_r, respectively. As a result of their self-

propulsion, they also exert a net force dipole on the suspending fluid with stresslet strength σ_0, which we assume to be negative as is the case for extensile swimmers such as bacteria and sperm. [167, 206] The suspension, with mean number density n, is confined in a finite domain with characteristic dimension H, which will be defined more precisely later. Dimensional analysis of the governing equations identifies four relevant dimensionless groups:

$$Re = \frac{\rho H^2 d_r}{\mu}, \quad Pe_s = \frac{v_0}{2 d_r H}, \quad \alpha = \frac{\sigma_0 n}{\mu d_r}, \quad \Lambda = \frac{d_r d_t}{v_0^2}. \tag{8.1}$$

The Reynolds number Re is typically very small for active suspensions; it will be set to 10^{-6} in all the simulations and to zero in the stability results shown below. The swimming Péclet number Pe_s denotes the ratio of the persistence length of swimmer trajectories to the size of the domain and is a measure of confinement. The activity parameter α compares the destabilizing effects of active stresses and of concentration to dissipative processes, namely viscosity and orientation decorrelation by rotational diffusion. Finally, Λ is a swimmer-specific parameter comparing diffusive processes to the strength of self-propulsion: the limit of $\Lambda \to 0$ describes athermal swimmers, whereas $\Lambda \to \infty$ corresponds to Brownian particles that do not swim.

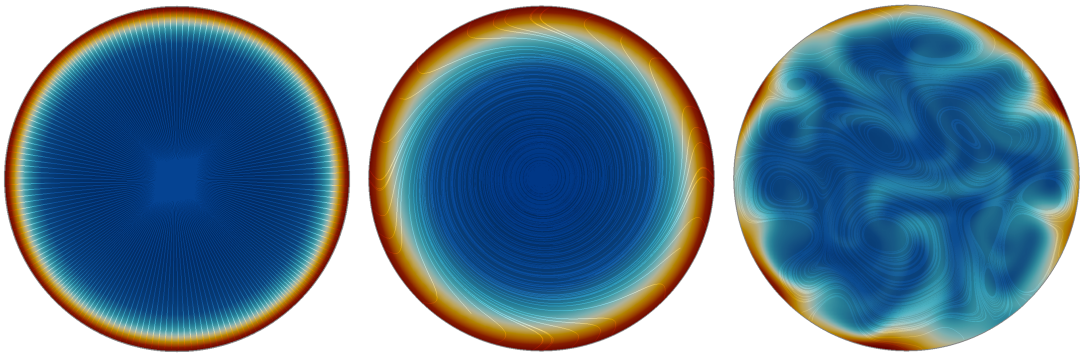

(a) $\alpha = -1$ (b) $\alpha = -20$ (c) $\alpha = -200$

Figure 8.1: Concentration profiles and streamlines of the net particle velocity $\mathbf{V}(\mathbf{x}) = 2Pe_s\mathbf{m}(\mathbf{x})/c(\mathbf{x}) + \mathbf{u}(\mathbf{x})$ showing three distinct regimes in a circular domain: (a) equilibrium base state with no flow (phase I); (b) double vortex flow (phase II); and (c) turbulent swirling state (phase III). Red indicates high concentration while blue is associated to a lower concentration. Results shown are for $Pe_s = 0.5$ and $\Lambda = 0.1$. Also see electronic supplementary material for a movie showing the dynamics in each case.

We adopt a two-dimensional continuum mean-field description of the active suspension based on the probability density function $P(\mathbf{x}, \mathbf{p}, t)$ of finding a particle at position $\mathbf{x}$

with orientation $\mathbf{p}$ at time t, where $\mathbf{p}$ is a unit vector defining the swimming direction and orientation of the bacteria. [160] Following prior studies, [140] we approximate P in terms of its first three orientational moments: (see §1.1.2)

$$P(\mathbf{x}, \mathbf{p}, t) \approx \frac{1}{2\pi} \left[c(\mathbf{x}, t) + 2\mathbf{p} \cdot \mathbf{m}(\mathbf{x}, t) + 4\mathbf{pp} : \mathbf{D}(\mathbf{x}, t) \right], \tag{8.2}$$

where c, $\mathbf{m}$, and $\mathbf{D}$ are defined as integrals over the unit circle C of orientations:

$$c(\mathbf{x}, t) = \int_C P(\mathbf{x}, \mathbf{p}, t)\, d\mathbf{p}, \tag{8.3}$$

$$\mathbf{m}(\mathbf{x}, t) = \int_C \mathbf{p}\, P(\mathbf{x}, \mathbf{p}, t)\, d\mathbf{p}, \tag{8.4}$$

$$\mathbf{D}(\mathbf{x}, t) = \int_C \left(\mathbf{pp} - \frac{\mathbf{I}}{2} \right) P(\mathbf{x}, \mathbf{p}, t)\, d\mathbf{p}. \tag{8.5}$$

The zeroth moment c is the local concentration, whereas the first and second moments $\mathbf{m}$ and $\mathbf{D}$ describe the local polarization and nematic alignment in the suspension, respectively. Starting from a Smoluchowski equation for $P(\mathbf{x}, \mathbf{p}, t)$, [160] hierarchical evolution equations for the moments can be obtained, which are written as:

$$\partial_t c = -\nabla \cdot \mathbf{F}_c, \tag{8.6}$$

$$\partial_t \mathbf{m} = -\nabla \cdot \mathbf{F}_m + \tfrac{1}{2}\gamma \mathbf{E} \cdot \mathbf{m} - \mathbf{W} \cdot \mathbf{m} - \mathbf{m}, \tag{8.7}$$

$$\partial_t \mathbf{D} = -\nabla \cdot \mathbf{F}_D + \tfrac{1}{2}\gamma c \mathbf{E} + \tfrac{2}{3}\gamma \mathbf{E} \cdot \mathbf{D} - \tfrac{1}{3}\gamma \left(\mathbf{D} : \mathbf{E} \right) \mathbf{I} + \mathbf{D} \cdot \mathbf{W} - \mathbf{W} \cdot \mathbf{D} - 4\mathbf{D}, \tag{8.8}$$

where the dimensionless shape parameter γ denotes Bretherton's constant; [194] we set $\gamma = 1$ in the present study as is adequate for slender swimmers. Variables have been made dimensionless using length scale H and time scale d_r^{-1}. The source terms on the right-hand side of Eqs. (8.7)–(8.8) arise from alignment and rotation by the rate-of-strain and vorticity tensors $\mathbf{E}$ and $\mathbf{W}$ of the disturbance velocity field $\mathbf{u}$, and from rotational diffusion which promotes relaxation towards isotropy with $\mathbf{m} = \mathbf{0}$ and $\mathbf{D} = \mathbf{0}$. The fluxes in the equations for c, $\mathbf{m}$, and $\mathbf{D}$ include contributions from advection by the flow, self-propulsion

and translational diffusion, and are given by

$$\mathbf{F}_c = \mathbf{u}\, c + 2Pe_s\, \mathbf{m} - 4\Lambda Pe_s^2 \nabla c, \tag{8.9}$$

$$\mathbf{F}_m = \mathbf{u}\, \mathbf{m} + 2Pe_s \left(\mathbf{D} + c\tfrac{\mathbf{I}}{2}\right) - 4\Lambda Pe_s^2 \nabla \mathbf{m}, \tag{8.10}$$

$$\mathbf{F}_D = \mathbf{u}\, \mathbf{D} + 2Pe_s \left(\mathbf{T} - \mathbf{m}\tfrac{\mathbf{I}}{2}\right) - 4\Lambda Pe_s^2 \nabla \mathbf{D}, \tag{8.11}$$

where the third-order tensor $\mathbf{T}$ is the third orientational moment and is related to the polarization according to the closure approximation implied by Eq. (8.2) as

$$T_{ijk} = \frac{1}{4}\left(m_i \delta_{jk} + m_j \delta_{ik} + m_k \delta_{ij}\right). \tag{8.12}$$

Direct steric interactions between swimmers are neglected within this model. Their leading effect is expected to be an enhancement of local nematic alignment due to the elongated shape of the particles; this effect could easily be incorporated in our model using a nematic alignment potential as previously done by Ezhilan *et al.*, [162] though hydrodynamic interactions alone are sufficient to capture all the phenomenology observed in experiments.

Finally, the disturbance fluid velocity field $\mathbf{u}$ satisfies the incompressible Navier-Stokes equations forced by the divergence of the active stress tensor $\alpha\mathbf{D}$:

$$\nabla \cdot \mathbf{u} = 0, \quad Re\left(\partial_t \mathbf{u} + \mathbf{u} \cdot \nabla \mathbf{u}\right) = -\nabla p + \nabla^2 \mathbf{u} + \alpha \nabla \cdot \mathbf{D}. \tag{8.13}$$

Note that additional passive stresses also arise due to the inextensibility of the particles in the flow field they generate: we neglect those here as it can be shown that they only act to increase the Newtonian viscosity in the limit of weak flows relevant to the spontaneous flow transitions investigated here, and therefore only renormalize the value of α at the instability threshold. Including these stresses would be straightforward and the reader is referred to our previous work [2, 169] on the rheology of active suspensions for more details.

In all of our simulations and analysis, we enforce a no-slip boundary condition on the velocity $\mathbf{u}$ on the domain boundary S. The natural boundary condition for the particle distributions is a no-translational-flux condition on the probability density function P, which translates into no-flux conditions on the orientational moments upon closure of the equations: [51] $\mathbf{n}\cdot\mathbf{F}_c = \mathbf{n}\cdot\mathbf{F}_m = \mathbf{n}\cdot\mathbf{F}_D = 0$, where $\mathbf{n}$ is the local unit normal. These conditions express the balance between self-propulsion and translational diffusion in the wall-normal direction, and

were shown to correctly capture particle distributions near boundaries in confined systems. [51]

8.2.2 Numerical approach

We solve the governing equations numerically using a hybrid finite-difference finite-volume framework. [272–275] The method is implemented on adaptive quadtree grids and the domain boundaries are represented using the level-set method. At each time step of the algorithm, the moment equations (8.6)–(8.8) are solved semi-implicitly: the diffusive terms are treated implicitly and the advective terms are computed using a semi-Lagrangian approach for improved stability, whereas the remaining coupling terms are treated explicitly. Values of the concentration field are stored at the cell centers to improve its total conservation, while the polarization and nematic order parameter fields are stored at the mesh nodes for better accuracy. Knowledge of the second moment $\mathbf{D}$ allows one to calculate the divergence of the active stress $\alpha\nabla\cdot\mathbf{D}$, which is an input to the Navier-Stokes solver [275] used to update the fluid velocity field. A detailed description of the algorithm will be presented elsewhere.

8.3 Results and discussion

8.3.1 Circular disks

Motivated by the experiments of Wioland *et al.* [164] in quasi-two-dimensional droplets, we first investigate the dynamics in circular domains, where we take the confinement length scale H to be the radius of the disk. Our simulations in this case show that the collective self-organization depends critically on the level of activity (parameter α) and degree of confinement (swimming Péclet number Pe_s). Specifically, three distinct phases illustrated in Fig. 8.1 are observed depending on the values of α and Pe_s: an axisymmetric equilibrium state with no fluid flow (phase I), an axisymmetric and steady double vortex (phase II), and a turbulent-like unsteady chaotic state (phase III). In some cases, more complex axisymmetric flow patterns can also be observed before the transition to chaos, including triple vortices as illustrated in Fig. 8.2; such flow patterns are only very rarely observed and we do not discuss them further. Transitions between the three regimes, which are characterized in more detail below, can be captured in a phase diagram in the (α, Pe_s)-plane as shown

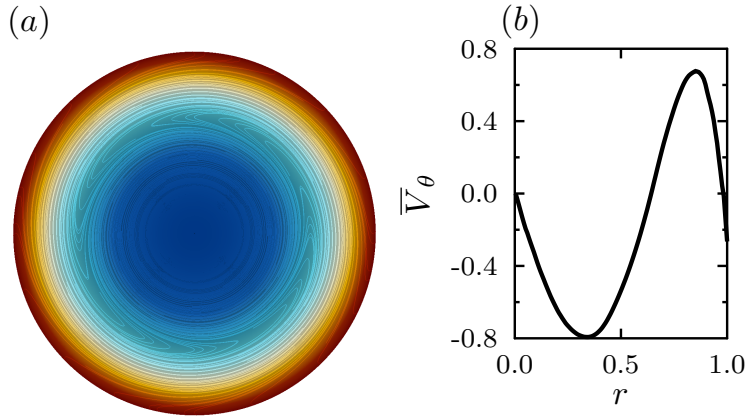

Figure 8.2: Axisymmetric triple vortex in which the net particle velocity V_θ changes sign twice across the disk radius; this state is only rarely observed and therefore not included in the phase diagram of Fig. 8.3. (a) Concentration profile and streamlines of the net particle velocity. (b) Radial profile of the azimuthal particle velocity averaged over the azimuthal direction. Parameter values for this simulation are $Pe_s = 0.2$, $\alpha = -40$, and $\Lambda = 0.2$.

in Fig. 8.3(a), where we find that either increasing activity or decreasing confinement successively destabilizes phase I into phase II followed by phase III. While distinguishing between these states is straightforward by simple observation of the dynamics, we also introduce an order parameter as a quantitative measure:

$$\Phi = \left\langle \frac{2}{\pi} \int_\Omega \frac{|V_\theta|}{|\mathbf{V}|} d\mathbf{x} - 1 \right\rangle_t, \tag{8.14}$$

where $\mathbf{V} = 2Pe_s\,\mathbf{m}(\mathbf{x})/c(\mathbf{x}) + \mathbf{u}(\mathbf{x})$ is the net velocity of the active particles due to both swimming and advection by the flow, V_θ is its azimuthal component, Ω is the circular domain, and $\langle\cdot\rangle_t$ denotes a time average. Note that the velocity $\mathbf{V}$ is the same as that measured in experiments, which typically perform particle-image velocimetry based on swimmer displacements. [164, 166] The order parameter in Eq. (8.14) is defined such that $\Phi = -1$ for purely radial motion (phase I), $\Phi = +1$ for purely azimuthal motion (phase II), and $\Phi = \sqrt{2} - 1$ for a system in which motion occurs equally along the radial and azimuthal directions (phase III). A plot of Φ vs $|\alpha|$ for various values of Pe_s is shown in Fig. 8.3(b), where it indeed jumps from -1 to $\approx +1$ as the transition from phase I to phase II occurs, before eventually decreasing to a value close to $\sqrt{2} - 1$ as the chaotic state of phase III emerges. We now proceed to characterize the three phases in more detail.

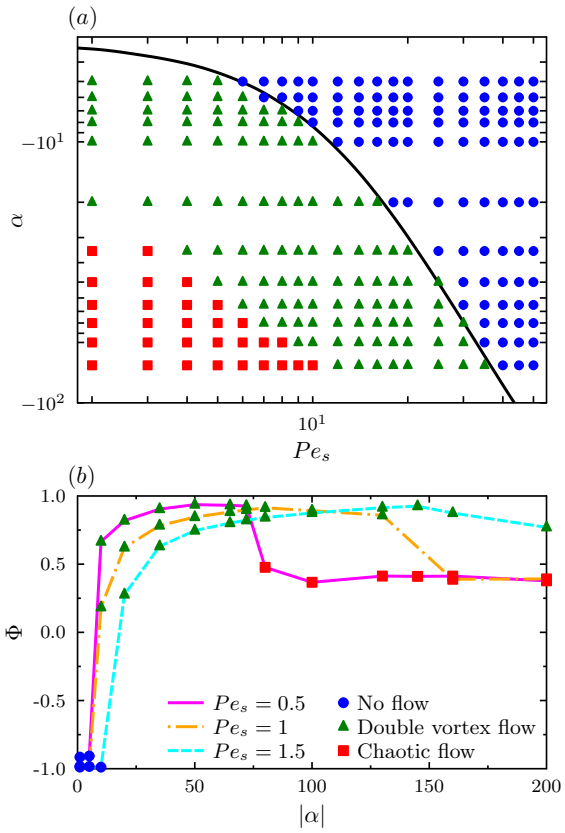

Figure 8.3: Flow transitions in circular disks. (a) Phase diagram in the (α, Pe_s)-plane for $\Lambda = 0.1$ showing the transitions between phases I, II and III. The black curve shows the marginal stability for the equilibrium state of phase I as predicted by a linear stability analysis. (b) Order parameter Φ defined in Eq. (8.14) as a function of activity $|\alpha|$ for three different values of Pe_s. $\Phi = -1$ corresponds to purely radial motion, $\Phi = +1$ to purely azimuthal motion, and $\Phi = \sqrt{2} - 1$ to equal amounts of radial and azimuthal motion.

Phase I: Equilibrium state with no flow

This regime, illustrated in Fig. 8.1(a), occurs for low levels of activity (small $|\alpha|$) and strong levels of confinement (large Pe_s), and is characterized by the absence of hydrodynamic flow. As is known to be the case in dilute confined active suspensions, [51] particles tend to accumulate near the system boundaries and on average point towards the boundary, which leads to a net radial polarization $m_r(r) > 0$ that reaches its maximum at the walls. The azimuthal polarization m_θ is zero in this case, as are off-diagonal components $D_{r\theta}$ and $D_{\theta r}$ of the nematic order tensor. An analytical solution for the first two moments can in fact be derived in this case by neglecting nematic alignment ($\mathbf{D} = \mathbf{0}$), which is a good approximation as shown by full numerical simulations. If the nematic order tensor is neglected ($\mathbf{D} = \mathbf{0}$), which is a good approximation at equilibrium as shown by the full numerical solution, simple

closed-form analytical solutions can be derived for the radial concentration and polarization profiles which we provide here. In axisymmetric geometries, the steady governing equations for $c(r)$ and $m_r(r)$ obtained by setting the $\mathbf{F}_c$ and $\mathbf{F}_m$ in Eqs. (8.9)–(8.10) in the absence of flow simplify to:

$$-\frac{d}{dr}(rm_r) + 2\Lambda Pe_s \frac{d}{dr}\left(r\frac{dc}{dr}\right) = 0, \tag{8.15}$$

$$-\frac{dc}{dr} + 4\Lambda Pe_s \frac{d}{dr}\left[\frac{1}{r}\frac{d}{dr}(rm_r)\right] - m_r = 0. \tag{8.16}$$

In a circular disk, the boundary conditions at $r = 1$ are:

$$-m_r + 2\Lambda Pe_s \frac{dc}{dr} = 0, \tag{8.17}$$

$$-\frac{c}{2} + 2\Lambda Pe_s \frac{dm_r}{dr} = 0, \tag{8.18}$$

and we also require that the solution remain bounded at $r = 0$ and satisfy the normalization

$$\int_0^1 c(r) r dr = \frac{1}{2}. \tag{8.19}$$

Integrating Eq. (8.15) once easily shows that the boundary condition of Eq. (8.17) in fact applies everywhere across the gap and expresses the local balance between swimming and diffusive fluxes. Inserting Eq. (8.17) into Eq. (8.16) and manipulating then provides a modified Bessel equation for $m_r(r)$:

$$r^2\frac{d^2m_r}{dr^2} + r\frac{dm_r}{dr} - (1 + \Omega^2 r^2)m_r = 0, \tag{8.20}$$

where

$$\Omega^2 = \frac{1}{4Pe_s^2\Lambda}\left(1 + \frac{1}{2\Lambda}\right). \tag{8.21}$$

A small manipulation predicts a dimensionless characteristic thickness for the wall accumulation layer given by

$$\Omega^{-1} = 2\Lambda Pe_s\sqrt{2/(1 + 2\Lambda)}, \tag{8.22}$$

which can also be interpreted as the length scale over which the effects of the boundary are screened by diffusive processes. [52] As first discussed by Ezhilan & Saintillan, [51] two interesting limiting cases are found. When $\Lambda \to 0$ (strong-propulsion limit), the thickness

of the layer is set by the balance of swimming and translational diffusion and is given by $\Omega^{-1}H \approx \sqrt{2}\, d_t/v_0$; on the other hand, the weak-propulsion limit of $\Lambda \to \infty$ yields a thickness of $\Omega^{-1}H \approx \sqrt{d_t/d_r}$, which is a purely diffusive length scale. After applying boundary conditions, the concentration and polarization profiles are obtained as

$$c(r) = A_1 + A_2 I_0(\Omega r), \quad m_r(r) = A_2 I_1(\Omega r), \tag{8.23}$$

where the constants A_1 and A_2 are expressed in terms of incomplete Bessel functions as

$$A_1 = 1 - \frac{2}{\Omega} I_1(\Omega) A_2, \tag{8.24}$$

$$A_2 = \left[(4\Lambda^2 Pe_s^2 - 1) I_0(\Omega) + \frac{2}{\Omega} I_1(\Omega) + 4\Lambda^2 Pe_s^2 \Omega^2 I_2(\Omega) \right]^{-1}. \tag{8.25}$$

The expression for $c(r)$ in Eq. (8.23) is identical to that previously obtained by Yan & Brady. [52] The solution inside an annulus is also easily obtained by applying boundary conditions of Eqs. (8.17)–(8.18) at both walls $r = r_{\min}$ and $r_{\min} + 2$ but is omitted here for brevity. The solution in a straight channel was also previously calculated by Ezhilan & Saintillan. [51]

Phase II: Steady axisymmetric vortex

Upon decreasing confinement or increasing the level of activity, a first transition is observed from the equilibrium state to a steady axisymmetric double vortex shown in Fig. 8.1(b), as a consequence of the coupled effect of nematic alignment induced by hydrodynamic interactions and base-state heterogeneities in the concentration and radial polarization profiles. The direction of rotation in this case is arbitrary with equal probabilities for clockwise and counter-clockwise motions, though it is found to remain the same for the duration of the simulation. More details on this regime, which is identical to that reported in the experiments of Wioland *et al.* [164], are shown in Fig. 8.4, where profiles of the azimuthal components of the fluid velocity u_θ, net particle velocity V_θ, polarization m_θ, and active flow forcing $f_\theta = \alpha r^{-2} \partial_r (r^2 D_{r\theta})$ are plotted for different parameter values. While the azimuthal fluid velocity u_θ always points in the same direction, the net particle velocity V_θ follows the fluid flow near the center of the domain but changes sign at a distance away from the boundary, indicating that particles near the circular wall move against the local flow in agreement with experiments and previous models. [164, 165] Fig. 8.4(c) in fact shows that the azimuthal

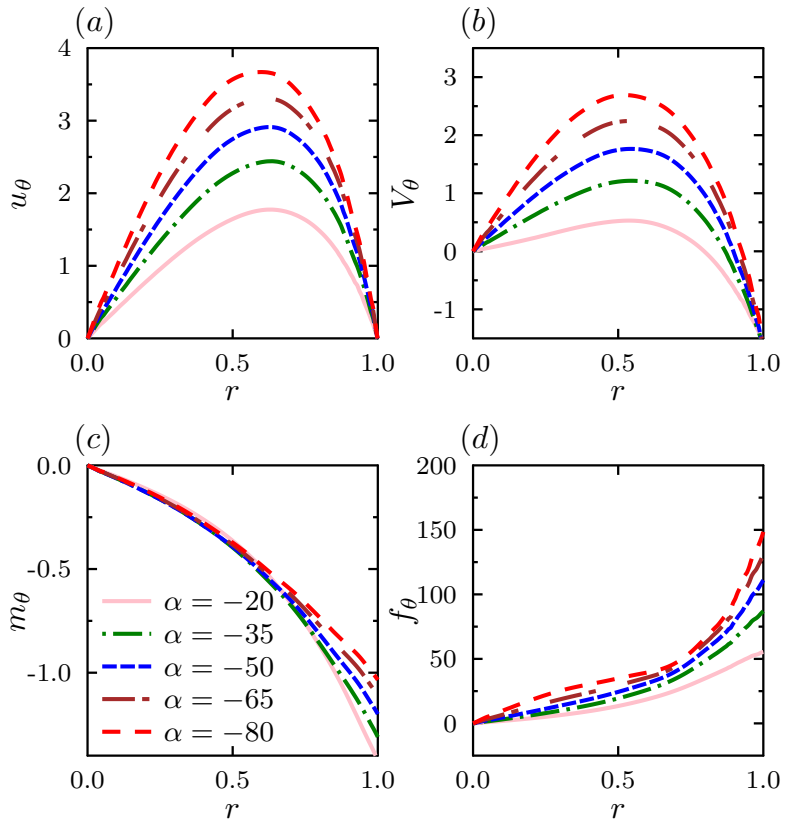

Figure 8.4: Double vortex flow in a circular disk (phase II): radial profiles of (a) the azimuthal fluid velocity u_θ, (b) the azimuthal net particle velocity V_θ, (c) the azimuthal polarization m_θ, and (d) the active flow forcing $f_\theta = \alpha r^{-2}\partial_r(r^2 D_{r\theta})$ for different levels of activity, for $Pe_s = 1$ and $\Lambda = 0.1$.

polarization is negative, i.e. particles swim against the flow everywhere but only overcome it near the wall. This observation is consistent with the well-known phenomenon of upstream swimming, by which near-wall bacteria tend to swim against the fluid in pressure-driven channel flows of active suspensions. [51, 198, 201, 202, 276] As the transition from phase I to phase II occurs, we also find that particle accumulation at the boundary is weakened, which is a consequence of the alignment of the particles with the hydrodynamic flow, which reduces the wall-normal polarization and therefore hinders the ability of the particles to swim towards the wall; a similar effect is again also known to occur in pressure-driven channel flows. [51, 119]

Mechanistic insight into the formation of the double vortex can be gained by performing a linear stability analysis, in which we theoretically analyze the growth of axisymmetric perturbations to the equilibrium base state with no flow (phase I). Results from this analysis are summarized in Fig. 8.5. The analysis indeed reveals a linear instability of the equilibrium

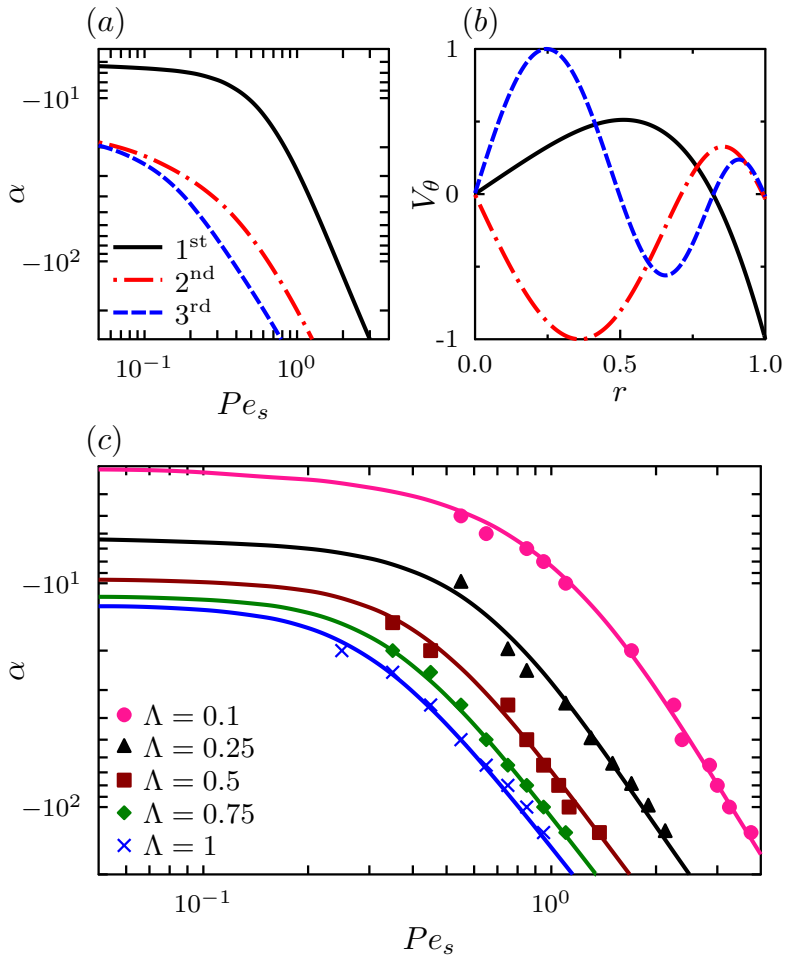

Figure 8.5: Linear stability of the equilibrium base state (phase I) in a circular disk. (a) Marginal stability curves in the (α, Pe_s)-plane for the first three unstable modes at $\Lambda = 0.25$. (b) Unstable eigenmodes for the net particle velocity V_θ for $Pe_s = 0.5$, and $\Lambda = 0.25$ at the onset of instability. (c) Marginal stability curves for the first unstable mode for different values of Λ obtained by linear stability analysis (full lines); symbols show the marginal curve for the transition from phase I to phase II in numerical simulations.

base state, with a hierarchy of unstable modes for which we plot the marginal stability curves in the (α, Pe_s)-plane in Fig. 8.5(a) and the net azimuthal velocity V_θ in Fig. 8.5(b). The first unstable mode has a structure that is very similar to the nonlinear flow field of Fig. 8.4(b), with a vortex core and a counter-rotating boundary layer near the domain wall. Subsequent modes, which become unstable at higher values of $|\alpha|$ as shown in Fig. 8.5(a), exhibit more and more complex structures with alternating layers rotating in opposite directions. These modes are only very rarely observed in simulations, and an example of a triple vortex similar for the second unstable mode is shown in Fig. 8.2; in most cases, however, we find that the double vortex instead destabilizes directly into the chaotic state.

The linearized theory also sheds light on the mechanism for the transition, which can be summarized as follows: (i) At equilibrium (phase I), particles near the boundary have a net polarization towards the wall; [51] (ii) A weak azimuthal flow perturbation causes these particles to rotate due to shear and align at an angle with respect to the radial direction, leading to a net shear nematic alignment $D_{r\theta}$ which is strongest near the wall, as well as an azimuthal polarization in the direction opposite to the fluid flow; (iii) Hydrodynamic disturbances induced by the swimming activity in the nematically-aligned region tend to reinforce the flow perturbation in the case of pushers via the active forcing term $f_\theta = \alpha r^{-2}\partial_r(r^2 D_{r\theta})$ in the θ-momentum equation. In particular, it can be checked both in theory and simulations that suspensions of pullers for which $\alpha > 0$ are always stable and only exhibit phase I. A more quantitative comparison between theory and simulations is shown in Fig. 8.5(c), where the marginal stability curves for the first unstable mode for different values of Λ are found to match the numerical transition from phase I to phase II. Fig. 8.5(c) also shows the influence of the parameter Λ: increasing its value has a stabilizing effect due to diffusion, which smoothes out the wall accumulation layer responsible for driving the flow.

The low- and high-Péclet limits for the marginal stability of the equilibrium state can also be characterized more precisely as illustrated in Fig. 8.6. In weakly confined systems ($Pe_s \to 0$), the marginal value of α for instability becomes independent of system size as shown by the constant asymptote in Fig. 8.5(c): in this case, the instability is primarily driven by processes inside the accumulation layer. We now derive an approximate expression for the critical value of α. The stability analysis is performed by perturbing the governing equations about the equlibrium state, which we denote by $(c^0, \mathbf{m}^0, \mathbf{D}^0)$. We focus here on the marginal stability, for which the growth rate is set to zero. In large domains, the effect of boundary curvature on the structure of the accumulation layer is negligible, which prompts us to use Cartesian coordinates. Upon linearization of the equations, we arrive at a coupled system for the variables m_x' and D_{xy}' (where $'$ refers to perturbations):

$$0 = -2Pe_s\frac{dD_{xy}'}{dy} + 4\Lambda Pe_s^2\frac{d^2m_x'}{dy^2} - \frac{3}{4}\alpha_c D_{xy}' m_y^0 - m_x', \tag{8.26}$$

$$0 = -\frac{1}{2}Pe_s\frac{dm_x'}{dy} + 4\Lambda Pe_s^2\frac{d^2D_{xy}'}{dy^2} - \alpha_c D_{xy}'\left(\frac{c^0}{4} + D_{yy}^0\right) - 4D_{xy}'. \tag{8.27}$$

These constitute an eigenvalue problem for (m_x', D_{xy}') with corresponding eigenvalue α_c. In the low-Pe_s limit, the dominant balance in Eq. (8.27) is between the last two terms, which

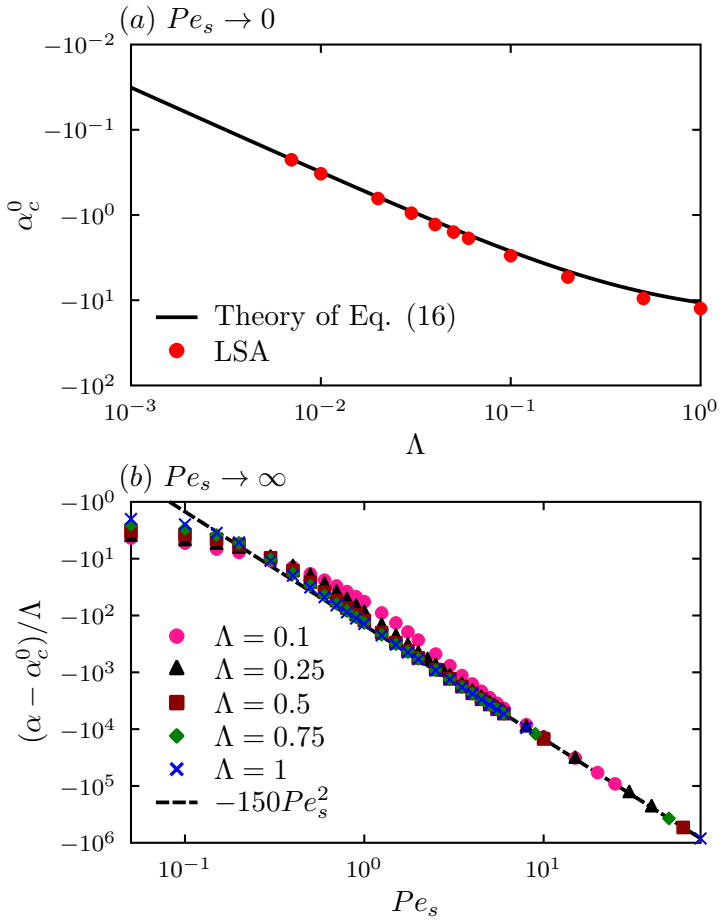

Figure 8.6: Analytical prediction of the marginal stability curve. (a) Low-Pe_s asymptote α_c^0 for the critical value of the activity parameter leading to instability of the equilibrium state: the plot compares the theoretical prediction of Eq. (8.29) to the full numerical solution of the linear stability problem (LSA). (b) High-Pe_s asymptote: the plot shows $(\alpha - \alpha_c^0)/\Lambda$ as a function of Pe_s and confirms the scaling prediction of Eq. (8.30) with fitting parameter $\beta \approx 150$.

capture flow alignment and rotational diffusion. An estimate for α_c can then be obtained by balancing these two terms and by using the maximum values of c^0 and D_{yy}^0, which are attained at the walls:

$$\alpha_c^0 \approx \frac{-4}{\frac{c^0_{wall}}{4} + D^0_{yy,wall}} \qquad \text{as} \quad Pe_s \to 0, \tag{8.28}$$

, and it becomes

$$\alpha_c^0 \approx -\frac{32\Lambda}{1+2\Lambda} \qquad \text{as} \quad Pe_s \to 0, \tag{8.29}$$

which matches the numerical solution of the linear stability problem excellently, especially for small values of Λ, as shown in Fig. 8.6(a). In the high-Pe_s limit (strong confinement),

the dominant balance now takes place between the second and third terms in Eq. (8.27), which describe translational diffusion and shear alignment, being the former the stabilizing factor. While the use of Cartesian coordinates is no longer justified in this case, the form of the equations still suggests an asymptote of the type

$$\alpha_c^{\infty} \approx -\beta \Lambda Pe_s^2 \qquad \text{as} \quad Pe_s \to \infty, \tag{8.30}$$

where β is an unknown constant. Plotting $(\alpha - \alpha_c^0)/\Lambda$ as a function of Pe_s in Fig. 8.6(b) indeed collapses all the marginal stability curves onto a single power-law consistent with Eq. (8.30), where the fitting parameter β is found to depend very weakly on Λ and to asymptote to $\beta \approx 150$ at high values of Λ. A composite approximation for the marginal stability curve can therefore be written as

$$\alpha_c \approx -\frac{32\Lambda}{1+2\Lambda} - 150\Lambda Pe_s^2, \tag{8.31}$$

which provides an excellent fit to our numerical data over a wide range of parameter values. The high-Pe_s asymptote of Eq. (8.30) can also be used to define a critical domain diameter for the emergence a double vortex in strong confinement:

$$D_c \approx 5\sqrt{\frac{6\mu d_t}{n\sigma_0}}. \tag{8.32}$$

Interestingly, this critical domain size only depends upon d_t and does not involve d_r. The scaling with number density $D_c \sim n^{-1/2}$ also differs from the scaling of n^{-1} for the critical system size for the onset of collective motion in bulk systems. [277]

Phase III: Turbulent swirling state

As the level of activity keeps increasing and confinement is decreased, phase II becomes unstable itself leading to phase III, which is an unsteady chaotic state analogous to that observed in unbounded systems. [162, 223] There is no clear structure to the flow in this case, which is instead characterized by local jets and vortices driven by active stresses. Note that the transition to phase III is not predicted by our linear theory, which can only account for axisymmetric disturbances. Based on previous analyses of unbounded active turbulence, [112, 223, 267] we hypothesize that the transition nonetheless results from a linear instability

of the double vortex of phase II to two-dimensional disturbances, though a more detailed theoretical analysis remains to be done in this case.

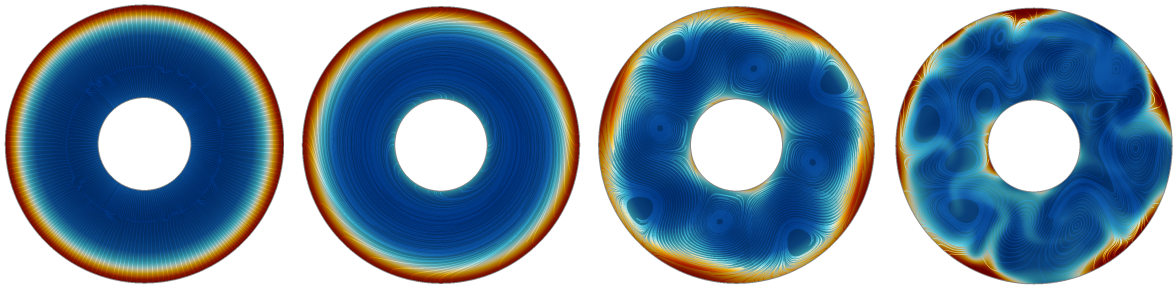

(a) $\alpha = -10$ (b) $\alpha = -40$ (c) $\alpha = -70$ (d) $\alpha = -100$

Figure 8.7: Concentration profiles and streamlines of the net particle velocity showing four distinct regimes in a circular annulus: (a) equilibrium base state with no flow (phase I); (b) axisymmetric azimuthal flow with net pumping (phase II); (c) azimuthal flow with net pumping and traveling waves (phase III); and (d) turbulent swirling state (phase IV). Red indicates high concentration while blue is associated to a lower concentration. Results shown are for $Pe_s = 0.5$ and $\Lambda = 0.5$. Also see electronic supplementary material for a movie showing the dynamics in each case.

8.3.2 Periodic channels: circular annuli

We now turn our attention to the case of periodic channels and first focus on annulus geometries in which the two boundaries are concentric circles. We use the channel halfwidth as the characteristic length scale H, and introduce an additional parameter as the dimensionless inner radius $r_{\min}$. The phenomenology in this case is illustrated in Fig. 8.7, where four distinct regimes are observed: an axisymmetric equilibrium state with no fluid flow (phase I), an axisymmetric spontaneously flowing state with net fluid pumping (phase II), a spontaneously flowing state with net fluid pumping and traveling density waves (phase III), and a turbulent-like chaotic state (phase IV). With the exception of phase III (traveling waves), these regimes are qualitatively similar to those found in circular disks. Transitions between the different states also show similar trends in the (α, Pe_s)-plane, as depicted in the phase diagram of Fig. 8.8(a) where phase III occupies a thin region between phases II and IV. Transitions are also characterized in Fig. 8.8(b), where the absolute value of the mean azimuthal particle velocity $|\overline{V}_\theta|$ is plotted as a function of $|\alpha|$ for different Péclet numbers. As expected, the transition from equilibrium to net pumping is accompanied by a bifurcation from zero to a finite flow rate; the flow rate initially increases with activity up to the point

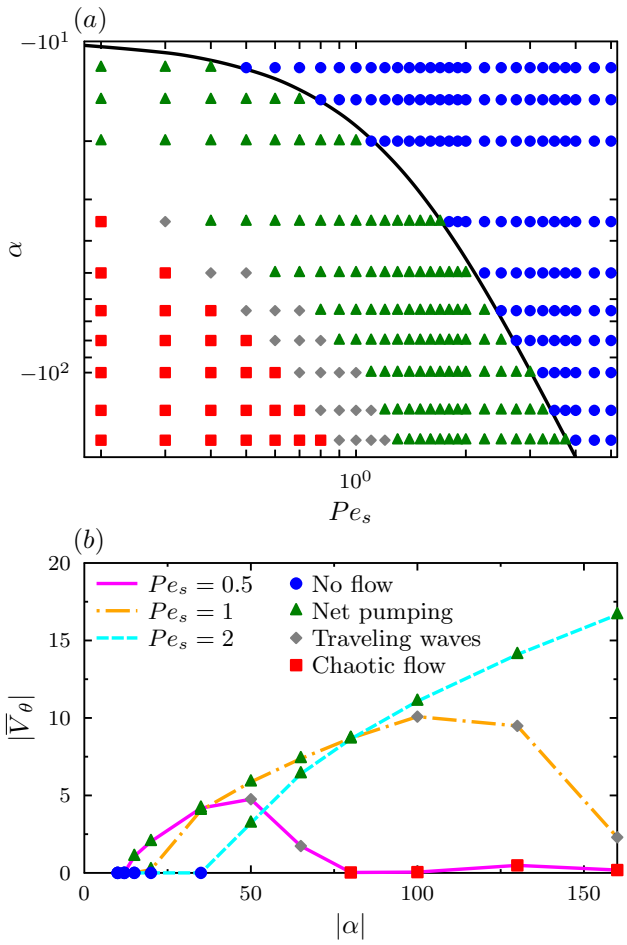

Figure 8.8: Flow transitions in circular annuli. (a) Phase diagram in the (α, Pe_s) plane for $\Lambda = 0.5$ and $r_{\min} = 1$, showing the transitions between phases I, II, III, and IV. The black curve shows the marginal stability for the equilibrium state of phase I as predicted by a linear stability analysis. (b) Mean azimuthal particle velocity $|\overline{V}_\theta|$ as a function of activity $|\alpha|$ for three different values of Pe_s.

when traveling waves appear, after which it start decreasing to reach zero in the chaotic state. We now discuss the various regimes in more detail.

Phase I: Equilibrium state with no flow

The equilibrium state shown in Fig. 8.7(a) is very similar to that found in circular domains, and is characterized by particle accumulation and wall normal polarization at the outer boundary. The particle distribution at the inner boundary, however, shows a subtle dependence on parameter values and can either show accumulation (with $m_r < 0$) or depletion (with $m_r > 0$). This is illustrated in Fig. 8.9(a)-(b), where we plot radial concentration and polarization profiles across the gap for different channel widths (i.e. different values of

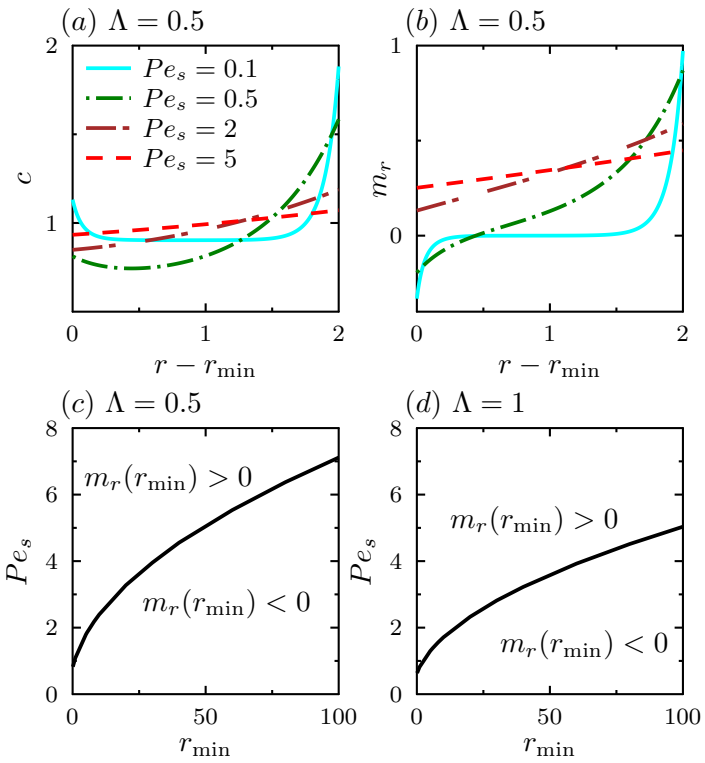

Figure 8.9: Equilibrium distribution (phase I) inside an annulus. (a) Concentration and (b) polarization profiles across the gap as functions of Pe_s, for $\Lambda = 0.5$ and $r_{\min} = Pe_s$, which is equivalent to varying gap width in dimensional terms. (c)-(d) Transition from accumulation to depletion at $r = r_{\min}$ in the $(Pe_s, r_{\min})$-plane for $\Lambda = 0.5$ and 1, respectively.

Pe_s and $r_{\min}$ at a fixed ratio of $Pe_s/r_{\min}$): in wide channels (small Pe_s) accumulation occurs at both boundaries, but a depletion is observed in narrow channels (large Pe_s) in which case attraction by the outer boundary dominates due to curvature effects and propagates across the entire gap due to diffusion in spite of the presence of the inner wall. Depletion at the inner boundary occurs in strongly diffusive systems or under strong confinement, where both the concentration and polarization profiles become linear across the gap. The transition between the two types of distributions is captured in Fig. 8.9(c) in terms of Pe_s and $r_{\min}$ for $\Lambda = 0.5$: as $r_{\min}$ decreases for a fixed gap width, the curvature of the outer boundary becomes more positive while that of the inner boundary becomes more negative, leading to a higher symmetry breaking between walls thus fostering depletion at the inner wall. The same transition is captured in Fig. 8.9(d) for $\Lambda = 1$, where particle attraction by the outer wall is yet stronger as translational diffusion is enhanced.

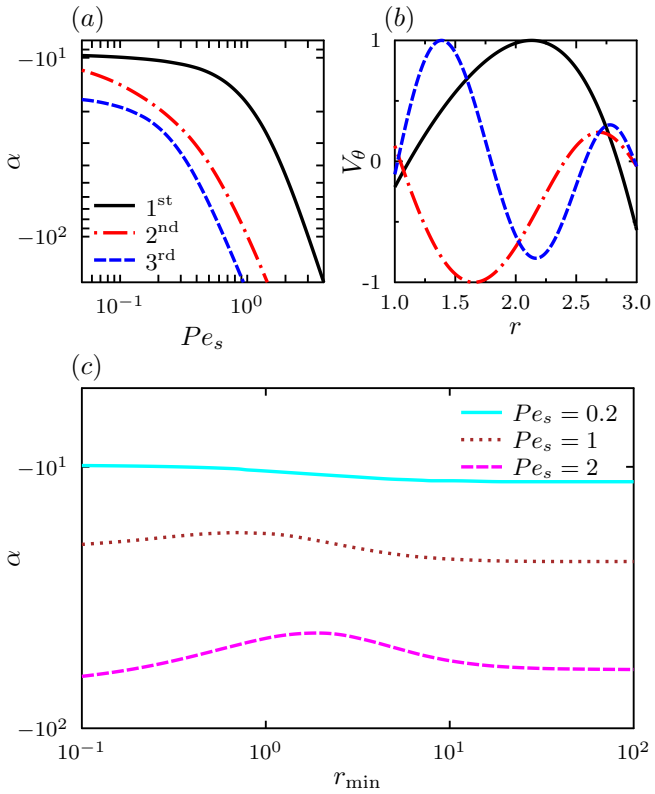

Figure 8.10: Linear stability of the equilibrium base state (phase I) in a circular annulus. (a) Marginal stability curves in the (α, Pe)-plane for the first unstable modes at $\Lambda = 0.5$ and $r_{\min} = 1$ (b) Unstable eigenmodes for the net particle velocity V_θ for $Pe = 0.5$, $\Lambda = 0.5$, and $r_{\min} = 1$ at the onset of instability. (c) Marginal stability curves for the first unstable mode in the $(\alpha, r_{\min})$ plane for different values of Pe_s and for $\Lambda = 0.5$.

Phase II: Spontaneous flow with net pumping

As activity is increased or confinement is decreased, a first transition to an axisymmetric flowing state with net fluid pumping occurs (phase II). As previously seen in Fig. 8.8(b), the mean azimuthal velocity $|\overline{V}_\theta|$ is non-zero in this regime and increases monotonically with the level of activity up to the point where traveling waves appear (phase III below). The transition to unidirectional flow is similar to that reported in both bacterial [166] and sperm [218] suspensions. It was also predicted in a few previous theoretical and numerical models, [219, 220] though these typically imposed anchoring boundary conditions on the nematic order parameter, which are not appropriate to describe suspensions of swimmers such as bacteria.

As in the case of the disk, the transition to spontaneous flow can be understood as a linear instability of the equilibrium base state (phase I) as analyzed more precisely in

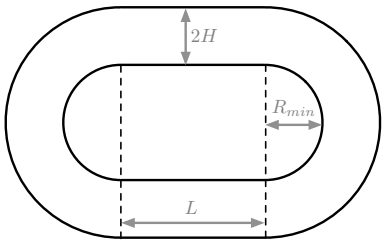

Figure 8.11: Racetrack geometry: each boundary is composed of two straight sections (length L) and two half-circles (radii $r_{\min}$ and $r_{\min} + 2H$). The distance between the two walls is $2H$, where the half-width H is chosen for non-dimensionalization.

Fig. 8.10. Here again, an infinite series of unstable modes exists, which involve increasingly complex azimuthal flow fields with alternating layers rotating in opposite directions, for which we show the marginal stability curves and profiles of the net particle velocity in Fig. 8.10(a)-(b). The first unstable mode, which causes the strongest pumping, is typically observed in simulations, though higher modes are also seen on rare occasions. As shown in Fig. 8.10(b), upstream swimming generally occurs near the annulus boundaries; this is always true of the outer boundary, though it is in some cases suppressed near the inner boundary when accumulation does not occur there as explained in Fig. 8.9. The dependence of the transition to net pumping on the inner radius $r_{\min}$ is illustrated in Fig. 8.10(c): the marginal stability curve varies only weakly with $r_{\min}$ and has a non-monotonic dependence, which again reflects the change in the nature of the equilibrium base state found in Fig. 8.9. In very large annuli ($r_{\min} \to \infty$), the effect of boundary curvature becomes negligible locally and the marginal stability curve asymptotes to that for a straight channel.

Phase III: Spontaneous flow with traveling waves

At yet higher levels of activity, net pumping persists but the azimuthal symmetry of the flow is lost and periodic traveling density waves appear as shown in Fig. 8.7(c) as well as Fig. 8.12 below. Such waves were also observed in experiments on both bacterial [166] and sperm suspensions. [218] As illustrated in Fig. 8.8(b), the average azimuthal velocity $|\overline{V}_\theta|$ in this regime systematically decreases with activity level, as more and more of the motion takes place in the radial direction. As for the other steady states discussed previously, this one was found to be stable over long time intervals. A full characterization of these waves is beyond the scope of the present work. As either $|\alpha|$ is increased or Pe_s decreased, the waves become more intense up to the point when the chaotic state of phase IV emerges; this state

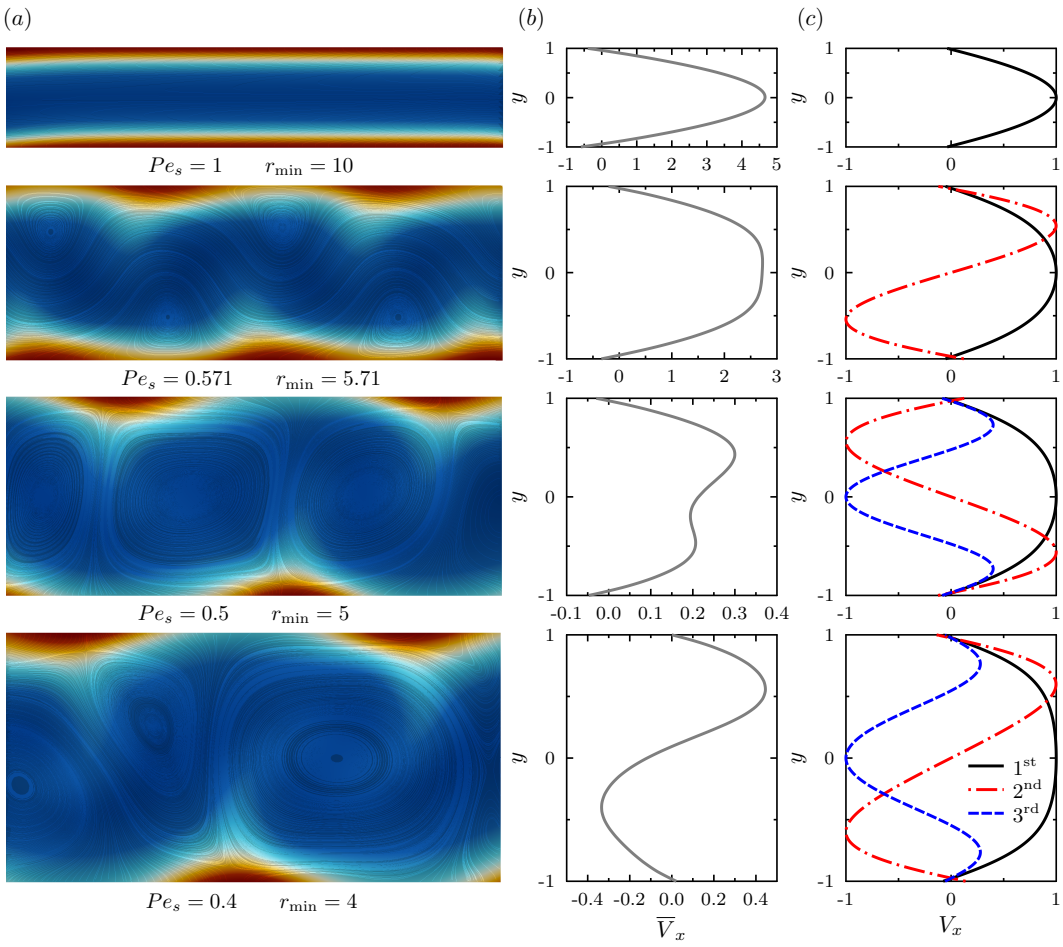

Figure 8.12: (a) Concentration profiles and streamlines of the net particle velocity in straight sections of periodic racetracks, showing four different flow regimes (from top to bottom). (b) Average net velocity profiles across the gap in each case. (c) Unstable linear eigenmodes for these parameter values, obtained in straight channels. Results shown are for $\alpha = -60$ and $\Lambda = 0.5$. Also see electronic supplementary material for a movie showing the dynamics in each case.

is similar to phase III observed above in circular domains.

8.3.3 Periodic channels: racetracks

For direct comparison with the experiments of Wioland *et al.*, [166] we consider as a final example racetrack geometries composed of straight sections of length L connected by two half-annuli as shown in Fig. 8.11. The characteristic length scale for non-dimensionalization is still taken to be the channel half-width H. We focus here on the dynamics in the straight sections; the various flow regimes in this case echo those found in circular annuli and are illustrated in Fig. 8.12(a)-(b), showing instantaneous flow patterns and corresponding mean

velocity profiles. A transition to net pumping is first observed upon increasing channel width at a fixed value of α, followed by the appearance of traveling waves. As the waves become stronger the flow takes the form of alternating counter-rotating vortices and eventually destabilizes into chaos. This phenomenology is identical to that observed in the experiments [166] (see Fig. 4 of that reference). The mean velocity profiles are also consistent with the theoretically predicted unstable linear eigenmodes shown in Fig. 8.12(c) for the same parameter values. The last row in Fig. 8.12 demonstrates the possibility of a more complex flow regime that is only rarely observed: here the flow has a complex unsteady structure, but the mean velocity profile highlights two counter-flowing streams near the top and bottom walls and resembles the second unstable linear mode.

We finish by describing the relationship between the onset of spontaneous pumping in confinement and the effective rheology of the system. In recent work, Alonso-Matilla *et al.* [2] calculated the effective relative viscosity η_r in a dilute active suspension confined in a planar channel and subject to an applied pressure-driven flow, where η_r is defined as the ratio of the flow rate in pure fluid by that in the presence of swimmers at a given pressure gradient. In agreement with previous experiments in the same geometry, [118] suspensions of pushers were found to enhance the flow, i.e. decrease the effective viscosity of the suspension as a result of activity. This effect was found to be the strongest in the limit of vanishing flow strength, and the zero-flow-rate viscosity η_r^0 was further found to decrease with increasing $|\alpha|$, until it eventually reaches zero suggesting an apparent transition to superfluidity. The exact dependence of η_r^0 with activity is plotted in Fig. 8.13(a), where it is found that the value of $|\alpha|$ for which η_r^0 reaches zero coincides precisely with the prediction of the linear theory for the marginal stability of the equilibrium state and onset of spontaneous flow. This provides an additional interpretation for the transition to pumping as a consequence of apparent superfluidity: as the resistance of the system to flow is effectively zero, a small perturbation in the fluid velocity can amplify at no cost leading to unidirectional flow. In the flowing state, the input of mechanical energy by the swimmers exactly balances viscous dissipation in the solvent. This interpretation is further borne out by Fig. 8.13(b), which plots the mean flow rate in the spontaneous flow regime as a function of the length L of the straight section of the racetrack. Remarkably, we observe that the flow rate in the pumping regime is completely independent of channel length, another signature of an effectively frictionless flow.

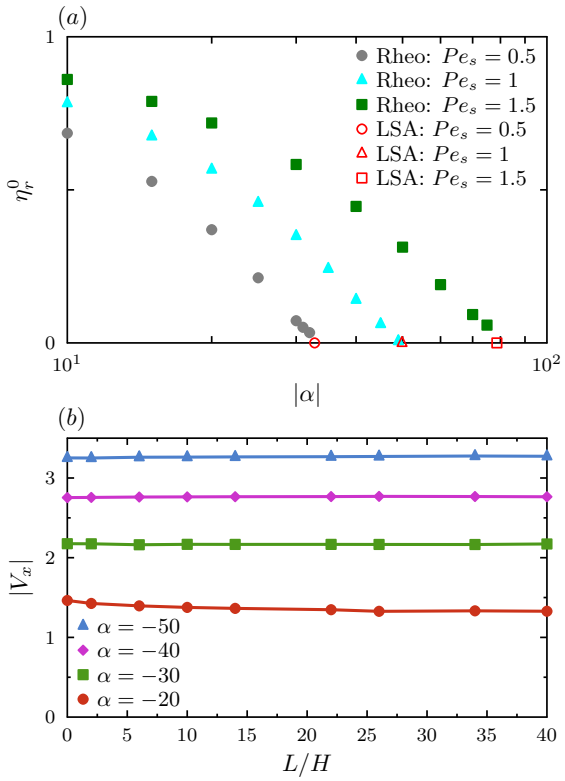

Figure 8.13: (a) Zero-flow-rate relative velocity η_r as a function of activity $|\alpha|$ in a suspension of pushers confined between two flat plates, obtained using the model of Alonso-Matilla *et al.* [2] As activity increases, the relative viscosity decreases and reaches superfluidity at the critical value of $|\alpha|$ for the onset of spontaneous flows as predicted by our linear stability analysis (LSA). This calculation was performed in three dimensions for ease of comparison with the rheological model. (b) Average longitudinal velocity $|V_\parallel|$ as a function of channel length L in periodic racetracks in the spontaneous flow regimes (phases II and III).

8.4 Concluding remarks

We have used a combination of numerical simulations and theory to explore the effect of confinement and geometry on the onset and structure of spontaneous flows in semi-dilute suspensions of active swimming microorganisms. A mean-field theory based on the coupled Smoluchowski and Navier-Stokes equations was used to describe the dynamical evolution of swimmer configurations. We solved these governing equations numerically in two dimensions and compared our numerical results with predictions from a linear stability analysis. Our results agree well with prior experimental studies and were able to capture and explain the spontaneous directed motions arising in pusher suspensions.

We first analyzed the dynamics of swimmers in circular disks, where three distinct flow regimes were found depending on the level of activity and degree of confinement: equi-

librium with no flow, a steady double vortex, and a swirling chaotic state. The equilibrium state manifests at low levels of activity or strong confinement, where the spatial and orientational distribution of particles is axisymmetric and the net disturbance flow generated by the swimmers vanishes. Particles accumulate at the boundaries and on average are radially polarized towards the wall, reaching their maximum polarization at the boundaries. Increasing the level of activity or decreasing confinement destabilizes the system into the double vortex state, and a mechanism based on the shear alignment of the swimmers in the disturbance flow they generate inside the accumulation layer was uncovered. By the same shear alignment mechanism, swimmers were in fact shown to orient against the flow throughout the domain allowing them to swim upstream near the boundary, thus leading to the double vortex structure reported in experiments where bacterial velocities were measured. A further increase in the level of activity or a decrease in confinement originates a second transition to a turbulent-like chaotic state analogous to that observed in bulk systems.

We then turned our focus to swimmer dynamics in periodic geometries. Our simulations in circular annuli captured four flow regimes quite similar to those found in circular disks: an equilibrium state with no flow, an axisymmetric state with net fluid pumping, the emergence of traveling density waves, followed by a chaotic state. The transitions between regimes were again found to be governed by the level of activity and degree of confinement, with only a weak dependence on the inner radius dimension. Similar transitions were also observed in periodic racetracks, where we were able to connect the onset of spontaneous pumping with the effective rheology of the suspension. Specifically, the transition to net pumping was shown to occur at the same level of activity at which the zero-shear-rate viscosity becomes zero in a pressure-driven planar channel flow, suggesting that spontaneous flows in confinement are in fact a consequence of the apparent superfluidity of the system. This conclusion was further supported by observing that the net flow rate is independent of channel length in periodic racetracks.

Our numerical and theoretical results both underscore the subtle interplay between confinement, geometry, and activity in semi-dilute active suspensions. While this study focused on fairly simple geometries previously considered in experiments, we anticipate that a wealth of more complex flow regimes might arise in other types of geometries. Continuum modeling as performed in this work proves to be a valuable tool for the understanding and prediction of these flows and could also play a useful role in the design of microfluidic devices for bioengineering applications involving bacteria.

8.5 Acknowledgements

Chapter 8, in part, is a manuscript published in *Soft Matter*; authored by M. Theillard, R. Alonso-Matilla and D. Saintillan, "Geometric control of active collective motion". The dissertation author is a co-author of this work. We thank Barath Ezhilan, Jérémie Palacci, Hugo Wioland, Zvonimir Dogic, and Michael Shelley for valuable discussions.

Chapter 9

Conclusions and suggested directions for future work

In this thesis, we have combined hydrodynamic theory and statistical mechanics to understand the macroscopic evolution of active suspensions under different external conditions in confinement. We considered several problems, and proposed the underlying physical mechanisms responsible for the results observed through theory and numerical simulations. A close agreement between some of our results and previous studies has been identified, and new observations and applications have been provided.

In Chapters 2 and 3 we presented a macro-continuum transport model, based on generalized Taylor dispersion theory, to predict the asymptotic transport velocity and dispersivity of active Brownian particles in two-dimensional periodic porous media. We started by considering the evolution of a single-particle and used a formal averaging procedure to obtain expressions for its long-time mean velocity vector and dispersivity dyadic, and derived a macroscale Eulerian interpretation for these coefficients under external fluid and chemical fields. We investigated the role of particle activity, external fields and porous lattice geometry on the asymptotic particle transport properties. Physical explanations were provided for all the results, and the macro-continuum model showed perfect agreement with Langevin simulations. Cross stream migration due to particle activity was found to be the cause of a decrease in the effect of shear-induced dispersion, and weak flows were found to reduce axial dispersion. Further studies need to be done to confirm our predictions and develop advanced techniques to control microbial dispersion.

In chapters 4 and 5 the interactions between active particles and boundaries were in-

vestigated. More specifically, in chapter 4 we considered a dilute suspension of athermal run-and-tumble swimmers confined between two osmotic parallel flat plates. A semi-analytical solution method based on a kinetic model comprised of two probability density functions was proposed. The full probability density functions were determined, the mechanical swim pressure exerted on the walls was calculated, and the effect of confinement on the pressure was further analyzed. In chapter 5, we analyzed the temporal evolution of an air/fluid interface of a viscous fluid film and jet containing active Brownian particles. The active forces on the free boundary were modeled through the fluid, and the direct contact force was set to zero in order to satisfy Newton's third law. Linear stability analysis was carried out to explore the stability region in parameter space. Full understanding of how momentum is transmitted from active units into hard boundaries would provide an opportunity to use active systems as energy sources to move cargo in viscous environments. In most existing studies, the calculation of the mechanical force exerted on a boundary by a suspension of microorganisms has been done by assuming that the wall is osmotic, or by considering that the fluid behaves as a sink of momentum, for both thermal [126–128] as well as athermal [14] swimmers. In the absence of intermolecular forces, such as van der Waals or electrostatic forces, the exchange of momentum between living microorganisms and hard boundaries must be attributed to both direct-contact forces and hydrodynamic forces. Hydrodynamics not only contribute to an additional pressure, but also modify the orientation of the swimmers, thus changing the direct-contact force on the walls. Determining the active mechanical pressure on a hard wall without neglecting the presence of the fluid is rather complicated. A recent study [135] addressed the contribution of hydrodynamics on the pressure of an active suspension, comprised of fixed-speed particles, on a non-permeable hard boundary by adding a varying particle drag coefficient to include the hydrodynamic effect with the wall. As a non-deformable particle approaches a rigid boundary, the separation between the bacterial membrane and the wall becomes smaller and the microorganism squeezes the fluid out of the intermediate region. The lubrication forces become important, and the propulsive force necessary to keep the speed of the microorganism constant diverges because the pressure in the gap becomes very large. A parallel approach would be to consider constant force swimmers. In an ideal situation where the bacterial outer membrane is rigid, the Reynolds number of the fluid is zero and the wall roughness is negligible, a constant force swimmer can never reach the wall in finite time. If any of these assumptions is broken, direct contact with the wall would occur and the bacterium would feel a reaction force in the opposite

direction and the swimmer would stop. It would be worth to explore the modeling of the mechanical pressure exerted by a constant-force swimmer on rigid walls, where lubrication forces would prevent the particles from physically touching the wall and the swim pressure would decrease due to hydrodynamics. The solution of this problem would offer insights on how to transport cargo through viscous environments by using active matter systems.

In chapter 6 we studied the effective rheology of a dilute active suspension of self-propelled particles confined between two flat plates and subject to an imposed Poiseuille parabolic flow. Numerical results were discussed and good agreement with experiments was demonstrated. Specifically, our results confirmed the apparent transition to superfluidity reported in recent experiments on pusher suspensions at intermediate densities. In chapter 8 we used a combination of numerical simulations and theory to explore the effect of confinement and geometry on the onset and structure of spontaneous flows in semi-dilute suspensions of active swimming microorganisms. We showed that a system comprised of many independent bacterial cells self-organizes, resulting in a collective motion that is capable of pumping fluid through a micro-channel as well as forming different suspension structures. Our work captured and explained the spontaneous directed motions arising in pusher suspensions, in agreement with prior experimental studies, and we made a connection between the onset of spontaneous pumping with the effective rheology of the suspension. It would be interesting to determine under which geometric variations and external fields (e.g. chemical stimuli, light), the global performance of the bacterial micro-pump would be maximized. In chapter 7, we additionally explored the possibility of driving flows with magnetotactic bacteria, in a controlled manner, and upon the application of a magnetic field. The use of magnetotactic bacterial suspensions as tunable active fluids is a promising avenue, and its rheological response in an external flow was shown to be controlled for the case of spherical particles, by an applied uniform magnetic field. Our current work can be extended to more general systems. For instance, a suspension of non-spherical particles could be considered. In this case, the straining part of the velocity gradient would modify the angular velocity of the particles, and a symmetric contribution to the stress due to the magnetic field would arise. In addition, the particle dipole moment was assumed to be collinear with the direction of motion of the particles, which is a characteristic present in most magnetotactic bacteria so that they can orient and swim along the geomagnetic field lines of the Earth. One could extend the analysis to artificial particles whose dipole moments are oriented at an angle with respect to the swimming direction. Other generalizations include the consideration of Neel

relaxation times, magnetic and steric interactions, non spatially uniform magnetic fields or even time-dependent fields.

Bibliography

[1] Avron J, Gat O, Kenneth O. Optimal swimming at low Reynolds numbers. Physical review letters. 2004;93(18):186001.

[2] Alonso-Matilla R, Ezhilan B, Saintillan D. Microfluidic rheology of active particle suspensions: Kinetic theory. Biomicrofluidics. 2016;10(4):043505.

[3] Waisbord N, Lefèvre CT, Bocquet L, Ybert C, Cottin-Bizonne C. Destabilization of a flow focused suspension of magnetotactic bacteria. Physical Review Fluids. 2016;1(5):053203.

[4] Rosensweig RE. Ferrohydrodynamics. Courier Corporation; 2013.

[5] Pedley TJ, Kessler J. The orientation of spheroidal microorganisms swimming in a flow field. Proc R Soc Lond B. 1987;231(1262):47–70.

[6] Uhlenbeck GE, Ornstein LS. On the theory of the Brownian motion. Physical review. 1930;36(5):823.

[7] Jeffery GB; The Royal Society. The motion of ellipsoidal particles immersed in a viscous fluid. Proc R Soc Lond A. 1922;102(715):161–179.

[8] Chandrasekhar S. Stochastic problems in physics and astronomy. Reviews of modern physics. 1943;15(1):1.

[9] Wang MC, Uhlenbeck GE. On the theory of the Brownian motion II. Reviews of modern physics. 1945;17(2-3):323.

[10] Hubbard PS. Rotational brownian motion. Physical Review A. 1972;6(6):2421.

[11] Kolmogorov AN. Foundations of the Theory of Probability: Second English Edition. Courier Dover Publications; 2018.

[12] Saintillan D. D. Saintillan and MJ Shelley, CR Phys. 14, 497 (2013). CR Phys. 2013;14:497.

[13] Theillard M, Alonso-Matilla R, Saintillan D. Geometric control of active collective motion. Soft Matter. 2017;13(2):363–375.

[14] Ezhilan B, Alonso-Matilla R, Saintillan D. On the distribution and swim pressure of run-and-tumble particles in confinement. Journal of Fluid Mechanics. 2015;781.

[15] Eisenbach M, Tur-Kaspa I. Do human eggs attract spermatozoa? BioEssays. 1999;21(3):203–210.

[16] GRANT L. The sticking and emigration of white blood cells in inflammation. In: The Inflammatory Process (Second Edition), Volume 2. Elsevier; 1973. p. 205–249.

[17] Berg HC, Brown DA, et al. Chemotaxis in Escherichia coli analysed by three-dimensional tracking. Nature. 1972;239(5374):500–504.

[18] Armitage JP, Schmitt R. Bacterial chemotaxis: Rhodobacter sphaeroide and Sinorhizobium meliloti-variations on a theme? Microbiology. 1997;143(12):3671–3682.

[19] Block SM, Segall JE, Berg HC. Impulse responses in bacterial chemotaxis. Cell. 1982;31(1):215–226.

[20] Block SM, Segall JE, Berg HC. Adaptation kinetics in bacterial chemotaxis. Journal of bacteriology. 1983;154(1):312–323.

[21] Segall JE, Block SM, Berg HC. Temporal comparisons in bacterial chemotaxis. Proceedings of the National Academy of Sciences. 1986;83(23):8987–8991.

[22] Othmer HG, Dunbar SR, Alt W. Models of dispersal in biological systems. Journal of mathematical biology. 1988;26(3):263–298.

[23] Macnab RM. Sensing the Environment. In: Biological regulation and development. Springer; 1980. p. 377–412.

[24] Stroock DW. Some stochastic processes which arise from a model of the motion of a bacterium. Zeitschrift für Wahrscheinlichkeitstheorie und verwandte Gebiete. 1974;28(4):305–315.

[25] Alt W. Biased random walk models for chemotaxis and related diffusion approximations. Journal of mathematical biology. 1980;9(2):147–177.

[26] Ford RM, Cummings PT. On the relationship between cell balance equations for chemotactic cell populations. SIAM Journal on Applied Mathematics. 1992;52(5):1426–1441.

[27] Batchelor G. The stress system in a suspension of force-free particles. Journal of fluid mechanics. 1970;41(3):545–570.

[28] Spagnolie SE. Complex fluids in biological systems. Biological and Medical Physics, Biomedical Engineering. 2015;.

[29] Saintillan D. Kinetic models for biologically active suspensions. In: Natural Locomotion in Fluids and on Surfaces. Springer; 2012. p. 53–71.

[30] Bechinger C, Di Leonardo R, Löwen H, Reichhardt C, Volpe G, Volpe G. Active particles in complex and crowded environments. Rev Mod Phys. 2016;88(4):045006.

[31] Volpe G, Buttinoni I, Vogt D, Kümmerer HJ, Bechinger C. Microswimmers in patterned environments. Soft Matter. 2011;7(19):8810–8815.

[32] Mijalkov M, Volpe G. Sorting of chiral microswimmers. Soft Matter. 2013;9(28):6376–6381.

[33] Galajda P, Keymer J, Chaikin P, Austin R. A wall of funnels concentrates swimming bacteria. Journal of bacteriology. 2007;189(23):8704–8707.

[34] Reichhardt C, Reichhardt CO. Dynamics and separation of circularly moving particles in asymmetrically patterned arrays. Physical Review E. 2013;88(4):042306.

[35] Potiguar FQ, Farias G, Ferreira W. Self-propelled particle transport in regular arrays of rigid asymmetric obstacles. Phys Rev E. 2014;90(1):012307.

[36] Yariv E, Schnitzer O. Ratcheting of Brownian swimmers in periodically corrugated channels: A reduced Fokker-Planck approach. Physical Review E. 2014;90(3):032115.

[37] Reichhardt C, Reichhardt CO. Active matter transport and jamming on disordered landscapes. Physical Review E. 2014;90(1):012701.

[38] Kaiser A, Wensink H, Löwen H. How to capture active particles. Physical review letters. 2012;108(26):268307.

[39] Chepizhko O, Peruani F. Diffusion, subdiffusion, and trapping of active particles in heterogeneous media. Phys Rev Lett. 2013;111(16):160604.

[40] Kaiser A, Popowa K, Wensink H, Löwen H. Capturing self-propelled particles in a moving microwedge. Physical Review E. 2013;88(2):022311.

[41] Berke AP, Turner L, Berg HC, Lauga E. Hydrodynamic attraction of swimming microorganisms by surfaces. Physical Review Letters. 2008;101(3):038102.

[42] Takagi D, Palacci J, Braunschweig AB, Shelley MJ, Zhang J. Hydrodynamic capture of microswimmers into sphere-bound orbits. Soft Matter. 2014;10(11):1784–1789.

[43] Spagnolie SE, Moreno-Flores GR, Bartolo D, Lauga E. Geometric capture and escape of a microswimmer colliding with an obstacle. Soft Matter. 2015;11(17):3396–3411.

[44] Berg HC. Random walks in biology. Princeton University Press; 1993.

[45] Zheng X, ten Hagen B, Kaiser A, Wu M, Cui H, Silber-Li Z, et al. Non-Gaussian statistics for the motion of self-propelled Janus particles: Experiment versus theory. Physical Review E. 2013;88(3):032304.

[46] Golestanian R. Anomalous diffusion of symmetric and asymmetric active colloids. Physical review letters. 2009;102(18):188305.

[47] Ten Hagen B, Wittkowski R, Löwen H. Brownian dynamics of a self-propelled particle in shear flow. Physical Review E. 2011;84(3):031105.

[48] Sandoval M, Marath NK, Subramanian G, Lauga E. Stochastic dynamics of active swimmers in linear flows. Journal of Fluid Mechanics. 2014;742:50–70.

[49] Sandoval M, Hidalgo-Gonzalez JC, Jimenez-Aquino JI. Self-driven particles in linear flows and trapped in a harmonic potential. Physical Review E. 2018;97(3):032603.

[50] Apaza L, Sandoval M. Ballistic behavior and trapping of self-driven particles in a Poiseuille flow. Physical Review E. 2016;93(6):062602.

[51] Ezhilan B, Saintillan D. Transport of a dilute active suspension in pressure-driven channel flow. Journal of Fluid Mechanics. 2015;777:482–522.

[52] Yan W, Brady JF. The force on a boundary in active matter. Journal of Fluid Mechanics. 2015;785.

[53] Taylor GI. Dispersion of soluble matter in solvent flowing slowly through a tube. Proc R Soc Lond A. 1953;219(1137):186–203.

[54] Aris R; The Royal Society. On the dispersion of a solute in a fluid flowing through a tube. Proc R Soc Lond A. 1956;235(1200):67–77.

[55] Altshuler E, Mino G, Pérez-Penichet C, del Río L, Lindner A, Rousselet A, et al. Flow-controlled densification and anomalous dispersion of E. coli through a constriction. Soft Matter. 2013;9(6):1864–1870.

[56] Creppy A, Clément E, Douarche C, D'Angelo MV, Auradou H. Motility induces a double positive effect of E. coli dispersion in porous media. arXiv preprint arXiv:180201879. 2018;.

[57] Wykes MSD, Zhong X, Tong J, Adachi T, Liu Y, Ristroph L, et al. Guiding microscale swimmers using teardrop-shaped posts. Soft Matter. 2017;13(27):4681–4688.

[58] Tong J, Shelley MJ. Directed migration of microscale swimmers by an array of shaped obstacles: modeling and shape optimization. arXiv preprint arXiv:170904449. 2017;.

[59] Brown AT, Vladescu ID, Dawson A, Vissers T, Schwarz-Linek J, Lintuvuori JS, et al. Swimming in a crystal. Soft Matter. 2016;12(1):131–140.

[60] Sosa-Hernández JE, Santillán M, Santana-Solano J. Motility of Escherichia coli in a quasi-two-dimensional porous medium. Phys Rev E. 2017;95(3):032404.

[61] Morin A, Cardozo DL, Chikkadi V, Bartolo D. Diffusion, subdiffusion, and localization of active colloids in random post lattices. Phys Rev E. 2017;96(4):042611.

[62] Chamolly A, Ishikawa T, Lauga E. Active particles in periodic lattices. New J Phys. 2017;19(11):115001.

[63] Khalilian H, Fazli H. Obstruction enhances the diffusivity of self-propelled rod-like particles. J Chem Phys. 2016;145(16):164909.

[64] Brenner H. Dispersion resulting from flow through spatially periodic porous media. Phil Trans R Soc Lond A. 1980;297(1430):81–133.

[65] Edwards D, Shapiro M, Brenner H, Shapira M. Dispersion of inert solutes in spatially periodic, two-dimensional model porous media. Transport in Porous Media. 1991;6(4):337–358.

[66] Sangani A, Acrivos A. Slow flow past periodic arrays of cylinders with application to heat transfer. International journal of Multiphase flow. 1982;8(3):193–206.

[67] Yan W, Brady JF. The curved kinetic boundary layer of active matter. Soft matter. 2018;14(2):279–290.

[68] Miño GL, Baabour M, Chertcoff R, Gutkind G, Clément E, Auradou H, et al. E coli Accumulation behind an Obstacle. Advances in Microbiology. 2018;8(06):451.

[69] Laachi N, Kenward M, Yariv E, Dorfman KD. Force-driven transport through periodic entropy barriers. EPL (Europhysics Letters). 2007;80(5):50009.

[70] Bai H, Cochet N, Drelich A, Pauss A, Lamy E. Comparison of transport between two bacteria in saturated porous media with distinct pore size distribution. Rsc Advances. 2016;6(18):14602–14614.

[71] Pandey G, Jain RK. Bacterial chemotaxis toward environmental pollutants: role in bioremediation. Applied and Environmental Microbiology. 2002;68(12):5789–5795.

[72] Ford RM, Harvey RW. Role of chemotaxis in the transport of bacteria through saturated porous media. Advances in Water Resources. 2007;30(6-7):1608–1617.

[73] Ortega-Calvo J, Marchenko A, Vorobyov A, Borovick R. Chemotaxis in polycyclic aromatic hydrocarbon-degrading bacteria isolated from coal-tar-and oil-polluted rhizospheres. FEMS microbiology ecology. 2003;44(3):373–381.

[74] Olson MS, Ford RM, Smith JA, Fernandez EJ. Quantification of bacterial chemotaxis in porous media using magnetic resonance imaging. Environmental science & technology. 2004;38(14):3864–3870.

[75] Ghosh PK, Li Y, Marchegiani G, Marchesoni F. Communication: Memory effects and active Brownian diffusion. AIP Publishing; 2015.

[76] Kim HJ, Huh D, Hamilton G, Ingber DE. Human gut-on-a-chip inhabited by microbial flora that experiences intestinal peristalsis-like motions and flow. Lab on a Chip. 2012;12(12):2165–2174.

[77] Van Loosdrecht M, Lyklema J, Norde W, Schraa G, Zehnder A. Electrophoretic mobility and hydrophobicity as a measured to predict the initial steps of bacterial adhesion. Applied and Environmental Microbiology. 1987;53(8):1898–1901.

[78] Harvey RW, Garabedian SP. Use of colloid filtration theory in modeling movement of bacteria through a contaminated sandy aquifer. Environmental science & technology. 1991;25(1):178–185.

[79] Brenner H. Macrotransport processes. Elsevier; 2013.

[80] Taylor G. Conditions under which dispersion of a solute in a stream of solvent can be used to measure molecular diffusion. Proceedings of the Royal Society of London Series A, Mathematical and Physical Sciences. 1954;p. 473–477.

[81] Brenner H. Macrotransport processes. Langmuir. 1990;6(12):1715–1724.

[82] Bird RB, Stewart WE, Lightfoot EN. Transport phenomena. 1960. Madison, USA. 1960;.

[83] Chilukuri S, Collins CH, Underhill PT. Dispersion of flagellated swimming microorganisms in planar Poiseuille flow. Physics of Fluids. 2015;27(3):031902.

[84] Engelmann TW. Neue Methode zur Untersuchung der Sauerstoffausscheidung pflanzlicher und thierischer Organismen. Archiv für die gesamte Physiologie des Menschen und der Tiere. 1881;25(1):285–292.

[85] Drews G. Contributions of Theodor Wilhelm Engelmann on phototaxis, chemotaxis, and photosynthesis. Photosynthesis research. 2005;83(1):25–34.

[86] Pfeffer W. Uber Chemotaktische Bewegungen von Bacterien, Flagellaten und Volvocineen. Untersuch Bot Inst Tubingen. 1888;2:582–661.

[87] Clayton RK. On the interplay of environmental factors affecting taxis and motility in Rhodospirillum rubrum. Archiv für Mikrobiologie. 1958;29(2):189–212.

[88] Sherris J, Preston N, Shoesmith J. The influence of oxygen and arginine on the motility of a strain of Pseudomonas sp. Microbiology. 1957;16(1):86–96.

[89] Baracchini O, Sherris J. The chemotactic effect of oxygen on bacteria. The Journal of Pathology. 1959;77(2):565–574.

[90] Adler J. Chemotaxis in bacteria. Science. 1966;153(3737):708–716.

[91] Adler J, Dahl MM. A method for measuring the motility of bacteria and for comparing random and non-random motility. Microbiology. 1967;46(2):161–173.

[92] Keller EF, Segel LA. Traveling bands of chemotactic bacteria: a theoretical analysis. Journal of theoretical biology. 1971;30(2):235–248.

[93] Nossal R. Growth and movement of rings of chemotactic bacteria. Experimental cell research. 1972;75(1):138–142.

[94] Budrene EO, Berg HC. Complex patterns formed by motile cells of Escherichia coli. Nature. 1991;349(6310):630.

[95] Brenner MP, Levitov LS, Budrene EO. Physical mechanisms for chemotactic pattern formation by bacteria. Biophysical journal. 1998;74(4):1677–1693.

[96] Croze OA, Ferguson GP, Cates ME, Poon WC. Migration of chemotactic bacteria in soft agar: role of gel concentration. Biophysical journal. 2011;101(3):525–534.

[97] Locsei J, Pedley T. Run and tumble chemotaxis in a shear flow: the effect of temporal comparisons, persistence, rotational diffusion, and cell shape. Bulletin of mathematical biology. 2009;71(5):1089–1116.

[98] Subramanian G, Koch DL, Fitzgibbon SR. The stability of a homogeneous suspension of chemotactic bacteria. Physics of Fluids. 2011;23(4):041901.

[99] Kasyap T, Koch DL. Chemotaxis driven instability of a confined bacterial suspension. Physical review letters. 2012;108(3):038101.

[100] Ezhilan B, Pahlavan AA, Saintillan D. Chaotic dynamics and oxygen transport in thin films of aerotactic bacteria. Physics of Fluids. 2012;24(9):091701.

[101] Lushi E, Goldstein RE, Shelley MJ. Collective chemotactic dynamics in the presence of self-generated fluid flows. Physical Review E. 2012;86(4):040902.

[102] Rolfe RD. The role of probiotic cultures in the control of gastrointestinal health. The Journal of nutrition. 2000;130(2):396S–402S.

[103] Larsen SH, Adler J, Gargus JJ, Hogg RW. Chemomechanical coupling without ATP: the source of energy for motility and chemotaxis in bacteria. Proceedings of the National Academy of Sciences. 1974;71(4):1239–1243.

[104] Berg H. A physicist looks at bacterial chemotaxis. In: Cold Spring Harbor Symposia on Quantitative Biology. vol. 53. Cold Spring Harbor Laboratory Press; 1988. p. 1–9.

[105] Eisenbach M. Chemotaxis. World Scientific Publishing Company; 2004.

[106] Berg HC, Purcell EM. Physics of chemoreception. Biophysical journal. 1977;20(2):193–219.

[107] Berg HC, Anderson RA. Bacteria swim by rotating their flagellar filaments. Nature. 1973;245(5425):380.

[108] Eisenbach M. Functions of the flagellar modes of rotation in bacterial motility and chemotaxis. Molecular microbiology. 1990;4(2):161–167.

[109] Macnab RM, Koshland D. The gradient-sensing mechanism in bacterial chemotaxis. Proceedings of the National Academy of Sciences. 1972;69(9):2509–2512.

[110] Brown DA, Berg HC. Temporal stimulation of chemotaxis in Escherichia coli. Proceedings of the National Academy of Sciences. 1974;71(4):1388–1392.

[111] Rivero MA, Tranquillo RT, Buettner HM, Lauffenburger DA. Transport models for chemotactic cell populations based on individual cell behavior. Chemical engineering science. 1989;44(12):2881–2897.

[112] Subramanian G, Koch DL. Critical bacterial concentration for the onset of collective swimming. Journal of Fluid Mechanics. 2009;632:359–400.

[113] Lushi E. Stability and dynamics of anisotropically tumbling chemotactic swimmers. Physical Review E. 2016;94(2):022414.

[114] Schnitzer MJ. Theory of continuum random walks and application to chemotaxis. Physical Review E. 1993;48(4):2553.

[115] Lovely PS, Dahlquist F. Statistical measures of bacterial motility and chemotaxis. Journal of theoretical biology. 1975;50(2):477–496.

[116] Berg HC. E. coli in Motion. Springer Science & Business Media; 2008.

[117] Bearon R. An extension of generalized Taylor dispersion in unbounded homogeneous shear flows to run-and-tumble chemotactic bacteria. Physics of Fluids. 2003;15(6):1552–1563.

[118] Gachelin J, Mino G, Berthet H, Lindner A, Rousselet A, Clément É. Non-Newtonian viscosity of Escherichia coli suspensions. Physical review letters. 2013;110(26):268103.

[119] Figueroa-Morales N, Miño GL, Rivera A, Caballero R, Clément E, Altshuler E, et al. Living on the edge: transfer and traffic of E. coli in a confined flow. Soft Matter. 2015;11(31):6284–6293.

[120] Hernandez-Ortiz JP, Stoltz CG, Graham MD. Transport and collective dynamics in suspensions of confined swimming particles. Physical review letters. 2005;95(20):204501.

[121] Elgeti J, Gompper G. Wall accumulation of self-propelled spheres. EPL (Europhysics Letters). 2013;101(4):48003.

[122] Li GJ, Ardekani AM. Hydrodynamic interaction of microswimmers near a wall. Physical Review E. 2014;90(1):013010.

[123] Li G, Bensson J, Nisimova L, Munger D, Mahautmr P, Tang JX, et al. Accumulation of swimming bacteria near a solid surface. Physical Review E. 2011;84(4):041932.

[124] Lee CF. Active particles under confinement: aggregation at the wall and gradient formation inside a channel. New Journal of Physics. 2013;15(5):055007.

[125] Elgeti J, Gompper G. Run-and-tumble dynamics of self-propelled particles in confinement. EPL (Europhysics Letters). 2015;109(5):58003.

[126] Takatori SC, Yan W, Brady JF. Swim pressure: stress generation in active matter. Physical review letters. 2014;113(2):028103.

[127] Yang X, Manning ML, Marchetti MC. Aggregation and segregation of confined active particles. Soft matter. 2014;10(34):6477–6484.

[128] Winkler RG, Wysocki A, Gompper G. Virial pressure in systems of spherical active Brownian particles. Soft matter. 2015;11(33):6680–6691.

[129] Solon AP, Stenhammar J, Wittkowski R, Kardar M, Kafri Y, Cates ME, et al. Pressure and phase equilibria in interacting active Brownian spheres. Physical review letters. 2015;114(19):198301.

[130] Takatori SC, Brady JF. Towards a thermodynamics of active matter. Physical Review E. 2015;91(3):032117.

[131] Ray D, Reichhardt C, Reichhardt CO. Casimir effect in active matter systems. Physical Review E. 2014;90(1):013019.

[132] Mallory S, Šarić A, Valeriani C, Cacciuto A. Anomalous thermomechanical properties of a self-propelled colloidal fluid. Physical Review E. 2014;89(5):052303.

[133] Ginot F, Theurkauff I, Levis D, Ybert C, Bocquet L, Berthier L, et al. Nonequilibrium equation of state in suspensions of active colloids. Physical Review X. 2015;5(1):011004.

[134] Solon AP, Fily Y, Baskaran A, Cates ME, Kafri Y, Kardar M, et al. Pressure is not a state function for generic active fluids. Nature Physics. 2015;11(8):673.

[135] Burkholder EW, Brady JF. Do hydrodynamic interactions affect the swim pressure? Soft matter. 2018;14(18):3581–3589.

[136] Fily Y, Baskaran A, Hagan MF. Dynamics of self-propelled particles under strong confinement. Soft matter. 2014;10(30):5609–5617.

[137] Wysocki A, Elgeti J, Gompper G. Giant adsorption of microswimmers: duality of shape asymmetry and wall curvature. Physical Review E. 2015;91(5):050302.

[138] Kantsler V, Dunkel J, Polin M, Goldstein RE. Ciliary contact interactions dominate surface scattering of swimming eukaryotes. Proceedings of the National Academy of Sciences. 2013;110(4):1187–1192.

[139] Molaei M, Barry M, Stocker R, Sheng J. Failed escape: solid surfaces prevent tumbling of Escherichia coli. Physical review letters. 2014;113(6):068103.

[140] Saintillan D, Shelley MJ. Active suspensions and their nonlinear models. Comptes Rendus Physique. 2013;14(6):497–517.

[141] Ramia M, Tullock D, Phan-Thien N. The role of hydrodynamic interaction in the locomotion of microorganisms. Biophysical journal. 1993;65(2):755–778.

[142] Fauci LJ, McDonald A. Sperm motility in the presence of boundaries. Bulletin of mathematical biology. 1995;57(5):679–699.

[143] Frymier PD, Ford RM, Berg HC, Cummings PT. Three-dimensional tracking of motile bacteria near a solid planar surface. Proceedings of the National Academy of Sciences. 1995;92(13):6195–6199.

[144] Cosson J, Huitorel P, Gagnon C. How spermatozoa come to be confined to surfaces. Cytoskeleton. 2003;54(1):56–63.

[145] DiLuzio WR, Turner L, Mayer M, Garstecki P, Weibel DB, Berg HC, et al. Escherichia coli swim on the right-hand side. Nature. 2005;435(7046):1271.

[146] Lauga E, DiLuzio WR, Whitesides GM, Stone HA. Swimming in circles: motion of bacteria near solid boundaries. Biophysical journal. 2006;90(2):400–412.

[147] Zilman G, Novak J, Benayahu Y. How do larvae attach to a solid in a laminar flow? Marine biology. 2008;154(1):1–26.

[148] Zargar R, Najafi A, Miri M. Three-sphere low-Reynolds-number swimmer near a wall. Physical Review E. 2009;80(2):026308.

[149] Kaya T, Koser H. Characterization of hydrodynamic surface interactions of Escherichia coli cell bodies in shear flow. Physical review letters. 2009;103(13):138103.

[150] Li G, Tang JX. Accumulation of microswimmers near a surface mediated by collision and rotational Brownian motion. Physical review letters. 2009;103(7):078101.

[151] Drescher K, Leptos KC, Tuval I, Ishikawa T, Pedley TJ, Goldstein RE. Dancing volvox: hydrodynamic bound states of swimming algae. Physical Review Letters. 2009;102(16):168101.

[152] Crowdy DG, Or Y. Two-dimensional point singularity model of a low-Reynolds-number swimmer near a wall. Physical Review E. 2010;81(3):036313.

[153] Ishimoto K, Cosson J, Gaffney EA. A simulation study of sperm motility hydrodynamics near fish eggs and spheres. Journal of theoretical biology. 2016;389:187–197.

[154] Childress S, Levandowsky M, Spiegel E. Pattern formation in a suspension of swimming microorganisms: equations and stability theory. Journal of Fluid Mechanics. 1975;69(3):591–613.

[155] Kessler JO. Gyrotactic buoyant convection and spontaneous pattern formation in algal cell cultures. In: Nonequilibrium cooperative phenomena in physics and related fields. Springer; 1984. p. 241–248.

[156] Pedley T, Hill N, Kessler J. The growth of bioconvection patterns in a uniform suspension of gyrotactic micro-organisms. Journal of Fluid Mechanics. 1988;195:223–237.

[157] Pedley T, Kessler J. A new continuum model for suspensions of gyrotactic microorganisms. Journal of Fluid Mechanics. 1990;212:155–182.

[158] Simha RA, Ramaswamy S. Hydrodynamic fluctuations and instabilities in ordered suspensions of self-propelled particles. Physical review letters. 2002;89(5):058101.

[159] Saintillan D, Shelley MJ. Orientational order and instabilities in suspensions of self-locomoting rods. Physical review letters. 2007;99(5):058102.

[160] Saintillan D, Shelley MJ. Instabilities, pattern formation, and mixing in active suspensions. Physics of Fluids. 2008;20(12):123304.

[161] Sokolov A, Goldstein RE, Feldchtein FI, Aranson IS. Enhanced mixing and spatial instability in concentrated bacterial suspensions. Physical Review E. 2009;80(3):031903.

[162] Ezhilan B, Shelley MJ, Saintillan D. Instabilities and nonlinear dynamics of concentrated active suspensions. Physics of Fluids. 2013;25(7):070607.

[163] Saintillan D, Shelley MJ. Emergence of coherent structures and large-scale flows in motile suspensions. Journal of the Royal Society Interface. 2011;p. rsif20110355.

[164] Wioland H, Woodhouse FG, Dunkel J, Kessler JO, Goldstein RE. Confinement stabilizes a bacterial suspension into a spiral vortex. Physical review letters. 2013;110(26):268102.

[165] Lushi E, Wioland H, Goldstein RE. Fluid flows created by swimming bacteria drive self-organization in confined suspensions. Proceedings of the National Academy of Sciences. 2014;111(27):9733–9738.

[166] Wioland H, Lushi E, Goldstein RE. Directed collective motion of bacteria under channel confinement. New Journal of Physics. 2016;18(7):075002.

[167] Hatwalne Y, Ramaswamy S, Rao M, Simha RA. Rheology of active-particle suspensions. Physical review letters. 2004;92(11):118101.

[168] Sokolov A, Aranson IS. Reduction of viscosity in suspension of swimming bacteria. Physical Review Letters. 2009;103(14):148101.

[169] Saintillan D. The dilute rheology of swimming suspensions: A simple kinetic model. Experimental Mechanics. 2010;50(9):1275–1281.

[170] López HM, Gachelin J, Douarche C, Auradou H, Clément E. Turning bacteria suspensions into superfluids. Physical review letters. 2015;115(2):028301.

[171] Takatori S, Brady J. Superfluid behavior of active suspensions from diffusive stretching. Physical review letters. 2017;118(1):018003.

[172] Nambiar S, Nott P, Subramanian G. Stress relaxation in a dilute bacterial suspension. Journal of Fluid Mechanics. 2017;812:41–64.

[173] Alonso-Matilla R, Saintillan D. Microfluidic flow actuation using magnetoactive suspensions. EPL (Europhysics Letters). 2018;121(2):24002.

[174] Nürnberg A, Kitzing T, Grosse R. Nucleating actin for invasion. Nature Reviews Cancer. 2011;11(3):177.

[175] Hoshino D, Branch KM, Weaver AM. Signaling inputs to invadopodia and podosomes. J Cell Sci. 2013;126(14):2979–2989.

[176] Martin P, Parkhurst SM. Parallels between tissue repair and embryo morphogenesis. Development. 2004;131(13):3021–3034.

[177] Sherratt J, Murray J. Mathematical analysis of a basic model for epidermal wound healing. Journal of mathematical biology. 1991;29(5):389–404.

[178] Dale PD, Maini PK, Sherratt JA. Mathematical modeling of corneal epithelial wound healing. Mathematical biosciences. 1994;124(2):127–147.

[179] Mark S, Shlomovitz R, Gov NS, Poujade M, Grasland-Mongrain E, Silberzan P. Physical model of the dynamic instability in an expanding cell culture. Biophysical journal. 2010;98(3):361–370.

[180] Zimmermann J, Basan M, Levine H. An instability at the edge of a tissue of collectively migrating cells can lead to finger formation during wound healing. The European Physical Journal Special Topics. 2014;223(7):1259–1264.

[181] Sanchez T, Chen DT, DeCamp SJ, Heymann M, Dogic Z. Spontaneous motion in hierarchically assembled active matter. Nature. 2012;491(7424):431.

[182] Giomi L, DeSimone A. Spontaneous division and motility in active nematic droplets. Physical review letters. 2014;112(14):147802.

[183] Keber FC, Loiseau E, Sanchez T, DeCamp SJ, Giomi L, Bowick MJ, et al. Topology and dynamics of active nematic vesicles. Science. 2014;345(6201):1135–1139.

[184] Poulard C, Cazabat A. Spontaneous spreading of nematic liquid crystals. Langmuir. 2005;21(14):6270–6276.

[185] Poulard C, Voué M, De Coninck J, Cazabat A. Spreading of nematic liquid crystals on hydrophobic substrates. Colloids and Surfaces A: Physicochemical and Engineering Aspects. 2006;282:240–246.

[186] Tjhung E, Marenduzzo D, Cates ME. Spontaneous symmetry breaking in active droplets provides a generic route to motility. Proceedings of the National Academy of Sciences. 2012;109(31):12381–12386.

[187] Joanny JF, Ramaswamy S. A drop of active matter. Journal of Fluid Mechanics. 2012;705:46–57.

[188] Whitfield CA, Marenduzzo D, Voituriez R, Hawkins RJ. Active polar fluid flow in finite droplets. The European Physical Journal E. 2014;37(2):8.

[189] Khoromskaia D, Alexander GP. Motility of active fluid drops on surfaces. Physical Review E. 2015;92(6):062311.

[190] Ben Amar M, Cummings L. Fingering instabilities in driven thin nematic films. Physics of Fluids. 2001;13(5):1160–1166.

[191] Voituriez R, Joanny J, Prost J. Generic phase diagram of active polar films. Physical review letters. 2006;96(2):028102.

[192] Sankararaman S, Ramaswamy S. Instabilities and waves in thin films of living fluids. Physical review letters. 2009;102(11):118107.

[193] Blow ML, Aqil M, Liebchen B, Marenduzzo D. Motility of active nematic films driven by ?active anchoring? Soft matter. 2017;13(36):6137–6144.

[194] Bretherton FP. The motion of rigid particles in a shear flow at low Reynolds number. Journal of Fluid Mechanics. 1962;14(2):284–304.

[195] Yiantsios SG, Higgins BG. Rayleigh–Taylor instability in thin viscous films. Physics of Fluids A: Fluid Dynamics. 1989;1(9):1484–1501.

[196] Suarez S, Pacey A. Sperm transport in the female reproductive tract. Human reproduction update. 2006;12(1):23–37.

[197] Denissenko P, Kantsler V, Smith DJ, Kirkman-Brown J. Human spermatozoa migration in microchannels reveals boundary-following navigation. Proceedings of the National Academy of Sciences. 2012;109(21):8007–8010.

[198] Kantsler V, Dunkel J, Blayney M, Goldstein RE. Rheotaxis facilitates upstream navigation of mammalian sperm cells. Elife. 2014;3.

[199] Hulme SE, DiLuzio WR, Shevkoplyas SS, Turner L, Mayer M, Berg HC, et al. Using ratchets and sorters to fractionate motile cells of Escherichia coli by length. Lab on a Chip. 2008;8(11):1888–1895.

[200] Lambert G, Liao D, Austin RH. Collective escape of chemotactic swimmers through microscopic ratchets. Physical review letters. 2010;104(16):168102.

[201] Hill J, Kalkanci O, McMurry JL, Koser H. Hydrodynamic surface interactions enable Escherichia coli to seek efficient routes to swim upstream. Physical review letters. 2007;98(6):068101.

[202] Kaya T, Koser H. Direct upstream motility in Escherichia coli. Biophysical journal. 2012;102(7):1514–1523.

[203] Rusconi R, Guasto JS, Stocker R. Bacterial transport suppressed by fluid shear. Nature physics. 2014;10(3):212.

[204] Drescher K, Goldstein RE, Michel N, Polin M, Tuval I. Direct measurement of the flow field around swimming microorganisms. Physical Review Letters. 2010;105(16):168101.

[205] Guasto JS, Johnson KA, Gollub JP. Oscillatory flows induced by microorganisms swimming in two dimensions. Physical review letters. 2010;105(16):168102.

[206] Drescher K, Dunkel J, Cisneros LH, Ganguly S, Goldstein RE. Fluid dynamics and noise in bacterial cell–cell and cell–surface scattering. Proceedings of the National Academy of Sciences. 2011;108(27):10940–10945.

[207] Haines BM, Aranson IS, Berlyand L, Karpeev DA. Effective viscosity of dilute bacterial suspensions: a two-dimensional model. Physical biology. 2008;5(4):046003.

[208] Haines BM, Sokolov A, Aranson IS, Berlyand L, Karpeev DA. Three-dimensional model for the effective viscosity of bacterial suspensions. Physical Review E. 2009;80(4):041922.

[209] Saintillan D. Extensional rheology of active suspensions. Physical Review E. 2010;81(5):056307.

[210] Heidenreich S, Hess S, Klapp SH. Nonlinear rheology of active particle suspensions: Insights from an analytical approach. Physical Review E. 2011;83(1):011907.

[211] Ryan SD, Haines BM, Berlyand L, Ziebert F, Aranson IS. Viscosity of bacterial suspensions: Hydrodynamic interactions and self-induced noise. Physical Review E. 2011;83(5):050904.

[212] Bozorgi Y, Underhill PT. Large-amplitude oscillatory shear rheology of dilute active suspensions. Rheologica Acta. 2014;53(12):899–909.

[213] Forest MG, Phuworawong P, Wang Q, Zhou R. Rheological signatures in limit cycle behaviour of dilute, active, polar liquid crystalline polymers in steady shear. Phil Trans R Soc A. 2014;372(2029):20130362.

[214] Moradi M, Najafi A. Rheological properties of a dilute suspension of self-propelled particles. EPL (Europhysics Letters). 2015;109(2):24001.

[215] Batchelor G. The stress generated in a non-dilute suspension of elongated particles by pure straining motion. Journal of Fluid Mechanics. 1971;46(4):813–829.

[216] Brenner H. Rheology of a dilute suspension of axisymmetric Brownian particles. International journal of multiphase flow. 1974;1(2):195–341.

[217] Hinch E, Leal L. Constitutive equations in suspension mechanics. Part 2. Approximate forms for a suspension of rigid particles affected by Brownian rotations. Journal of Fluid Mechanics. 1976;76(1):187–208.

[218] Creppy A, Plouraboué F, Praud O, Druart X, Cazin S, Yu H, et al. Symmetry-breaking phase transitions in highly concentrated semen. Journal of The Royal Society Interface. 2016;13(123):20160575.

[219] Voituriez R, Joanny JF, Prost J. Spontaneous flow transition in active polar gels. EPL (Europhysics Letters). 2005;70(3):404.

[220] Ravnik M, Yeomans JM. Confined active nematic flow in cylindrical capillaries. Physical review letters. 2013;110(2):026001.

[221] Rafaï S, Jibuti L, Peyla P. Effective viscosity of microswimmer suspensions. Physical Review Letters. 2010;104(9):098102.

[222] McDonnell AG, Gopesh TC, Lo J, O'Bryan M, Yeo LY, Friend JR, et al. Motility induced changes in viscosity of suspensions of swimming microbes in extensional flows. Soft Matter. 2015;11(23):4658–4668.

[223] Saintillan D, Shelley MJ. Instabilities and pattern formation in active particle suspensions: kinetic theory and continuum simulations. Physical Review Letters. 2008;100(17):178103.

[224] Batchelor G. Slender-body theory for particles of arbitrary cross-section in Stokes flow. Journal of Fluid Mechanics. 1970;44(3):419–440.

[225] Nash R, Adhikari R, Tailleur J, Cates M. Run-and-tumble particles with hydrodynamics: Sedimentation, trapping, and upstream swimming. Physical review letters. 2010;104(25):258101.

[226] Costanzo A, Di Leonardo R, Ruocco G, Angelani L. Transport of self-propelling bacteria in micro-channel flow. Journal of Physics: Condensed Matter. 2012;24(6):065101.

[227] Chilukuri S, Collins CH, Underhill PT. Impact of external flow on the dynamics of swimming microorganisms near surfaces. Journal of Physics: Condensed Matter. 2014;26(11):115101.

[228] Bearon R, Hazel A. The trapping in high-shear regions of slender bacteria undergoing chemotaxis in a channel. Journal of Fluid Mechanics. 2015;771.

[229] Schiek RL, Shaqfeh ES. A nonlocal theory for stress in bound, Brownian suspensions of slender, rigid fibres. Journal of Fluid Mechanics. 1995;296:271–324.

[230] Saintillan D. Rheology of active fluids. Annual Review of Fluid Mechanics. 2018;50:563–592.

[231] Guazzelli E, Morris JF. A physical introduction to suspension dynamics. vol. 45. Cambridge University Press; 2011.

[232] Sheng P, Wen W. Electrorheological fluids: mechanisms, dynamics, and microfluidics applications. Annual review of fluid mechanics. 2012;44:143–174.

[233] De Vicente J, Klingenberg DJ, Hidalgo-Alvarez R. Magnetorheological fluids: a review. Soft matter. 2011;7(8):3701–3710.

[234] McTague JP. Magnetoviscosity of magnetic colloids. The Journal of Chemical Physics. 1969;51(1):133–136.

[235] Brenner H. Rheology of a dilute suspension of dipolar spherical particles in an external field. Journal of Colloid and Interface Science. 1970;32(1):141–158.

[236] Hall W, Busenberg S. Viscosity of magnetic suspensions. The Journal of Chemical Physics. 1969;51(1):137–144.

[237] Levi A, Hobson R, McCourt F. Magnetoviscosity of colloidal suspensions. Canadian Journal of Physics. 1973;51(2):180–194.

[238] Leal L. On the effect of particle couples on the motion of a dilute suspension of spheroids. Journal of Fluid Mechanics. 1971;46(2):395–416.

[239] He X, Elborai S, Kim D, Lee SH, Zahn M. Effective magnetoviscosity of planar-Couette magnetic fluid flow. Journal of applied physics. 2005;97(10):10Q302.

[240] Blakemore R. Magnetotactic bacteria. Science. 1975;190(4212):377–379.

[241] van Oene MM, Dickinson LE, Pedaci F, Köber M, Dulin D, Lipfert J, et al. Biological magnetometry: torque on superparamagnetic beads in magnetic fields. Physical review letters. 2015;114(21):218301.

[242] Matsunaga D, Meng F, Zöttl A, Golestanian R, Yeomans JM. Focusing and sorting of ellipsoidal magnetic particles in microchannels. Physical review letters. 2017;119(19):198002.

[243] Lauga E, Nadal F. Clustering instability of focused swimmers. EPL (Europhysics Letters). 2017;116(6):64004.

[244] Meng F, Matsunaga D, Golestanian R. Clustering of magnetic swimmers in a Poiseuille flow. Physical review letters. 2018;120(18):188101.

[245] Frankel RB. Magnetic guidance of organisms. Annual review of biophysics and bioengineering. 1984;13(1):85–103.

[246] Saintillan D, Shelley MJ. Theory of active suspensions. In: Complex Fluids in biological systems. Springer; 2015. p. 319–355.

[247] Doi M, Edwards SF. The theory of polymer dynamics. vol. 73. oxford university press; 1988.

[248] Kim S, Karrila SJ. Microhydrodynamics: principles and selected applications. Courier Corporation; 2013.

[249] Brenner H, Weissman MH. Rheology of a dilute suspension of dipolar spherical particles in an external field. II. Effects of rotary Brownian motion. Journal of Colloid and Interface Science. 1972;41(3):499–531.

[250] Jansons KM. Determination of the constitutive equations for a magnetic fluid. Journal of Fluid Mechanics. 1983;137:187–216.

[251] Vincenti B, Douarche C, Clement E. Actuated rheology of magnetic micro-swimmers suspensions: Emergence of motor and brake states. Physical Review Fluids. 2018;3(3):033302.

[252] Marchetti MC, Joanny JF, Ramaswamy S, Liverpool TB, Prost J, Rao M, et al. Hydrodynamics of soft active matter. Reviews of Modern Physics. 2013;85(3):1143.

[253] Cisneros LH, Kessler JO, Ganguly S, Goldstein RE. Dynamics of swimming bacteria: Transition to directional order at high concentration. Physical Review E. 2011;83(6):061907.

[254] Wensink HH, Dunkel J, Heidenreich S, Drescher K, Goldstein RE, Löwen H, et al. Meso-scale turbulence in living fluids. Proceedings of the National Academy of Sciences. 2012;109(36):14308–14313.

[255] Dunkel J, Heidenreich S, Drescher K, Wensink HH, Bär M, Goldstein RE. Fluid dynamics of bacterial turbulence. Physical review letters. 2013;110(22):228102.

[256] Gachelin J, Rousselet A, Lindner A, Clement E. Collective motion in an active suspension of Escherichia coli bacteria. New Journal of Physics. 2014;16(2):025003.

[257] Surrey T, Nédélec F, Leibler S, Karsenti E. Physical properties determining self-organization of motors and microtubules. Science. 2001;292(5519):1167–1171.

[258] Schaller V, Weber C, Semmrich C, Frey E, Bausch AR. Polar patterns of driven filaments. Nature. 2010;467(7311):73.

[259] Bricard A, Caussin JB, Desreumaux N, Dauchot O, Bartolo D. Emergence of macroscopic directed motion in populations of motile colloids. Nature. 2013;503(7474):95.

[260] Bricard A, Caussin JB, Das D, Savoie C, Chikkadi V, Shitara K, et al. Emergent vortices in populations of colloidal rollers. Nature communications. 2015;6:7470.

[261] Kudrolli A, Lumay G, Volfson D, Tsimring LS. Swarming and swirling in self-propelled polar granular rods. Physical review letters. 2008;100(5):058001.

[262] Deseigne J, Dauchot O, Chaté H. Collective motion of vibrated polar disks. Physical review letters. 2010;105(9):098001.

[263] Tsang ACH, Kanso E. Circularly confined microswimmers exhibit multiple global patterns. Physical Review E. 2015;91(4):043008.

[264] Lefauve A, Saintillan D. Globally aligned states and hydrodynamic traffic jams in confined suspensions of active asymmetric particles. Physical Review E. 2014;89(2):021002.

[265] Tsang ACH, Kanso E. Density shock waves in confined microswimmers. Physical review letters. 2016;116(4):048101.

[266] Lauga E, Powers TR. The hydrodynamics of swimming microorganisms. Reports on Progress in Physics. 2009;72(9):096601.

[267] Baskaran A, Marchetti MC. Statistical mechanics and hydrodynamics of bacterial suspensions. Proceedings of the National Academy of Sciences. 2009;106(37):15567–15572.

[268] Vladescu I, Marsden E, Schwarz-Linek J, Martinez V, Arlt J, Morozov A, et al. Filling an emulsion drop with motile bacteria. Physical review letters. 2014;113(26):268101.

[269] Spagnolie SE, Lauga E. Hydrodynamics of self-propulsion near a boundary: predictions and accuracy of far-field approximations. Journal of Fluid Mechanics. 2012;700:105–147.

[270] Schaar K, Zöttl A, Stark H. Detention times of microswimmers close to surfaces: influence of hydrodynamic interactions and noise. Physical review letters. 2015;115(3):038101.

[271] Wioland H, Woodhouse FG, Dunkel J, Goldstein RE. Ferromagnetic and antiferromagnetic order in bacterial vortex lattices. Nature physics. 2016;12(4):341.

[272] Min C, Gibou F, Ceniceros HD. A supra-convergent finite difference scheme for the variable coefficient Poisson equation on non-graded grids. Journal of Computational Physics. 2006;218(1):123–140.

[273] Mirzadeh M, Theillard M, Gibou F. A second-order discretization of the nonlinear Poisson–Boltzmann equation over irregular geometries using non-graded adaptive Cartesian grids. Journal of Computational Physics. 2011;230(5):2125–2140.

[274] Theillard M, Rycroft CH, Gibou F. A multigrid method on non-graded adaptive octree and quadtree Cartesian grids. Journal of Scientific Computing. 2013;55(1):1–15.

[275] Guittet A, Theillard M, Gibou F. A stable projection method for the incompressible Navier–Stokes equations on arbitrary geometries and adaptive Quad/Octrees. Journal of Computational Physics. 2015;292:215–238.

[276] Mathijssen AJ, Shendruk TN, Yeomans JM, Doostmohammadi A. Upstream swimming in microbiological flows. Physical review letters. 2016;116(2):028104.

[277] Hohenegger C, Shelley MJ. Stability of active suspensions. Physical Review E. 2010;81(4):046311.